UNIVERSITÀ DEGLI STUDI DI MILANO

Department of Physics

PhD School in Physics, Astrophysics and Applied Physics

Cycle XXXIII

Constraints on neutron star structure from pulsar glitches

Disciplinary Scientific Sector FIS/05

Supervisor: Prof. Pierre M. Pizzochero

Co-supervisor: Dr. Marco Antonelli

School Director: Prof. Matteo Paris

PhD Thesis of:

Alessandro Montoli

Academic year 2020–2021

Final examination committee:

External Referee: Doctor Cristóbal M. Espinoza, Universidad de Santiago de Chile, Departamento de Física

External Referee: Professor Andrew Melatos, University of Melbourne, School of Physics

External Member: Professor Francesca Gulminelli, Université Caen Normandie, LPC/ENSICAEN, CNRS/IN2P3

External Member: Professor Nils Andersson, University of Southampton, Mathematical Sciences and STAG Research Centre

External Member: Professor Michał Bejger, Nicolaus Copernicus Astronomical Center, Polish Academy of Sciences

Final examination:

Friday, December 18, 2020

Università degli Studi di Milano, Dipartimento di Fisica, Milano, Italy

Cover illustration:

Chart on which Jocelyn Bell Burnell first recognised evidence of PSR B1919+21, courtesy of the Churchill Archives Centre

MIUR subjects:

FIS/05 - Astronomia e Astrofisica

PACS:

97.60.Gb	Pulsars
97.60.Jd	Neutron stars
26.60.-c	Nuclear matter aspects of neutron stars

Keywords: stars: neutron, pulsars: general, dense matter, gravitation, pulsars: individual: PSR J0835-4510, superfluidity, glitch, Vela Pulsar, neutron stars masses

Abstract

Neutron stars are among the densest objects in the Universe, making them a perfect laboratory to study nuclear matter under extreme conditions. Pulsars – rapidly rotating magnetised neutron stars – are one of their possible manifestations, being observed as an extremely regular periodic emission in the radio spectrum. This radiation is produced by converting their rotational energy and, because of this, pulsars are expected to spin down. Some of them, however, have been observed exhibiting sudden accelerations in their rotation, also known as glitches. Nowadays, pulsar glitches are interpreted as the manifestation of vortex dynamics in the internal neutron superfluid, which lags behind the observable charged component in spinning down, occasionally releasing angular momentum to it and giving rise to a glitch.

In this work, we will present three different observational characteristics of a glitching pulsar – its largest glitch, its average acceleration due to glitches and its short-time evolution after a glitch – and we will try to extract information about the neutron star from each of them. In particular, we will try to set constraints on the mass of the star, the moment of inertia of its reservoir component and several other quantities tied to the glitch phenomenon, with the ultimate goal of increasing our knowledge about the properties of matter at densities above those of terrestrial nuclei.

Contents

Introduction

Since the first speculations about their existence in the Thirties and the first theoretical studies done until their discovery in the late Sixties, many advances have been made in the description of neutron stars, one of the possible remnants of an ordinary star, and more specifically its core after a core-collapse supernova.

With a mass of approximately $1.5 M_\odot$, packed by gravity in a sphere of radius ≈ 10 km, neutron stars are among the densest objects in the Universe and can easily exceed the nuclear saturation density, i.e. the density inside heavy atomic nuclei. In fact, it is not infrequent to come across models which predict central densities ten times larger than this value and claim the existence of exotic matter, like hyperons, meson condensates and quark-gluon plasma. As it is not possible to achieve such densities on Earth, these objects are arguably one of the few ways to study nuclear matter above the saturation density, making them the perfect playground for nuclear physics. One of the most important consequences of these extreme densities is the onset of nuclear superfluidity, which causes many phenomena observable at macroscopic scale, such as pulsar glitches. Moreover, due to their extreme compactness, neutron stars experience extreme gravitational forces, so a complete and thorough description should be carried out in a General Relativistic framework. Their Schwarzschild radius is, in fact, approximately $0.2-0.4$ times their radius, meaning that spacetime is curved around and inside neutron stars and their physical description is affected by important general relativistic corrections. Finally, neutron stars present an extremely varied phenomenology. Their emission spans the entire electromagnetic spectrum, ranging from radio frequencies to gamma rays, with both continuous and discontinuous emissions, both regular and sporadic. We can indirectly observe neutrino emission during the first stage of their lives, by measuring the cooling of their surface temperature over the years (see, e.g., the neutron star in the Cassiopeia supernova remnant, Heinke and Ho, 2010; Yakovlev et al., 2011), and directly detect it during the supernova phase (so far only in SN 1987A). They are also good candidates for emitting continuous gravitational waves, and it has also been possible to detect gravitational waves from neutron stars in binary systems. All these three lines of research about neutron stars – the nuclear one, the

one related to General Relativity and the observational one – are highly intertwined. In fact, it is not possible to obtain serious theoretical constraints or observational predictions on a neutron star phenomenon without keeping into account all these three aspects. As an example, the observation of a neutron star of about two solar masses (Demorest et al., 2010; Antoniadis et al., 2013; Fonseca et al., 2016; Linares et al., 2018; Cromartie et al., 2020) has put a serious constraint on the physics of nuclear matter over saturation density, and ruled out several models.

One of the possible manifestations of neutron stars are pulsars, which are rapidly rotating neutron stars emitting a collimated beam of radiation. When this beam is pointed in the direction of Earth, we observe a pulse in the radio spectrum, much like a lighthouse. On average, this pulsation is extremely stable, even more stable than atomic clocks (Milner et al., 2019). These objects slow down, due to a hydromagnetic torque exerted by the pulsar wind they emit, except for sudden accelerations of their pulsation frequency. These phenomena are called glitches. The current interpretation of glitches is related to the presence of a neutron superfluid in the star interior, which lags behind the observable charged component in spinning down, effectively storing angular momentum. This angular momentum reservoir is occasionally released, giving rise to a glitch. It is clear that an accurate modelling of the glitch phenomenon is necessary in order to explain the observed glitch behaviour. On the other hand, the latter can be an important test for the input variables of the model. In other words, it is possible to constrain some of the characteristics of a neutron star with its glitching behaviour. This is the leitmotif of this thesis: each Chapter presents a different observational feature of pulsar glitches which can be employed to provide new information about the internal structure of neutron stars. With this in mind, we divide this thesis into four Chapters:

Chapter 1 We present here some key features of neutron stars, talking about structure, Equations of State, phenomenology and the basic modelling of pulsar glitches.

Chapter 2 Glitch modelling can be employed to find the maximum angular momentum reservoir that can be stored in a neutron star between glitches and, as a consequence, the largest glitch achievable by a pulsar. This value can be easily compared with the largest observed glitch of a particular object, and some constraints can be set on the microphysical inputs of the model and on the mass of the star. All the modelling have been performed in the general relativistic framework. This Chapter is based on the work published in Antonelli et al. (2018).

Chapter 3 Pulsar activity is a well-known and widely used parameter in the field of pulsar glitches. It summarises the average acceleration of a neutron star's rotation due to the presence of glitches. After some considerations about the calculation of this parameter, we present two different models. The first one (studied in a general relativistic framework and already well-known in the literature, see Link et al. 1999) constrains the moment of inertia of the superfluid component, and

the mass of a star as a consequence. The second one is an extension of the model presented in the preceding Chapter, and includes the information contained in both the activity parameter and the largest displayed glitch, providing an improved – albeit more model-dependent – constraint on the mass of the glitcher. The distribution of these mass constraints for a set of stars will be compared with the distribution of the neutron star masses measured in binary systems. This Chapter is based on a work which is yet to be published (Montoli et al., 2020a) and a work which has already been published (Montoli et al., 2020c), while the final Section is based on original work.

Chapter 4 In 2016, a glitch in the Vela pulsar has been measured with unprecedented precision, allowing for a timing measurement of every pulse during the glitch. This observation and, more in general, the possibility of observing a glitch in the act have opened a completely new path for glitch modelling. For the first time it has been possible to infer the existence of a glitch overshoot, a fast transient which can occur in the very first instants of a glitch. In this Chapter we analytically solve a very simple model which can account for the presence of a glitch overshoot. After that, we present a first estimate of the phenomenological parameters of the model, made with a least mean squares fit on the 2016 Vela glitch. Finally, we show a more thorough analysis based on Bayesian inference, predicting the probability distributions for each parameter of the model. The work presented in this Chapter has been published in two different papers (Pizzochero et al., 2020; Montoli et al., 2020b).

CHAPTER 1

Neutron stars overview

In this Chapter we will present some of the most important properties of neutron stars. After recounting some of the most meaningful events in the history of theoretical speculation and discovery of neutron stars, we will describe how they take shape, starting from a main sequence star and ending with the formation of a compact object. We will then rapidly study the neutron star structure, along with some hypotheses that have been put forward about their internal composition. This subject will be better examined in a subsequent Section, where we will talk about the Equation of State of nuclear matter inside a neutron star, along with some methods which have been proposed to pinpoint this quantity. After that, we will review the extremely diverse phenomenology of neutron stars. Finally, we will specifically talk about pulsars, spending some words about timing anomalies and glitches: we will present some models for these phenomena, along with some mentions to superfluidity.

For more complete reviews about neutron stars, we refer to the books Shapiro and Teukolsky (1983), Haensel et al. (2007) and Glendenning (2000) and the reviews Chamel and Haensel (2008) and Haskell and Sedrakian (2018).

1.1 Brief history of neutron stars

The first idea of the existence of neutron stars was given by Lev Landau well before their discovery and before the discovery of the neutron. In fact, he calculated the maximum mass of white dwarfs (independently of Chandrasekhar 1931) and inferred the existence of stars where atomic nuclei are in so close contact, that the star can be represented as one gigantic nucleus (Landau, 1932). The neutron was discovered a year later, by James Chadwick (Chadwick, 1932).

In 1934, Walter Baade and Fritz Zwicky proposed neutron stars as an explanation for the immense energy release during a supernova explosion, the final instant of a massive star. They described a neutron star as a cold compact object, composed by neutrons packed in extremely high densities. This description is not that far from the currently accepted one.

Another important step in the understanding of these objects was made in 1939, when Richard Tolman (Tolman, 1939) and J. Robert Oppenheimer & George Volkoff (Oppenheimer and Volkoff, 1939) independently developed the equation of hydrostatic equilibrium in the general relativistic framework (nowadays also known as TOV equation). Similarly to the Newtonian counterpart, it is possible to solve the internal structure of a neutron star using this equation in addition to another equation, the Equation of State (EoS), that describes the dependence between the various thermodynamic functions, such as pressure and energy density. The calculation of an appropriate EoS of dense matter for the internal composition of a neutron star starting from the microphysics has been an important challenge for both before and after the Second World War. Still today, the calculation of the actual EoS of a neutron star is topic of discussion.

The first attempts to find neutron stars were made in the 1960s. A neutron star was expected to have a surface temperature of the order of $\sim 10^6 - 10^7$ K, which corresponds to a peak in the X-ray frequencies of a black body spectrum. Since these wavelengths are absorbed by the terrestrial atmosphere, the first X-ray detectors were launched on rockets and balloons. The first discovered X-ray source was Sco X-1, in the Scorpius constellation, by Riccardo Giacconi and his team (Giacconi et al., 1962) and after that many others have been discovered. However, the first attempts failed to prove the relation between X-ray sources and neutron stars. Today we know that Sco X-1 is a binary system containing an accreting neutron star and a main sequence star.

The discovery of neutron stars has been made with different methods and in a completely different spectral window. Franco Pacini, in a paper published on *Nature* (Pacini, 1967), showed that a rapidly rotating neutron star with a strong dipole magnetic field can convert its rotational energy into electromagnetic radiation and, subsequently, accelerate particles to high energies. During the same year, Jocelyn Bell – a graduate student supervised by Anthony Hewish – discovered a weak radio source, emitting with periodic pulses and extreme regularity (the period was of 1.337 s, Hewish et al. 1968). Many hypotheses regarding the nature of these objects were proposed, including the possibility of extraterrestrial life. The winning idea was that of Gold (1968) in which these pulsating radio sources (*pulsars*) were rotating magnetised neutron stars (as predicted by Pacini). In 1968, the discovery of a pulsar in the Crab Nebula (remnant of the supernova SN 1054, observed by the Chinese in 1054, Comella et al. 1969), see Figure 1.1, and one in the Vela supernova remnant (whose supernova light reached Earth about 11000 years ago, Large et al. 1968), see Figure 1.2, was the first confirmation of the link between supernovae, neutron stars and pulsars. In particular, Crab pulsar period was so short ($P \approx 33$ ms) that it seemed unlikely the source was a rotating white dwarf.

Figure 1.1: Composite image of Crab supernova remnant. Blue corresponds to X-ray wavelengths (from Chandra X-ray Observatory), red/yellow to visible (Hubble Space Telescope) and violet to infrared (Spitzer Space Telescope). The Crab pulsar can be spotted as a white dot near the centre.

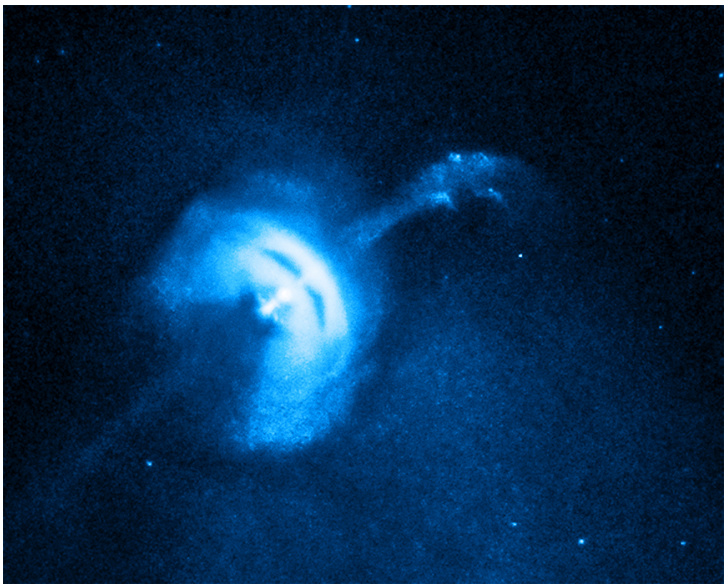

Figure 1.2: The Vela pulsar, along its surrounding pulsar wind nebula, as seen by the Chandra X-ray Observatory.

1.2 From main sequence to compact objects

In this Section we will review the formation of neutron stars, one of the possible endings for a star. The contents of this Section are based on Glendenning (2000).

Generally speaking, once the mass of a classical star is known, it is possible to have an idea of which will be its ultimate fate. The starting point is a main sequence star, which is a star in whose core groups of four hydrogen nuclei fuse together and form a helium nucleus. This can happen if there is a core temperature high enough to activate thermonuclear reactions (i.e. if the thermal energy of one proton is high enough to have a sizeable probability to overcome another proton's Coulomb barrier through tunnel effect). Once all the nuclear fuel in the core has exhausted, the core cannot be supported anymore and collapses. While collapsing, its temperature raises and, if the stellar mass is high enough, it can reach the value necessary to activate new thermonuclear reactions (that is, helium nuclei fusing together to obtain a carbon or oxygen nucleus). Again, once all the nuclear fuel is used, the core undergoes another collapse and the temperature rise might cause new nuclear reactions, if the stellar mass is high enough. For example, the Sun is not massive enough to overcome this step, and it will eventually die as a white dwarf composed by carbon and oxygen. The evolution continues in this sequence of quasi-equilibrium phases, with higher temperatures reached in the stellar core and more elements participating in a more complex nuclear reaction network. If the star had, during its main sequence, a mass greater than $\simeq 8M_\odot$, it could synthesise the most stable nuclear element: iron. Its isotope with mass number 56 has the highest nuclear binding energy per nucleon than any other, thus it is not possible to find any other nuclear fusion or fission reactions that is exothermic and can sustain the hydrodynamical equilibrium (see Figure 1.3). Thus all the iron produced deposits on an inert and isothermic core supported by electron degeneracy pressure, which eventually collapses when the Chandrasekhar limit of $1.4M_\odot$ is reached.

During the collapse, the core temperature raises and matter starts to neutronise. First, photodissociation transforms ^{56}Fe in helium nuclei (α particles) and neutrons:

$$^{56}\mathrm{Fe} + \gamma \rightleftharpoons 13\,\alpha + 4\,\mathrm{n}\,.$$

Then, at higher temperatures, α particles get photodissociated as well:

$$\alpha + \gamma \rightleftharpoons 2\,\mathrm{p} + 2\,\mathrm{n}\,.$$

Electron captures cannot take place under normal conditions, since the rest mass difference between the neutron and the proton is ≈ 1.3 MeV, well above the electron rest mass $m_e = 0.5$ MeV. Electrons, thus, need to be highly relativistic in order to make electron capture possible. In the collapsing core, electrons are degenerate, so most of their energy is not given by the thermal motion, but by Fermi energy. When density becomes high enough to make electrons ultrarelativistic, electron capture finally takes place, both by free protons

$$\mathrm{p} + \mathrm{e}^- \rightharpoonup \mathrm{n} + \nu_\mathrm{e}$$

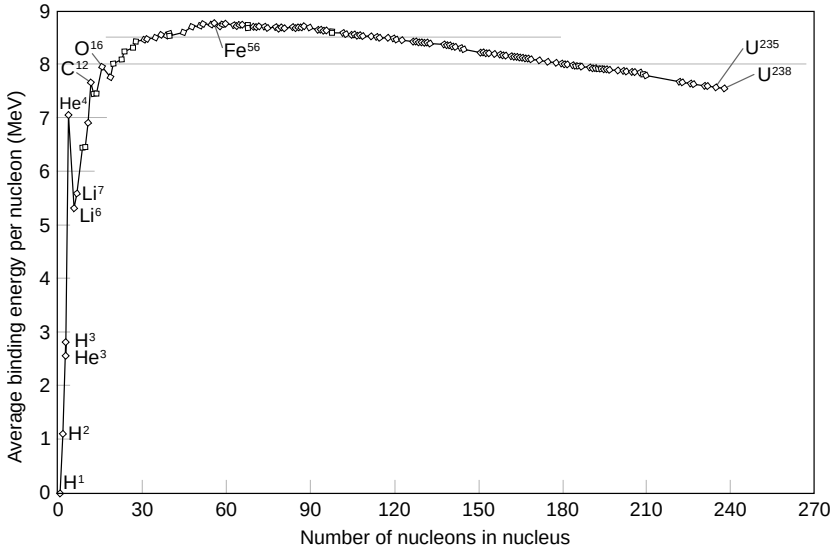

Figure 1.3: Nuclear binding energy per nucleon for some of the most common isotopes, as a function of the mass number. The maximum of the curve is given by the nuclear binding energy of ^{56}Fe. Starting from this value, any fission (fusion) – i.e. the production of elements with smaller (larger) mass number – will need energy to take place.

and by nuclei

$$(\mathrm{Z},\,\mathrm{A}) + \mathrm{e}^{-} \rightharpoonup (\mathrm{Z}{-}1,\,\mathrm{A}) + \nu_{\mathrm{e}}\,.$$

The increasing number of neutrons causes a degeneracy pressure which partially balances gravity, slowing down the core collapse. This is eventually stopped when baryons are so close to each other that they feel the strong repulsive part of the nuclear interaction. The collapse is in this way reverted and a shock wave originates from the surface of the collapsed core, now a protoneutron star. This shock wave is not strong enough to blast away the infalling material, since it loses energy by dissociating heavy elements nearby the core, and stalls. In its early life, however, the protoneutron star produces a huge amount of neutrinos, which escape interacting with the stalled shock wave and reinvigorating it. In this way a core-collapse supernova occurs. Historically, supernovae are classified using the hydrogen spectral lines, instead of the occurring physical phenomenon: so core-collapse supernovae are more known by astronomers as Type II supernovae (if hydrogen spectral lines are present) or Type Ib or Ic supernovae (if hydrogen spectral lines are absent).

Finally, if the initial mass of the star is way larger than $8M_{\odot}$ (say, $20-30M_{\odot}$), not even the neutrinos are able to revive the stalled shock wave, and the formation of a black hole is more likely. Of course, we also have to consider that a supernova is not necessarily a spherically symmetric phenomenon: because of this, neutron stars can acquire a high proper motion. This is one of the hypotheses why the neutron star of the supernova SN 1987A has not been detected.

1.3 Structure

A neutron star can be subdivided in four main internal regions: the outer crust, the inner crust, the outer core and the inner core (see e.g. Haensel et al. 2007 for a general review, or Chamel and Haensel 2008 for a review focussed on the crust).

The outer crust is solid. It is comprised by ions, which are arranged in a crystalline body-centred cubic (BCC) lattice, and free electrons. A very thin surface layer contains a non-degenerate electron gas. Going inside the star, this gas becomes more degenerate, and reaches ultrarelativistic regimes at densities $\rho \gg 10^6$ g cm^{-3}. To maintain β-equilibrium at higher densities, namely to have equilibrium in the reaction

$$\mathrm{n} \rightleftharpoons \mathrm{p} + \mathrm{e}^- + \overline{\nu}_\mathrm{e}\,, \tag{1.1}$$

electron captures by the protons inside nuclear clusters can occur, and ions get more neutron-rich in deeper layers of the star.

At densities of $\rho_{\mathrm{ND}} \approx 4 \times 10^{11}$ g cm^{-3}, also known as neutron drip density, nuclear clusters start to be unstable and neutrons leak out. This neutron drip line marks the beginning of the inner crust. In this region neutron-rich nuclei are still arranged in a crystalline lattice, but this time are immersed in a gas of free neutrons in a superfluid state. It is expected that not only electrons, but also free neutrons screen the interaction between nuclear clusters, leading to a more inhomogeneous configuration than that of a BCC lattice.

The outer core starts at $\approx 1.6 \times 10^{14}$ g cm^{-3} (about a half of the saturation density ρ_0) and extends to $\approx 2\rho_0$. Nuclei disappear at the crust-core interface, so outer core is mainly composed of a neutron fluid, with small percentage of protons, electrons and possibly muons (extended nuclear matter). The nature of the transition between inner crust and outer core is uncertain: it might be abrupt, but it also might be smooth, with a series of phase transitions in which nuclei are no longer spherical, but arranged in more exotic forms (like plates and rods). These arrangements are called “pasta” phase, and they are caused by the competition between the surface tension of nuclear clusters and the Coulomb interaction between protons in their inside (see Figure 1.4). The presence of these layers can have a strong observational impact on phenomena like glitches and gravitational wave emission (Gearheart et al., 2011).

At densities higher than the saturation density, the ground state of matter is essentially unknown (see Figure 1.5). Thus, the inner core – which starts at $\rho \gtrsim 2\rho_0$ – has a composition which is very model-dependent. New particles appear once the density is high enough to satisfy the corresponding β-equilibrium equation (similar to that in Equation (1.1)). Several hypotheses have been put forward, which are hyperonisation of matter (i.e. the appearance of hyperons, such as Σ^- and Λ), the appearance of boson condensates (such as pion or kaon condensates) or a phase transition to a quark-gluon plasma (a plasma of up, down and strange quarks and gluons). Depending on which hypothesis is considered, we can define several types of neutron star:

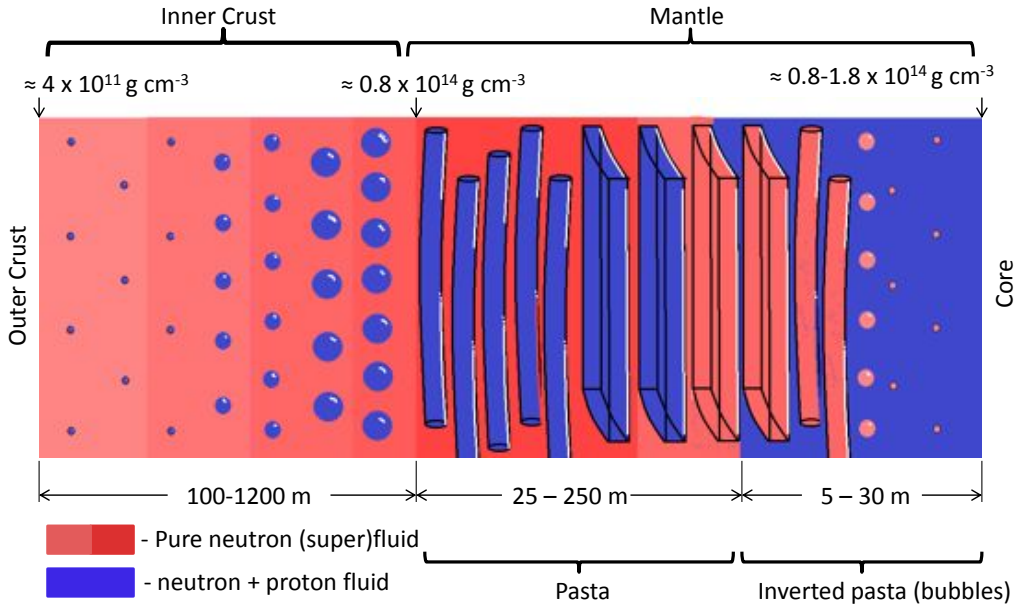

Figure 1.4: Cartoon representation of the inner neutron star crust, figure taken from Newton et al. (2011). Here the "mantle" is also displayed, which is a theoretically speculated region in the deeper parts of the inner crust, where nuclei are no longer spherical.

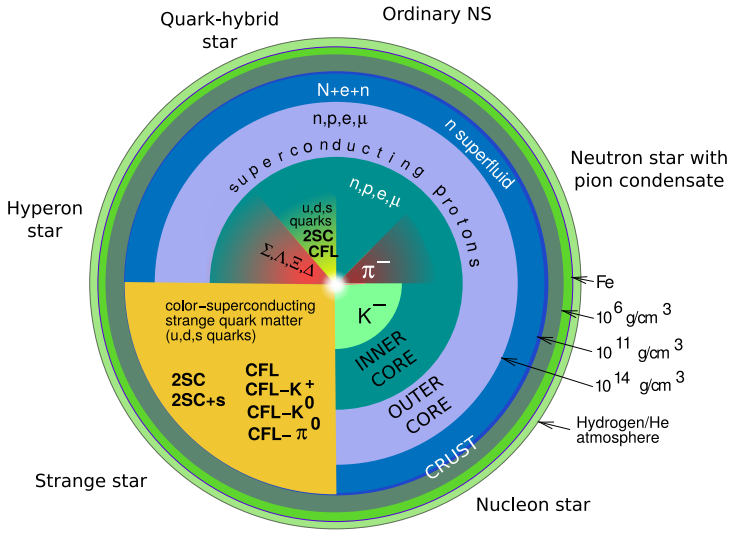

Figure 1.5: Sketch of the various theoretical compositions of a neutron (or quark) star. Figure adapted from Weber et al. (2007).

- *ordinary neutron stars*, with a core made of extended nuclear matter.
- *hyperon stars*, with an inner core made of hyperons and an outer core made of extended nuclear matter.
- *hybrid stars*, with an inner core of quark-gluon plasma, a shell of hyperonic matter and a shell of extended nuclear matter.

A special mention goes to quark stars (Itoh, 1970), which are completely different from the stars mentioned above: they are entirely – not only the core, but also the crust – comprised of quark-gluon plasma, except for a thin external shell of ordinary matter. Moreover, quark stars are bounded by strong force, unlike hadronic stars, which are kept together by gravity. The mass-radius relation for this kind of stars is quite particular (see Figure 1.6).

It is not clear whether the real structure of a neutron star corresponds to just one of the possibilities presented above, or if there may exist at the same time different types of objects with different internal structures. In the latter direction, some theories have been put forward, which claim the coexistence of hadronic neutron stars and hybrid stars, with different radii for the same mass (hence the name "twin stars", Glendenning and Kettner 2000) or the coexistence of hadronic and quark stars (the "two families" scenario, Drago et al. 2014, 2016; Drago and Pagliara 2016).

1.4 Equations of state

As mentioned in the Introduction, neutron stars macroscopic structure cannot be described in the framework of Newtonian gravity. Rather, we need the general relativistic equation for hydrostatic equilibrium, also known as Tolman-Oppenheimer-Volkoff (TOV) equation:

$$\frac{\mathrm{d}P}{\mathrm{d}r} = -\frac{G(\rho(r)+P(r)/c^2)(m(r)+4\pi r^3 P(r)/c^2)}{r(r-2Gm(r)/c^2)}, \tag{1.2}$$

where $m(r)$ is the enclosed mass at radius r, $P(r)$ is the pressure profile and $\rho(r)$ is the mass density profile. It should be stressed that $\rho(r)$ is not the rest mass density, since we are in a relativistic framework. We can also notice that in the limit of $c \to +\infty$, the TOV becomes the Newtonian equation for hydrostatic equilibrium.

The TOV equation has to be solved together with an equation for $m(r)$, much similar to the Newtonian counterpart

$$\frac{\mathrm{d}m}{\mathrm{d}r} = 4\pi r^2 \rho(r), \tag{1.3}$$

and with boundary conditions

$$\begin{aligned} m(r=0) &= 0 \\ \rho(r=0) &= \rho_c \\ P(r=R) &= 0, \end{aligned} \tag{1.4}$$

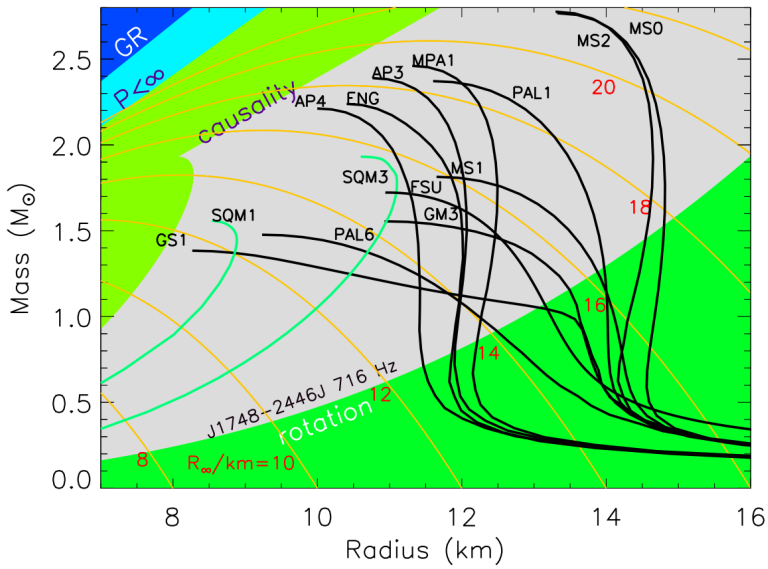

Figure 1.6: Mass–radius relations for several EoSs, taken from Lattimer (2012). Green curves (SQM1 and SQM3) are the EoSs for quark stars, while black curves are the hadronic EoSs. Orange curves show the radiation radius R_∞, while dark blue, light blue, light green and dark green regions show, respectively, the prohibited regions excluded by general relativity, finite pressure, causality and mass-shedding limit for the fastest rotating known pulsar, PSR J1748-2446ad. See text for further details.

namely we ask the enclosed mass to be zero at $r = 0$, we set a central mass-energy density ρ_c, and we define the radius of the star R as the radius where the pressure is null. It is easy to see that the total gravitational mass of the star can be defined as $M = m(r = R)$. As we have only two equations and three variables – $m(r)$, $\rho(r)$ and $P(r)$ – we need a third equation to solve the system, which is an Equation of State (EoS). An EoS is a relation between the thermodynamic quantities of a system, where all the microphysical information about the composition and behaviour of the nuclear matter is included. Note that in our case nucleons inside a neutron star have a Fermi energy larger than the energy given by thermal motion. In this sense, a neutron star is essentially a cold object, even though it has an internal temperature of the order of 10^9 K. Thus, our EoS will be a one parameter EoS, in which temperature will not appear explicitly: in other words, it will be an equation $P = P(\rho)$.

We have to notice that we can build a family of neutron star models parametrised by central density (also called mass–radius or M–R curves). Some M–R curves for various EoSs are plotted in Figure 1.6. Not every combination of mass and radius is permitted. First of all, the star radius should be larger than the Schwarzschild radius, i.e. we want that (dark blue region in the Figure):

$$R > \frac{2GM}{c^2}.$$

Secondly, pressure at the centre of the star should be finite. This is not a problem in the Newtonian case, since there are no finite values of M and ρ_c which can cause P_c to be infinity. In the relativistic case, it can be shown that only for values

$$\frac{GM}{Rc^2} < \frac{4}{9}$$

P is assured to be finite (light blue region). Then, another problem is that of causality. We want speed of sound inside the star to be lower than that of light, that is (light green region):

$$c_s^2 = \left.\frac{\mathrm{d}P}{\mathrm{d}\rho}\right|_S < c^2,$$

where S is the entropy of the star. Of course, the speed of sound depends on the EoS of the star, but a constraint like that in Figure 1.6 can be obtained by assuming a (theoretical) maximally compact EoS (Koranda et al., 1997). Finally, the dark green prohibited region is a rotational constraint: to be stable, the star does not have to lose material at the equator due to centrifugal forces caused by rotation. This limit can be expressed in a simple way in the Newtonian framework by the Kepler angular velocity:

$$\Omega_K = \sqrt{\frac{GM}{R^3}}.$$

This kind of limit will not work in the case of a general relativistic framework, due to the presence of a dragging of the local inertial frame (see Chapter 2). The value of the Kepler frequency will be somewhat different and rather complicated, and its derivation will be not treated here (see Chapter 6 of Glendenning 2000). In Figure 1.6, it is showed the limit in the case of the fastest rotating observed pulsar, PSR J1748-2446ad.

An important thing to notice is that, for a fixed EoS, the TOV equation gives a maximum mass for a star described with that EoS: stars more massive than that mass are unstable. A first calculation for neutron star maximum mass has been made by Oppenheimer and Volkoff (Oppenheimer and Volkoff, 1939). They used a simple EoS composed of a strongly degenerate non-interacting and non-relativistic gas of neutrons. The maximum mass they calculated was $\approx 0.71 M_\odot$, considerably smaller than the typical measured value of $1.4 M_\odot$ for the neutron star mass. Thus, neutron stars must be described with an EoS which includes the strong nuclear forces. Due to the current uncertainties in the nuclear interaction, however, this is not an easy task. In principle, one would like to describe the neutron star matter starting from QCD, but there are no ab-initio QCD calculations available for that. Usually, there are two approaches for calculating the EoS. One approach is the *ab-initio* approach: the idea is that of solving the many-body problem starting from realistic two- and three-body nucleon interactions. One example for this class of EoS is given by the APR EoS (Akmal et al., 1998), obtained with the Argonne v_{18} two-body potential (Wiringa et al., 1995), along with the Urbana IX three-body interaction (Pudliner et al., 1995). The other approach is the phenomenological one: here the EoS is based on an effective

density-dependent nucleon-nucleon interaction, with parameters fitted on nuclear properties. In this class many popular models are based on the Skyrme interaction (Skyrme, 1958), like the EoS based on the SLy4 force (Douchin and Haensel, 2001). Other EoSs calculated with the Skyrme interaction (along with a phenomenological pairing interaction) are those of the MSk/BSk families. The idea is that of calculating the binding energy of nuclei by means of the Hartree-Fock+BCS formalism (MSk, Tondeur et al., 2000) or the Hartree-Fock-Bogolioubov formalism (BSk, Samyn et al., 2002) and fit the phenomenological parameters of the Skyrme interaction with the measured masses of nuclei of the Audi-Wapstra compilation (Audi and Wapstra, 1995). Throughout the years, many new ingredients have been added to the model, yielding the BSk20 and BSk21 forces we will use in the next Chapters (Goriely et al., 2010). Recently, a newer version of these interactions has been published, also based on newer laboratory measurements of nuclear masses (BSk22, BSk24, BSk25 and BSk26, Pearson et al., 2018). These models, however, are non-relativistic: one model which include relativistic effects is the relativistic mean field model (Serot and Walecka, 1986), of which the DDME2 EoS we will employ later is an example (Lalazissis et al., 2005).

If we observe a star with a mass greater than the maximum mass of a given EoS, we are sure that EoS cannot describe the internal structure of that star. This is a peculiar trait of this field of research: a single observation can put constraints on the microphysics of neutron stars. The current constraint given by observations shows that the maximum mass given by an EoS should be of at least two solar masses (Demorest et al., 2010; Antoniadis et al., 2013; Fonseca et al., 2016), but slightly more massive stars have been recently detected ($2.27^{+0.17}_{-0.15}\,M_\odot$, see Linares et al. 2018, and $2.14^{+0.10}_{-0.09}\,M_\odot$, see Cromartie et al. 2020), which would suggest an even tighter constraint. Beside the type of modelling behind it, an EoS can be roughly classified with respect to its stiffness. A softer EoS is more compressible, giving a smaller radius, a denser core and, thus, a smaller maximum mass. Conversely, a stiffer EoS is less compressible, less compact (i.e., with smaller general relativistic corrections), and less dense in the centre. Thus, an EoS cannot be too soft, otherwise it would not be able to explain the observed masses of some stars. As we mentioned in the previous Section, the inner core composition is currently unknown: it could be made of nucleons, but also some more exotic phases may be present, like hyperons, pion or kaon condensates, or deconfined quark matter. Laboratory data on the interactions between these species are very scarce with respect to those regarding the nucleon interactions, so we cannot put tight constraints on the EoS parameters. The addition of new species, however, without a repulsive interaction (and the replacement of neutrons with a large Fermi energy with new species with lower Fermi energy) can lower the pressure in the star's core, leading to a softer EoS (see, e.g., Baldo et al., 2000; Vidaña et al., 2000). Thus, for instance, the addition of hyperons in a EoS model reduces its maximum mass. This is the so-called hyperon puzzle: it is not easy to include hyperons in a model and yet satisfy the $2M_\odot$ constraint (Bombaci, 2017).

The equation of state can be constrained by both measurements in the nuclear and

astrophysical regimes. Nuclear constraints are obtained from many different types of measurements of the characteristic of terrestrial nuclei. We will not review these constraints here (see, e.g., Fortin et al., 2016, for a review of the current constraints given by nuclear measurements and an analysis on different EoSs). Astrophysical constraints can be obtained by measuring masses, radii and several other macroscopic quantities, like moment of inertia and tidal deformability. Beside the already cited methods of constraining the EoS with the maximum mass of a star, other constraints can be obtained by simultaneously measuring the mass and the radius of a star. As in the case of non-degenerate stars, masses can be measured only in binary systems, applying the third Kepler's law (Özel and Freire, 2016). We can divide binary systems in two classes: X-ray binaries and radio pulsar binaries (see also Section 1.5). X-ray binaries are binary systems containing a neutron star (observed only in X wavelengths and not in radio) and a companion star. The X-ray emission is due to accretion from the companion star, usually a classical star. On the contrary, a radio pulsar binary is a binary with at least a radio pulsar. In the first case, we can measure orbital sizes and periods by measuring Doppler shifting and orbital variability of the emission from at least one of the two star. Some uncertainties are given by the unknown angle of inclination of the orbital plane to the line of sight. However, we can set some geometrical constraints evaluating eclipse duration and/or variation on the optical light curve. A similar procedure can be applied in the case of a radio binary pulsar, using pulsar timing instead of surface X-ray emission. In the case of a radio pulsar binary composed by two compact objects (neutron star-white dwarf or neutron star-neutron star), several effects due to General Relativity have to be taken into account for measuring masses (Özel and Freire, 2016), such as orbital period decay due to gravitational waves emission (see e.g. the Hulse-Taylor binary pulsar, PSR 1913+16) or Shapiro time delay, a delay in the pulsar timing due to the passage of the radiation close to a strong gravitational field (i.e. that of the compact companion).

If a neutron star is isolated, we cannot measure its mass, but we can give an estimate on its radius. One method is that of evaluating the radiation radius. Assuming that a neutron star emits like a black body, we can measure the star's colour temperature by fitting its spectrum with a black body spectrum. In this way, measuring the total luminosity of the star and keeping in mind the corrections due to gravitational redshift, we can evaluate an upper limit to the actual radius, also known as radiation or apparent radius:

$$R_\infty = \frac{R}{\sqrt{1-2GM/Rc^2}}.$$

However, a significant complication stems from the fact that the emission is modulated by the star's atmosphere and magnetic field, which causes a non-thermal component. In other words, a neutron star is not a perfect black body (some atmospheric modifications of the black body spectrum are presented, e.g., in Zavlin et al., 1996). Combined mass-radius measurements on a single object can put interesting constraints on the EoS: of course, this is not simple with standard methods, as masses can be measured only for stars in binary systems, while radii are generally measured for isolated neutron

stars. To deal with this issue, the NICER experiment has been recently deployed on the International Space Station and it is operating since July 2017. One of its aims is that of constraining the mass-radius relation with a precision of $\approx 5\%$ for a few neutron stars, by observing the rotating hot spot from non-accreting millisecond pulsars. Very recently, two different estimates of the mass and radius of PSR J0030+0451 have been proposed (Riley et al., 2019; Miller et al., 2019). Other kind of constraints on the nuclear EoS can be obtained from neutron star cooling, which allows for determining the presence of superfluidity (Shternin et al., 2011). One of the most studied objects for cooling is the neutron star in the Cassiopeia A supernova remnant (Heinke and Ho, 2010; Shternin et al., 2011, see Figure 1.8). Finally, the recent observation of gravitational waves in binary neutron stars (GW170817, see Abbott et al., 2017), which allows for a constraint on the tidal deformability of a star and on the maximum mass of the star (Most et al., 2018). From all these constraints, it is possible to invert the mass-radius relation and obtain information about the EoS, with methods ranging from Bayesian analysis to neural network employment (Sieniawska et al., 2018; Fasano et al., 2019; Traversi et al., 2020; Morawski and Bejger, 2020).

1.5 Neutron star phenomenology

From the observational point of view, neutron stars show a wide variety of behaviours, which are typical of the particular class of stars we are considering. Usually, they are classified according to their primary energy source for the emission of radiation (Harding, 2013), that are the rotational, the magnetic, the thermal and the accretion energy.

Rotation-powered pulsars (RPP) are those neutron stars which spin down due to the torques from magnetic dipole radiation and particle emission. To date, more than 2800 pulsars are known, and are reported on the ATNF Pulsar Catalog[1] (Manchester et al., 2005). Their spin down is usually steady, except for some unexpected spin-ups, also called glitches, which will be discussed in more detail later. The basic modelisation of a RPP is that of a rotating dipole in the vacuum, inclined by an angle α with respect to the rotation axis (the so-called lighthouse model). The total energy emitted by a pulsar is given by the Larmor formula:

$$\dot{E} = -\frac{2|\ddot{\mu}|^2}{3c^3}, \tag{1.5}$$

where μ is the magnetic dipole vector. In the case of a star with radius R, rotating with an angular velocity Ω and with a polar magnetic field B_p, μ can be written as:

$$\mu = \frac{B_p R^3}{2}\left(\hat{e}_{\parallel}\cos\alpha + \hat{e}_{\perp 1}\sin\alpha\sin\Omega t + \hat{e}_{\perp 2}\sin\alpha\cos\Omega t\right), \tag{1.6}$$

[1] https://www.atnf.csiro.au/research/pulsar/psrcat

where $\hat{e}_{\parallel}$ is the versor parallel to the rotation axis and $\hat{e}_{\perp 1,2}$ are the ones perpendicular to it. Thus, the power emitted by the pulsar depends in a simple way on a few quantities:

$$\dot{E} \propto (B_p \sin\alpha)^2 R^6 \Omega^4. \tag{1.7}$$

This model, however, is not physically correct: a real pulsar does not lie in the vacuum, but it is immersed in a magnetosphere of charged particles teared off from its surface by the electric fields induced by rotation of the intense magnetic fields. These particles are then accelerated and emit the coherent and pulsated radiation we observe from Earth. The simplest model that includes magnetosphere is that of Goldreich and Julian (1969), in which the magnetic dipole is aligned with the rotation axis. Also this model foresees a power emission with the same dependence of that of the lighthouse model in Equation (1.7).

This emission of radiation causes the system to lose energy. If we assume the energy to be supplied by the rotational energy of the pulsar $E = I\Omega^2/2$, where I is the moment of inertia of the star, we have a variation of the energy on time given by $\dot{E} = I\Omega\dot{\Omega}$. This hypothesis of rotation-powered pulsar yields a slowdown of the star, given by:

$$\dot{\Omega} \propto \frac{(B_p \sin\alpha)^2 R^6 \Omega^3}{I}. \tag{1.8}$$

This relation, however, does not take into account the possibility of gravitational waves emission. We can define a braking index n, defined by the relation:

$$\dot{\Omega} \propto -\Omega^n. \tag{1.9}$$

Thus, for the emission of a magnetic dipole, $n = 3$, while for gravitational radiation emission it can be demonstrated that $n = 5$ (Shapiro and Teukolsky, 1983). From these simple considerations we can give an estimate of the pulsar age. Starting from the relation (1.9), if we measure the quantities Ω and $\dot{\Omega}$ now (quantities that we will indicate with an "o" subscript), we can write:

$$\dot{\Omega} = -\frac{\Omega^{n-1}}{T\Omega_o^{n-1}},$$

where T represent a characteristic time given by $\Omega_o/\dot{\Omega}_o$. By integrating this equation from a time $t = 0$ (and $\Omega = \Omega_i$) to the current time $t = \tau$ (and $\Omega = \Omega_o$), we obtain:

$$\tau = \frac{T}{n-1}\left[1 - \left(\frac{\Omega_o}{\Omega_i}\right)^{n-1}\right].$$

If we assume that the angular velocity when the star was born is much greater than the current one (i.e. $\Omega_o \ll \Omega_i$), the pulsar age assumes a much simpler form:

$$\tau \approx \frac{T}{n-1} = \frac{1}{n-1}\frac{\Omega_o}{\dot{\Omega}_o}. \tag{1.10}$$

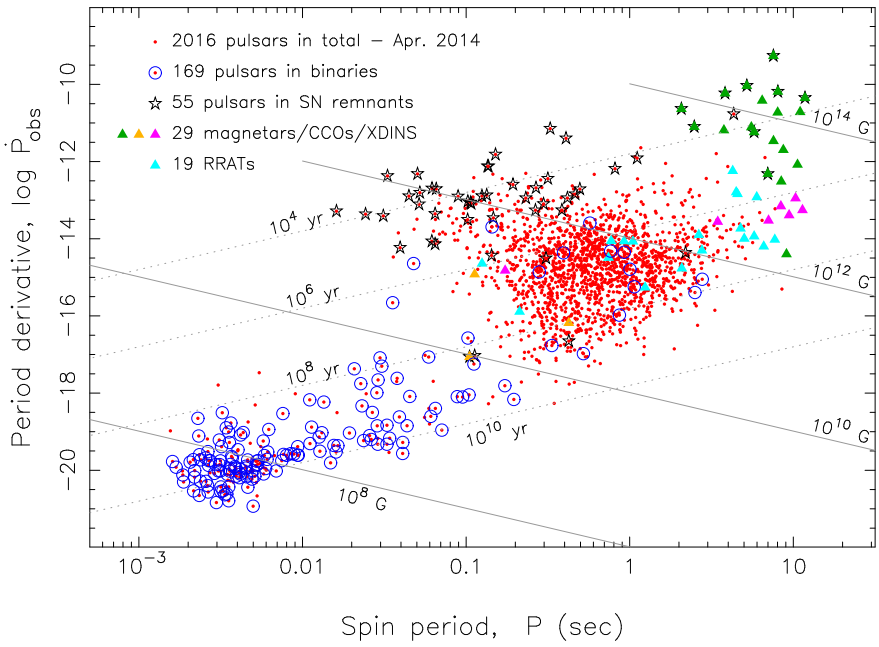

Figure 1.7: $P-\dot{P}$ diagram, taken from Tauris et al. (2015). Lines of constant magnetic field and lines of constant age are depicted.

Pulsars are generally classified by period and period derivative on a $P-\dot{P}$ diagram, which is the analogue of the Hertzsprung- Russel diagram for classical stars (Figure 1.7). Starting from this diagram it is possible to infer some interesting characteristics of pulsars, such as their age, or their magnetic field, by employing the relations in (1.10) and (1.8) as functions of period and period derivative.

The pulsar population can further be divided in two subclasses: the normal pulsars, which have characteristic age $\tau < 100$ Myr, and the millisecond pulsars (MSPs), with $\tau \gtrsim 100$ Myr and very short periods, of the order of ~ 1 ms. MSPs are not thought to be born with these extreme periods, but instead to be born as normal RPPs and to have acquired angular momentum through accretion (Alpar et al., 1982). This hypothesis is supported by the fact that almost 80% of MSPs are in binary systems, and that they have a weaker magnetic field when compared to that of standard RPPs – as it can be inferred from the $P-\dot{P}$ diagram – probably reduced or submerged during accretion. The spin evolution of MSPs is extremely steady. In fact, MSPs have been seen glitching only twice (Cognard and Backer, 2004; McKee et al., 2016). This feature makes them particularly useful for gravitational wave detection: by monitoring small fluctuations in the period of a set of MSPs (also known as pulsar timing array), it is possible to infer

the passage through Earth of a gravitational wave, by estimating the correlation of these fluctuations (Hobbs et al., 2010a). More recently, thanks to the LAT experiment on the Fermi Gamma-Ray Space Telescope, new discoveries have been made on a particular class of MSPs, the eclipsing binary MSPs, or spider pulsars (Linares, 2019). These objects are MSPs with a very low-mass companion, typically less than $0.1 M_\odot$ for the black widow pulsar, and $0.1 - 0.4 M_\odot$ for the redback pulsars, (Roberts, 2013). They generally have very high mass, higher than that of standard RPPs. In fact, one of the most massive neutron star ever discovered, PSR J2215+5135, is a redback pulsar, with $M = 2.27^{+0.17}_{-0.15} M_\odot$ (Linares et al., 2018). These objects are thus particularly important for the study of the maximum mass of a neutron star, which can pose serious limits on their internal structure and on the description of high-density matter.

A final class of RPP – discovered only recently (McLaughlin et al., 2006) – is that of the Rotating Radio Transients (RRATs, see Keane and McLaughlin, 2011, for a review). From the timing point of view, they present a transient behaviour, with both long periods of no radio emission and periods of regular pulsation highly modulated. It is not clear how these objects can be explained.

Neutron stars which use the magnetic energy as primary source for the emission are called magnetars. From the observational point of view, magnetars present themselves in two different ways (Mereghetti et al., 2015): with transients in the γ spectrum (Soft Gamma Repeaters, SGRs) or with a regular emission in the soft X-ray range (Anomalous X-Ray Pulsars, AXPs). Only later these two type of objects have been interpreted as the same class, i.e. neutron stars with a very strong magnetic field (Thompson and Duncan, 1995, 1996). Magnetars usually present a longer period than that of a RPP, and a larger spin down rate. Many theories have been proposed for the formation of these intense magnetic field. One possibility is that the magnetic field of a magnetar is the same of its progenitor star, amplified by magnetic flux conservation. This hypothesis, however, is unlikely, since too few progenitor stars with strong enough magnetic fields have been observed in order to account for the magnetar birth rate inferred. Another possibility is that this fossil field is amplified in the protoneutron star phase by dynamo action driven by convection or differential rotation (Duncan and Thompson, 1992; Thompson and Duncan, 1993). Also this possibility has some issues, since the core-envelope coupling in the protoneutron star phase brakes the star too efficiently to explain the observed spin distribution (actually, this problem also affects the fossil field scenario). An up-to-date catalogue of observed magnetars can be found on the McGill Online Magnetar Catalog[2] (Olausen and Kaspi, 2014).

Accreting neutron stars are generally divided into two categories. Those neutron stars with a companion which transfers its matter by filling its Roche Lobe (it can be either a low-mass main sequence star, a white dwarf or a red giant), are said to be in a Low-mass X-ray Binary (LMXB). In these systems, the matter is transferred through an accretion disk. Due to this reason, also angular momentum is transferred to the more compact object. This is why LMXBs are generally thought to be the systems where

[2] http://www.physics.mcgill.ca/~pulsar/magnetar/main.html

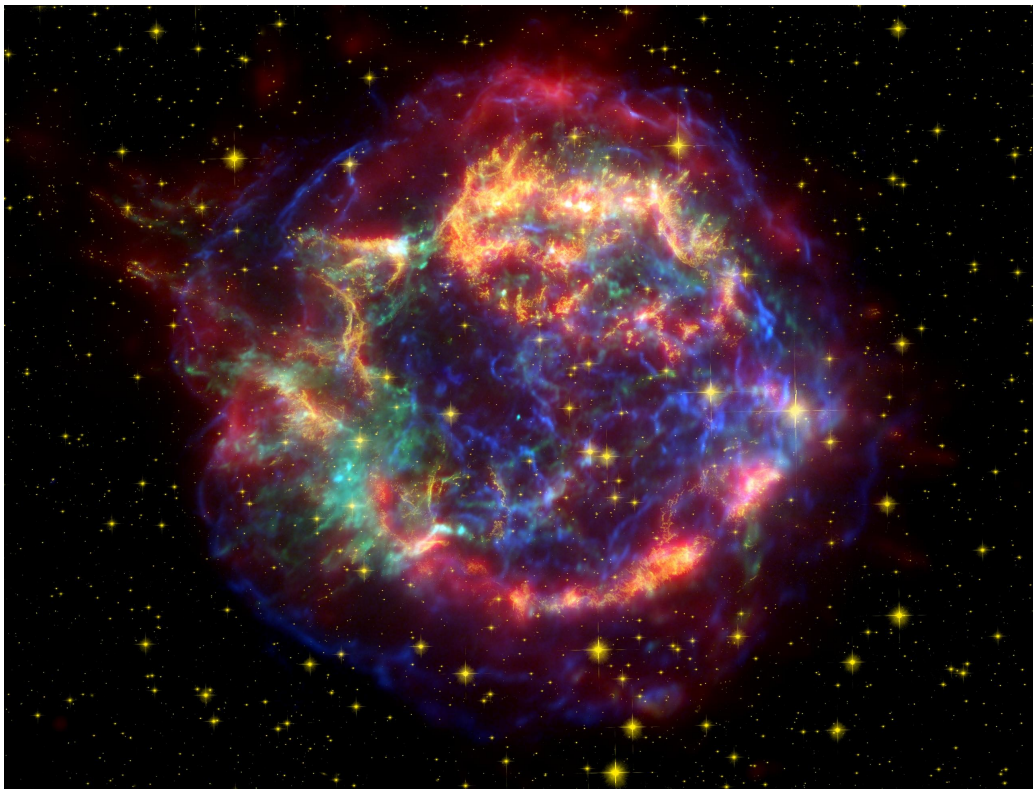

Figure 1.8: Composite image of the Cassiopeia A supernova remnant. Blue/green corresponds to the X-ray frequencies (from the Chandra X-ray Observatory), gold to visible (Hubble Space Telescope) and red is the infrared data (Spitzer Space Telescope). The blue dot just off-centre is the neutron star.

millisecond pulsars are born. Note that a LMXB can be also comprised by a black hole and a companion accreting on it. On the other hand, if the companion star is more massive (for example, a O or B main sequence star), the system is called High-mass X-ray Binary (HMXB). In this system, matter is accreted on the compact object through the wind of the companion star.

Finally, the class of thermally emitting neutron stars presents different very different behaviours. One subclass is that of the Central Compact Objects (CCOs). These are X-ray thermal sources near the centre of supernova remnants – hence very young neutron stars – which do not seem to have any emission in other frequencies. One notable example is the CCO in the Cassiopeia A supernova remnant (see Figure 1.8). Due to their purely thermal emission, CCOs are generally employed as benchmark for neutron star cooling theories. Some of these objects (like J1852+0040 in Kes79, Halpern and Gotthelf 2010, or J0822.0–4300 in Puppis A, Gotthelf and Halpern 2009) have shown pulsations, and the measured P and $\dot{P}$ infer a very young age (10^3-10^4 yr) and unusually low magnetic fields (hence dubbed anti-magnetar). Another subclass

of thermally emitting neutron stars is that of the Isolated Neutron Stars (INS). They present many similarities to the CCOs, with the differences that they are not associated to any supernova remnant, and that they have a very low pulsating frequency. Only seven objects of this class are known (also called the Magnificent Seven). It is not clear how these stars are connected to the rest of the RPP population. They could be either normal RPPs with the radio beam which does not cross our viewing angle, or dead radio pulsars.

1.6 Pulsar timing and pulsar glitches

Radio pulsars spin with an extremely rapid rotation and with an extremely stable period, outperforming the best atomic clocks (Milner et al., 2019). Their spin frequency can be measured by means of pulsar timing, i.e. the regular monitoring of a neutron star's rotation by recording the time of arrival (TOA) of a pulse, which can be obtained by folding a few minute-time observations. Since the rotational period of a pulsar is nearly constant, the spin-down model can be obtained by fitting these pulses – after systematic effects like Earth motion or the pulsar proper motion are taken into account – with a Taylor expansion of the pulsation frequency ν around a reference time t_0:

$$\nu_{sd}(t) = \nu_0 + \dot{\nu}_0(t - t_0) + \frac{1}{2}\ddot{\nu}_0(t - t_0)^2 . \tag{1.11}$$

Usually, this equation provides a good fit to data and higher terms of the expansion in ν are not needed. Any slow and stochastic deviation from this formula is called timing noise (see, e.g., Hobbs et al., 2010b), whose cause is still not well understood. It can be linked to various effects like a precession of the neutron star, turbulence in the internal superfluid (Melatos and Link, 2014) or changes in the magnetic fields (Kramer et al., 2006; Lyne et al., 2010). This phenomenon will not be treated here.

On the other hand, abrupt changes in the pulsar frequency and frequency time derivative are glitches (see Figure 1.9). Pulsar glitches are a sudden spin up of a rotating neutron star, followed by a period of slow recovery after which the values evolve back to the pre-glitch ones. We used the term "sudden", as at the present time the rise timescale of a glitch cannot be resolved, but only upper limits can be put (see Dodson et al. 2002; Ashton et al. 2019b; Montoli et al. 2020b, but also Chapter 4). Timing anomalies can be studied as residuals with respect to the spin down model in Equation (1.11):

$$\varphi(t) = 2\pi \int_{t_0}^{t} (\nu(t) - \nu_{sd}(t))\, \mathrm{d}t , \tag{1.12}$$

where $\nu(t)$ is the true pulse frequency (thus, including all the deviations from (1.11)). $\varphi(t)$ are the phase residuals, and indicate the advance (if it is positive) or the delay (if it is negative) of a pulsar with respect to the spin down model in units of radians. Of course, if there are no deviations from the spin down model in (1.11), $\nu(t) = \nu_{sd}(t)$,

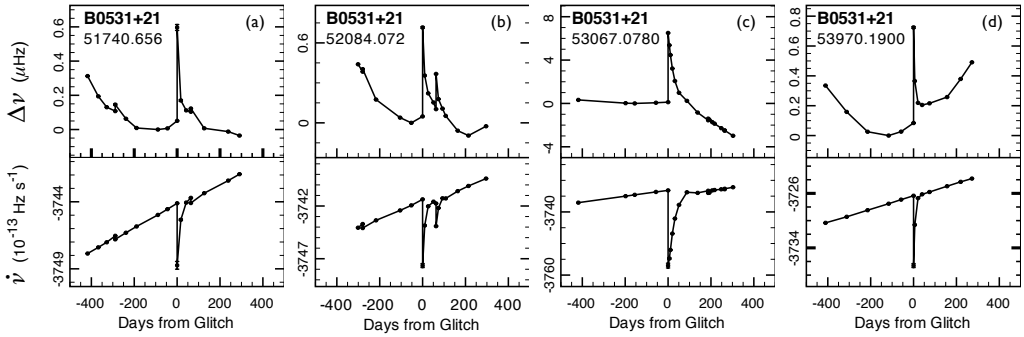

Figure 1.9: Four glitches of the Crab pulsar (PSR B0531+21 or PSR J0534+2200) measured by Espinoza et al. (2011). Every plot shows the frequency residuals and frequency time derivative against time. The zero on the abscissa corresponds to the glitch epoch, which is indicated in Modified Julian Day (MJD) below the pulsar name.

and $\varphi(t) = 0$ for all t. We can also study the residuals by rescaling them by the star's angular velocity

$$r(t) = -\frac{\varphi(t)}{\Omega_0}, \tag{1.13}$$

where $\Omega_0 = 2\pi\nu(t = t_0)$ is the angular velocity of the star (assumed as constant) at the reference time. This function indicates in seconds how early (if it is negative) or late (if it is positive) with respect to the spin down (1.11) a new pulse from the neutron star is detected. If a pulsar glitch is detected, this function is monotonically decreasing (see Figure 1.10).

The first glitch was detected in 1969, just a couple of years after the discovery of pulsars, in the Vela pulsar (Radhakrishnan and Manchester, 1969; Reichley and Downs, 1969). Nowadays, more than 550 glitches have been observed in 190 pulsars[3] (see Figure 1.11). This value corresponds to about 7% of the pulsar population. Most of the stars have glitched only once, but there are some objects – like Vela (PSR B0833-45, or PSR J0835-4510), Crab (PSR B0531+21, or PSR J0534+2200) or PSR J0537-6910 (the most prolific glitcher, with 45 glitches, Antonopoulou et al. 2018) – which have been seen glitching more than 10 times. It seems to be a correlation between glitching activity (which can be summarised by the activity parameter, see Chapter 3) and pulsar age. Middle-aged pulsars (i.e. with age $\approx 10^4$ yr) glitch the most, while activity is smaller for very young or for older pulsars (Shemar and Lyne, 1996). All glitches have been observed in isolated stars, with one notable exception of a small glitch in an accreting pulsar (Serim et al., 2017). Glitch sizes are generally evaluated with respect to the pulsar frequency and span several orders of magnitude, ranging from $\Delta\nu/\nu \approx 10^{-12}$ to $\Delta\nu/\nu \approx 10^{-5}$ (see, e.g., Espinoza et al., 2011).

[3] See `http://www.jb.man.ac.uk/pulsar/glitches.html` for an up-do-date catalogue of pulsar glitches (Espinoza et al., 2011)

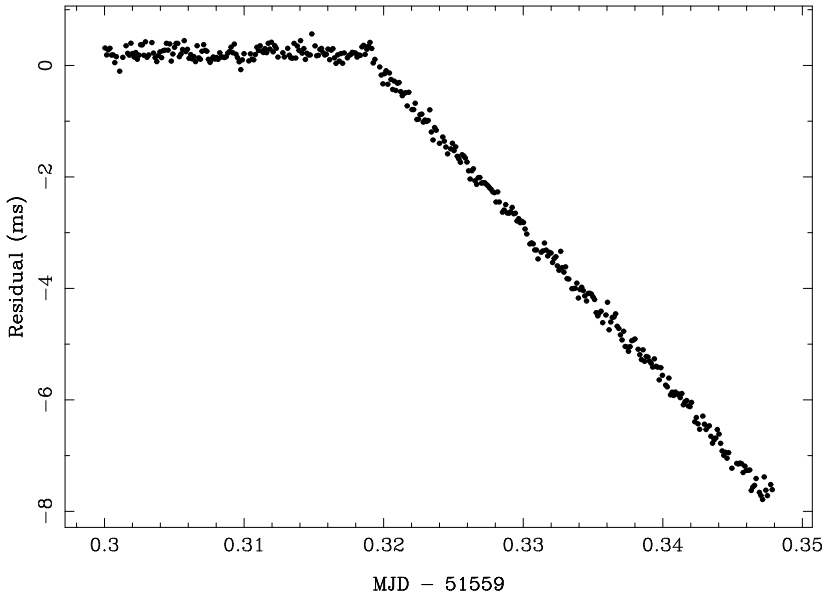

Figure 1.10: Timing residuals of the 2000 Vela glitch, figure taken from Dodson et al. (2002).

After the unresolved rise (which can be still be modelled, see Chapter 4), a slow relaxation towards the pre-glitch spin-down takes place (see, e.g., the lower row of plots in Figure 1.9). Setting the reference time as the time of glitch, this can be fitted with a function

$$\nu(t) = \nu_{sd}(t) + \Delta\nu_p + \Delta\dot{\nu}_p t + \sum_{i=1}^{N} \Delta\nu_i e^{-t/\tau_i}, \tag{1.14}$$

where $\Delta\nu_p$ and $\Delta\dot{\nu}_p$ are the permanent step in the frequency and frequency derivative and $\Delta\nu_i$ are the amplitudes of the decaying parts of the glitch, with timescales τ_i. The time variable is set so that $t = 0$ corresponds to the instant in which the neutron star glitches, and $\Delta\nu_p + \sum_i \Delta\nu_i$ represents the total size in frequency of the glitch. The relaxation parameters in the above equation vary from glitch to glitch, even for the same pulsar. However, it was this slow relaxation what suggested the presence (and involvement) of a superfluid inside the pulsar (see below).

In the next Sections, we will rapidly go through some models for pulsar glitches, as an introduction for the next Chapters. An up-to-date and more complete review on pulsar glitch models can be found in Haskell and Melatos (2015).

1.6.1 First models

As we have already said, a pulsar glitch is a sudden increase in the observed pulsation frequency of a pulsar, which is directly linked to the rotational frequency of the magnetosphere of the neutron star. Thus, pulsar glitches can be thought as a spin up of that part of the star which is anchored to the magnetic field, i.e. the crust and

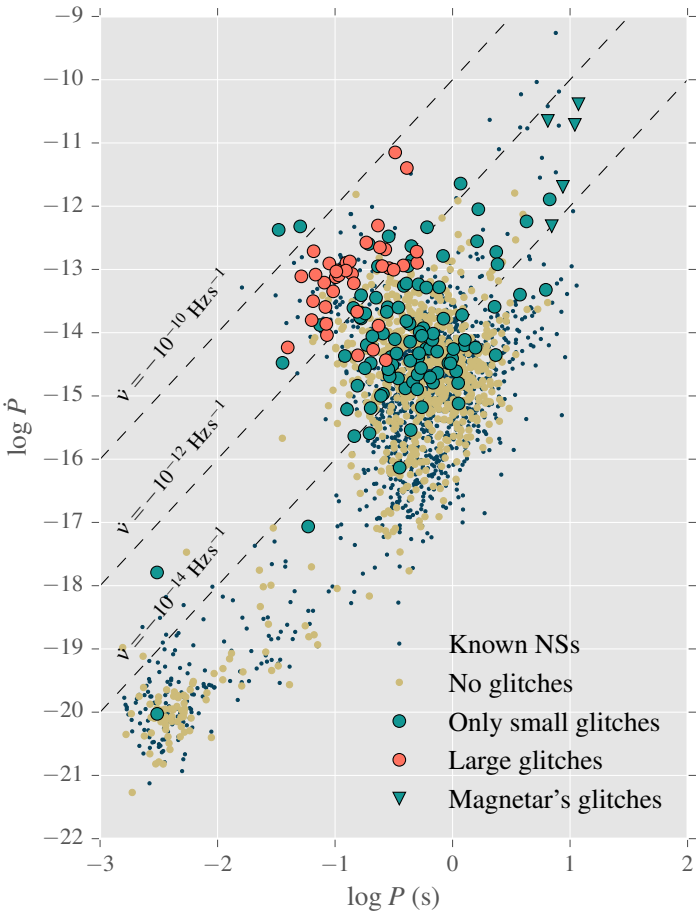

Figure 1.11: $P - \dot{P}$ diagram of all known neutron stars, with glitchers highlighted in green and red. Figure taken from Fuentes et al. (2017).

the charged particles. Of course, the star's crust cannot accelerate its rotation on its own accord. So there must be a way to store angular momentum in the star while the pulsar is slowing down. This is the basic idea behind the glitch phenomenon.

The first model proposed after the discovery of a pulsar glitch in the Vela pulsar was that of crust quakes (Ruderman, 1969). In this model a glitch originates from the outer crust, which is constituted by a crystalline lattice that can support stress. The shape of the crust is, of course, influenced by the rotation frequency of the star: we are expecting a rotating star not to have a perfectly spherical form, but somewhat oblate, due to centrifugal forces. A simple example in the Newtonian context is that of the Maclaurin ellipsoid, an axisymmetric figure of equilibrium for a self-gravitating fluid with constant density. As the star spins down, we are expecting it to adjust its shape in order to achieve a new equilibrium shape, but since the crust is rigid, stress builds up and it is eventually released spasmodically as crust quakes. This starquake

causes a rearrangement in the form of the crust, a change of the moment of inertia and thus an acceleration of the star rotation. This can be seen in a simple way by exploiting the fact that $L = I\Omega$, where L is the total angular momentum of the star, I the total moment of inertia and Ω the angular velocity, and the angular momentum conservation:

$$\Delta L = \Delta I \Omega + I \Delta \Omega \,.$$

The variations have been calculated between the after- and before-glitch quantities. Angular momentum conservation yields $\Delta L = 0$, thus giving:

$$\frac{\Delta \Omega}{\Omega} = -\frac{\Delta I}{I}, \tag{1.15}$$

which means the glitch amplitude to be proportional to the variation of the moment of inertia during the quake. For a typical neutron star with mass $M \approx 1.4 M_\odot$ and radius $R \approx 10$ km, it would require about ten million years to accumulate enough stress to cause the large glitches in Vela (Smoluchowski, 1970; Baym and Pines, 1971). Just two years after the first detected one, however, Vela displayed a second glitch, and continued to exhibit large glitches every 2-3 years for the following fifty years (see Figure 1.12). This discordance between theory and observations is the main reason why crustal deformation is no longer considered as the way to store angular momentum for glitches. Nowadays, starquakes are considered one of the possible triggers for vortex-mediated glitches (see below), although it seems unlikely that the star can develop enough stress between glitches to break the crust, which is required to be constantly in a stressed state, near the failure threshold (Franco et al., 2000; Giliberti et al., 2019). This is the case, for example, for large glitches of the Vela pulsar (Giliberti et al., 2020), but on the other hand starquakes may be able to explain glitches of the Crab pulsar (Alpar et al., 1994, 1996; Crawford and Demiański, 2003; Akbal and Alpar, 2018).

After the microscopic theorisation of superconductivity due to Bardeen et al. (1957), the subsequent application of the BCS formalism to nuclear matter explained the energy gap in the excitation spectra of nuclei, the odd-even mass staggering and the reduced moment of inertia of nuclei (Bohr et al., 1958). The application of the BCS theory to nuclear matter allowed also for the study of neutron superfluidity in neutron star well before the discovery of pulsars (Migdal, 1959). If neutrons inside neutron stars were normal (i.e. not superfluid), they would be strongly interacting with protons, and the glitch would damp on a nuclear timescale (of the order of 10^{-17} s, see Baym et al. 1969a). One year after the first Vela glitch, the spin down rate relaxed to the value it had before the glitch, hinting at the involvement of superfluidity in the process. A first inclusion of the neutron superfluid in the glitch modelling has been proposed in Baym et al. (1969b): here, the glitch rise is caused by a starquake, while the slow relaxation is due to the presence of a neutron superfluid. This model thus divides the star into two components: a normal component, indicated with a "c" subscript, which is comprised by the solid crust and everything strongly coupled with it by the magnetic fields,

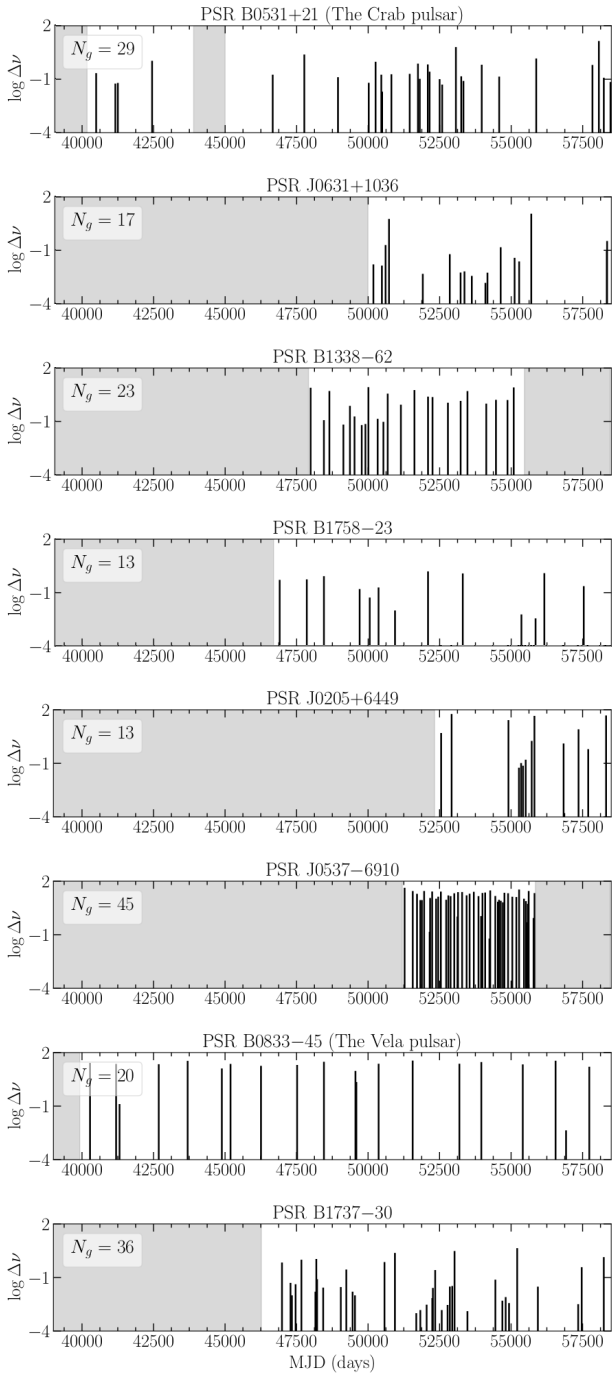

Figure 1.12: Glitch sizes as a function of the glitch epoch for the eight pulsars with the currently largest number of glitches. The grey areas are the periods when observations have not been made for more than three months. N_g is the number of glitches detected in each pulsar (figure taken from Fuentes et al. 2019).

and a superfluid component, indicated with a "s" subscript. The rotational dynamics of the neutron star is described by two equations, one for the angular momentum conservation and one for the rate of exchange of angular momentum between the two components:

$$\begin{cases} I_c\dot{\Omega}_c + I_s\dot{\Omega}_s = -\alpha \\ I_s\dot{\Omega}_s = \frac{I_c}{\tau_c}(\Omega_c - \Omega_s) \end{cases} \tag{1.16}$$

where α indicates the braking torque caused by the radiation emission (assumed constant here) and τ_c is a relaxation timescale describing the mutual friction which couples the normal and the superfluid component after the glitch. By considering the stationary state as when both the components slow down at the same rate (that is, $\dot{\Omega}_s = \dot{\Omega}_c \equiv \dot{\Omega}_\infty$), we can solve the system considering an instantaneous glitch of size $\Delta\Omega_{\rm gl}$:

$$\Omega_c = \Omega_\infty + \Delta\Omega_{\rm gl}(1 - Q + Qe^{-t/\tau}), \tag{1.17}$$

where Q is the so-called healing parameter, that represents the degree at which the star returns to the pre-glitch slowdown. Note that in the above model the glitch size $\Delta\Omega_{\rm gl}$ is given by some unknown physical phenomenon: it can still be a crustquake (as originally assumed by the authors of Baym et al. 1969b) or a different phenomenon, which is able to explain these large and relatively frequent events.

1.6.2 Vortex-mediated glitches

As discussed above, nuclear matter inside neutron stars is expected to be superfluid. In the BCS theory of superconductivity the coupling of electrons with lattice phonons leads to an attractive interaction between electrons despite the repulsive Coulomb force. These Cooper pairs of electrons with same angular momentum and different spin behave like bosons, in a sense that they do not obey Pauli exclusion principle and can occupy a single-particle quantum state. Thus, below a critical temperature, these pairs condensate like bosons in the single-particle quantum state at the lowest energy, causing superconductivity. After its formulation, BCS theory was applied to nuclear matter (Bohr et al., 1958). In this case, the attractive interaction between nucleons is given by the strong force. In neutron stars, neutrons are expected to form a superfluid in the inner crust and in the core. Neutron-proton pairs could in principle exist, but they are quite rare due to the asymmetry of nuclear matter inside the star. Hadrons become superfluid when the energy associated with temperature is smaller than the superfluid gap Δ, which can be interpreted as the binding energy of the Cooper pair. Δ is usually of the order of the MeV in a neutron star, while the temperature, after some months from the formation, can drop to values of the order of keV.

One of the peculiarities of a rotating superfluid is that it rotates by forming an array of vortices with quantised circulation $\kappa = \hbar/2m_n$, where m_n is the mass of the particle comprising the superfluid (in our case, the neutron mass). Note that while these vortices' radii have a size of the order of the nuclear scale, their lengths are macroscopic. A superfluid that rotates with angular velocity $\Omega(r)$ along an axis

at $r = 0$ is threaded by a number $n(r)$ of vortices per surface area given by the Feynman-Onsager relation:

$$r\frac{\mathrm{d}\Omega}{\mathrm{d}r} + 2\Omega(r) = \kappa n(r)\,. \tag{1.18}$$

It is easy to see that if vortices move outwards the angular velocity decreases: this is the basic idea behind the vortex-mediated glitch model (Anderson and Itoh, 1975). Quantised vortices of the neutron superfluid may pin to impurities in the crust of the star (either nuclear clusters or the space between them) or to fluxoids in the core of the star (which are the analogue of the superfluid vortices for the proton superconductor in the core of the star) and stop their motion (Ruderman, 1976; Alpar, 1977; Epstein and Baym, 1988; Jones, 1991). Thus, as long as vortices are pinned, the superfluid component cannot spin down. A glitch occurs when a huge number of vortices unpin and repin after having drifted to outer regions of the star. The trigger of the sudden unpinning is not clear: it is possible that a crust quake causes the unpinning of some vortices, which in turn cause an avalanche while moving outwards in the star. The observable consequences of this phenomenon are related to the vortex knock-on process (Warszawski and Melatos, 2013) and to details on the propagation of a vortex avalanche (Haskell and Melatos, 2016; Haskell, 2016). Nevertheless, vortex avalanches can be studied in terms of self-organised critical systems by means of a state-dependent Poisson process (Fulgenzi et al., 2017; Melatos et al., 2018; Carlin and Melatos, 2019b). Alternatively, glitches might be also caused by superfluid instabilities (Andersson et al., 2003; Mastrano and Melatos, 2005; Glampedakis and Andersson, 2009) and their evolution related to superfluid turbulence (Melatos and Peralta, 2007; Khomenko et al., 2019). In any case, the unpinning causes the superfluid to slow down and, thus, the observable normal component to spin up.

Let us consider the neutron star interior as composed by two different fluids: a superfluid, which we will denote now on with a "n" subscript, and a normal fluid, which we will denote with a "p" subscript. The first one is inviscid, and composed by neutrons in a superfluid state, which rotates by forming an array of quantised vortices. The latter is a charge-neutral fluid comprised by protons, electrons and everything coupled to the crust and the magnetic field on short timescales (Easson, 1979). Because of this, the rotation we observe from Earth is that of the normal component.

Since we are dealing with a system comprised by a superfluid and a normal fluid, an important effect can arise: that of entrainment (for a review, see Chamel 2017a). A first formalisation of this phenomenon dates back to the seminal work of Andreev and Bashkin (1976) on the interaction in ^{4}He and ^{3}He mixtures. The independent motion of a superfluid and a normal fluid can cause a non-dissipative interaction between them, and in particular one fluid can induce a motion on the other, depending on how strongly they interact. This causes a non-trivial relation between the velocities of the two fluids and their linear momentum. In fact, it can be demonstrated that the momentum of a particle of one fluid is not simply the product between the particle's

mass and its velocity, but a linear combination of the velocities of the two fluids. Thus for a species $x = n, p$ (see, e.g., Prix et al. 2002):

$$\boldsymbol{p}_x = m_x[\boldsymbol{v}_x + \varepsilon_x(\boldsymbol{v}_y - \boldsymbol{v}_x)], \tag{1.19}$$

where ε_x denotes the entrainment parameter. We can define an effective mass of the particle $m_x^* = m_x(1-\varepsilon_x)$, which modifies the above equation as:

$$\boldsymbol{p}_x = m_x^* \boldsymbol{v}_x + (m_x - m_x^*)\boldsymbol{v}_y. \tag{1.20}$$

Thus the particle momentum of each of the two fluids is not aligned with its respective velocity. It is important to notice the relation (Chamel and Haensel, 2008):

$$\varepsilon_n \rho_n = \varepsilon_p \rho_p \,. \tag{1.21}$$

The entrainment parameter (or equivalently, the effective mass) depends on the mass density of the two-fluid system. What microscopically causes the entrainment between the two components inside a neutron star and how to calculate this parameter is still an open question. For the core of a neutron star, where both superfluid neutrons and the charged component move as fluids, the entrainment is due to the nuclear interaction between the species (Chamel and Haensel, 2006). On the other hand, in the crust – where only the superfluid is free to move, and the charged component is arranged in a crustal lattice – the entrainment phenomenon is due to Bragg scattering of the superfluid neutrons with the crust (Chamel, 2012). The issue here is the calculation of this parameter, which is computationally very expensive. Moreover, the entrainment effect is severely affected by the particular nuclear model we are considering (Martin and Urban, 2016; Watanabe and Pethick, 2017) and by the arrangement of the crustal lattice, which – in the limit of an amorphous crust – can make it almost negligible (Sauls et al., 2020). In the following, we will employ the entrainment parameter calculated by Chamel and collaborators, which is large and negative in the crust of the star (Chamel, 2012), and small and positive in the core (Chamel and Haensel, 2006, see Figure 1.13).

Beside entrainment, the motion of the superfluid component is also impacted by those interactions affecting the motion of superfluid vortices, namely the Magnus force, drag force and pinning force. Magnus force is a general aspect of fluid dynamics. It arises when a spinning object is immersed in a background flow. The physical meaning of this force is quite easy: the velocity field induced by the spinning object – in our case, the vortex – sums (subtracts) to that of the background velocity causing lower (higher) pressure on that side. This difference of pressure produces an effective force, which is the Magnus force. Of course, if the spinning object is at rest in the frame of reference of the background flow, no Magnus force occurs. In the case of a vortex in a neutron star, Magnus force is induced on it if it is not comoving with the background flow of superfluid neutrons. The vortex experiences a force per unit length:

$$\boldsymbol{f}_M = \rho_n \boldsymbol{\kappa} \times (\boldsymbol{v}_L - \boldsymbol{v}_n), \tag{1.22}$$

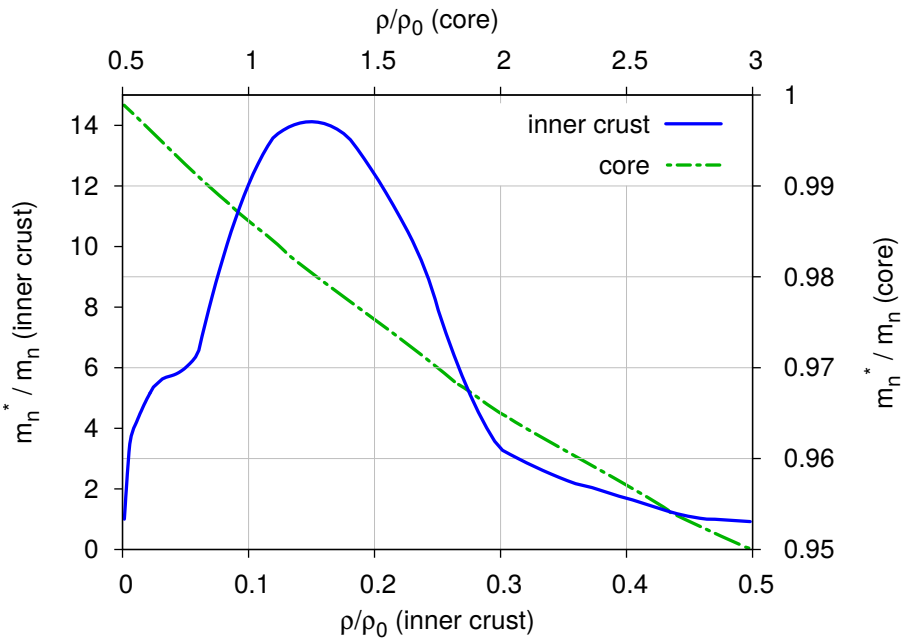

Figure 1.13: Effective neutron mass in the crust (plotted with data from Chamel (2012), in blue) and in the core (plotted with data from Chamel and Haensel (2006), in green). The figure has been taken from Antonelli and Pizzochero (2017).

where ρ_n is the mass density of the background flow (in the case of a neutron star, that of the superfluid component), $\boldsymbol{\kappa}$ is the vorticity vector (thus tangent to the vortex line), $\boldsymbol{v}_L$ is the velocity of the vortex line and $\boldsymbol{v}_n$ is the velocity of the background neutron superfluid. It can be demonstrated (see, e.g., Andersson et al., 2006; Antonelli and Haskell, 2020) that also in the presence of entrainment the Magnus force preserves its form described in Equation (1.22), but the vector $\boldsymbol{\kappa}$ is now defined as

$$\boldsymbol{\kappa} = \frac{h}{2m_n} \frac{\nabla \times \boldsymbol{p}_n}{|\nabla \times \boldsymbol{p}_n|},$$

that is, a vector with modulus equal to the quantised vorticity κ and direction given by $\nabla \times \boldsymbol{p}_n$.

The dissipative drag force acts between the vortices and the proton-electron fluid. It can be written in a phenomenological way as:

$$\boldsymbol{f}_D = -\eta(\boldsymbol{v}_L - \boldsymbol{v}_p), \tag{1.23}$$

where $\boldsymbol{v}_p$ is the velocity of the normal component and η is the drag parameter. This quantity also appears in the literature as $\mathcal{R} = \eta/(\rho_n \kappa)$, which is related to the large-scale hydrodynamic mutual friction coefficient by (see, e.g., Glampedakis et al., 2011):

$$\mathcal{B} = \frac{\mathcal{R}}{1+\mathcal{R}^2}. \tag{1.24}$$

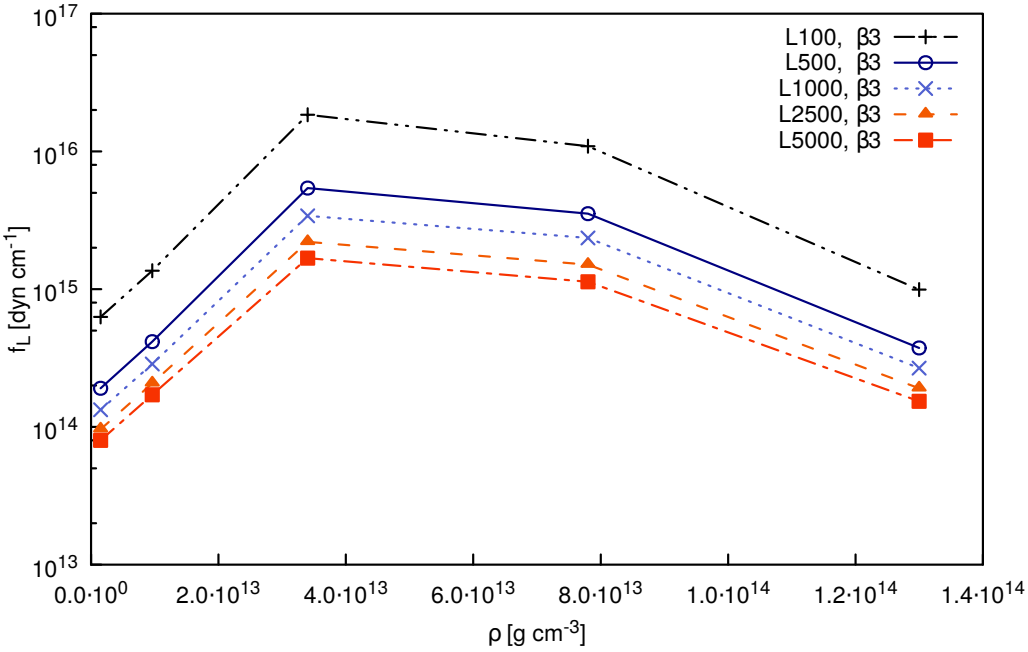

Figure 1.14: Pinning force at different densities in the inner crust, taken from Seveso et al. (2016). L indicates the length scale over which a vortex can be considered rigid (in unity of Wigner-Seitz cell radius). In this thesis we will use the $L = 5000$ case.

All these parameters depend on which dissipative phenomenon is considered. In the core of the neutron star, entrainment effect causes a flow of superconducting protons around each neutron superfluid vortex line, which causes the presence of a large magnetic field (of the order of 10^{14} G) along every line. The scattering of electrons off these magnetic fields leads to a dissipative mutual friction between the superfluid and the normal fluid (Alpar et al., 1984a). Since we need a flow of entrained protons around neutron superfluid vortices, this mechanism is valid only within the core of the star, as the protons in the crust are forced into nuclear clusters. In the crust, vortices can excite phonons in the crustal lattice if the relative velocity between the vortex and the lattice is small (say, $|\boldsymbol{v}_L - \boldsymbol{v}_p| < 10^2$ cm/s, see Jones 1990) or Kelvin waves can form on the superfluid vortices, if the relative velocity is larger (see Jones, 1992; Epstein and Baym, 1992). A recent review on the calculation of the drag parameter due to Kelvin waves excitation has been presented in Graber et al. (2018).

Finally, pinning force keeps the vortices fixed in position, preventing them to have a natural outward motion due to drag force. Vortices can pin threading nuclear clusters (nuclear pinning, which occurs at densities similar to that of the crust-core interface) or passing through two of them (interstitial pinning, occurring at lower densities, close to the neutron drip one). We will not discuss here the complex problem of the derivation of the pinning force per unit length, since it depends in a complex way on

several quantities, like vortex rigidity and orientation. Many calculations and studies have been performed throughout the years (Ruderman, 1976; Alpar, 1977; Epstein and Baym, 1988; Jones, 1991), considering simple geometries. More recently, Link (2009) studied the pinning force due to a crust made of randomly displaced ions. In the next Chapters we will make use of the pinning force in Seveso et al. (2016), which describes a realistic maximum pinning force calculated averaging over all orientations of a vortex with respect to a BCC lattice (see Figure 1.14). In partitular, we will employ the pinning force calculated by assuming a vortex rigidity length of 5000 Wigner-Seitz radii[4]: this parameter is justified by comparing the angular momentum reservoir which can be stored in the star with the average waiting time and glitch size of the Vela pulsar (Seveso et al., 2016). We have to consider, however, that in between glitches it is possible that vortices unpin because of thermal effects and repin in the outer regions of the star. This phenomenon, also known as vortex creep (Alpar et al., 1984b), may influence the amount of angular momentum which can be stored between glitches, and the spin evolution over time of the post-glitch relaxation.

These three forces act together on every superfluid vortex. If a vortex is pinned, it corotates with the normal component, thus only pinning and Magnus force will act on it. Pinning also prevents the superfluid to spin down and an angular velocity lag between the two components builds up. When the lag is high enough, i.e. when Magnus force is high enough to be greater than pinning force, vortices unpin and move outward. If many vortices are unpinned at the same time, their massive outward migration causes the pulsar to glitch.

[4]The crust is decomposed into a set of independent spheres centered around each nuclear cluster, with a radius (the Wigner-Seitz radius) which includes enough electrons to ensure charge neutrality (in other words, it includes the same number of protons and electrons).

CHAPTER 2

Largest observed glitch

One possibility to extract information about a pulsar's structure is given by employing the largest glitch displayed by it (Antonelli and Pizzochero, 2017; Pizzochero et al., 2017). This measurement allows us to put a constraint – by assuming an EoS for the neutron star matter – on the mass of the star. The advantage of this kind of constraint is dual: on the one hand, the largest glitch amplitude does not have to be calculated like the activity parameter (see Section 3.1). For each pulsar which displays glitches, we just need to take the largest one, and try to set some constraints on the neutron star structure from it. Of course, the largest measured glitch may not be the largest event achievable by that star, but a new larger glitch simply puts a tighter constraint. On the other hand, this constraint is not much model-dependent, as the only microphysical ingredient needed is the maximum pinning force of the star in the crust.

In this Chapter we will discuss the method for obtaining this kind of constraint on the neutron star structure, as first presented in Antonelli and Pizzochero (2017) and Pizzochero et al. (2017) and later revised in a fully general relativistic formulation in Antonelli et al. (2018).

2.1 Analytical calculation

Let us start by assuming a neutron star spacetime that is asymptotically flat, stationary and axisymmetric. Let us choose a global chart with Schwarzschild-like coordinates $(t, r, \vartheta, \varphi)$ such that the Killing vector associated with stationarity is ∂_t and that associated to angular momentum conservation is ∂_φ. The most general axially-symmetric metric can be written as (see Hartle and Sharp, 1967):

$$g = -e^{2\Phi(r,\vartheta)}c^2\mathrm{d}t^2 + e^{2\Lambda(r,\vartheta)}\mathrm{d}r^2 + e^{2\Xi(r,\vartheta)}\left[r^2\mathrm{d}\vartheta^2 + r^2\sin^2\vartheta\,(\mathrm{d}\varphi - \omega(r,\vartheta)\,\mathrm{d}t)^2\right], \tag{2.1}$$

where Φ, Λ, Ξ and ω are four metric functions. The coordinates ϑ and φ represent, respectively, the polar and azimuthal angles with respect to the rotational axis of the star (defined as the set of points where the circular Killing vector vanishes). The star

is assumed to be static, i.e. it rotates with a constant angular velocity Ω throughout the whole star. This metric function can be simplified within the approximation of slow rotation, introduced by Hartle (1967): for a star with mass M and radius R, the slow-rotation condition can be written as

$$\frac{R^3\Omega^2}{GM} \ll 1\,. \tag{2.2}$$

In other words, we are asking the star to rotate on a much slower rate than the mass-shedding angular velocity. For a typical pulsar with $M \sim 1.4M_\odot$ and $R \sim 10$ km, spinning at $\Omega \sim 70$ rad/s (like the Vela pulsar), this approximation works well. The slow-rotation framework is less safe for a millisecond pulsar: the fastest pulsar known to date – PSR J1748–2446ad, $\Omega = 4501$ rad/s – gives $R^3\Omega^2/GM \approx 0.11$ for the mass and radius assumed above (Haensel et al., 2007). Anyway, so far only two millisecond pulsars have been seen glitching (J1824-2452A, Cognard and Backer 2004, and J0613-0200, McKee et al. 2016). Neither, however, displays sufficiently large glitches to be constrained by this model, so we can safely assume slow rotation from now on. Following Hartle (1967), at first order in Ω the metric in Equation (2.1) reduces to

$$g = -e^{2\Phi(r)}c^2\mathrm{d}t^2 + e^{2\Lambda(r)}\mathrm{d}r^2 + r^2\mathrm{d}\vartheta^2 + r^2\sin^2\vartheta\,[\mathrm{d}\varphi - \omega(r,\vartheta)\mathrm{d}t]^2\,. \tag{2.3}$$

The metric functions that appear here depend only on r and are not the same of Equation (2.1). $\omega(r)$, in particular, represents the dragging of the inertial frame due to the rotation of the neutron star, and it can be calculated solving an additional equation. We will not review the method here, as it can be found in many articles or books (see, e.g., Haensel and Proszynski 1982 or Glendenning 2000 and references therein). The centrifugal force and consequent star deformation appear when second-order corrections in Ω are taken into account and the spherical structure becomes oblate. The neutron star structure, thus, can still be described by solving the TOV equation for spherically-distributed matter, along with an equation of state.

Let us consider a rigidly-rotating normal component (labelled by p) and a superfluid component (labelled by n) that can rotate non-uniformly with angular velocity $\Omega_n = \Omega_p + \Omega_{np}$, but still around a common and constant rotation axis. In other words, we are assuming that no precession in the star rotation is present. Within this formalism, the slow-rotation approximation is performed at first order in Ω_p. Differently from what has been done in Hartle (1967), here we have two fluids, rotating with different angular velocities. Therefore, we have to assume that the two fluids are almost corotating, namely that Ω_{np} is small with respect to Ω_p (or, analogously, that the angular velocities of the two components are similar), which can be safely assumed for the present case of pinning-induced lag. Note that Ω_{np} is not a parameter in which the expansion is performed: the parameters are Ω_p and Ω_n, which are assumed to be of the same order of magnitude. We will not report the calculation here, but it can be shown (Antonelli et al., 2018) that, with the hypothesis of quasi-corotation

of the two components and the additional one of chemical equilibrium, the Komar angular momentum (i.e. the conserved quantity due to the presence of the Killing vector associated to angular momentum conservation, see, e.g., Rezzolla and Zanotti, 2013) of a sphere of radius R can be expressed as

$$L = \frac{8\pi}{3c^2}\int_0^R dr\; r^4 e^{\Lambda(r)-\Phi(r)}\left[\rho(r)c^2 + P(r)\right]\cdot\left[\Omega_p - \omega(r) + y_n\Omega_{np}\right]. \tag{2.4}$$

Here we have also introduced the mass-energy density and pressure profiles $\rho(r)$ and $P(r)$, and the superfluid fraction y_n, defined as the fraction between the number density of the free neutrons n_n and the number baryon density n_B. The total angular momentum of the star L can always be split as:

$$L = I\Omega_p + \Delta L[\Omega_{np}]. \tag{2.5}$$

The reason for this separation is the following: as a first approximation, the star rotates as a whole with angular momentum $I\Omega_p$. It is easy to see that the coefficient I is exactly the moment of inertia of a sphere in the slow rotation approximation (Hartle, 1967)

$$I = \frac{8\pi}{3c^2}\int_0^R dr\; r^4 e^{\Lambda(r)-\Phi(r)}\left[\rho(r)c^2 + P(r)\right]\frac{\Omega_p - \omega(r)}{\Omega_p}. \tag{2.6}$$

The functional ΔL accounts for the extra angular momentum due to the presence of pinning inside the star, which translates in an angular velocity lag Ω_{np}. In the slow rotation approximation case, this functional equals:

$$\Delta L[\Omega_{np}] = \frac{8\pi}{3c^2}\int_0^R dr\; r^4 e^{\Lambda(r)-\Phi(r)}\left[\rho(r)c^2 + P(r)\right]y_n\Omega_{np}. \tag{2.7}$$

We remark that in the decomposition of the total angular momentum as in (2.5) only the global part $I\Omega_p$ contains the effect of frame dragging. The reservoir $\Delta L[\Omega_{np}]$ presents no factor $\omega(r)$. This is not surprising, as the corrections due to frame dragging are encoded as $\Omega - \omega(r)$ and cancel out when considering the lag between the two components. We have to deal with the subtle problem of justifying chemical equilibrium, which is an hypothesis we have used in order to write the angular momentum in (2.4) as a function of the total mass-energy density ρ and pressure P instead of the chemical potential of the two species (see Antonelli et al., 2018). Andersson and Comer (2001) showed that chemical equilibrium between the two components in a neutron star implies corotation of them, and it is thus only approximatively realised in our context where the fluids must rotate differentially in order to produce a glitch (the slowness of electroweak interactions, however, may help to maintain equilibrium). Later, Sourie et al. (2016) have shown the inverse reasoning: starting from the hypothesis of corotation and assuming chemical equilibrium at the centre of the star, it is possible to infer chemical equilibrium throughout the entire star. The additional

condition of quasi-corotation is then necessary to ensure very small departures from chemical equilibrium and from rigid rotation, and thus guarantee the consistency of Equation (2.5) with the rigid-body Hartle's formalism.

We can introduce the partial moment of inertia I_n as the normalisation factor of the distribution defined by ΔL

$$I_n = \frac{8\pi}{3c^2}\int_0^{R_d} dr\; r^4 e^{-\Phi+\Lambda}\, y_n\left(\rho c^2 + P\right), \tag{2.8}$$

where R_d is the neutron-drip radius, which is placed at $n_d \approx 2.6\times 10^{-4}\,\mathrm{fm}^{-3}$, namely at the outer edge of the inner crust. This allows to define the average lag $\langle\,\Omega_{np}\,\rangle$ (weighted with I_n) and hence write the angular momentum of the reservoir as

$$\Delta L[\Omega_{np}] = I_n\langle\,\Omega_{np}\,\rangle\,. \tag{2.9}$$

We point out that, although we used the same symbol, the quantity I_n does not represent the moment of inertia I_n^{tot} of the entire n-component, but only that of the reservoir associated with a given lag, in the sense of Equation (2.9). In fact, for rigid rotation of the n-component, this is given by

$$I_n^{\mathrm{tot}} = \frac{8\pi}{3c^2}\int_0^{R} dr\; r^4 e^{\Lambda-\Phi} y_n\left(\rho c^2 + P\right)\frac{\Omega_n-\omega}{\Omega_n}, \tag{2.10}$$

consistently with Equation (2.6). While in the Newtonian framework the two quantities are the same, in the relativistic context they are distinguished concepts.

It is easy to see that – in the slow rotation case, but also in the Newtonian case, see Section 3.3 – the functional in (2.7) is linear in Ω_{np}, thus allowing us to write the time derivative of the above equation as:

$$I\dot{\Omega}_p + \Delta L[\partial_t\Omega_{np}] = -I|\dot{\Omega}_\infty|\,, \tag{2.11}$$

where $-I|\dot{\Omega}_\infty|$ represents the angular momentum loss due to electromagnetic emission. Let us now trigger a glitch, and integrate this equation between a time t_{pre} just before the glitch and a time t_{post} immediately after it. Let us also assume that the time interval is sufficiently small so that we can neglect the term proportional to $|\dot{\Omega}_\infty|$, and let us ignore possible time variation in the moments of inertia (caused, for instance, by starquakes). With these assumptions, and again by making use of the linearity of ΔL, the integration yields:

$$I\left[\Omega_p(t_{\mathrm{post}}) - \Omega_p(t_{\mathrm{pre}})\right] = \Delta L[\Omega_{np}(t_{\mathrm{pre}})] - \Delta L[\Omega_{np}(t_{\mathrm{post}})]\,. \tag{2.12}$$

Finally, we would like to obtain the maximal glitch amplitude, which can be obtained by asking the angular momentum associated with the reservoir to be null after the glitch, i.e. $\Delta L[\Omega_{np}(t_{\mathrm{post}})] = 0$:

$$\Delta\Omega_{\mathrm{m}}(t) = \frac{\Delta L[\Omega_{np}(t)]}{I}, \tag{2.13}$$

where we have defined the glitch jump as $\Delta\Omega_{\rm m} \equiv \Omega_p(t_{\rm post}) - \Omega_p(t_{\rm pre})$ and redefined $t_{\rm pre}$ as t. Unsurprisingly, the glitch amplitude in Equation (2.13) does not explicitly depend on entrainment: it is a direct consequence of the fact that the total angular momentum of the star (2.4) is independent of it. However, the lag Ω_{np} is a dynamical variable of the model and its evolution is affected by entrainment.

We want to maximise $\Delta\Omega_{\rm m}$, in order to obtain a theoretical upper bound to the observed glitch amplitudes. What we would like to do is to find the value of Ω_{np} such that the glitch size $\Delta\Omega_{\rm m}$ is maximum. This value can be obtained by assuming that all the vortices inside the star are pinned and subcritical: in this way, the lag between the two components is the maximum achievable, which corresponds to the maximum angular momentum reservoir ΔL, and thus the maximum glitch amplitude. Let us call this critical lag $\Omega_{np}^{\rm cr}$. The condition of subcriticality can be achieved by asking that for every vortex in the neutron star the pinning force (which keeps the vortices stuck in their pinning site) and the Magnus force (which tries to move them from their place) are equal in modulus. In other words, all the vortices are about to unpin, and a further increase of the angular velocity lag would increase the Magnus force, causing the unpinning of the vortices. The Magnus force modulus per unit length in General Relativity has exactly the same form as the Newtonian one (Langlois et al., 1998):

$$f_M = \kappa m_n y_n n_B v_L, \tag{2.14}$$

where v_L is the speed of a segment of vortex line as seen in the local frame comoving with the superfluid flow. It can be shown (Antonelli et al., 2018) that if we want to write the above relation in terms of the angular velocity lag, this has to be written as:

$$f_M = \kappa m_n y_n n_B e^{-\Phi} x \Omega_{np} \tag{2.15}$$

where x represents the cylindrical radius.

We have to keep in mind, however, that perfect pinning – that occurs all vortices are pinned in the inter-glitch time and there is no vortex creep – is probably never realised in neutron stars, but it is useful to perform this thought experiment. In fact, an imperfect pinning in the star would only yield a smaller value of the theoretical maximum glitch amplitude, thus confirming that the one we are about to calculate is the maximum theoretically achievable. The upper limit $\Delta\Omega_{\rm max}$ on the glitch amplitude is thus obtained by artificially emptying the whole reservoir of pinned superfluid, namely

$$\Delta\Omega_{\rm max} \equiv \Delta\Omega_{\rm m}[\Omega_{np}^{\rm cr}]. \tag{2.16}$$

Estimates of $\Omega_{np}^{\rm cr}$ are based on the still poorly-known physics of vortices in the crust, as well as in the core of neutron stars. Therefore we construct the critical lag in two different physical scenarios: when vortex lines have an overall rigidity so that they collectively organise into a stable array of paraxial vortex lines, and the scenario where vortices are slack (i.e. tensionless) at the hydrodynamic scale, so that any macroscopic portion of superfluid can flow independently from the others. It is interesting to study these two extreme cases, as we expect real vortices to behave in a way that is in between them.

2.1.1 Rigid vortices

Let us restrict ourselves to the case of rigid vortices directed along the rotation axis, as done in Antonelli and Pizzochero (2017). This is also the case employed to study the maximum glitch amplitude in the Newtonian framework in Pizzochero et al. (2017). This hypothesis is an extreme scenario, and it is not realised in the interior of a neutron star. However, we will introduce this model in order to have a direct comparison with the tensionless vortices model we will introduce below. Moreover, the rigid vortices model has the advantage of simplifying the three-dimensional vortex dynamics problem in a more treatable one-dimensional one, by projecting the motion of every vortex on the equatorial plane of the star.

The idea of rigidity can be represented by studying the unpinning condition in an integral way. In other words, if γ_x represent a vortex which threads the equatorial plane of the star at a cylindrical coordinate x, the unpinning condition for that vortex is

$$\int_{\gamma_x} \mathrm{d}l\, f_M = \int_{\gamma_x} \mathrm{d}l\, f_P, \tag{2.17}$$

where $\mathrm{d}l$ is the arc length along a vortex. Note that this unpinning condition is non-local. Of course, other prescriptions for the unpinning condition of a rigid vortex can be chosen: with this prescription, however, even if the Magnus force per unit length is not large enough to overcome the pinning force at every point of the curve γ_x, the integrated Magnus force should be able to unpin the vortex, by acting through vortex rigidity. This integration allows us to reduce the motion of a vortex to the motion of a point on the equatorial plane. Of course, there is also the additional complication of defining a set of curves γ_x for the vortices.

The critical lag can be obtained by substituting the relativistic Magnus force in (2.15) into this unpinning condition. However, we immediately face a problem: the lag Ω_{np} cannot be easily brought outside the integral in the presence of entrainment, since – as shown in (Antonelli and Pizzochero, 2017) – the angular velocity lag is no longer columnar. One way to overcome this difficulty is to define a rescaled lag Ω_{vp} as:

$$\Omega_{vp} \equiv \frac{\Omega_{np}}{1-\varepsilon_n(r)}. \tag{2.18}$$

This rescaled angular velocity is again columnar, thus it will be constant along a single vortex line γ_x. This value will therefore only depend on the cylindrical radius x. Note that, from Equation (2.7) we can also derive the partial moment of inertia of the auxiliary v-component

$$I_v = \frac{8\pi}{3c^2} \int_0^{R_d} dr\; r^4 e^{-\Phi+\Lambda}\, \frac{y_n\left(\rho c^2 + P\right)}{1-\varepsilon_n}. \tag{2.19}$$

A similar definition, but with an additional factor $(\Omega_p - \omega(r))/\Omega_p$, is also present in the work of Newton et al. (2015) and in Section 3.2: in order to account for

entrainment in the crust in these cases, the moment of inertia is written by simply dividing the integrand in Equation (2.6) (limited to the neutron component) by the dimensionless effective neutron mass $m_n^*(r)/m_n = 1-\varepsilon_n(r)$. This is not inconsistent with our approach, since in those cases the moment of inertia of the entire (rigid) n-component $I_n^{\rm tot}$ is used.

The critical lag can be obtained by using Equation (2.17), and reads:

$$\Omega_{vp}^{cr}(x) = \frac{\int_{\gamma_x} \mathrm{d}l\, f_P}{\kappa\, x \int_{\gamma_x} \mathrm{d}l\, \frac{m_n n_n}{1-\varepsilon_n} \mathrm{e}^{-\Phi}}\,. \tag{2.20}$$

We have to notice, however, that the form of the line element $\mathrm{d}l$ is related to the metric we are using and on the form of the set of curves γ_x we are assuming. In our particular choice of metric (2.3), if we choose straight lines directed along the axis z of rotation, we obtain:

$$\mathrm{d}l = \sqrt{\frac{z^2}{r^2}\mathrm{e}^{2\Lambda} + \frac{x^2}{r^2}}\mathrm{d}z\,. \tag{2.21}$$

The assumption of straight lines is quite unrealistic. However, since the exact configuration of the superfluid vortices in a spinning-down neutron star is unknown we use this configuration as a test case for our model. It can be shown that numerically the critical lag (2.20) is very similar to the Newtonian one calculated in Antonelli and Pizzochero (2017). For this reason, we will not comment much on this equation here, delaying the discussion to the next Chapter, when we will consider the Newtonian critical lag.

The maximum glitch can be obtained by substituting the critical lag (2.20) into Equations (2.7) and (2.13). We obtain

$$\begin{aligned}\Delta\Omega_{\max} = \frac{4\pi}{I\kappa}\int_0^{R_d} dx\, x^2 \int_0^{z(x)} dz\, \frac{y_n\,(\rho c^2 + P)}{1-\varepsilon_n}\, e^{\Lambda-\Phi}\,. \\ \cdot \left(\int_{\gamma_x} dl\, f_P\right)\left(\int_{\gamma_x} dl\, \frac{m_n n_n c^2}{1-\varepsilon_n} e^{-\Phi}\right)^{-1}\end{aligned} \tag{2.22}$$

where R_d is the radius corresponding to the interface between the inner and the outer-crust (drip radius). We can see that this equation is entrainment-dependent. This is not a drawback of our choice for the curves γ_x: the dependence on entrainment cannot be cancelled out simply because the integral containing the mass-energy density and pressure and that containing the rest mass density do not simplify. If we consider the Newtonian limit (that is, $\Phi, \Lambda \to 0$ and $\rho = m_n n_B \gg P/c^2$), the above equation does not depend on the entrainment anymore, as in this case the two integrals containing it simplify themselves (Pizzochero et al., 2017):

$$\Delta\Omega_{\max} = \frac{4\pi}{I\kappa}\int_0^{R_d} \mathrm{d}x\, x^2 \int_{\gamma_x} \mathrm{d}l\, f_P(r) = \frac{\pi^2}{I\kappa}\int_0^{R_d} \mathrm{d}r\, r^3\, f_P(r)\,, \tag{2.23}$$

where the last equality has been obtained by making a change of variables. From here we can see that – if we assume the pinning to be limited to the crust of the star – this result does not depend on the extension of the superfluid inside the star, as long as these vortices reside at least in the crust. In fact, if we set $f_P(r) = 0$ in the core of the star, the maximum glitch amplitude would be the same, regardless of the extension (or not) of the vortices γ_x in the core. As we have seen, however, this is no longer analytically true in the general relativistic framework. Nevertheless, it will be shown in Section 2.2 that the presence of a curved spacetime, along with a strong entrainment, does not change much the value of the maximum glitch. Of course, here we are assuming for simplicity that the pinning of the superfluid vortices is limited to the crust: Equations (2.22) and (2.23) hold also if we assume pinning in the core of the star and we provide $f_P(r)$ for this region, which thus yields a different numerical value for the maximum glitch amplitude.

2.1.2 Tensionless vortices

The opposite possibility with respect to that of rigid vortex lines is that of having tensionless (or slack) vortices. In this case, we assume a local unpinning condition: we are asking that every infinitesimal element of the vortex line behaves independently from all the other ones. The unpinning condition (2.17) is then modified in

$$|\mathbf{f}_M| = f_P(r), \tag{2.24}$$

which is a local condition. The critical lag thus takes this much simpler form:

$$\Omega_{np}^{cr} = \frac{f_P(r)\, e^{\Phi(r)}}{\kappa\, r\, \sin\vartheta\, m_n\, n_B(r)\, c^2}\,. \tag{2.25}$$

We have to notice that, even if we had used the rescaled lag Ω_{vp} instead of the true lag Ω_{np}, the critical lag is always a two-variable function, i.e. it depends on both r and ϑ. This is just because we do not have to integrate along the vortex lines as we have done in the rigid case. So in the particular case of tensionless vortices there is no real advantage in using Ω_{vp} instead of Ω_{np} as there were when assuming rigid vortices.

The advantage of taking tensionless vortices is that we do not have to assume any vortex configuration, as the unpinning condition is simply local. We remark that a completely slack vortex at the microscopic scale would bend even over lengths of the Wigner-Seitz radius in the crust, making unrealistic the analysis of vortex pinning carried out by Seveso et al. (2016) that incorporates the presence of non-zero single-vortex tension to estimate the mesoscopic pinning force per unit length of vortex line. Moreover, this scenario of vortices that are tensionless at the macroscopic scale can lead to the development of superfluid turbulence: if vortices pass through the crust-core interface, the non-pinned section of the vortex immersed into the core can wrap around the rotation axis as described by Greenstein (1970) and vorticity can

develop toroidal components. We can now substitute the expression for the critical lag in Equation (2.16) in order to obtain the maximum glitch amplitude

$$\Delta\Omega_{\max} = \frac{\pi^2}{I\kappa}\int_0^{R_d} \mathrm{d}r\, r^3\, \mathrm{e}^{\Lambda(r)}\, \frac{\rho(r)c^2 + P(r)}{m_n n(r) c^2} f_p(r). \tag{2.26}$$

It is interesting to notice that this result depends only on the pinning force profile, the mass of the star and the EoS. Differently from the rigid case, the maximum glitch calculated with tensionless vortices does not display a dependence on the entrainment. This feature is retained also in the Newtonian limit. In fact, the Newtonian limit of (2.26) is exactly the same of one for the rigid vortices (2.23). This means that the result obtained in Pizzochero et al. (2017) holds for both the extreme cases of rigid and tensionless vortices, as long as we work in a Newtonian framework.

2.2 Numerical results

In Section 2.1, we presented the argument for the calculation of the maximum glitch size achievable by a pulsar of Antonelli et al. (2018) and generalised the model presented in Pizzochero et al. (2017), embedding it in a relativistic framework and proposing two different prescriptions to calculate the critical lag for unpinning and the corresponding maximum glitch amplitudes. We now discuss the numerical results for the partial moments of inertia and the maximum amplitudes; then, by following the simple argument proposed in Antonelli and Pizzochero (2017), we estimate $M_{\max}$.

The input used in our numerical calculations is summarised in Table (2.1); we adopted three unified barotropic EoSs (SLy4, BSk20 and BSk21), for which the superfluid fraction $y_n(n_B)$ is provided together with $P(n_B)$ and $\rho(n_B)$: these are calculated consistently for all regions of the neutron star (hence the adjective "unified"). For the mesoscopic pinning forces, we used the results of Seveso et al. (2016). In particular, we employed the more realistic case with $L = 5000$ Wigner-Seitz radii: note that smaller values of L would give rise to larger pinning forces (see Figure 1.14), which would in turn cause a larger maximum glitch and a less tight constraint on the mass. We are thus considering the weakest pinning force, in order to compare and test the outcomes with observational data. Note also that these pinning forces are given in terms of rest-mass density, i.e. they depend on n_B. For entrainment, we adopted the entrainment parameters calculated in Chamel and Haensel (2006) for the core and in Chamel (2012) for the crust (also given in terms of n_B).

2.2.1 Relativistic moments of inertia

It is well-known that the relativistic moment of inertia given in Equation (2.6) can have a marked discrepancy with respect to its non-relativistic counterpart. Although only the total moment of inertia appears in the calculation of the maximum glitch, it is interesting to discuss the relativistic corrections also to the partial ones, since they frequently appear in dynamical studies of pulsar glitches.

EoS	$n_{\rm edge}$ [fm^{-3}]	$M_{\rm max}$	Reference
SLy4	0.076	2.05 $M_\odot$	(Douchin and Haensel, 2001)
BSk20	0.0854	2.16 $M_\odot$	(Goriely et al., 2010)
BSk21	0.0809	2.28 $M_\odot$	(Goriely et al., 2010)
f_P	0.0776		$\beta = 3$, $L = 5000$ of Seveso et al. (2016)

Table 2.1: We list some properties of the three EoSs used: $M_{\rm max}$ is the maximum non-rotating gravitational mass that the EoS can sustain, while $n_{\rm edge}$ is the baryon density at the crust-core interface (see also Fantina et al., 2013, for a study of the global properties of non-rotating neutron stars constructed with the same EoSs used here). For comparison we also list the baryon density at which the pinning force used in this work becomes zero.

A word of caution is necessary, however, regarding the Newtonian framework: since the background configuration is actually fixed by the integration of the TOV equations, it is not clear what should be interpreted as "inertia" of the system in this spurious scenario. Indeed, most studies existing in the literature take the more consistent choice of always adopting the relativistic definition of density and use it in different prescriptions for the moments of inertia (either the Newtonian expressions or some general relativistic approximations, like the one discussed in Ravenhall and Pethick, 1994). Here we will adhere to the approach adopted in Antonelli and Pizzochero (2017) as well as in Pizzochero et al. (2017): in the Newtonian framework, we take ρ as the mass-energy density calculated from the TOV equation, even in the Newtonian case (that is, $\Phi, \Lambda \to 0$ and $\rho \gg P/c^2$). Note that the Newtonian maximum glitch amplitude of Equation (2.23) is not affected by this alternative choice, as long as one works coherently by using the same definition of the mass density ρ also in the Magnus force. This ambiguity is inherent to the spurious nature of the Newtonian scenario and disappears in the general relativistic framework.

In Figure 2.1 we compare the moments of inertia in the two frameworks (the labels N and GR stand for "Newtonian" and "general relativistic slow-rotation" respectively) by plotting I and I_n as a function of the gravitational mass M for the three unified EoSs. For the moment of inertia I_n associated with the superfluid reservoir, we have chosen the scenario of vortices that thread continuously the entire star, so that both the crustal and core superfluid contribute to the angular momentum reservoir; as already mentioned, this is the scenario investigated in Antonelli and Pizzochero (2017) and in Pizzochero et al. (2017).

As expected from several existing studies with various EoSs, the total relativistic moment of inertia is significantly larger than its Newtonian counterpart, with discrepancies up to 50% for large stellar masses. The discrepancies are even more dramatic for the reservoir, where I_n always exceeds the total moment of inertia I, indicating that the effect of $1 - \omega/\Omega_p$ in the integrand of I is more severe than the diminishing effect of y_n in the integrand of I_n. Although unusual this result is not a physical contradiction, as discussed previously. The only consistency requirement is $I_n^{\rm tot} < I$, which holds by

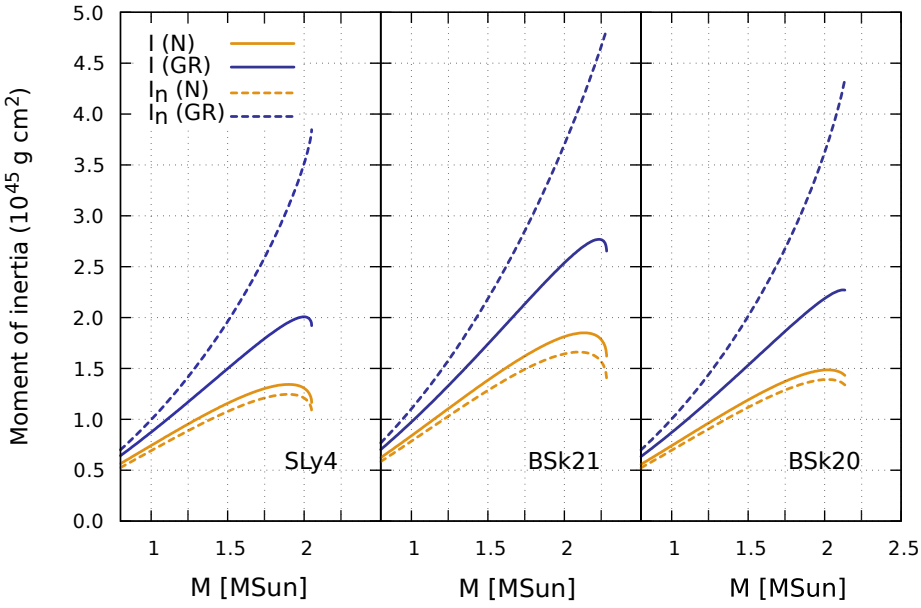

Figure 2.1: Moments of inertia I (solid lines) and I_n (dashed lines) are shown for the three EoSs considered and for the mass interval $[0.8\,M_\odot, 2.5\,M_\odot]$. A comparison is made between the non-relativistic moments of inertia (orange curves, labeled by "N") and the relativistic ones calculated in the slow-rotation approximation (dark blue curves, labeled by "GR"). The curves are terminated at the maximum mass allowed by each EoS, as reported in Table 2.1.

construction.

To better visualise the difference between the two frameworks, in Figure 2.2 we plot the ratios I_n/I and I_ν/I as a function of mass in the N and GR scenarios for the three EoSs: this kind of ratio is often found in dynamical studies of pulsar glitches. In particular, the figure allows to estimate the influence of entrainment: the advantage of using the ν-component (determined only by the vortex configuration) is that I_ν encodes entirely the effect of entrainment on the physical n-component. When entrainment parameters are set to zero I_ν tends to I_n: therefore, comparison of the two quantities quantifies the global dynamical effect of the non-dissipative coupling between the two components for a given vortex configuration. For the case under study of core plus crust continuous reservoir, the differences are altogether quite small, no more than some percent in the GR scenario. Moreover, for masses larger than $\sim 1.1\,M_\odot$ we find that $I_\nu > I_n$, while smaller masses yield $I_\nu < I_n$, in both frameworks: the entrainment parameters adopted here are large and negative in the crust, but small and positive in the core.

When the superfluid reservoir extends into the core, the crust contribution to I_ν dominates for light stars (which present a thick crust), while for more massive stars (with thinner crusts) it is the core contribution that prevails. This is different from the case in which the superfluid reservoir is confined into the crust, defined as the

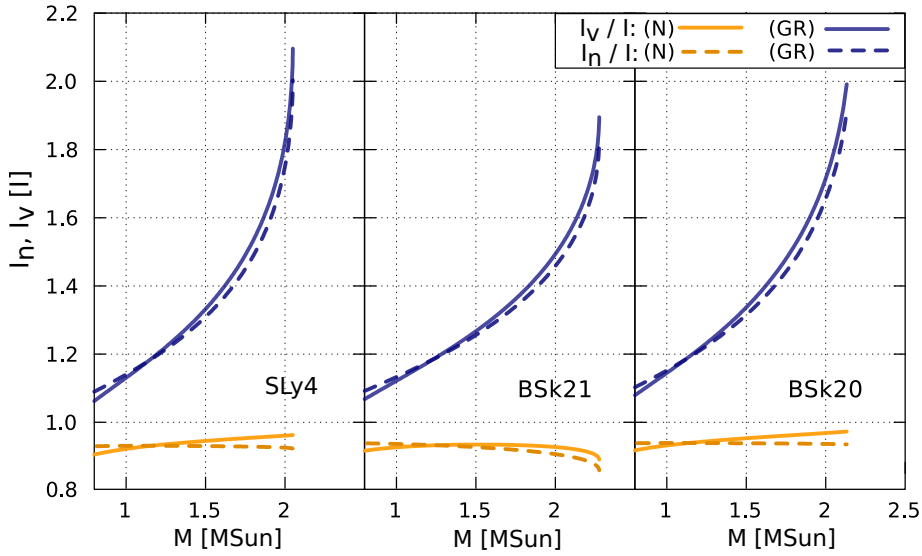

Figure 2.2: Moments of inertia of the superfluid component in the whole star in units of the total moment of inertia for the mass range $[0.8\,M_\odot, 2.5\,M_\odot]$. We make comparison between two cases: when strong entrainment is present (and thus the quantity of interest is I_v/I, solid lines) and when the entrainment profile is zero (in this case I_v is equal to I_n and we plot the ratio I_n/I, dashed lines). In both cases we show the curves calculated in the Newtonian framework (orange curves, labeled by "N") and in the slow-rotation approximation (blue curves, labeled by "GR").

region where $n_B < n_{\rm edge}$ (see Table 2.1): entrainment has a marked decreasing effect on the moment of inertia of the crustal superfluid (see Andersson et al., 2012; Chamel, 2013). As seen in the Figure 2.3, the presence of entrainment actually reduces by a factor 3-4 the effective moment of inertia of the crustal superfluid. On the other hand, the presence of relativistic corrections works in the opposite direction, by slightly increasing I_v/I.

2.2.2 Maximum glitch amplitudes

Let us now discuss and compare the maximum glitch amplitudes in the Newtonian and relativistic frameworks. Once the input has been fixed (EoS, pinning forces and entrainment coefficient), the maximum glitch amplitude depends only on the stellar mass. In the following, we will discuss three cases, corresponding to the different scenarios explored in Section 2.1:

Model N – This is the Newtonian framework adopted in Pizzochero et al. (2017): the maximum glitch amplitude as a function of mass $\Delta\Omega_{\rm max}(M)$ is calculated with Equation (2.23). As already remarked, the Newtonian result does not depend on the entrainment parameters and it is not necessary to specify how vortices are arranged, since both the parallel and slack vortex configurations give the same result. Moreover,

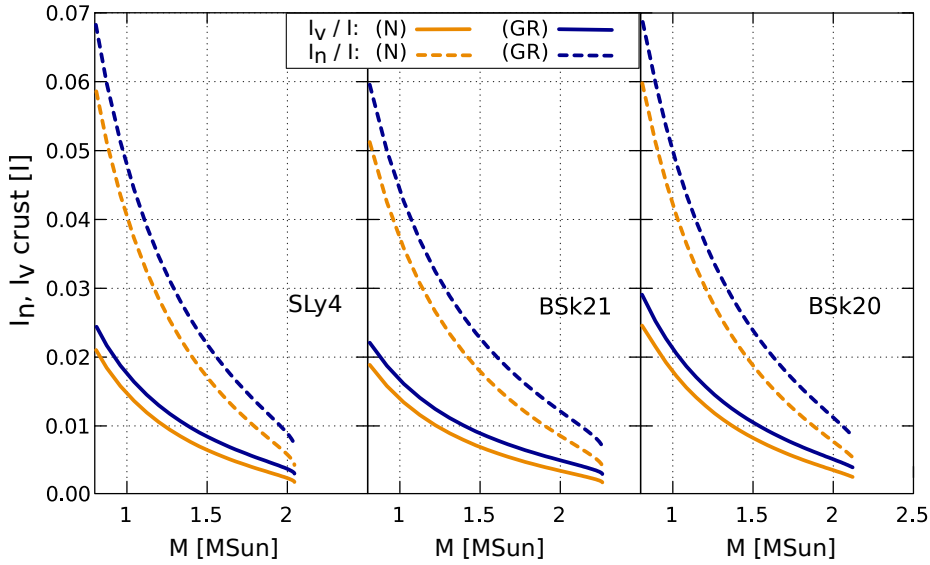

Figure 2.3: Moments of inertia of the superfluid in the crustal pinning region in units of the total moment of inertia for the mass range $[0.8\,M_\odot, 2.5\,M_\odot]$; as in Figure 2.2, I_v/I is the case with entrainment (solid lines), while I_n/I is the case without entrainment (dashed lines). Again, we show the curves calculated in the Newtonian framework (orange curves, labeled by "N") and in the slow-rotation approximation (blue curves, labeled by "GR").

also the extension of vortices inside the core is unimportant, as long as vortex lines extend at least across the region where pinning is present. In this Chapter we assumed the scenario of only crustal pinning and, as reported in Table 2.1, the region of non-zero pinning lies inside the inner crust for the three EoSs considered. Therefore the Newtonian results for $\Delta\Omega_{\rm max}(M)$ are valid for both cases of continuous vortex lines and only crustal reservoir.

Model R – This is the relativistic generalisation of model N for the case of straight rigid vortices, where the non-local unpinning condition is implemented: the function $\Delta\Omega_{\rm max}(M)$ is calculated from Equation (2.22). In this case the presence of entrainment and the extension of vortices affect $\Delta\Omega_{\rm max}(M)$; the results shown here refer to continuous vortices across the star interior, the general scenario adopted in Antonelli and Pizzochero (2017) and Pizzochero et al. (2017). We remind that Equation (2.22) was actually derived in a non-rigorous way, so that model R should be taken more as a test for the dependence of the maximum glitch amplitudes on phenomenologically reasonable (albeit not consistent) critical lags, like that of Equation (2.20).

Model S – This is the relativistic generalisation of model N for the case of slack vortices, where the local unpinning condition is implemented: the function $\Delta\Omega_{\rm max}(M)$ is calculated from Equation (2.26). This seems to be a natural generalisation of its Newtonian counterpart, and all the remarks made for model N are still valid in this GR extension.

To show an example of the typical result, in Figure 2.4 we fix the SLy4 EoS and

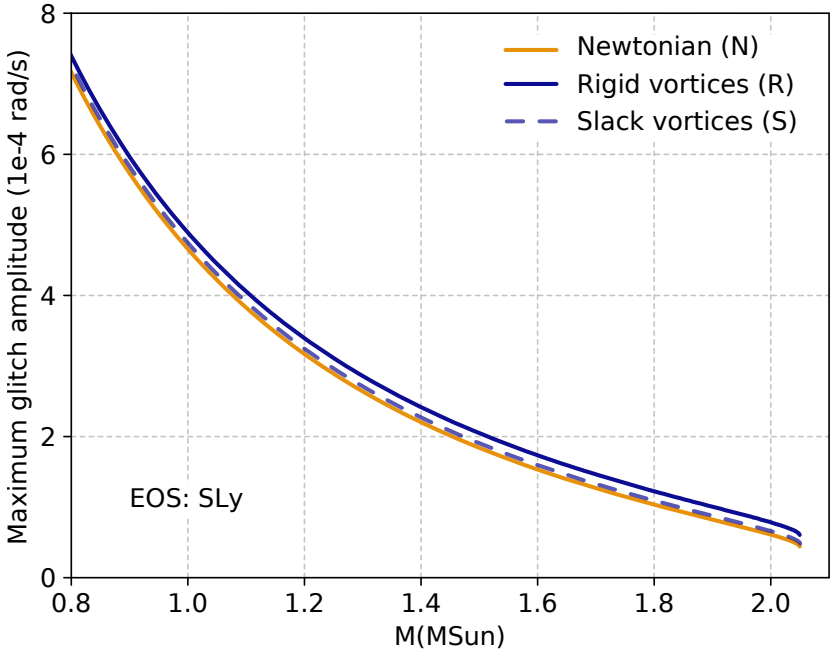

Figure 2.4: Maximum glitch amplitude calculated as a function of mass for the SLy4 EoS in the case of rigid vortices (R) and tensionless vortices (slack, S) in General Relativity and in the Newtonian case (N).

plot the function $\Delta\Omega_{\rm max}(M)$ for the three models. We observe that both relativistic models give maximum glitch amplitudes that are slightly larger than their Newtonian counterpart, with model S closer to the non-relativistic case.

To better visualise our general results, in Figure 2.5 we show for the three EoSs the relative difference between the relativistic models R and S and the Newtonian one, namely we plot the curves $\Delta\Omega^{\rm R}_{\rm max}/\Delta\Omega^{\rm N}_{\rm max} - 1$ and $\Delta\Omega^{\rm S}_{\rm max}/\Delta\Omega^{\rm N}_{\rm max} - 1$, where the superscript indicates the model used. We observe that in model R the relativistic corrections increase with stellar mass, with values between 5% and 30% for all EoSs; conversely, for model S the dependence on mass of the corrections is weak, with values between 3% and 5% for all the masses allowed by the EoSs.

2.2.3 Relativistic corrections to the upper bounds on pulsar masses

Now, following the argument of Antonelli and Pizzochero (2017) and using the results of the previous subsection, we estimate the upper bound on pulsar masses that can be obtained from observations. As it is possible to see from Figure 2.4, the maximum glitch is inversely proportional to the mass of the star. In other words, lighter stars can achieve the largest glitches: if we observe a large glitch from a pulsar, all the stellar models which predict a largest glitch smaller than the one observed are ruled out. In this way we can put an upper limit on the mass of the glitching star. This method

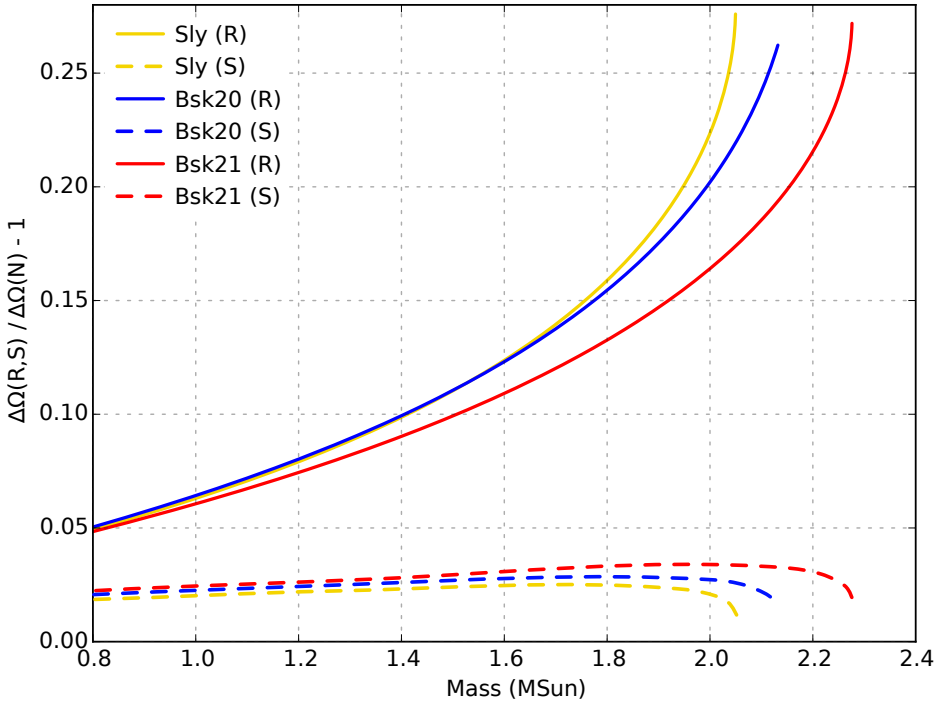

Figure 2.5: Relativistic corrections to the maximum glitch amplitudes $\Delta\Omega_{\rm max}(M)$ for the three EoSs (identified by different colors). We plot the quantities $\Delta\Omega^{\rm R}_{\rm max}/\Delta\Omega^{\rm N}_{\rm max}-1$ (solid lines) and $\Delta\Omega^{\rm S}_{\rm max}/\Delta\Omega^{\rm N}_{\rm max}-1$ (dashed lines), where the superscript indicates the model used (see Figure (2.4)).

has been applied to a sample of large glitchers in Pizzochero et al. (2017): an upper limit on the stellar mass can be obtained from the largest recorded glitch, while future observations of even larger glitches will further constrain the mass. See, for instance, the Crab pulsar, which has recently displayed its largest glitch (Shaw et al., 2018), thus improving its mass constraint.

For a given pulsar, whose largest observed glitch amplitude is $\Delta\Omega$, the upper bound on the mass $M_{\rm max}$ is given by $\Delta\Omega = \Delta\Omega_{\rm max}(M_{\rm max})$. The value of $M_{\rm max}$ is only dependent on the choice of the pinning force and the EoS used to calculate the function $\Delta\Omega_{\rm max}(M)$ for models N and S, while model R requires also the entrainment coefficients (as discussed previously, however, from the results in Figure (2.2) we expect the maximum glitch to vary at most by some percent when entrainment is set to zero). A graphical representation of the procedure used to estimate the upper bound is shown in Figure (2.6), where we plot the inverted function $M = M(\Delta\Omega_{\rm max})$ for the three EoSs; here, the curves refer to model R, the one showing the largest relativistic corrections, but qualitatively these curves are very similar in all models, as can be seen in Figure 2.4. Vertical dotted lines indicate the maximum glitch recorded for a small sample of large glitchers (the glitch amplitudes are extracted from the Jodrell Bank

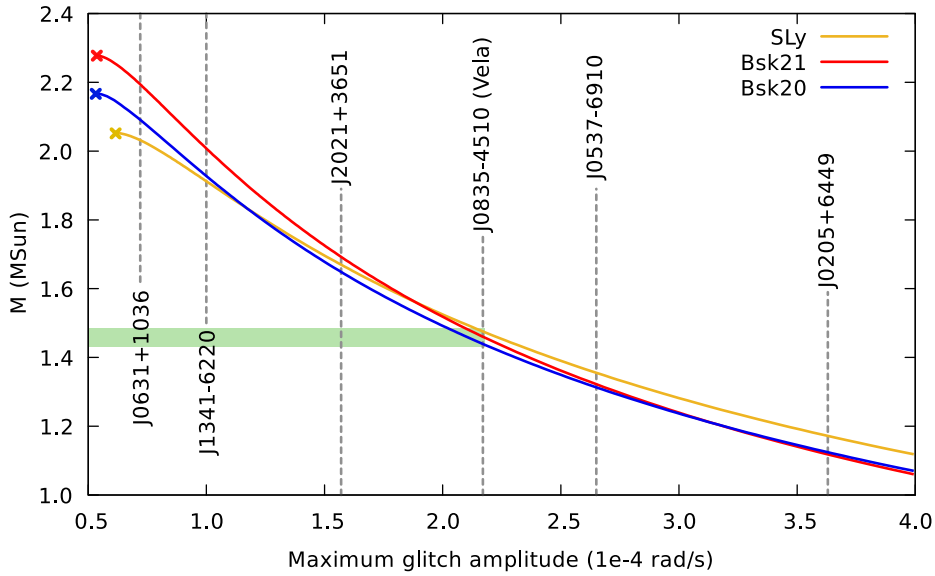

Figure 2.6: Graphical representation of the upper mass limit for a glitching pulsar. In the figure we plot the inverse of the function $\Delta\Omega_{\max}(M)$ for the three EoSs; the scenario considered here is that of model R (straight rigid vortices that thread the whole star). We also report the largest observed glitch $\Delta\Omega$ for some of the pulsars studied in Pizzochero et al. (2017): the errors on $\Delta\Omega$ are negligible, except for J0537-6910 and J0205+6449, which have a relative error of $\approx 10\%$. For each pulsar, the value of $M_{\max}$ is found by considering the intersection of the gray dashed lines (corresponding to the value of $\Delta\Omega$) with one of the three curves. Taking the Vela as an example, the range of $M_{\max}$ arising from the EoSs considered here is highlighted with a shaded band.

Glitch Catalogue[1]).

As an example, let us consider the benchmark case of the Vela pulsar (J0835-4510), whose largest observed glitch to date has amplitude 2.17×10^{-4} rad/s. By looking at Figure 2.6, the Vela should have a mass lower than $M_{\max} \approx 1.5\, M_\odot$, when SLy4 or BSk21 are used, slightly less for BSk20. Instead of listing the mass upper bounds corresponding to all the glitchers with maximum recorded glitch larger than $\approx 5 \times 10^{-5}$ rad/s and their deviation with respect to the Newtonian result, we prefer to plot the discrepancy between the relativistic and non-relativistic values of $M_{\max}$ as a function of the maximum glitch amplitude. Note that the minimum value for which it is possible to employ this method – i.e. 5×10^{-5} rad/s – is dictated by the maximum mass achievable by the different EoSs, see Figure 2.6. In fact, glitch sizes smaller than this value do not provide constraints with this method, as they would lie on the left of the curves for all the EoSs under consideration. The assumption of zero angular momentum reservoir after the largest glitch is a working hypothesis we made to obtain the maximum glitch amplitude in (2.16). Nevertheless, finite-size effects in

[1]Data available at `www.jb.man.ac.uk/pulsar/glitches.html`, see also Espinoza et al. (2011).

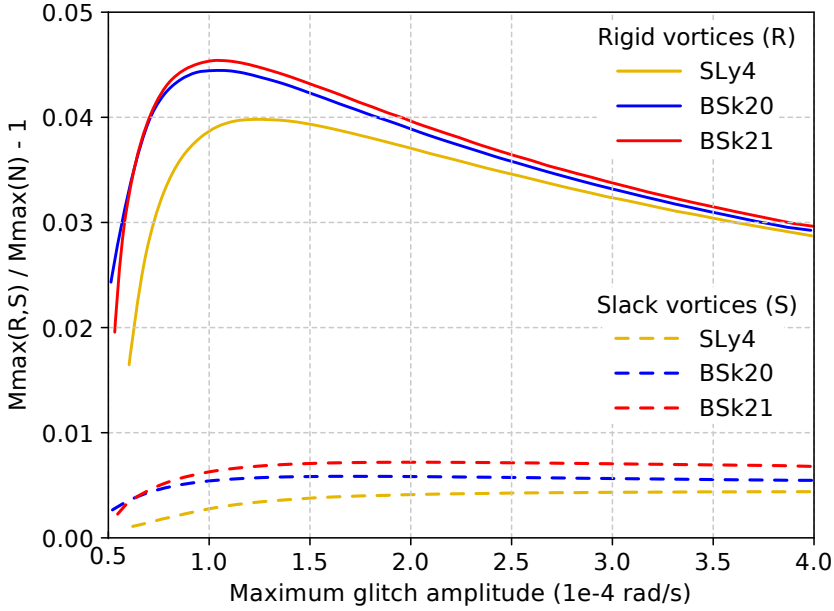

Figure 2.7: Magnitude of the general relativistic corrections to the mass upper bound $M_{\max}$ as a function of the maximum observed glitch, for the SLy4, BSk20 and BSk21 EoSs and for the rigid and tensionless cases.

the reservoir have been observed – through correlations between glitch size and the following waiting time – only in PSR J0537-6910 so far (Melatos et al., 2018). Note, however, that if a pulsar does not deplete its reservoir after its largest glitch, it would mean that is not its maximum glitch achievable: a largest glitch is always possible, by depleting the reservoir more. This supports the fact that the constraint given by the largest glitch is an upper limit on the mass.

In Figure 2.7 we show for the three EoSs the relative difference between the relativistic models R and S and the Newtonian one, namely we plot the curves $M^{\mathrm{R}}_{\max}/M^{\mathrm{N}}_{\max} - 1$ and $M^{\mathrm{S}}_{\max}/M^{\mathrm{N}}_{\max} - 1$, where the superscript indicates the model used. The main remark is that the relativistic corrections to $M_{\max}$ are always positive and small, less than 5% for all masses allowed by the EoSs; in particular, for model S the discrepancies are smaller than 1%. The conclusion is that the upper bounds on masses presented in Pizzochero et al. (2017) are quite robust: in the scenario of slack vortex lines, they are uniquely determined by the pinning force profile and the EoS adopted, while they are independent on entrainment and on the extension of vortices in the core, and are basically unaffected by general relativistic corrections.

CHAPTER 3

Activity parameter

Some information about the structure of a glitching pulsar can be obtained from its glitching behaviour. In particular, how frequent and how large its glitches are. One way to encode this information is a study on the glitch size and waiting time distributions (see, e.g., Melatos et al. 2008, Howitt et al. 2018 and Fuentes et al. 2019). While calculating these functions is probably the method to extract information in the most complete way, it is possible to summarise the behaviour of a glitcher in the activity parameter, which is a quantity that expresses the average acceleration of a pulsar due to glitches. In this Chapter we will discuss some approaches for calculating the activity parameter, and some constraints on the mass and moments of inertia of a neutron star which can be obtained from this quantity.

3.1 Calculation of the activity parameter

The activity parameter was first introduced in McKenna and Lyne (1990). It encodes a quick estimate of a pulsar glitching behaviour, i.e. how large glitches the pulsar displays and how frequently. If we assume that a particular object has undergone $N_{\rm gl}$ glitches at times t_i with size $\Delta\Omega_i$ – with $i = 1, ..., N_{\rm gl}$ – the absolute activity can be defined as:

$$\mathcal{A}_a = \frac{1}{T_{\rm obs}} \sum_{i=1}^{N_{gl}} \Delta\Omega_i \,, \tag{3.1}$$

where $T_{\rm obs} \approx t_{N_{gl}} - t_1$ is the temporal duration of the observation. Note that defining this parameter in this way, we are assuming that no observations have been made before the first and after the last glitch: it is thus possible for $T_{\rm obs}$ to be much longer, yielding a lower value for the activity. Moreover, we are assuming that the stars are regularly monitored, without missing any glitch. This is, of course, not the case, but while large glitches can be easily detected, small glitches, easier to miss, do not contribute to the activity in a significant way. It is useful to define the dimensionless

activity parameter $\mathcal{G}$ as

$$\mathcal{G} \equiv \frac{\mathcal{A}_a}{|\dot{\Omega}_\infty|}\,. \tag{3.2}$$

This variable gives us an idea of the amount of spin down reversed by glitches, and it allows for comparing different objects with different spin down rates. In the literature, the absolute activity is usually calculated by fitting the data, rather than using the above definition (see, e.g., Wong et al., 2001). An example of the activity fit performed with a least-squares linear fit is shown in Figure 3.1 for the six pulsars which have displayed the currently largest number of glitches. The motivation behind the choice of an ordinary linear regression is simple: we are assuming a homogeneity in time, which implies that the statistical properties of the random process do not depend on the window of observation. In particular, the mean rate must be practically constant in time (note that this is not true for some objects, like the Crab, see Carlin et al., 2019). The idea of pulsar activity $\mathcal{A}_a$ fits well this concept. However, we immediately face two problems: on the one hand, the choice of fitting the activity with a linear regression causes a problem of statistical significance (Montoli et al., 2020c). We need at least three (or, better, more than three) glitches in order to perform a reliable fit. Moreover, we need at least two glitches with comparable orders of magnitude: a linear regression would poorly fit a set of data with just one large glitch and many others with sizes several orders of magnitude smaller. This characteristic can be quantified with a parameter which summarises the number of maximal glitches that would be needed to account for the observed total spin-up:

$$N_{\max} = \frac{\sum_{i=1}^{N} \Delta\Omega_i}{\Delta\Omega_{\max}}\,, \tag{3.3}$$

where $\Delta\Omega_{\max}$ is the largest displayed glitch. On the other hand, even if the glitches respect the above conditions and they are all of similar sizes (for example, in the cases of PSR J0537-6910 or of the Vela pulsar, see Figure 3.1), a linear fit may not be the ideal choice. In fact, a linear fit implies the presence of a strong correlation between glitch sizes and the waiting times between them. This feature, however, is not present in any of the pulsars which have been studied, where instead it seems to be very little correlation between glitch sizes and the waiting times before and after them (Melatos et al., 2018) – with the notable exception of PSR J0537-6910, which presents correlation between glitch sizes and the following waiting time (Middleditch et al., 2006; Antonopoulou et al., 2018; Ferdman et al., 2018; Ho et al., 2020) – and autocorrelations in sizes and waiting times (except for the Crab's glitch sizes, see Carlin and Melatos, 2019a).

In order to solve this issue, we present here two alternative ways to estimate the activity of a pulsar (see also Montoli et al., 2020a). One requires to calculate the probability distributions for the waiting times and sizes of the glitches of a particular pulsar, and then to obtain an estimate of the pulsar activity probability distribution starting from this information. The other method is much simpler, and makes use of the bootstrap method.

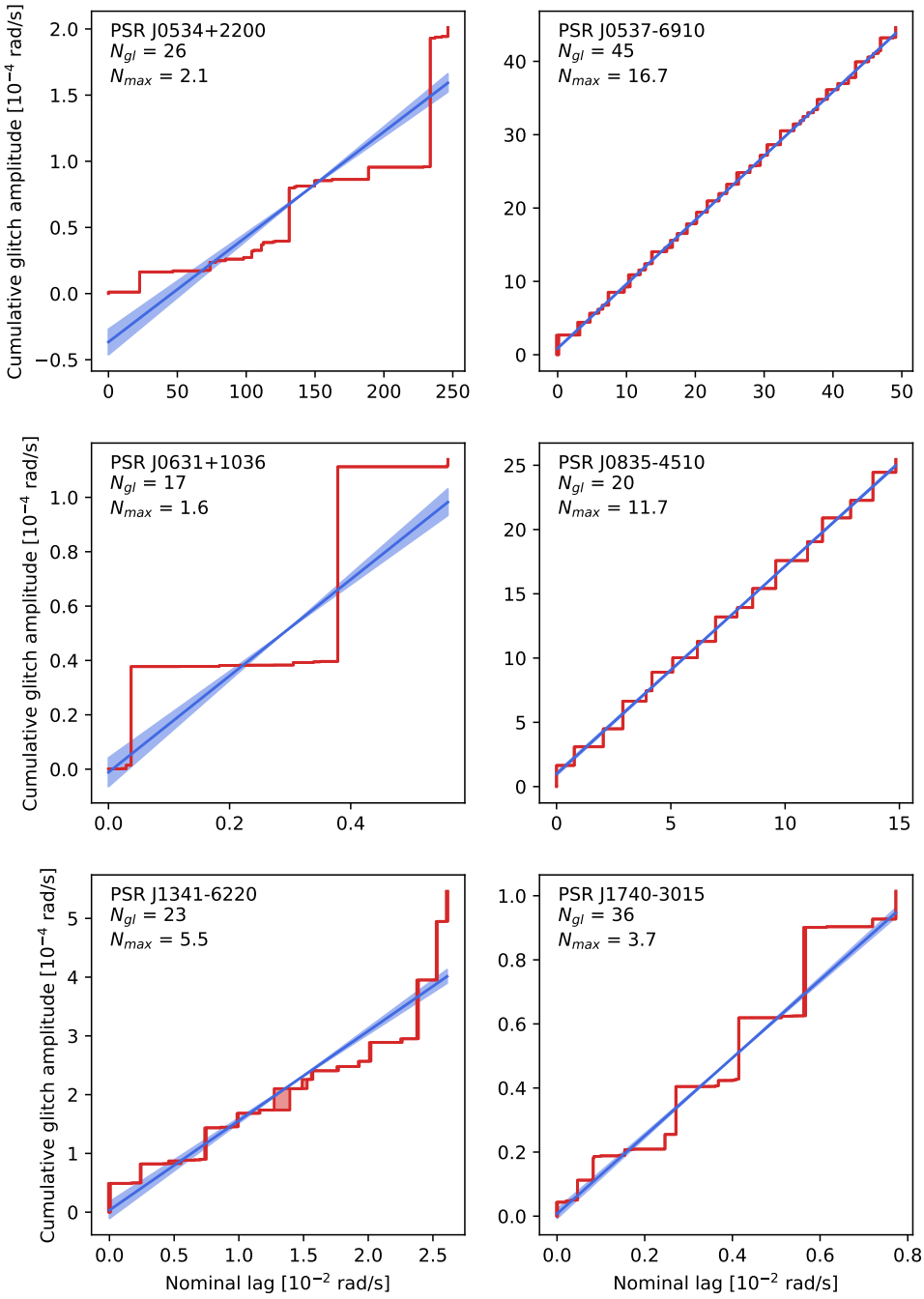

Figure 3.1: Pulsar activity calculated with a least-squares linear fit (in blue) on the midpoints of the glitch steps in the cumulative glitch sequence (see Wong et al., 2001), for the six pulsars with the largest number of glitches (in red). The blue-shaded region indicates the 1σ error on the activity. The plots are made with the nominal lag $t|\dot{\Omega}_\infty|$ on the x-axis (see Equation (3.36)), so that the slopes of the curves are the dimensionless activities $\mathcal{G}$.

Probability distribution estimates for the waiting times and sizes of glitches have already been performed in many works in the literature, and in many different ways. In Melatos et al. (2008) the best fitting distribution is studied by minimising the Kolmogorov-Smirnov statistic, in Fuentes et al. (2019) different distributions are studied with the maximum likelihood technique and compared with the Akaike Information Criterion, while in Howitt et al. (2018) the empirical distributions have been smoothed with a Kernel Density Estimator. Here we would like to study the best fitting probability distribution for both the sizes and waiting times in a fully Bayesian framework and try to infer the probability distribution of the activity parameter after N glitches $\mathcal{A}_N$. To do so, we have to choose a set of probability distribution candidates among which we find the best fitting for a particular pulsar and its waiting times/sizes. We choose a uniform distribution, a Pareto (power law) distribution, an exponential distribution, a gamma distribution, a truncated normal and a Rayleigh distribution.

The uniform distribution has been chosen as a test distribution: it is one of the simplest distribution, so it can be useful as a benchmark distribution with respect to which we study how well a particular model performs. In particular, we decide to further simplify this function, by keeping the left bound fixed at $x_{\min} = 0$. The Pareto distribution has a power-law-like behaviour, which is the expected probability distribution for the sizes if the glitch phenomenon is a self-organised one, as in vortex avalanches (Melatos et al., 2008; Warszawski and Melatos, 2008):

$$P(x \mid x_{\min}, a) = \begin{cases} \frac{a}{x_{\min}} \left(\frac{x}{x_{\min}}\right)^{-a-1} & \text{if } x \geq x_{\min} \\ 0 & \text{elsewhere} \end{cases} \tag{3.4}$$

On the other hand, an exponential distribution is also the expected one for the waiting times in a self-organised system:

$$P(x \mid \lambda) = \begin{cases} \lambda\, e^{-\lambda x} & \text{if } x \geq 0 \\ 0 & \text{elsewhere} \end{cases} \tag{3.5}$$

We also try to study a more general distribution, the gamma distribution, which includes both the trends of a Pareto distribution and an exponential one:

$$P(x \mid \alpha, \beta) = \begin{cases} \frac{\beta^\alpha}{\Gamma(\alpha)} x^{\alpha-1} e^{-\beta x} & \text{if } x \geq 0 \\ 0 & \text{elsewhere} \end{cases} \tag{3.6}$$

where Γ is the gamma function. Finally, we study also the possibility of a preferred glitch size and waiting time, by including a truncated normal and a Rayleigh distributions. It is important that the normal distribution is truncated, as we do not expect glitches of negative sizes or negative waiting times.

$$P(x \mid \mu, \sigma, x_{\min}) = \begin{cases} \frac{1}{C} \exp\left(-\frac{(x-\mu)^2}{2\sigma^2}\right) & \text{if } x \geq x_{\min} \\ 0 & \text{elsewhere} \end{cases} \tag{3.7}$$

where C is the normalisation constant. Also the Rayleigh distribution has suitable characteristics, as it is defined for only for positive values, it shares some similarities with the normal distribution, and it has fewer parameters than the truncated normal.

$$P(x\,|\,\sigma) = \begin{cases} \frac{x}{\sigma^2}\exp\left(-\frac{x^2}{2\sigma^2}\right) & \text{if } x \geq 0 \\ 0 & \text{elsewhere} \end{cases} \tag{3.8}$$

We have to keep in mind, however, that it is not a symmetric distribution, i.e. it has non-null skewness.

Given a set of data $\mathcal{D}$, the probability distribution of the set of parameters $\mathcal{P}$ of a particular model $\mathcal{M}$ (i.e. one of the probability distribution we have assumed above for the data) is given by the Bayes theorem:

$$P(\mathcal{P}|\,\mathcal{D},\,\mathcal{M}) = \frac{P(\mathcal{D}|\,\mathcal{P},\,\mathcal{M})\,P(\mathcal{P}|\,\mathcal{M})}{P(\mathcal{D}|\,\mathcal{M})}, \tag{3.9}$$

where $P(\mathcal{P}|\,\mathcal{D},\,\mathcal{M})$, $P(\mathcal{D}|\,\mathcal{P},\,\mathcal{M})$, $P(\mathcal{P}|\,\mathcal{M})$ and $P(\mathcal{D}|\,\mathcal{M})$ are the posterior distribution, the likelihood, the prior distribution and the evidence, respectively. Let us assume a probability distribution $P(x|\,\mathcal{P})$ for the data we are interested in among the six described before, that the measurements have no uncertainties and that each datum is independent of the others. In this case, the likelihood of the parameters is given by:

$$P(\mathcal{D}|\,\mathcal{P}) = \prod_{i\in\text{data}} P(x_i|\,\mathcal{P}). \tag{3.10}$$

If we have more than one model, we can calculate which of two of them is more likely by calculating the ratio (also known as Bayes factor, see, e.g., MacKay 2003)

$$K_{ij} = \frac{P(\mathcal{M}_i|\,\mathcal{D})}{P(\mathcal{M}_j|\,\mathcal{D})} = \frac{P(\mathcal{D}|\,\mathcal{M}_i)}{P(\mathcal{D}|\,\mathcal{M}_j)}, \tag{3.11}$$

where the last equality has been obtained by employing the Bayes theorem, and by assuming no particular preference *a priori* of one model $\mathcal{M}_i$ with respect to another. So if we want to compare two different models we have to perform a Bayesian inference (3.9) and study the ratio of the evidences calculated in this way. A positive natural logarithm of the Bayes' factor yields a preference of model $\mathcal{M}_i$ with respect to $\mathcal{M}_j$, the other way around if it is negative. The other ingredient necessary to perform the inference in (3.9) is a prior distribution. The idea employed here is that of using the Jeffey's principle in order to find the most uninformative prior for each distribution (Gelman et al., 2013). As a rule of thumb, the prior on all "scale" parameters, like the standard deviation σ of the normal distribution, follow a log-uniform distribution, while all the "location" parameters, like the mean μ, follow a uniform distribution. The ranges of the parameters have been chosen not to cut the posterior distribution. We summarise the priors for the probability distribution described above in Table 3.1.

The pulsars we are interested in are all those pulsars with more than 15 glitches detected, namely the Crab pulsar (J0534+2200), J0537-6910, J0631+1036, the Vela

Model	Variable	Prior	Range (sizes)	Range (waiting times)
Uniform	$x_{\rm max}$	Uniform	(0, 10000)	(0, 14600) [days]
Pareto	$x_{\rm min}$	Log-uniform	(1e-5, 1e4)	(1, 14600) [days]
	a	Uniform	(0, 10)	(0, 10)
Exponential	λ	Uniform	(0,100)	(0,100) [days^{-1}]
Gamma	α	Uniform	(0, 10)	(0, 10)
	β	Uniform	(0, 100)	(0, 100) [days^{-1}]
Truncated	μ	Uniform	(0,10000)	(0, 14600) [days]
Normal	σ	Log-uniform	(10, 10000)	(10, 10000) [days^{-1}]
	$x_{\rm min}$	Uniform	(0,10000)	(0, 14600) [days]
Rayleigh	σ	Log-uniform	(10, 10000)	(10, 10000) [days]

Table 3.1: Priors for the different probability distributions used for sizes and waiting times. Note that the data for the sizes is in units of $10^{-9}\Omega$, where Ω is the angular velocity for the particular pulsar under examination.

pulsar (J0835-4510), J1341-6220 and J1740-3015. For the Crab pulsar, only the data after MJD 45000 has been considered, as there is a three-year gap with no observations between February 1979 and February 1982. Since then, it has been monitored on a daily basis (Espinoza et al., 2014; Lyne et al., 2015). The data has been retrieved from the Jodrell Bank Glitch Catalogue[1] (Espinoza et al., 2011). Note that all these pulsars are also present in the sample of Fuentes et al. (2019).

In this framework, a model $\mathcal{M}_i$ simply represents a different probability distribution for the sizes/waiting times. We test which of these models is the best one by calculating the evidence for each dataset and each pulsar and studying the Bayes factor. The Bayes factor can be calculated by the means of a nested sampling algorithm (`dynesty`, see Speagle, 2020; Ashton et al., 2019a). We report the results in Tables 3.2 and 3.3 for the sizes and waiting times, respectively. All the Bayes' factors are calculated with respect to the simplest model of a uniform distribution between 0 and a value $x_{\rm max}$. Keeping in mind that the natural logarithm of a Bayes' factor larger than 5 indicates a very strong evidence for a model with respect to another (Kass and Raftery, 1995), we can notice that for sizes the best describing distribution is the Pareto distribution for most of the pulsar, except for the Vela and PSR J0537-6910. This fact has already been noted in many previous works (Melatos et al., 2008; Fuentes et al., 2019). What is interesting is the best distribution describing these two exceptions: while for J0537-6910 the best fitting distribution is a truncated normal, thus indicating a preferred glitch size for it, it seems that the best probability distribution for the Vela pulsar is the uniform one. In other words, it seems that the Vela pulsar does not seem to have

[1] `www.jb.man.ac.uk/pulsar/glitches.html`, data retrieved on July 2020.

	Pareto	Gamma	Exponential	Truncated Normal	Rayleigh
J0534+2200	63.6	51.3	46.1	22.3	-32.9
J0537-6910	-55.0	-7.4	-5.1	5.1	-2.9
J0631+1036	52.8	37.4	16.0	6.1	-55.7
J0835-4510	-40.8	-20.8	-18.1	-5.0	-13.4
J1341-6220	6.1	1.8	2.3	3.2	-19.8
J1740-3015	81.4	67.6	39.6	21.5	-74.8

Table 3.2: Natural logarithm of the Bayes factor for the different size probability distribution of the different pulsars, calculated with respect to the simplest uniform model with constant $x_{\min} = 0$.

	Pareto	Gamma	Exponential	Truncated Normal	Rayleigh
J0534+2200	15.7	15.9	18.7	16.7	0.0
J0537-6910	-11.5	7.0	-2.0	11.3	15.3
J0631+1036	-0.9	0.6	3.2	4.6	-2.2
J0835-4510	-26.6	-14.0	-15.0	-2.5	-1.8
J1341-6220	-5.3	-3.4	-11.1	1.6	4.5
J1740-3015	3.4	8.7	11.1	12.1	1.4

Table 3.3: Natural logarithm of the Bayes factor for the different waiting time probability distribution of the different pulsars, calculated with respect to the simplest uniform model with constant $x_{\min} = 0$.

a preferred size for its glitches. A bit less clear is the situation for the waiting times. For some of the pulsars in the sample, the exponential model seems to be excluded (J0537-6910, Vela and J1341-6220, see also Howitt et al., 2018), while for all the others it is not excluded, but it is not the strongly preferred one either. In general, it seems there is not a particular predilection for one model with respect to another for almost all the pulsars, except perhaps J0537-6910 – which seems to be well described by a Rayleigh/truncated normal distribution.

One of the advantages of the nested sampling algorithm is that – as a by-product of the calculation of the evidence for a particular inference – it is able to produce samples of the posterior distribution of the parameters of the model. These posteriors can be then employed in order to find the inferred probability distribution by calculating the posterior predictive distribution, that is the probability of drawing a new value $\bar{x}$ given the data $\mathcal{D}$:

$$P(\bar{x}|\mathcal{D}, \mathcal{M}) = \int P(\bar{x}|\mathcal{P}, \mathcal{M})\, P(\mathcal{P}|\mathcal{D}, \mathcal{M})\, \mathrm{d}\mathcal{P}, \tag{3.12}$$

where the integration is performed on the whole parameter space. The model $\mathcal{M}$ which the above relation refers to is the best one as estimated by the Bayes factor. Starting from the probability distribution of the waiting times t and the sizes s it is possible to

infer some information about the probability distribution for the dimensionless glitch activity after N glitches $\mathcal{G}_N$. Keeping in mind the definition of the pulsar activity $\mathcal{G}$, it is possible to calculate its probability distribution, as it is a ratio of two random variables, the sum of sizes $\tilde{s}_N$ and of waiting times $\tilde{t}_{N-1}$. The latter, in turn, are sum of random variables themselves, i.e. the single glitch size s_i and the single waiting time t_i. Thus, it is possible to obtain:

$$\tilde{s}_N = \sum_{i=1}^{N} s_i \qquad \Rightarrow \qquad \tilde{s}_N \sim P_{\tilde{s}_N} = \underbrace{P_s * \ldots * P_s}_{N \text{ times}} \tag{3.13}$$

$$\tilde{t}_{N-1} = \sum_{i=1}^{N-1} t_i \qquad \Rightarrow \qquad \tilde{t}_{N-1} \sim P_{\tilde{t}_{N-1}} = \underbrace{P_t * \ldots * P_t}_{N-1 \text{ times}} \tag{3.14}$$

The random variable $\mathcal{G}_N$ is the ratio of the two random variables $\tilde{s}_N$ and $\tilde{t}_{N-1}$. The probability distribution of $\mathcal{G}_N$ can be obtained through the ratio distribution:

$$P_{\mathcal{G}_N}(g) = \frac{1}{N-1} \int_{-\infty}^{\infty} \mathrm{d}x \, |x| \, P_{\tilde{t}_{N-1}}(x) \, P_{\tilde{s}_N}(xg) \, . \tag{3.15}$$

Although it is a theoretically well-posed solution, it is troublesome to numerically obtain this distribution, as a convolution of N probability distributions, albeit identical, starts to be infeasible when N becomes large.

An alternative way of calculating activity is the bootstrap method (Efron, 1979). The idea is that of resampling with replacement the original data in order to calculate some statistics, as, e.g., the mean and standard deviation of the calculated activity. In our case, the samples are two: the waiting time sample (of length $N-1$) and the size sample (of length N). Of course, in our case we have to draw the same number of samples ($N-1$) in order to have a fair estimation of the activity mean and standard deviation. The pulsar activity is then calculated not by performing a linear fit to the resampled data, but by employing the definition in Equation (3.1). We can also take into account the possibility of a dependency between a glitch size and the preceding or the subsequent waiting time, so it is useful to also bootstrap on other two samples: the sample made up by ordered pairs $\{(s_i, t_{\mathrm{pre},i})\}_{i=2,\ldots,N}$, where $t_{\mathrm{pre},i}$ is the waiting time preceding the glitch of size s_i, and the sample comprised by ordered pairs $\{(s_i, t_{\mathrm{post},i})\}_{i=1,\ldots,N-1}$, where $t_{\mathrm{post},i}$ is the waiting time following a glitch of size s_i. We plot in Figure 3.2 the histograms obtained by resampling the data ten thousand times in all the three cases described above. In the same plot, also the dimensionless activities obtained as a result of the linear fit of the cumulative glitch data are displayed. Looking at the Figure, we can see that the activity calculated by means of bootstrapping is compatible with the results obtained from a linear fit, but it generally has larger standard deviations (see also Table 3.4). This is probably due to the fact that a linear fit implies a strong correlation between sizes and waiting times, which is not observed in glitching pulsars (Melatos et al., 2018). An interesting

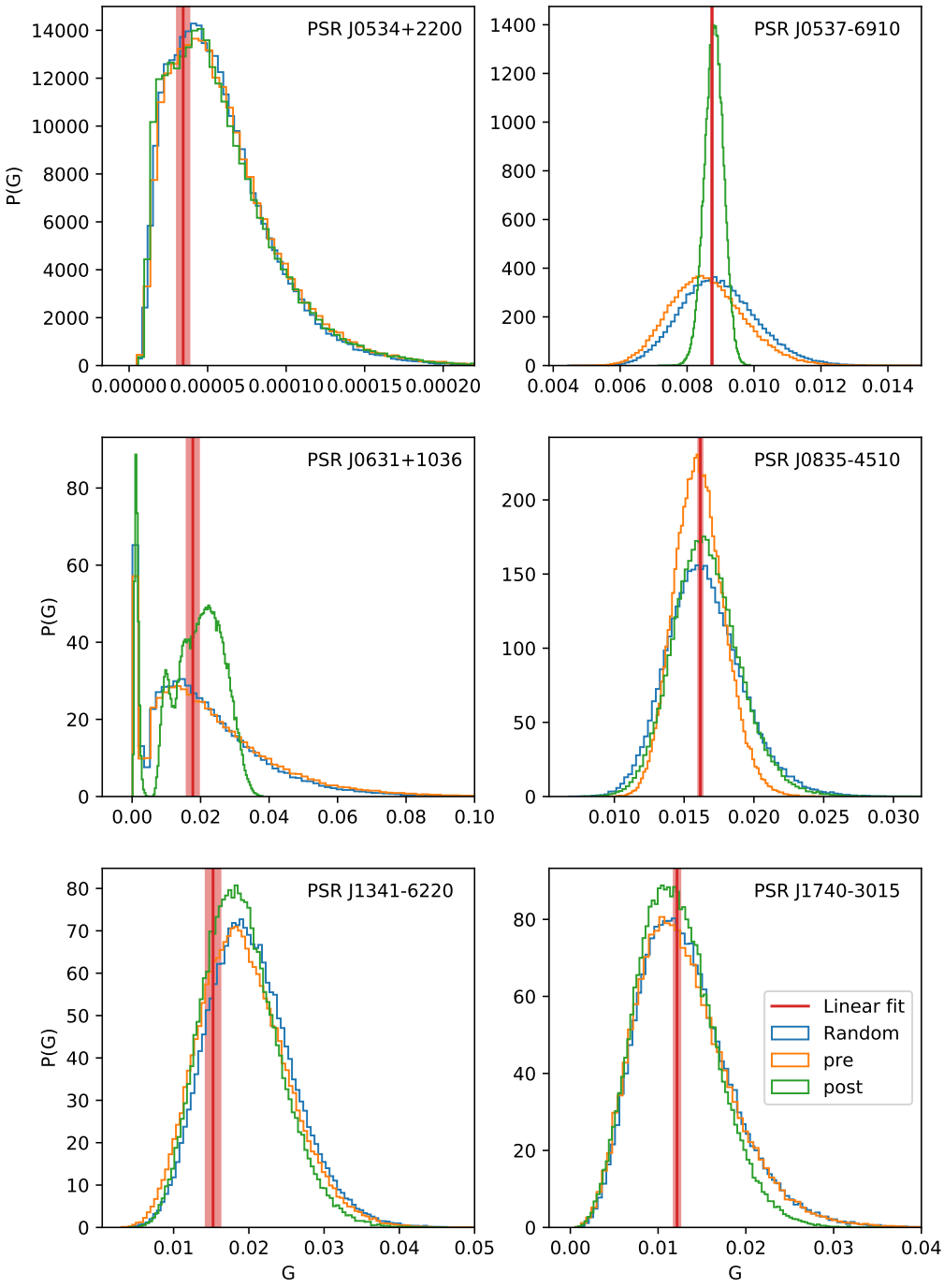

Figure 3.2: Dimensionless pulsar activity $\mathcal{G}$, calculated by sampling both the size and waiting time samples randomly (in blue), by sampling the pair (s, t_{pre}) (in orange) and the pair (s, t_{post}) (in green). The results of the linear fit of the cumulative glitch data is also plotted (in red, the shaded area is the 1σ region).

Pulsar	$\mathcal{G}_{\text{fit}}$ [%]	$\mathcal{G}_{\text{rand}}$ [%]	$\mathcal{G}_{\text{pre}}$ [%]	$\mathcal{G}_{\text{post}}$ [%]
0534+2200	0.0079 ± 0.0007	0.0082 ± 0.0046	0.0085 ± 0.0048	0.0083 ± 0.0049
0537-6910	0.8744 ± 0.0028	0.8942 ± 0.1143	0.8603 ± 0.1119	0.8801 ± 0.0290
0631+1036	1.7732 ± 0.1806	2.1142 ± 1.6717	2.2857 ± 1.7976	1.7972 ± 0.8544
0835-4510	1.6163 ± 0.0156	1.6484 ± 0.2723	1.6105 ± 0.1793	1.6604 ± 0.2407
1341-6220	1.5242 ± 0.0983	2.0235 ± 0.5697	1.9290 ± 0.5820	1.9007 ± 0.5105
1740-3015	1.2161 ± 0.0376	1.3120 ± 0.5337	1.2916 ± 0.5363	1.2133 ± 0.4490

Table 3.4: Dimensionless activities and their standard deviations, calculated for the six pulsars with the largest number of glitches, with a least-squares linear fit ($\mathcal{G}_{\text{fit}}$), with a bootstrap on the size and waiting time samples separately ($\mathcal{G}_{\text{rand}}$), and on the pairs size - preceding waiting time ($\mathcal{G}_{\text{pre}}$) and size - following waiting time ($\mathcal{G}_{\text{post}}$).

exception pointed out in Middleditch et al. (2006) is that of PSR J0537-6910, one of the few stars which presents a significant correlation between a glitch size and the following waiting time. This correlation shows its effects also in Figure 3.2: the histogram for J0537-6910, in the particular case of the sample of size-following waiting time pairs, is much more peaked than the other two cases. At lower confidence, also PSR J0631+1036 shows a correlation between size and the following waiting time, and Vela a correlation between size and the preceding waiting time (Melatos et al., 2018). These correlations show their effect in the histograms as well. It is also interesting to notice the peculiar form of the PSR J0631+1036 activity distribution: it shows two clear peaks, one on very small values and one around $\mathcal{G} \approx 0.02$. This is probably because of the particular glitch sequence of this star (see Figure 3.1): it displays two very large glitches, and many others with sizes several orders of magnitude smaller. Thus, it is likely that the peak on smaller values has been generated by sampling the small glitches only, while the peak on larger values occurs when one or both the large glitches have been sampled. Moreover, as a consequence of the particular glitch sequence for this star, the value of N_{max} for this star is smaller than the ones of the other stars in the sample.

In Figure 3.3 we try to give an idea of how much the activity changes when a new glitch occurs. The first point of each curve is the activity calculated with the definition in Equation (3.1) using the first ten glitches. Then, we update the activity value whenever a new glitch is displayed. In order to make a comparison with the activity calculated with the linear fit or with the bootstrap method, we decided to neglect the first glitch, to have the same number of glitch sizes and waiting times. We also plot the activity parameter calculated with the linear fit and the bootstrap method (with uncorrelated glitch sizes and waiting times), along with their uncertainties. We note that, as a general trend, the activity evolution of each star lies outside the error region for the linear fit, while it is usually well inside the bootstrap uncertainty. A notable exception is that of PSR J1341-6220, which is well below the error bar for both the activity calculations, except for the last three glitches. This is because these glitches are three of the largest ones displayed by this pulsar (see also Figure 3.1).

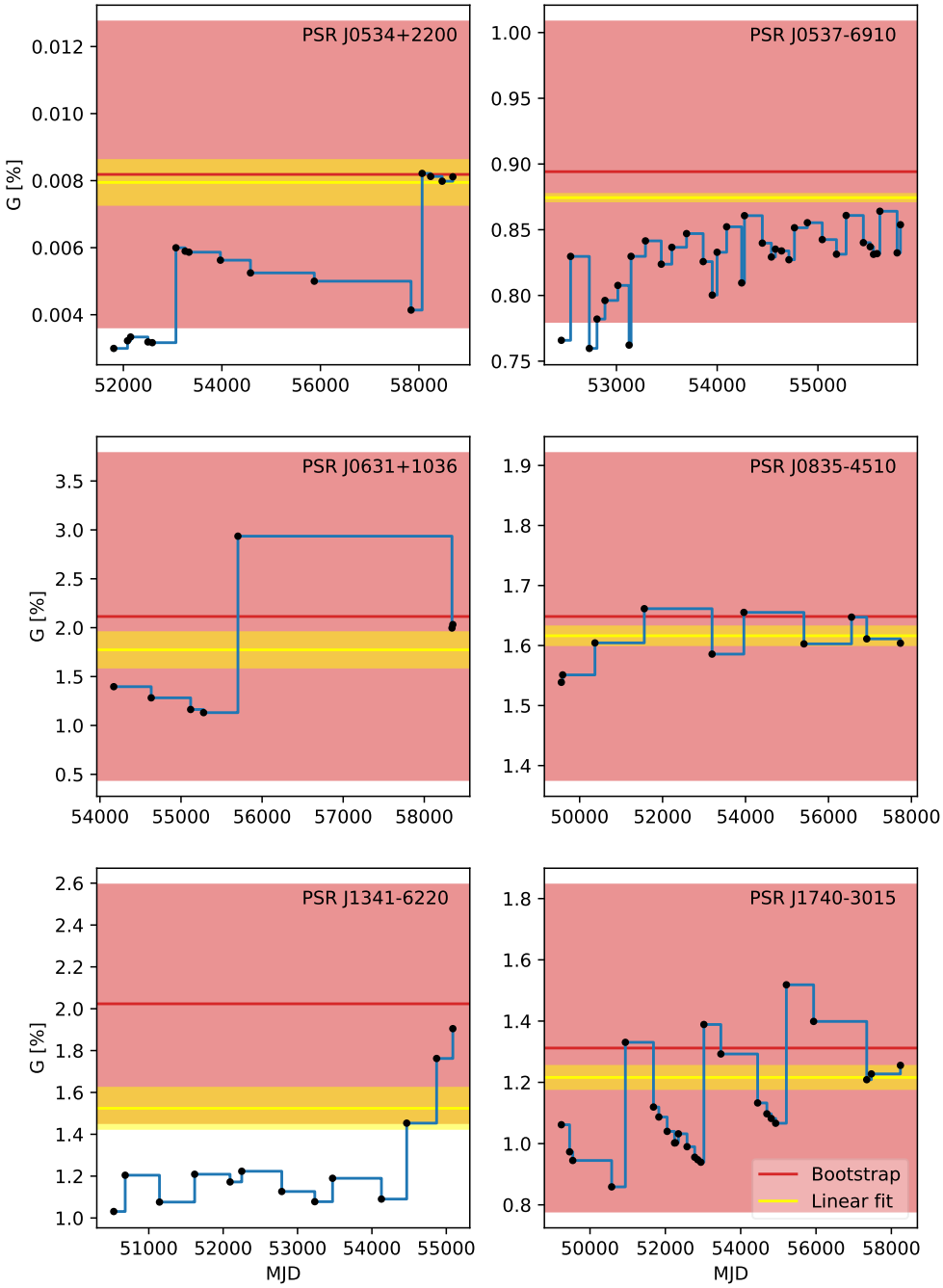

Figure 3.3: Evolution of the glitch activity over time. The first point of each curve is the activity calculated with the first ten glitches, with the first one neglected. The subsequent points are calculated by gradually adding all the glitches that pulsar displayed. The estimate of the linear fit (in yellow) and of the bootstrap with random waiting times and sizes (in red) are displayed, along with their uncertainties (shaded).

Also the activity evolution of PSR J0537-6910 is underestimated, but this is probably due to our choice of neglecting the first glitch, which is also the largest one in this object. For this pulsar and the Vela, the activity seems to have stabilised. This seems to correlate with the amount of time these objects have been observed, and their spin down rate $\dot{\Omega}$. The correlation is not simple, however, as the Crab has a higher spin down rate (see Table 3.5), and yet its activity is very noisy. In general, however, it is interesting to notice how variable the activity parameter is. A single large glitch can change its value dramatically, even doubling it (see, e.g., PSR J0631+1036 or the Crab pulsar after its November 2017 glitch, Shaw et al. 2018). This fact stresses the importance of having a much larger uncertainty on the activity, which is the result of not assuming a linear dependence between glitch sizes and waiting times.

3.2 Moment of inertia constraint

The activity parameter allows for many different ways to extract information from a glitching pulsar. In fact, this parameter allows to estimate the rate at which the angular momentum reservoir in the pulsar depletes due to glitches. The idea is that of using this parameter in order to constrain the moment of inertia of that part of the star which stores the angular momentum excess (Datta and Alpar, 1993). In this Section, we will present a revised version of the original argument of Link et al. (1999), Andersson et al. (2012) and Chamel (2013), as it is presented in Montoli et al. (2020a). Let us start from Equation (2.11). We are still working in a slow rotation framework. It is useful to divide Ω_p into the contributions due to the smooth relaxation (R) during the waiting times and the one from glitches (G),

$$\dot{\Omega}_p = \dot{\Omega}_p^G + \dot{\Omega}_p^R , \tag{3.16}$$

where $\dot{\Omega}_p^G$ are instantaneous accelerations of the star due to glitches, namely

$$\dot{\Omega}_p^G = \sum_i \delta(t - t_i)\Delta\Omega_i > 0 . \tag{3.17}$$

Analogous decomposition holds also for $\Delta L[\partial_t \Omega_{np}]$: during glitches $\Delta L[\partial_t \Omega_{np}^G] < 0$, while for the rest of the time $\Delta L[\partial_t \Omega_{np}^R] > 0$. Let us now introduce an average over a long time interval T (which does not have to coincide with the observational time $T_{\rm obs}$ in Equation (3.1)),

$$\langle f \rangle_T = T^{-1} \int_T dt\, f . \tag{3.18}$$

Averaging the total angular momentum balance (2.11) we get

$$\langle \Delta L[\partial_t \Omega_{np}^G] \rangle + I \langle \dot{\Omega}_p^G \rangle + \langle \Delta L[\partial_t \Omega_{np}^R] \rangle + I \langle \dot{\Omega}_p^R \rangle = -I |\dot{\Omega}_\infty| . \tag{3.19}$$

We can simplify the equation above by making two observations.

Firstly, due to the angular momentum conservation during a glitch, from the glitch contribution we get

$$\langle \Delta L[\partial_t \Omega^G_{np}] \rangle + I \langle \dot{\Omega}^G_p \rangle = 0 \,. \tag{3.20}$$

It is easy to notice that the quantity $\langle \dot{\Omega}^G_p \rangle$ corresponds to the average acceleration of the star due to glitches, i.e. it is the true activity of the pulsar $\mathcal{A}$. The above relation thus becomes

$$\langle \Delta L[\partial_t \Omega^G_{np}] \rangle = -I\mathcal{A} \,. \tag{3.21}$$

We have to stress that the activity here is the true activity of the star over a period T (which ideally should be very large), and it can be estimated through Equation (3.1) for a limited observation time span $T_{\rm obs}$.

Secondly, over the long period the star spins down as a whole: the lag oscillates between well-defined limits, implying that the average $\langle \Delta L[\partial_t \Omega_{np}] \rangle$ has to tend to 0, as T tends to infinity. Hence, the relaxation and glitch contributions must balance, such that

$$\langle \Delta L[\partial_t \Omega^R_{np}] \rangle = -\langle \Delta L[\partial_t \Omega^G_{np}] \rangle \,. \tag{3.22}$$

From the practical point of view we have to assume that, during the observational survey $T_{\rm obs}$, the star spins down as a whole on the average: this means that the measured activity is the true stationary one.

Finally, we can derive the constraint to the moment of inertia fraction given by the pulsar activity. As we have done in Chapter 2, it is useful to employ the formalism with the v—component, as in this case the vorticity is columnar also in the presence of entrainment. We have to stress the fact that all the relations obtained until now are still valid: the only difference is that ΔL is written as a function of the rescaled lag Ω_{vp} instead of the true lag Ω_{np}, by using Equation (2.18). Let us define the rescaled lag $\partial_t \Omega^P_{vp} > 0$, which is the maximum value of $\partial_t \Omega^R_{vp}$, and corresponds to the case when everything is perfectly pinned. Let us start from the Feynman-Onsager relation for a two-fluid system in the slow rotation framework. Keeping the same formalism of Chapter 2, this turns out to be (Antonelli et al., 2018):

$$\Omega_{vp}(r,\vartheta) = -\Omega_p + \omega(r) + \frac{\kappa m_n n_B e^{\Phi(r)} \mathcal{N}(r,\vartheta)}{2\pi(\rho_n c^2 + P)(r\sin\vartheta)^2} \,, \tag{3.23}$$

where $\mathcal{N}(r,\vartheta)$ is the number of vortices at (r,ϑ). When everything is pinned, it is easy to see that the time derivative of $\mathcal{N}$ is zero, as we do not expect the vortex configuration to change when vortices are pinned. Thus we obtain

$$\partial_t \Omega^P_{vp} = -\dot{\Omega}_p + \partial_t \omega \,. \tag{3.24}$$

We now have to calculate the time derivative of the drag of the inertial frames ω. Since we are working in the slow-rotation approximation, all the metric functions in (2.1) are approximated to the first order in Ω. So, as we have mentioned in the previous Chapter, all metric functions but ω can be derived from the usual TOV equations, as

the deformations from the spherical configuration arise only at the second order in Ω. The drag ω in the slow-rotation approximation is at the first order in Ω, namely:

$$\omega \approx \omega_1 \Omega \tag{3.25}$$

The slow-rotation approximation requires the spacetime to be stationary, i.e. $\partial_t \Omega = 0$. In our particular case, this is not completely true, but we can assume a quasi-stationary approach, which can be justified by the fact that the glitch rise time is expected to be orders of magnitude larger than the hydrodynamical timescale (Sourie et al., 2017). Since we are assuming that only Ω is time-dependent, and that $\omega_1 = \omega/\Omega$ depends only on the radial structure of the star (Hartle, 1967), Equation (3.24) can be written as:

$$\partial_t \Omega^P_{vp} = -\left(1 - \frac{\omega}{\Omega^P_p}\right) \dot{\Omega}^P_p \equiv -\tilde{\omega}\, \dot{\Omega}^P_p \,, \tag{3.26}$$

where we have defined $\tilde{\omega} = 1 - \omega/\Omega^P_p$. The angular momentum conservation holds also in the inter-glitch time, and also when the superfluid is perfectly pinned. We can then write

$$\langle \Delta L[\partial_t \Omega^P_{vp}] \rangle + I \dot{\Omega}^P_p = -I |\dot{\Omega}_\infty| \,. \tag{3.27}$$

Employing Equation (3.26), we find:

$$\dot{\Omega}^P_p (I - I_v) = -I |\dot{\Omega}_\infty| \,, \tag{3.28}$$

where we have defined $I_v \equiv \langle \Delta L[\tilde{\omega}] \rangle$. Note that this definition of I_v is different from that of Chapter 2, as it corresponds to the total angular momentum $I_v^{\rm tot}$ of the v-component.

Finally, let us now combine Equations (3.21) and (3.22). We have to notice that the angular momentum excess obtained by using Ω^P_{vp} is the maximum achievable by the star. So we expect, in general, that the extra angular momentum in the inter-glitch moments is smaller than the one when all the superfluid is pinned. All these considerations yield

$$\langle \Delta L[\partial_t \Omega^P_{vp}] \rangle > \langle \Delta L[\partial_t \Omega^R_{vp}] \rangle = I\mathcal{A} \,. \tag{3.29}$$

By substituting $\partial_t \Omega^P_{vp}$ from Equation (3.26) we obtain:

$$\dot{\Omega}^P_p \langle \Delta L[-\tilde{\omega}] \rangle > I\mathcal{A} \qquad \Rightarrow \qquad -\dot{\Omega}^P_p I_v > I\mathcal{A} \,, \tag{3.30}$$

and finally, substituting $\dot{\Omega}^P_p$ from Equation (3.28), we can find the constraint on the moment of inertia fraction of the superfluid component:

$$\frac{I\, I_v}{I - I_v} |\dot{\Omega}_\infty| > I\mathcal{A} \qquad \Rightarrow \qquad \frac{I_v}{I - I_v} > \mathcal{G} \tag{3.31}$$

Of course, this result can be obtained also in a Newtonian context, depending on what prescription we use for ΔL. In the slow rotation case, the value of I_v is (see Equation (2.7))

$$I_v = \frac{8\pi}{3c^2}\int_0^R dr\ r^4 e^{\Lambda(r)-\Phi(r)}\left[\frac{\rho(r)}{c^2}+P(r)\right]\frac{y_n(r)}{1-\varepsilon_n(r)}\frac{\Omega_p-\omega(r)}{\Omega_p}, \tag{3.32}$$

while the total moment of inertia is the usual one in the slow rotation framework (Equation (2.6)).

We have to remark that in Equation (3.32), y_n is the superfluid neutron baryon density divided by the total baryon density. This superfluid fraction $y_n(r)$ is, of course, null where there is no superfluid, and different from zero where there actually is the superfluid reservoir. For a long time, the region containing this superfluid has been thought to be the crust of the star. The first measurements of the activity parameter of the Vela pulsar and the moment of inertia fraction estimates for different EoSs seemed to be in full accordance and to respect Equation (3.31) (Link et al., 1999). Only later, the entrainment parameter $\varepsilon_n(r)$ in the crust of a neutron star has been calculated in Chamel (2012), by estimating the effects of Bragg scattering on the superflow due to the presence of the crustal lattice. These calculations yield a highly negative entrainment parameter in the crust, which implies a severely hindered motion of the superfluid component. This would reduce the amount of extra angular momentum stored in the crust between two glitches – and thus of I_v – making the requirement in (3.31) more difficult to be met. As a result of that, the only way for the star to acquire enough angular momentum between glitches to explain the observed activity is to have a large region inside it to store angular momentum (larger than the crust of the star), or to have an unreasonably small mass (see below). This problem has been evidenced in many papers (Andersson et al., 2012; Chamel, 2013; Ho et al., 2015; Delsate et al., 2016; Carreau et al., 2019).

If we assume the superfluid region to be limited in the crust of the star, and we fix the microphysical parameters, namely the EoS and the entrainment parameter, then the moment of inertia fraction in (3.31) is a function of the mass of the star only. Therefore, similarly to the case for maximum glitch amplitude, also here we obtain a constraint on the mass of the pulsar. Let us plot in Figure 3.4 some values of $I_v/(I-I_v)$ as a function of the mass for some EoSs and for the entrainment parameter calculated in Chamel (2012), assuming a superfluid reservoir limited to the crust. As we can see, a problem arises: the Vela pulsar (PSR J0835-4510) requires excessively low values for its mass, ranging from $\approx 1.1 M_\odot$ of the BSk20 EoS to $\approx 0.8 M_\odot$ for the SLy4 EoS. Things are marginally better if one considers the 1σ uncertainty calculated with the bootstrap method described in Section 3.1, with random waiting times and glitch sizes: for the BSk20 EoS, the Vela pulsar has an upper limit on the mass of $\approx 1.2 M_\odot$, which starts to be more reasonable. Note that this value is above the minimum mass of a neutron star estimated from calculations of core-collapse supernovae ($1.17\,M_\odot$, Suwa et al., 2018) and the smallest mass measured in a neutron star ($1.174 \pm 0.004\,M_\odot$,

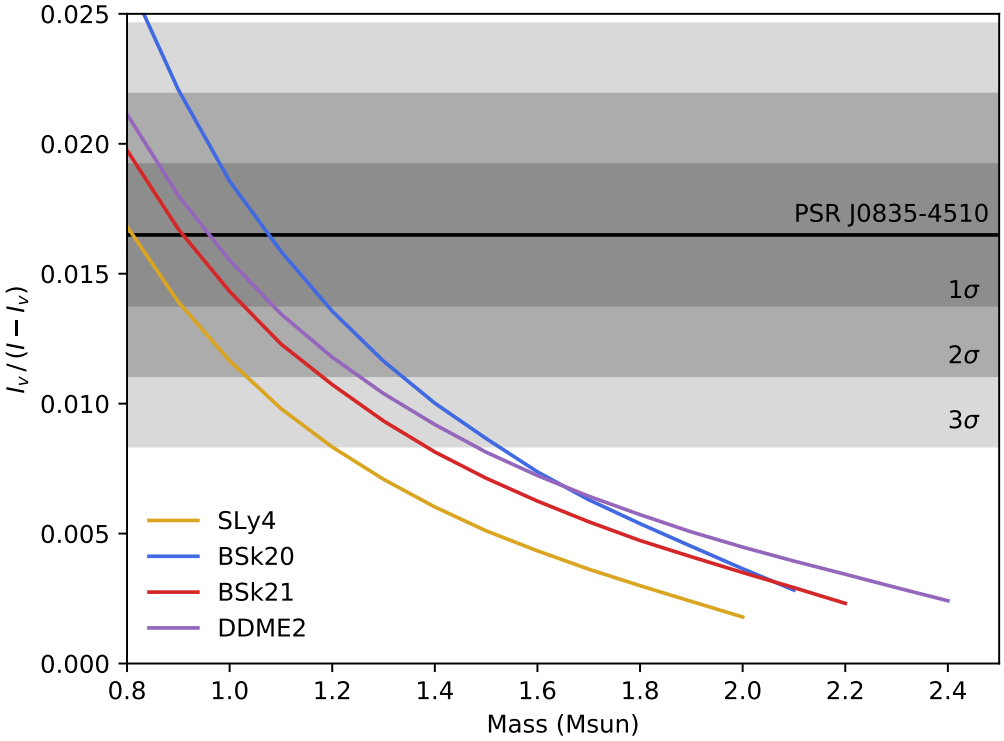

Figure 3.4: Activity constraint on the superfluid component moment of inertia plotted for some EoS: SLy4, (Douchin and Haensel, 2001), BSk20 and BSk21 (Goriely et al., 2010), and the DDME2 EoS (Lalazissis et al., 2005), glued with a SLy4 crust (following the method described in Fortin et al., 2016). The entrainment parameter is that calculated in Chamel (2012), and the superfluid reservoir is limited in the crust of the star. The dimensionless activity parameter $\mathcal{G}$ – calculated with the bootstrap method described in Section 3.1 (the case with random glitch sizes and waiting times) – is also plotted for the Vela pulsar, along with the 1σ, 2σ and 3σ uncertainties.

measured in PSR J0453+1559, Martinez et al., 2015). If we consider the 3σ error, then we can get up to $\approx 1.5 M_\odot$ for the same EoS. The solution to this problem, however, is not straightforward: the entrainment parameter in crust of the star calculated in Chamel (2012), the assumption of a superfluid reservoir limited in the crust of the star, and the measurement of the activity parameter seem not to be compatible with each other. This is why in the last years there has been a crisis in the widely accepted glitch paradigm, and in particular that of assuming the glitch reservoir to reside only in the crust of the star. Several ways have been proposed to overcome this impasse, including a maximally stiff EoS (Piekarewicz et al., 2014), a Bayesian analysis of the EoS uncertainty (Carreau et al., 2019) or an extension of the region where the neutron superfluid participates in the glitch beyond the crust-core transition, based on the assumption that only the superfluid in the $^1S_0$ state participates in the glitch

phenomenon and on an analysis of the temperature of the star (Ho et al., 2015). On the other hand, also different calculations of the entrainment parameter have been proposed, which include hydrodynamical approaches (Martin and Urban, 2016) or Bragg scattering in a disordered crustal lattice (Sauls et al., 2020), both of which yield milder entrainment effects in the crust.

Finally, let us comment on the differences and similarities between this model and the model presented in Chapter 2. In both cases the model depends on the EoS, and in both cases it depends on a particular microphysical parameter, the maximum pinning force for the largest glitch and the entrainment parameter for the activity constraint. Thus, the two different methods would allow for two tests on completely different microphysical parameters, if the real mass of the star is known. The most important difference between the two methods, however, is the fact that while the maximum glitch test is independent of the region where the superfluid resides (as long as it resides at least in the whole pinning region in the crust of the star), the entrainment test is not.

3.3 Revised maximum glitch mass constraint

A different approach on how to employ the activity parameter has been proposed in Pizzochero et al. (2017), and further developed in Montoli et al. (2020c). The idea is to improve the upper bound for the mass of the glitching pulsar given by the maximum glitch amplitude (see Chapter 2) by using the extra information from the observed timing properties encoded in the activity parameter. To do that, we have to start from Equation (2.13):

$$\Delta\Omega_{\mathrm{m}}(t) = \frac{\Delta L[\Omega_{np}(t)]}{I} \,. \tag{3.33}$$

As discussed in the previous Chapter, this Equation describes an upper limit on amplitude of a hypothetical glitch that is triggered at time t, when the lag is $\Omega_{np}(t)$, given that at $t = 0$ the angular momentum reservoir is completely empty. It may be possible to produce an even larger glitch by allowing the lag Ω_{np} to become negative, or by mimicking this behaviour by allowing for meridional flows (Ekman pumping, van Eysden and Melatos, 2010). This would produce a glitch overshoot, a fast-transient phase that, according to current glitch simulations (Haskell et al., 2012; Graber et al., 2018), could occur within the first seconds after a large glitch is triggered. Recent analyses of a glitch in the Vela pulsar (Palfreyman et al., 2018) point out that an overshoot is actually present in the timing data (Ashton et al., 2019b; Pizzochero et al., 2020; Montoli et al., 2020b, see also Chapter 4). However, for most of the data we use in this analysis, this is not a problem, as the observed glitch size is likely to correspond to the jump in frequency at later times, and not to the overshoot, which occurs on very short timescales.

The basic idea for the revised constraint is that we will not employ the critical lag, but instead we will try to study how the angular momentum reservoir depends on time

and to find an "average" reservoir, instead of the maximum one. Therefore, we need a prescription to obtain $\Delta L[\Omega_{np}(t)]$. A way to proceed would be to employ a set of two-fluid hydrodynamic equations encoding macroscopic mutual friction (Andersson et al., 2006; Antonelli and Pizzochero, 2017) and the effect of pinning (Seveso et al., 2016). Such equations would depend on the observed angular velocity Ω of the pulsar under study and on the inferred value of its secular spin down rate $\dot{\Omega}$. Moreover, the dynamical equations will also depend on some unknown structural properties of the star, like the EoS and the total mass, as well as on the parameters describing entrainment and pinning. Once the theoretical curve $\Delta\Omega_{\mathrm{m}}(t)$ has been obtained, we still need to compare it with some information extracted from the observed timing behaviour of the particular pulsar under study.

For simplicity, in this Section we will reduce to the Newtonian framework.

3.3.1 Newtonian unified model

Although the general form of the hydrodynamical equations is known, modelling mutual friction introduces some degree of arbitrariness, which is unavoidable due to the still poorly-understood vortex dynamics in neutron stars. The dynamical equations are therefore always phenomenological at some level, at least for what concerns aspects related to the unpinning and repinning of many vortices (Khomenko and Haskell, 2018). For this reason, we will employ the particular toy-model presented in Pizzochero et al. (2017). This model describes the rotational dynamics of a pulsar in a simplified way, but it captures the most important feature we are interested in: pulsars are slowly driven systems whose internal clock is set by the spin-down parameter $|\dot{\Omega}|$.

Let us take the Newtonian limit of Equation (3.33) and assume that the vortex lines are straight and rigid at the macroscopic scale. As we told in Chapter 2, this is an unrealistic hypothesis, but let us employ this prescription in order to simplify the motion of a three-dimensional vortex to a one-dimensional one, by projecting it onto the equatorial plane of the star. The reservoir of angular momentum ΔL due to the presence of a rescaled lag Ω_{vp} turns out to be

$$\Delta L[\Omega_{vp}] = 2\pi \int_0^R \mathrm{d}x\, x^3\, \Omega_{vp}(x) \int_{\gamma_x} \mathrm{d}l\, \frac{\rho_n(r)}{1-\varepsilon_n(r)}\,. \tag{3.34}$$

Let us also write the Newtonian version of the critical lag profile described in Equation (2.20), for rigid vortices directed along the rotation axis:

$$\Omega_{vp}^{\mathrm{cr}}(x) = \frac{\int_{\gamma_x} \mathrm{d}l\, f_P(r)}{\kappa\, x \int_{\gamma_x} \mathrm{d}l\, \frac{\rho_n(r)}{1-\varepsilon_n(r)}}\,. \tag{3.35}$$

We could now employ the set of two-fluid hydrodynamic equations described in Antonelli and Pizzochero (2017) to describe the angular momentum reservoir dependence on time. These equations, however, should be solved for every pulsar with its distinctive values of Ω and $\dot{\Omega}$. We circumvent this complication by introducing a common

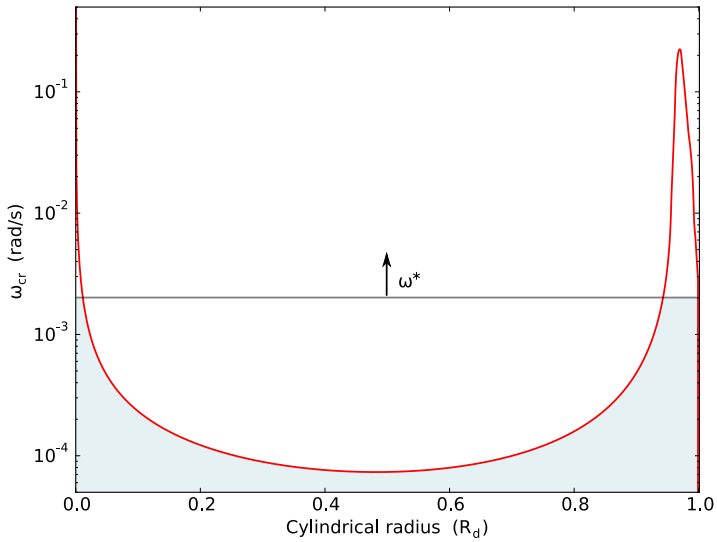

Figure 3.5: Depiction of the nominal lag evolution. Figure modified from Pizzochero et al. (2017).

unified timescale for pulsars with different spin down rates. By taking as $t = 0$ the moment in which $\Delta L = 0$, we define the nominal lag as

$$\omega^* = |\dot{\Omega}|\, t\,. \tag{3.36}$$

The nominal lag is just a rescaled measure of time that allows to treat all pulsars within a unified model, regardless of their particular rotational parameters Ω and $\dot{\Omega}$. The increasing value of ω^* determines the actual rescaled lag built between the two components since corotation,

$$\Omega_{vp}(x,\, \omega^*) = \min\left[\Omega^{\rm cr}_{vp}(x),\, \omega^*\right]. \tag{3.37}$$

The basic idea of the above Equation is described in Figure 3.5. The angular velocity lag Ω_{vp} fills up as the maximum between the nominal lag and the critical lag profile for a given cylindrical radius x.

Up to this point, we have not assumed anything about the location and extension of the region in which the neutron superfluid resides, i.e. the region in which $\rho_n > 0$. In the case of the maximum glitch amplitude, corresponding to the critical lag in Equation (3.35), we have

$$\Delta\Omega_{\rm max} = \Delta\Omega_{\rm m}(t \to \infty) = \Delta L[\Omega^{\rm cr}_{vp}(x)]\,/\,I\,. \tag{3.38}$$

It can be shown that (see Chapter 2)

$$\Delta\Omega_{\rm max} = \frac{\pi^2}{I\kappa}\int_0^{R_d} {\rm d}r\, r^3\, f_p(r)\,, \tag{3.39}$$

where R_d is the neutron-drip radius (the outer edge of the inner crust, at baryon density $n_d = 2.6 \times 10^{-4}$ fm^{-3}). Note that $\Delta\Omega_{\max}$ depends only on the extension of the pinning region. If f_P is non-zero only in the inner crust (i.e. for $R_c < r < R_d$, where R_c is the crust-core boundary), the integral in Equation (3.39) receives no contribution from the core. Therefore, $\Delta\Omega_{\max}$ does not depend on the vortex extension, provided that they extend at least in the pinning region of the crust of the star and that pinning in the core is negligible. On the contrary, the maximal glitch amplitude $\Delta\Omega_{\mathrm{m}}$ is different according to the region where we assume the presence of the superfluid, due to the explicit dependence on $\rho_n(r)$ in Equations (3.34) and (3.35): considering the superfluid limited to spherical shells ending at different depths in the core changes the value of $\Delta\Omega_{\mathrm{m}}(\omega^*)$.

The quantity $\Delta\Omega_{\mathrm{m}}(t)$ sets a theoretical limit for the glitch amplitude at time t in a pulsar that emptied its reservoir at $t = 0$. However, we do not know when a pulsar actually empties its reservoir of angular momentum (maybe never). A sequence of maximal glitches, each emptying the reservoir, would result in a strong positive correlation between the glitch amplitudes and the waiting time between them, in contrast with the idea of glitches as random events that rarely empty the reservoir significantly (Melatos et al., 2008). In such a system, the angular momentum released in each event is not expected to necessarily correlate with the angular momentum accumulated since the previous glitch: the effect of a finite-size reservoir, that can occasionally be emptied, is expected to generate only weak correlations between the glitch amplitude and the waiting time since the previous glitch. So far, these correlations induced by the finite size of the reservoir have been observed only for a few pulsars (Melatos et al., 2018).

The idea is to find a value for the typical timescale t_{act} between two events that may significantly empty the angular momentum reservoir. To do this we rely on an intrinsic property of the pulsar under study, the absolute activity $\mathcal{A}_a$, or its ratio with the spin down rate $\mathcal{G}$. As we can see form Table 3.5, there is no obvious dependence of $\mathcal{G}$ on the maximum glitch $\Delta\Omega_{\mathrm{obs}}$ observed for each object. Unlike the model described in Section 3.2, the one proposed in Pizzochero et al. (2017) and presented here allows for accounting for both these parameters. This allows for partially solving the intrinsic degeneracy present in the definition of $\mathcal{A}_a$, namely the fact that we can obtain the same activity from several small and frequent glitches or from a few big ones. From the activity and the largest observed glitch it is useful to define the characteristic time

$$t_{\mathrm{act}} = \frac{\Delta\Omega_{\mathrm{obs}}}{\mathcal{A}_a} = \frac{\Delta\Omega_{\mathrm{obs}}}{|\dot{\Omega}|\,\mathcal{G}}\,. \tag{3.40}$$

The idea behind this timescale is that of assuming that the star spins up with a (fixed) rate given by the activity parameter (which can be estimated via a long-term observation), and that the largest observed glitch depletes considerably the superfluid reservoir. t_{act} then represents the average inter-glitch time in an idealised object that has the same activity of the particular pulsar under study but displays a series of events of size $\Delta\Omega_{\mathrm{obs}}$. Starting from t_{act}, it is possible to define the related nominal

lag $\omega^*_{\rm act}$, and to build an average angular momentum reservoir ΔL. Thus, once the microphysical parameters of the star (EoS, pinning force, entrainment, and superfluid reservoir extension) are fixed, the angular momentum reservoir and, as a consequence, the maximal glitch $\Delta\Omega_m$ are function of the mass of the star and of the nominal lag only. If we employ the nominal lag $\omega^*_{\rm act}$ as a "special" value for the latter, the maximal glitch depends only on the mass of the star. An improved upper limit on the mass of the star can then be estimated, by measuring the maximum glitch amplitude of a star $\Delta\Omega_{\rm obs}$, and inverting the condition

$$\Delta\Omega_{\rm obs} \leq \Delta\Omega_m(M_{\rm act}, \omega^*_{\rm act}). \tag{3.41}$$

Since the largest observed glitch does not correspond to a complete exhaustion of the available reservoir, $M_{\rm act}$ is only an upper bound (a lighter star would still be compatible with the data). The estimate $M_{\rm act}$ provides a refinement of the (less model-dependent, as it does not depend on entrainment) absolute upper bound $M_{\rm max}$, given by emptying the fully-replenished reservoir compatible with pinning (as discussed in Pizzochero et al., 2017). Note that a comparison between these upper limits and a mass measurement in a single glitching pulsar can put constraints on the microphysics behind these models. However, it is rather difficult to obtain a mass measurement from a glitcher, as almost only isolated pulsars have been seen glitching, while mass measurements can be obtained in binary systems (see Section 3.3.4).

3.3.2 Selecting a sample of pulsars

In Montoli et al. (2020c) a sample from 166 known glitching pulsars has been selected, by retrieving glitch data from the Jodrell Bank Glitch Catalogue[2] (Espinoza et al., 2011) and angular velocities and spin down rates for each pulsar from the ATNF Pulsar Catalogue[3] (Manchester et al., 2005).

To keep the description simple, let us evaluate the activity by fitting the cumulative distribution of spin-up due to glitches (see Section 3.1). In order not to overestimate the effect of the first and last glitch in the sequence, we perform a least-squares fit of the midpoints of the frequency jumps (Wong et al., 2001). The sample should contain glitchers statistically relevant for our approach, namely pulsars whose activity can be determined and which are not too affected by observational biases, such as a short observational time T. To identify the single glitchers (pulsars which in the observational time have displayed a single large glitch and several ones orders of magnitude smaller) we employ the observational parameter $N_{\rm max}$ as defined in Equation (3.3). Single glitchers have $N_{\rm max} \approx 1$ and are not significant for the present analysis: at least two glitches of the same order of magnitude are necessary to give a rough estimate of $t_{\rm act}$. We interpret the smallness of $N_{\rm max}$ in single glitchers as an observational effect. As time goes by, these objects could eventually display another

[2] www.jb.man.ac.uk/pulsar/glitches.html, data retrieved on August 2018
[3] www.atnf.csiro.au/research/pulsar/psrcat

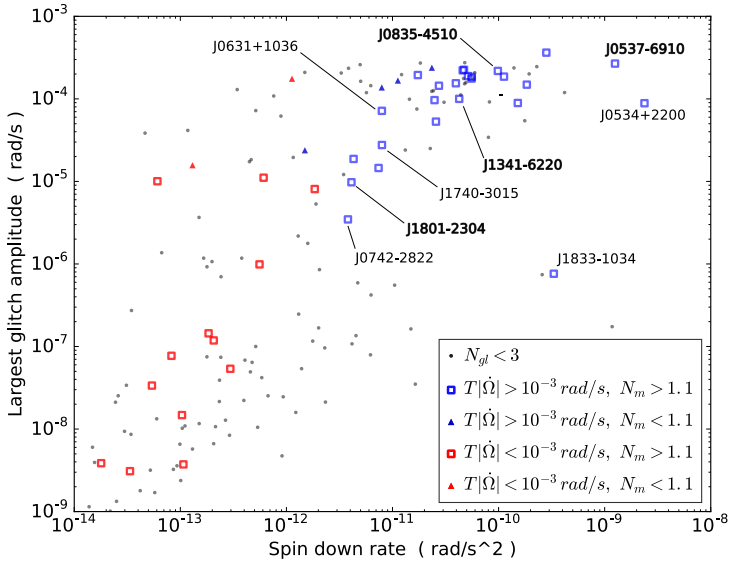

Figure 3.6: The largest glitch amplitude $\Delta\Omega_{\rm obs}$ observed in 166 glitching pulsars as a function of their spin-down rate, $|\dot{\Omega}|$. We indicate by grey points the pulsars with $N_{\rm gl} < 3$, by triangles the single glitchers with $N_{\rm max} \leq 1.1$, by squares the remaining objects with $N_{\rm gl} \geq 3$ and $N_{\rm max} > 1.1$. The four pulsars indicated with a bold name have $N_{\rm max} > 4$. The squares and triangles are displayed in red if $T|\dot{\Omega}| < 10^{-3}$ rad/s and in blue if $T|\dot{\Omega}| > 10^{-3}$ rad/s.

large glitch and an activity estimate will then be more reliable. By employing the definition of the activity, we can see that

$$N_{\rm max} \approx T \,/\, t_{\rm act}\,, \tag{3.42}$$

meaning that $N_{\rm max}$ represents the number of events that the idealised pulsar would have displayed in the observational time. A large value for $N_{\rm max}$ indicates that T has been long enough for the pulsar to potentially reach corotation several times: for this study, it is a better index of the statistical significance than $N_{\rm gl}$, the actual number of glitches detected during T.

In Figure 3.6 we display the largest observed glitch, $\Delta\Omega_{\rm obs}$, for the 166 glitchers as a function of the pulsar's spin-down rate, $|\dot{\Omega}|$. We indicate by points the objects with a number of displayed glitches $N_{\rm gl} < 3$: we are not interested in these pulsars, since at least 3 glitches are needed (but not sufficient) to try to give a rough fit of the activity of the star. Then, we indicate by triangles the single glitchers (defined by $N_{\rm max} \leq 1.1$): as discussed above, a reasonable activity cannot be determined with a single large event and thus these objects are also excluded from the sample. Finally, the remaining glitchers are indicated by squares: for these objects, an estimate of their activity can be obtained. Looking at the square symbols in Figure 3.6, it can be seen that fast evolving pulsars (i.e. with large $|\dot{\Omega}|$) exhibit large maximum events, while slowly evolving ones display only small values of $\Delta\Omega_{\rm obs}$, as already reported in previous works (McKenna and Lyne, 1990; Lyne et al., 2000; Espinoza et al., 2011;

Yu et al., 2013). Note that these tiny events, with $\Delta\Omega_{\rm obs} < 10^{-6}$ rad/s, may be due to a different glitch mechanism, not hidden by the more infrequent larger glitches (Fuentes et al., 2017; Ashton et al., 2017). This is probably an observational effect, as slowly evolving pulsars need more time to develop a lag sufficient for a large glitch, thus they need to be monitored for a longer interval T. To quantify the effect of the observational time T, we introduce the observational nominal lag $T\,|\dot{\Omega}|$. This quantity represents the maximum lag that could have been developed since the pulsar has been observed, and allows for comparison of different objects. Since the typical $\omega^*_{\rm act}$ is always larger than 10^{-3} rad/s (see Figure 3.6 and Table 3.5), it is reasonable to require that pulsars in the sample must have been observed long enough to develop at least such a lag. In the Figure, we denote by red symbols the glitchers with $T\,|\dot{\Omega}| < 10^{-3}$ rad/s, and by blue symbols those with $T\,|\dot{\Omega}| > 10^{-3}$ rad/s and use this criterion to distinguish the fast evolving pulsars from the slowly evolving ones.

Summarising, we select a sample of stars on which we will apply the model by requiring three specific conditions:

- $N_{\rm gl} \geq 3$ - This is required to fit the activity.
- $N_{\rm max} > 1.1$ - To eliminate the single glitchers from the sample. The low threshold 1.1 has been chosen to select, as a first tentative step, a large number of potentially interesting objects with diverse rotational parameters and glitch amplitudes. Changing the threshold to $N_{\rm max} > 1.5$, however, would only remove two objects from the sample.
- $T\,|\dot{\Omega}| > 10^{-3}$ rad/s - To eliminate the pulsars that evolve slowly (and so require a lot of time to replenish the reservoir) or that have not been observed for a sufficiently long period T.

In this way, we obtain the sample of 25 stars in Table 3.5.

3.3.3 Parameter study on the improved mass upper limit

We now study the dependence of the improved upper limit on the mass $M_{\rm act}$ on the extension of the superfluid reservoir. To do so, we perform different spherical cutoffs in the extension of the superfluid region involved in the glitch, by imposing that the reservoir extends from neutron drip density to $1\,n_0$, $0.75\,n_0$, $0.68\,n_0$ and $0.6\,n_0$, where $n_0 = 0.168\,{\rm fm}^{-3}$ is the nuclear saturation density (Chamel and Haensel, 2008). Finally, we consider a superfluid reservoir limited to the crust (where the crust-core boundary, n_c, is given by the specific EoS implemented). The choice of these cutoffs is justified by physical motivations: the region between the crust-core interface and $1\,n_0$ is the region where most of the theoretical superfluid gaps of singlet state $^1S_0$ go to zero. In particular, $0.68\,n_0$ corresponds to the value where the superfluid region ends in a neutron star with temperature $T \approx 10^8 K$, considering a SFB superfluid gap (Schwenk et al., 2003; Ho et al., 2015).

J-name	Ω [rad/s]	$\lvert\dot{\Omega}\rvert$ [10^{-11} rad/s^2]	$\mathcal{G}$ [%]	$N_{\rm gl}$	$N_{\rm max}$	$\Delta\Omega_{\rm obs}$ [10^{-4} rad/s]	$T\lvert\dot{\Omega}\rvert$ [10^{-3} rad/s]	$\omega^*_{\rm act}$ [10^{-3} rad/s]
J0205+6449	95.61	28.19	0.743 ± 0.073	6	2.39	3.633 ± 0.382	104.2	48.90 ± 7.05
J0534+2200	188.2	237.2	$(4.0 \pm 0.5) \times 10^{-3}$	27	2.19	0.886 ± 0.006	3636	2232 ± 292
J0537-6910	389.7	125.2	0.874 ± 0.003	45	16.66	2.677 ± 0.012	491.1	30.62 ± 0.17
J0631+1036	21.83	0.79	1.333 ± 0.213	15	1.55	0.716	3.79	5.37 ± 0.86
J0742-2822	37.68	0.38	0.107 ± 0.036	8	1.14	0.035 ± 0.001	2.99	3.23 ± 1.07
J0835-4510	70.34	9.84	1.616 ± 0.016	20	11.67	2.180 ± 0.008	148.4	13.49 ± 0.14
J1048-5832	50.81	3.96	1.623 ± 0.177	6	2.86	1.546	18.98	9.53 ± 1.04
J1105-6107	99.43	2.49	1.311 ± 0.184	5	2.30	0.966	10.48	7.37 ± 1.04
J1119-6127	15.40	15.18	0.175 ± 0.036	4	1.99	0.892 ± 0.031	81.29	50.9 ± 10.7
J1341-6220	32.50	4.25	1.524 ± 0.098	23	5.46	1.000	26.09	6.56 ± 0.42
J1413-6141	22.00	2.57	1.375 ± 0.107	7	2.38	0.530	6.65	3.86 ± 0.30
J1420-6048	92.16	11.24	1.366 ± 0.036	5	3.33	1.861 ± 0.012	37.00	13.62 ± 0.37
J1709-4429	61.32	5.57	1.389 ± 0.231	4	3.08	1.761 ± 0.016	28.54	12.68 ± 2.11
J1730-3350	45.05	2.74	1.403 ± 0.025	3	2.65	1.443	18.78	10.28 ± 0.19
J1737-3137	13.95	0.43	1.144 ± 0.194	4	1.18	0.187	2.06	1.64 ± 0.28
J1740-3015	10.35	0.80	1.216 ± 0.038	36	3.67	0.276	7.73	2.27 ± 0.07
J1801-2304	15.11	0.41	1.009 ± 0.035	13	4.22	0.098	3.77	0.97 ± 0.03
J1801-2451	50.30	5.15	1.720 ± 0.115	5	2.69	1.889	23.07	10.98 ± 0.73
J1803-2137	47.01	4.72	1.781 ± 0.107	5	3.34	2.253 ± 0.001	30.74	12.65 ± 0.76
J1826-1334	61.91	4.59	1.281 ± 0.199	6	3.33	2.217 ± 0.001	39.86	17.31 ± 2.68
J1833-1034	101.5	33.14	$(3.6 \pm 0.4) \times 10^{-3}$	4	2.04	0.008	27.86	21.27 ± 2.54
J1841-0524	14.10	0.74	1.532 ± 0.166	5	1.85	0.145	1.92	0.95 ± 0.10
J1932+2220	43.49	1.73	4.513 ± 0.729	3	2.13	1.945	6.39	4.31 ± 0.70
J2021+3651	60.57	5.59	1.609 ± 0.067	4	2.82	1.846 ± 0.001	22.09	11.47 ± 0.48
J2229+6114	121.7	18.45	0.522 ± 0.066	6	2.42	1.487 ± 0.005	52.66	28.48 ± 3.58

Table 3.5: The sample of pulsars used in this Section. No errors are reported when they are smaller than the symbols used in figures. The timing data and their observational uncertainties have been obtained by retrieving angular velocities and spin down rates from the ATNF Pulsar Catalogue (`www.atnf.csiro.au/research/pulsar/psrcat`, see also Manchester et al. 2005) and glitch data from the Jodrell Bank Glitch Catalogue (`www.jb.man.ac.uk/pulsar/glitches.html`, see also Espinoza et al. 2011).

We consider two unified EoSs, SLy4 (Douchin and Haensel, 2001), BSk20 (Goriely et al., 2010), and a stiffer relativistic mean field model, DDME2 (Lalazissis et al., 2005), see Table 3.6. The DDME2 EoS does not have any consistently calculated superfluid neutron fraction y_n in the crust, so that we glued it with the crust from the SLy4 EoS, keeping the crust-core transition density to be the one of SLy4. This operation has been carried out by ensuring the continuity of the chemical potential, as discussed by Fortin et al. (2016). This, while ensuring thermodynamic consistency, also produces a strong first-order phase transition at the crust-core interface: the $P(n_b)$ profile of the DDME2+SLy4 EoS turns out to be flat for n_b between $0.076\,\mathrm{fm}^{-3}$ and $0.084\,\mathrm{fm}^{-3}$ (namely, $0.45\,n_0$ and $0.5\,n_0$), and a corresponding density jump appears at the crust-core interface.

In Figure 3.7 we show the critical lag for straight vortex lines, given by Equation (3.35), for the different cutoffs considered here. The calculation was done with the BSk20 EoS, by employing the pinning force of Seveso et al. (2016) and the entrainment parameters obtained in Chamel and Haensel (2006) for the core and Chamel

EoS	$M_{\rm eos}\,[M_\odot]$	$n_c\,[n_0]$
SLy4	2.05	0.452
BSk20	2.16	0.508
DDME2 + SLy4	2.48	0.452

Table 3.6: The maximum neutron star mass and the baryon density corresponding to the crust-core transition for the EoSs used in this Section.

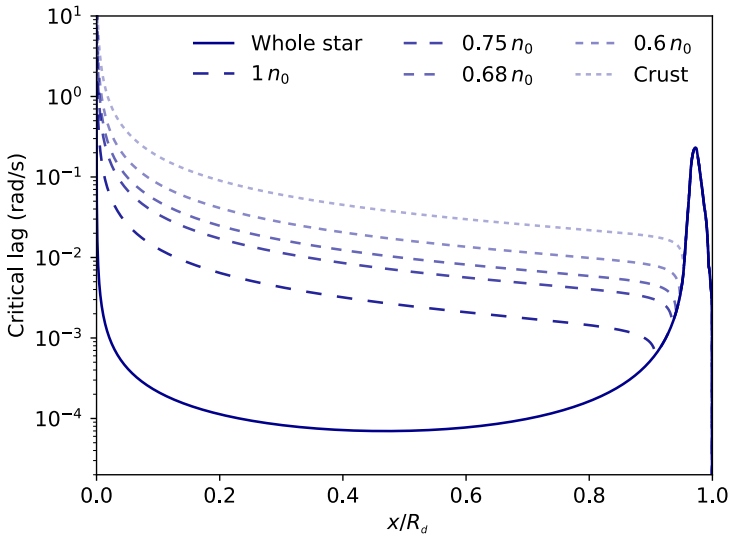

Figure 3.7: Example of critical lag $\Omega^{\rm cr}_{vp}$, as a function of the radius x/R_d and for the different cutoff densities $n_{\rm cut}$. The calculation refers to a $1.4\,M_\odot$ star, described by the BSk20 EoS.

(2012) for the crust. As expected, $\Omega^{\rm cr}_{vp}$ has higher values in the central region of the star for smaller superfluid reservoirs: since the superfluid extends in a smaller spherical layer, the superfluid vortices are less subject to the Magnus force. And because the critical lag is cutoff dependent, the lag Ω_{vp} (and hence $\Delta\Omega_{\rm m}$, via Equation (3.33)) evolves differently. However, $\Delta\Omega_{\rm max}$ does not depend on the cutoff we are considering, as the different form of the critical lag is compensated by the second integral over γ_x in Equation (3.34).

We now study the evolution of the maximal glitch, $\Delta\Omega_{\rm m}(\omega^*)$, as a function of the nominal lag. The results are shown in Figure 3.8, where it can be seen that the maximal glitch raises faster as a function of ω^* for more extended reservoirs, in particular for lower masses. On the other hand, for large values of ω^* the maximal glitch tends to $\Delta\Omega_{\rm max}$, which in the present scenario of crustal pinning does not depend on the superfluid cut. The stars of the sample seem to follow the form of the curves for the masses, especially in the case of a reservoir limited to the crust; this may be just a coincidence related to the fact that most pulsars of our sample are aligned along $\mathcal{G} \sim 1\%$, as also pointed out by Fuentes et al. 2017. As a consequence of this fact, the

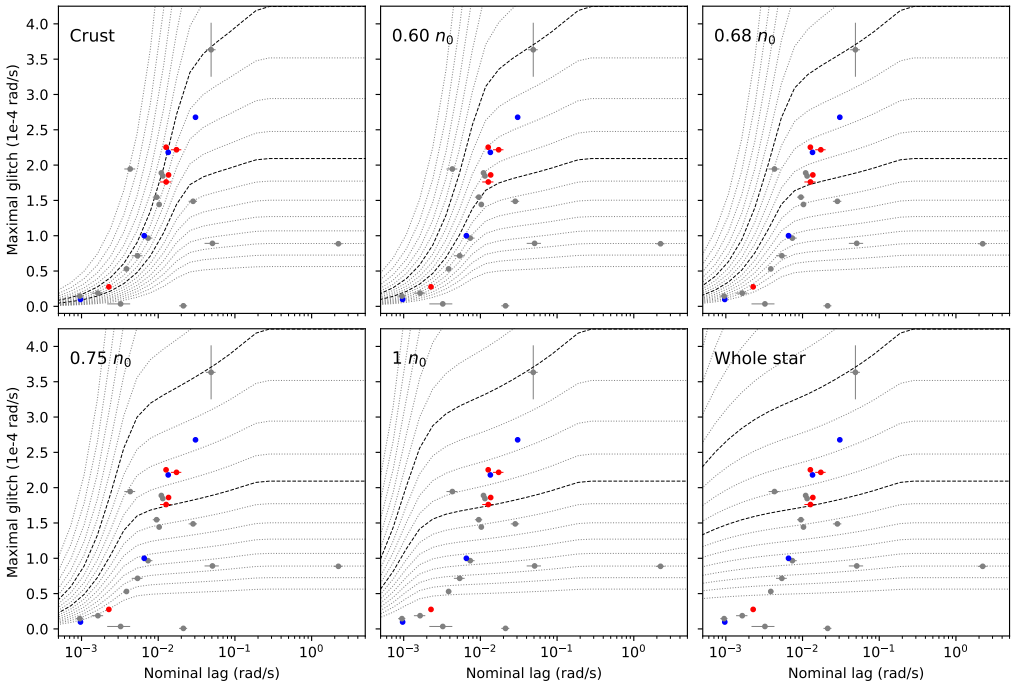

Figure 3.8: The maximal glitch $\Delta\Omega_{\rm m}(\omega^*, M, n_{\rm cut})$, as a function of the nominal lag ω^*, for different pulsar masses M and reservoir cutoffs $n_{\rm cut}$, in the case of the BSk20 EoS. The curves in each panel correspond to different masses, starting from $0.5M_\odot$ (the highest curve) up to $2.1M_\odot$ (the lowest one); the $1.0M_\odot$ and the $1.4M_\odot$ curves are highlighted (black dashed lines). We also display the values of the largest observed glitch $\Delta\Omega_{\rm obs}$ and the nominal lag $\omega^*_{\rm act}$ for the 25 pulsars in Table 3.5. Pulsars with $N_{\rm max} < 3$ are shown in grey, the ones with $3 < N_{\rm max} < 4$ in red, and the remaining ones with $N_{\rm max} > 4$ in blue.

mass estimates for the crust-limited reservoir will fall in a narrow range of values.

We notice that two objects (J0742-2822 and J1833-1034) are below the lowest curve, corresponding to the highest mass achievable from BSk20: they are not constrained by the reservoir, in the sense that any mass compatible with the EoS could yield such small glitches (with $\Delta\Omega_{\rm obs} < 5 \times 10^{-6}$ rad/s). Interestingly, this value is just below the dividing line $\Delta\Omega/2\pi \approx 10\,\mu$Hz found by Espinoza et al. (2011) by analysing the bimodal distribution of all measured glitch sizes. Hence, these unconstrained objects may belong to a subpopulation which is unable to release a sufficient amount of angular momentum to produce large glitches (see also the more recent analysis of Ashton et al. 2017 and Fuentes et al. 2017). Another viable hypothesis is that J0742-2822 and J1833-1034 have not displayed yet a glitch large enough. In fact, these pulsars still have small values of $N_{\rm max} \lesssim 2$, a case that resembles the Crab (J0534+2200, $N_{\rm max} = 2.2$), which only after 50 years of observations has displayed a glitch big enough to be relevant for the present analysis (Shaw et al., 2018). The very large value of $\omega^*_{\rm act}$ associated to the Crab may be due to its young age and possible

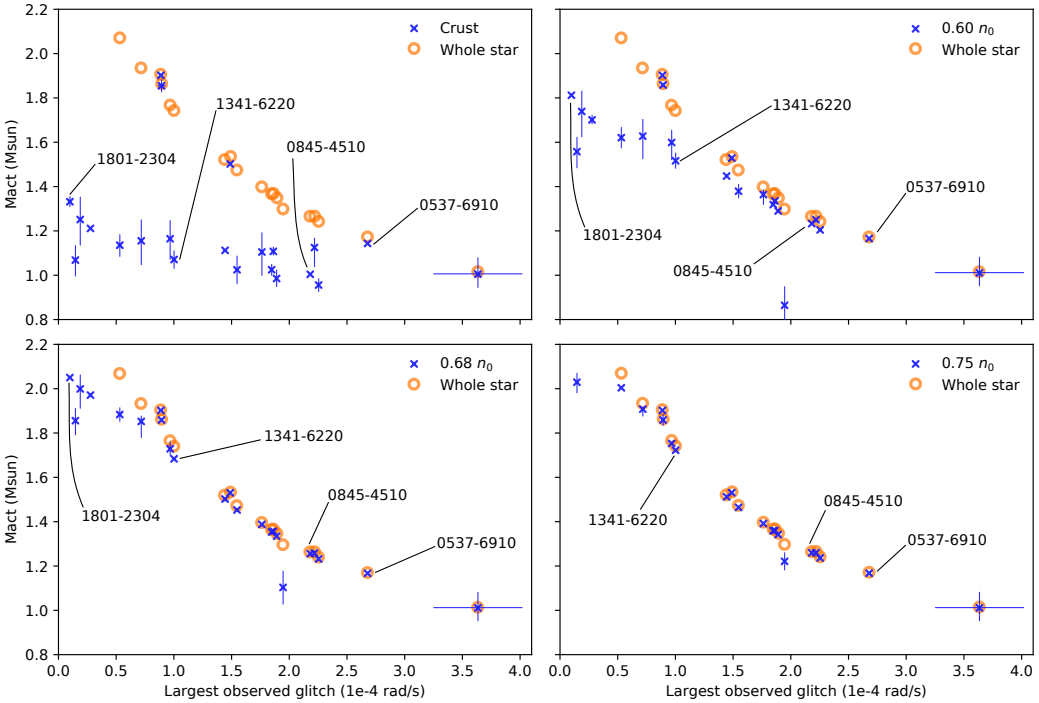

Figure 3.9: The 25 fitted values $M_{\rm act}$ as a function of $\Delta\Omega_{\rm obs}$ in the case of the BSk20 equation of state. Each panel refers to a different cutoff $n_{\rm cut}$ (blue crosses). Error bars are absent when smaller than the symbols used. For comparison, in every panel we also show the case of the reservoir extending to the whole star (orange circles, error bars not displayed). The $n_{\rm cut} = 1\,n_0$ cutoff is omitted, as it is almost identical to the whole star case. The four pulsars with $N_{\rm max} > 4$ are also indicated.

thermal effects favoured by high temperatures (e.g. enhanced vortex creep, implying longer times to build up the excess of angular momentum). Another peculiar object is PSR J1932+2220, with its low value of $\omega^*_{\rm act}$. In the crust-limited reservoir case, it is marginally fitted by the low $0.5\,M_\odot$ curve. However, we also notice that in the $0.68\,n_0$ case the star is well within the 1-1.4 $M_\odot$ region. Thus, for this star the superfluid reservoir should be extended to a small region in the outer core to obtain reasonable masses; future observations and improved statistics may change the situation (this pulsar has low values of both $N_{\rm max} = 2.1$ and $N_{\rm gl} = 3$).

For a given cutoff $n_{\rm cut}$, we invert the equation $\Delta\Omega_{\rm m}(\omega^*_{\rm act}, M_{\rm act}) = \Delta\Omega_{\rm obs}$ for each pulsar and find the value of $M_{\rm act}$. Figure 3.8 provides a graphical representation of this procedure. The results for the BSk20 EoS are shown in Figure 3.9, where we plot the mass estimate $M_{\rm act}$ as a function of the largest observed glitch $\Delta\Omega_{\rm obs}$. In each panel, we show the masses corresponding to a particular cutoff, and give as a reference the case of no-cutoff (reservoir extended to the entire star, the case previously considered in Pizzochero et al. 2017). The cutoff at $1\,n_0$ has been omitted, since the corresponding mass estimates are identical to the case of the whole star. Thus, with this model there is

no particular need to invoke inner parts of the core (where $n_b \gtrsim n_0$) to explain current glitch data. This is good news, considering the present uncertainty of theoretical calculations on the properties P-wave pairing gap in the core and the presence of a layer of normal matter between the triplet and singlet neutron superfluids.

It is possible to notice some general trends in our results. First, in Figure 3.9 we see an inverse correlation between amplitude of the largest glitch and estimated mass. Clearly, the inverse relation between the maximum theoretical glitch amplitude $\Delta\Omega_{\rm max}$ in (3.38) and the mass is obvious and expected, as lighter stars have thicker crusts. However, this inverse relation persists also when we use the maximal amplitude $\Delta\Omega_{\rm m}$ defined in (3.33): in this case the anti-correlation between the estimated mass and the largest glitch amplitude observed is less obvious because the parameter t in (3.33), which we estimated from the observed glitch activity via $t \approx \omega^*_{\rm act}/|\dot{\Omega}|$, is different for every pulsar. The slope of the curves in Figure 3.9 increases with increasing extension of the reservoir, being almost flat for the crust-only case and tending to the whole-star case already for $n_{\rm cut} \gtrsim 1\, n_0$. Also, if we extend the superfluid reservoir to deeper regions of the star we can fit fewer masses than in the case of a smaller reservoir: in Figure 3.8 some pulsars with small largest glitch and small nominal lag can only be constrained in the cases of shallower cutoffs.

Secondly, objects with a small nominal lag ($\omega^*_{\rm act} \lesssim 2\times10^{-2}$ rad/s) are more sensitive to changes of the cutoff than those with a large one. In fact, pulsars with small nominal lag show masses around $1.0-1.4\,M_\odot$ in the case of reservoir limited to the crust, while they show much larger masses (or they do not even get constrained) for more extended cutoffs. On the other hand, the five pulsars with the largest nominal lag ($\omega^*_{\rm act} \gtrsim 2.5\times10^{-2}$ rad/s) have their masses almost unaltered between the different cutoffs, as can be noticed in Figure 3.9. The reason for this is easy to understand in the case of the Crab, with its extreme value of the nominal lag: when ω^* is large enough, the lag as a function of time (3.37) has reached the critical value (3.35). As a consequence, the maximal glitch reaches a plateau, given by the maximum glitch amplitude (3.39). In fact, for pulsars with large $\omega^*_{\rm act}$, the maximal glitch corresponds to the maximum glitch: their mass estimates are independent on the superfluid reservoir extension or entrainment parameters, but strongly dependent on the pinning force considered. Although the four remaining pulsars with large nominal lag have not reached the plateau yet, they still lie in a region of the $(\omega^*, \Delta\Omega_{\rm obs})$ plane where the curves $\Delta\Omega_{\rm m}(\omega^*)$ are almost insensitive to the choice of the cutoff.

It is interesting to notice how, for the crust-limited reservoir, the masses of the pulsar are – except for the three pulsars with the largest $\omega^*_{\rm act}$ (Crab, J1119-6127 and J2229+6114) – all quite low, peaked around $\approx 1.1\,M_\odot$ and even less than $\approx 1\,M_\odot$ in some cases. This fact indicates that the crustal reservoir alone is not enough to describe pulsar glitches, as already noticed by Andersson et al. (2012) and Chamel (2013).

To better follow the dependence of the mass estimates on the cutoff, in Figure 3.10 we consider the four benchmark pulsars with $N_{\rm max} > 4$. For each of these objects, we plot $M_{\rm act}$ as a function of the superfluid region cutoff $n_{\rm cut}$ for the three different EoSs

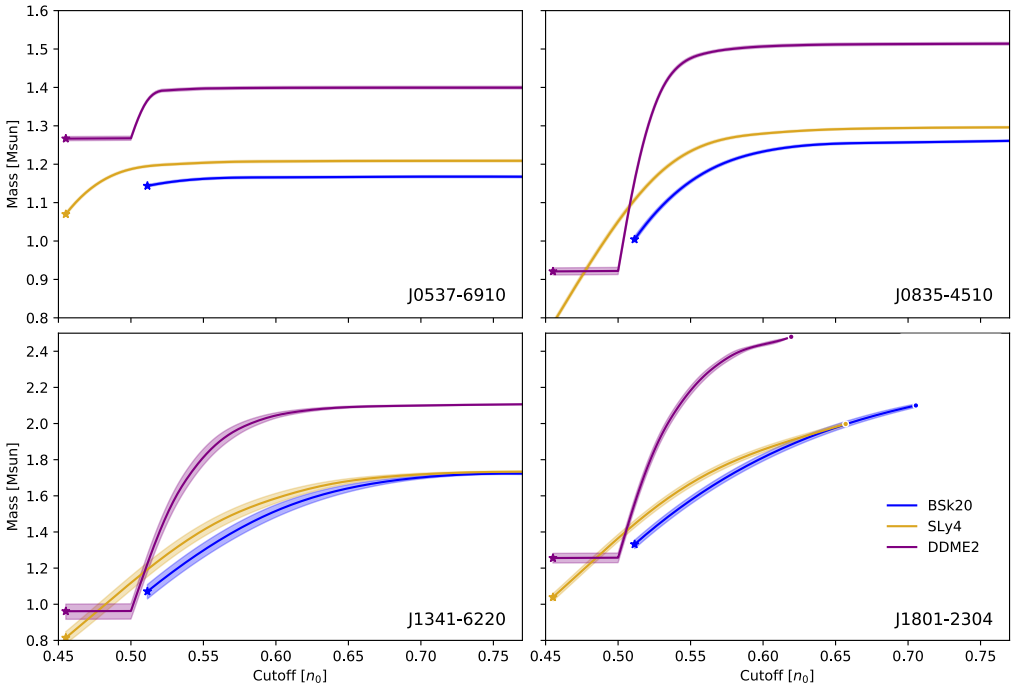

Figure 3.10: The mass $M_{\rm act}$ as a function of the cutoff baryon density for the superfluid reservoir, $n_{\rm cut}$, for the four pulsars in the sample which have $N_{\rm max} > 4$ and for the three EoSs considered: SLy4 (yellow), BSk20 (blue) and DDME2 (purple). All lines start with a star, which indicates the cutoff $n_{\rm cut} = n_c$ at the crust-core interface (crust-only case). In the case of J1801-2304, the lines end with a dot at $M_{\rm eos}$, the maximum mass allowed by each EoS. The shaded regions indicate the uncertainty on the mass estimate. The plateau in the DDME2 curves is a by-product of the presence of a strong first-order phase transition at the core-crust interface.

considered. The region of constant mass for DDME2 corresponds to the first-order phase transition mentioned before. The general trend of lower masses for smaller superfluid reservoir is preserved and, as expected, a stiffer EoS like DDME2 predicts larger masses than the two softer EoSs. Moreover, the star with the largest $\omega^*_{\rm act}$ in this figure, J0537-6910, shows small variability in mass between the cutoffs, reaching its plateau very soon (for $n_{\rm cut} > 0.55 n_0$), as opposed to the star with the smallest nominal lag, J1801-2304, which reaches the maximum mass allowed by each EoS well before $0.75\,n_0$ and shows no plateau. In these cases larger cutoffs just yield too much available reservoir of angular momentum, so that the pulsar is not constrained anymore: any mass $M_{\rm act}$ compatible with the EoS can produce its small observed glitches.

3.3.4 Comparison with measured masses

The aim of this Section is that of trying to understand to what extent the upper limits described in the previous Section are plausible, by comparing them with the neutron star masses measured in binary systems (Özel and Freire, 2016). Of course, none of the pulsars in the sample in Table 3.5 are in binary systems and have a measured mass: we are asking ourselves if the distribution of measured masses in binary systems are compatible with the constraints given in the previous Section. This causes two problems: first of all, it is not true that the stars in the sample described in Section 3.3.2 have the same characteristics of those in the sample of Özel and Freire (2016). In fact, while the stars in Özel and Freire (2016) are all in binary systems, all the pulsars in the sample of Section 3.3.2 are isolated stars. Their evolution is thus different, which means that the underlying mass distribution of the two samples can be intrinsically different. Secondly, it is not easy to statistically compare mass measurements with upper limits. To solve this problem let us assume in this Section $M_{\rm act}$ to be a mass estimate for a particular pulsar. In general, this is not true for any of the pulsars we have studied in the previous Section: it may be more true for some pulsars, whose largest glitches are approximately the theoretically largest those stars can achieve, and less for others.

From a statistical point of view, this problem is a two-sample problem. We have two different samples, each with its underlying probability distribution, and we would like to know whether these two distributions are the same. From a Bayesian point of view, this can be solved by studying the Bayes factor of two models: one which assumes that the two samples come from the same underlying distribution and one which assumes they do not. The Bayes factor can be calculated as (Borgwardt and Ghahramani, 2009)

$$K = \frac{P(\mathcal{D}_1, \mathcal{D}_2 | \mathcal{H}_1)}{P(\mathcal{D}_1, \mathcal{D}_2 | \mathcal{H}_2)} = \frac{P(\mathcal{D}_1, \mathcal{D}_2 | \mathcal{H}_1)}{P(\mathcal{D}_1 | \mathcal{H}_2) P(\mathcal{D}_2 | \mathcal{H}_2)}, \tag{3.43}$$

where $\mathcal{H}_1$ and $\mathcal{H}_2$ are the hypotheses that the two datasets $\mathcal{D}_1$ and $\mathcal{D}_2$ come from the same distribution or not, respectively. The last equality is justified by the fact that if the two datasets come from different distributions, then they are independent of each other, and the evidence can be split in that way.

The two datasets are the Özel and Freire (2016) dataset of masses of neutron stars measured in binary systems, and the dataset of $M_{\rm act}$ calculated with the procedure described in the previous Section on the pulsar sample defined in Table 3.5 (Montoli et al., 2020c). We show the dataset of Özel and Freire (2016) in Figure 3.11[4]. In their paper, the authors distinguish between four different classes of stars (see also Özel et al., 2012):

1. The double neutron stars, which are all those neutron stars which are in a double system with another neutron star.

[4]Data has been retrieved from http://xtreme.as.arizona.edu/NeutronStars/data/pulsar_masses.dat

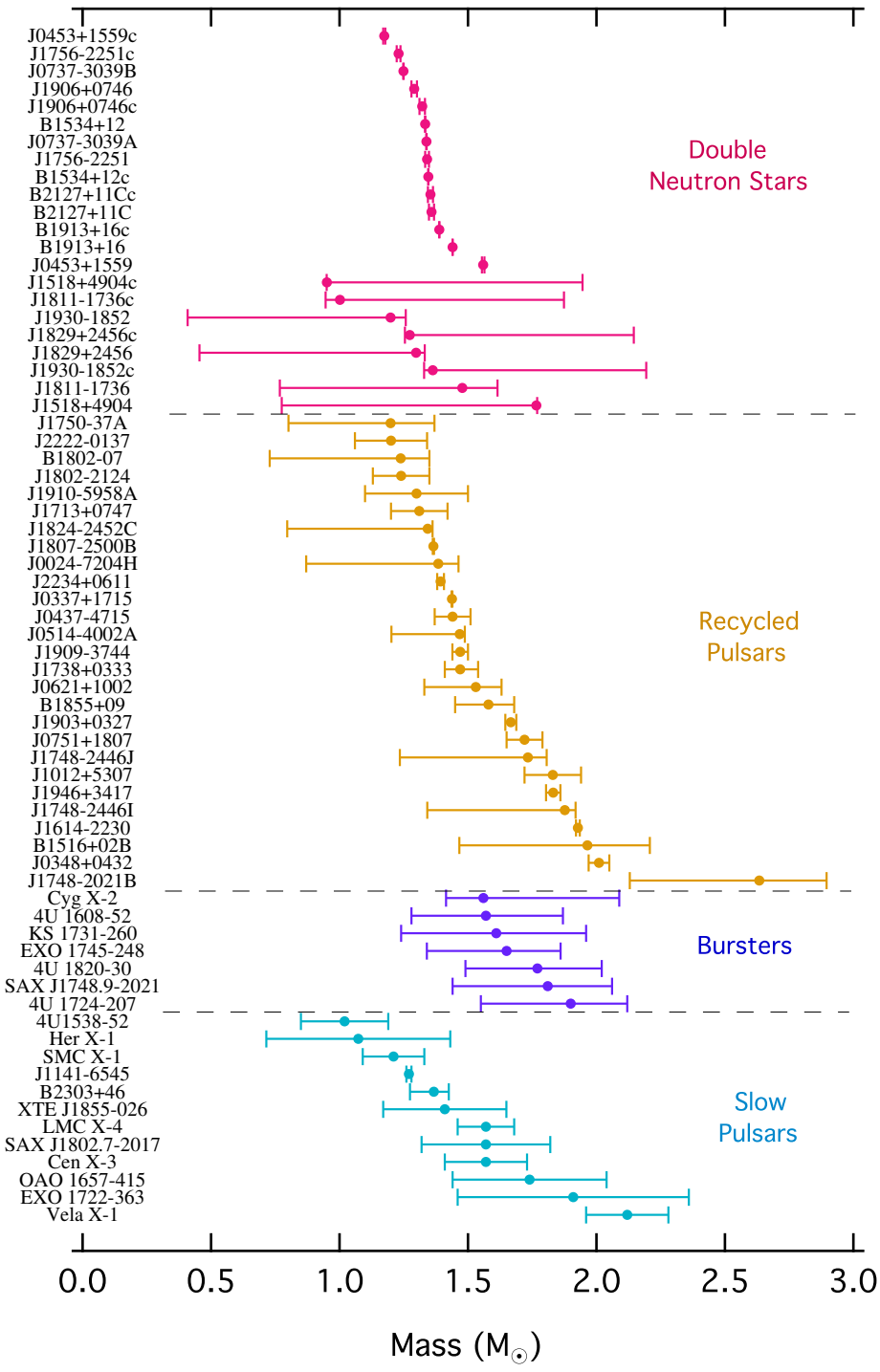

Figure 3.11: Measured mass of neutron stars in binary systems. Figure taken from Özel and Freire (2016).

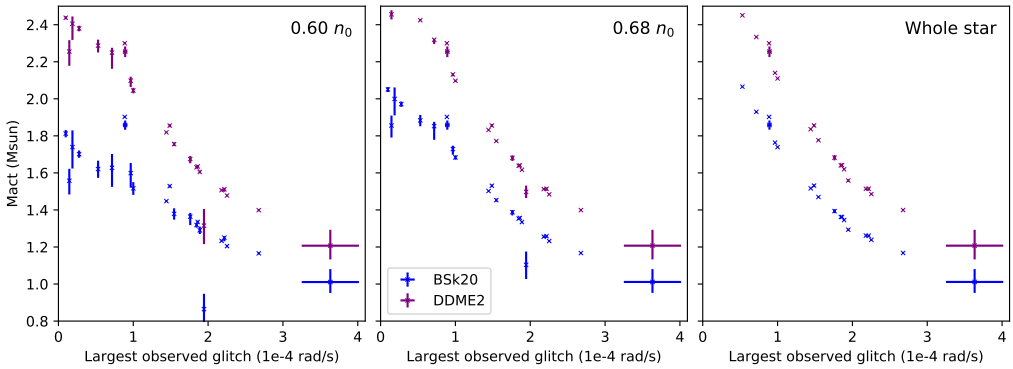

Figure 3.12: The six $M_{\rm act}$ samples employed, calculated with two different EoSs – BSk20 (blue) and DDME2+SLy4 (purple) – and three different superfluid cutoffs ($0.60n_0$, $0.68n_0$ and superfluid extended to the whole star). The error bar is not displayed if smaller than the symbols.

2. The recycled pulsars, i.e. all the stars which have undergone accretion.

3. The accreting X-ray bursters, whose masses have been measured through X-ray spectroscopy.

4. The slow pulsars, i.e. all those stars in binary systems which are slowly rotating, thus assuming that only little accretion has occurred on them.

As discussed in Özel et al. (2012), where the authors' aim was that of studying the neutron star birth mass distribution, these four categories can be grouped in two main families: those stars which have undergone accretion, and those which have not. All the double neutron stars and the slow pulsars belong to the first category, as we expect them to belong or to have belonged to a HMXB, so not having undergone much accretion. We are thus expecting these stars' masses to be near-birth. On the other hand, we expect the bursters and the recycled pulsars to be undergoing or to have undergone accretion, thus their mass is substantially different to that they had just after the supernova. In fact, in these categories belong all the stars in a binary system with a low-mass main-sequence star or with a white dwarf, hinting at a LMXB. The distinction between near-birth-mass stars and accreted stars is important: we do not expect isolated pulsars – like those in the sample in Table 3.5 – to have undergone much accretion during their lifetime. Nevertheless, we will compare the masses inferred in Section 3.3 with both the near-birth-mass sample (34 stars) and the full sample (68 stars) of Özel and Freire (2016).

As for the $M_{\rm act}$ sample, while we keep entrainment (Chamel and Haensel, 2006; Chamel, 2012) and pinning force (Seveso et al., 2016) fixed, we study two different equations of state, one soft (BSk20) and one stiff (DDME2, with a SLy4 crust), and three different superfluid cutoffs ($0.60n_0$, $0.68n_0$ and superfluid extended to the whole star). We do not consider the superfluid limited to the crust of the star, as it can be

seen by eye that the inferred mass distribution is quite unrealistic (Figure 3.9). We therefore have six different $M_{\rm act}$ samples, by varying the microphysical parameters (see Figure 3.12).

To calculate the evidences in Equation (3.43), we need to hypothesise a likelihood and a prior of a Bayesian inference. In this case, the objective of the inference are the parameters of the mass distribution. Let us assume we have measured a set of masses $\hat{m}_i$ with their associated errors $\hat{\sigma}_i$. If we assume these errors to be symmetric with respect to the measured value $\hat{m}_i$, we can use a Gaussian distribution to estimate the probability for the single measure $P(\hat{m}_i \,|\, m_i, \hat{\sigma}_i)$:

$$P(\hat{m}_i \,|\, m_i, \hat{\sigma}_i) = \frac{1}{\sqrt{2\pi\hat{\sigma}_i^2}} \exp\left(-\frac{(m_i - \hat{m}_i)^2}{2\hat{\sigma}_i^2}\right). \tag{3.44}$$

In other words, this is the probability of obtaining a particular measure $\hat{m}_i$ with associated error $\hat{\sigma}_i$ if the true value of the mass of the neutron star is m_i. As many of the measured masses in Özel and Freire (2016) have skewed errors (see Figure 3.11), however, it is important to employ a different type of distribution, in order to take into account asymmetric error bars. In Kiziltan et al. (2013), the authors use an asymmetric normal distribution for the errors (see also Fernandez and Steel, 1998):

$$\begin{aligned} AN(\hat{m}_i \,|\, m_i, c_i, d_i) = {} & \frac{2}{d_i\left(c_i + \frac{1}{c_i}\right)} \cdot \\ & \cdot \left[\varphi\left(\frac{c_i(m_i - \hat{m}_i)}{d_i}\right)\vartheta(m_i - \hat{m}_i) + \varphi\left(\frac{m_i - \hat{m}_i}{c_i d_i}\right)\vartheta(\hat{m}_i - m_i)\right], \end{aligned} \tag{3.45}$$

where ϑ is the usual Heaviside step function and φ is the standard normal distribution defined as:

$$\varphi(x) = \frac{1}{\sqrt{2\pi}} e^{-\frac{x^2}{2}}.$$

The relation between the two parameters c_i and d_i of the distribution and the left (l_i) and right (r_i) uncertainties on the measures can be obtained by imposing

$$AN(\hat{m}_i \,|\, m_i - l_i, c_i, d_i) = AN(\hat{m}_i \,|\, m_i + r_i, c_i, d_i),$$

which will give us $c_i = \sqrt{r_i/l_i}$ and the condition

$$\int_{-l_i}^{r_i} AN(\hat{m}_i \,|\, m_i, c_i, d_i)\, \mathrm{d}m_i = 0.6827,$$

that, solved numerically, will give us the value of d_i. Please note that the above condition can be easily written in a more compact (and easier to be implemented) way by making use of the error function. *A priori*, however, any skewed probability distribution is acceptable. In particular, since we are talking about masses, it may be interesting to consider an asymmetrical distribution with support on the positive

real numbers (like the gamma distribution): the relation between the errors and the parameters of the distribution could be obtained in the same way of the asymmetric normal in Kiziltan et al. (2013). It is even possible to obtain the probability distribution for the mass of a star for which only the mass ratio or the total mass of the binary system has been measured (see, for example, Özel et al. 2012 or Antoniadis et al. 2016). However, to keep things simple, we will neglect this possibility, and we will stick to the asymmetric normal distribution described above for all the stars for which a mass measurement has been performed.

After having modelled the probability distribution for the mass of a single neutron star, we need to choose a distribution for all the masses in the samples. Let us assume a generic distribution for the masses $P(m_i \,|\, \mathcal{P})$, where $\mathcal{P}$ indicates the vector of parameters of the distribution (for example, in the case of a Gaussian, these are the mean and the variance). In this way, we can obtain the probability of obtaining a particular measure $(\hat{m}_i, \hat{\sigma}_i)$, given the parameters of the distribution, by marginalising over the true mass of the neutron star:

$$P(\hat{m}_i \,|\hat{\sigma}_i, \mathcal{P}) = \int P(\hat{m}_i \,|\, \hat{\sigma}_i, m_i)\, P(m_i|\, \mathcal{P})\, \mathrm{d}m_i. \tag{3.46}$$

Since the masses are measured independently from each other (i.e. they are independent variables), we can write the likelihood of the distribution parameters for the whole set of data by simply multiplying the probability of obtaining a single datum:

$$P(\mathcal{D}|\, \mathcal{P}) = \prod_i P\,(\hat{m}_i|\, \mathcal{P}), \tag{3.47}$$

where we have dropped $\hat{\sigma}_i$ for simplicity and $\mathcal{D}$ indicates the set of measured masses $\hat{m}_i$. As we are not interested in the exact shape of the mass distribution, we will assume, for simplicity, as distributions a unimodal and a bimodal normal distribution. While the unimodal normal distribution is formally the same of Equation (3.44), the bimodal one needs an extra parameter r for mixing the two normal distributions:

$$P\,(m\,|\,\mu_1, \sigma_1, \mu_2, \sigma_2, r) = \frac{r}{\sqrt{2\pi\sigma_1^2}} \exp\left(-\frac{(m-\mu_1)^2}{2\sigma_1^2}\right) + \\ + \frac{1-r}{\sqrt{2\pi\sigma_2^2}} \exp\left(-\frac{(m-\mu_2)^2}{2\sigma_2^2}\right). \tag{3.48}$$

The prior distribution for the parameters of these distributions are chosen to be:

$$\begin{aligned} P(\mu_j) &= \mathrm{Unif}(0.5M_\odot, 2.5M_\odot) \\ P(\sigma_j) &= \mathrm{Unif}(0.01M_\odot, 1M_\odot) \\ P(r) &= \mathrm{Unif}(0, 1) \end{aligned}$$

Özel and Freire sample	$M_{\rm act}$ sample EoS	Cutoff	$\ln K$
Full	BSk20	whole	4.96
		0.68	3.86
		0.60	2.54
	DDME2	whole	-3.34
		0.68	-4.08
		0.60	-6.26
Birth	BSk20	whole	1.93
		0.68	-0.53
		0.60	0.21
	DDME2	whole	-8.86
		0.68	-9.40
		0.60	-10.86

Table 3.7: Bayes factor of the Bayesian two-sample test. The first column indicates which Özel and Freire (2016) sample have been used for the comparison, while the second two columns are the EoS and the cutoff of the $M_{\rm act}$ sample used. In the last column we report the natural logarithm of the Bayes factor (Equation (3.43)).

where $j = 1, 2$ for the bimodal distribution, and $j = 1$ for the unimodal. Finally, the evidence for this inference can be calculated as:

$$P(\mathcal{D}) = \int \mathrm{d}\mathcal{P}\, P(\mathcal{D}\,|\,\mathcal{P})\, P(\mathcal{P})\,. \tag{3.49}$$

This calculation cannot be performed analytically, so to obtain the numerical value of the evidence the nested sampler MULTINEST have been employed (Feroz et al., 2009), as implemented in the `pymultinest` Python module (Buchner et al., 2014). We report the Bayes factors (3.43) in Table 3.7. These have been calculated by choosing the best model (i.e. the one with the largest evidence) between the unimodal and the bimodal normal distributions for each sample under consideration, thus the largest evidence for the first sample, the second sample, and the combined one. A positive natural logarithm of the Bayes factor means that the two samples under considerations are likely to come from the same underlying distribution, while – on the contrary – a negative one implies the unlikelihood that the two samples come from the same distribution. The statistical significance of this implication is usually quantified by taking into account the reference paper of Kass and Raftery (1995). If $|\ln K| < 1$, then the evidence is too poor to claim that one model is more likely than the other. If $1 < |\ln K| < 3$ there is positive evidence for one model with respect to another, if $3 < |\ln K| < 5$ the evidence is strong, while if $|\ln K| > 5$ the evidence is very strong. As we can see from Table 3.7, the BSk20 $M_{\rm act}$ samples generally has a better compatibility with the measured masses than the DDME2 samples. In fact, there is strong evidence

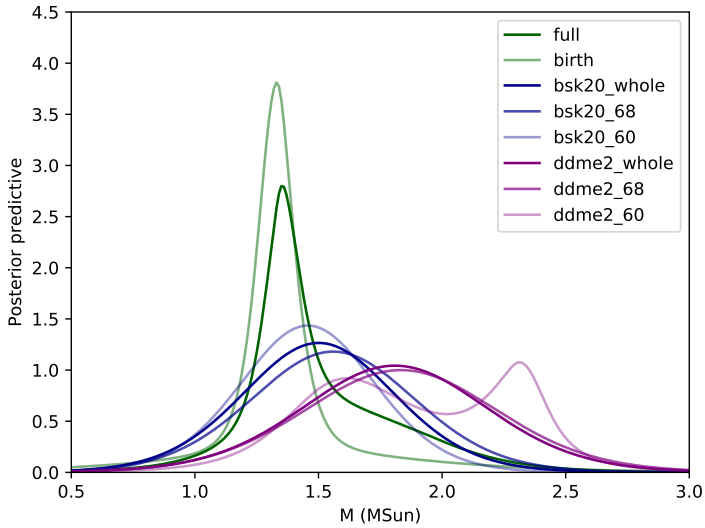

Figure 3.13: Posterior predictive of the Özel and Freire (2016) samples and of the $M_{\rm act}$ samples considered.

that the DDME2 samples come from a different distribution with respect to both the Özel and Freire (2016) samples, in all the cases considered. On the other hand, some BSk20 samples present a positive evidence, meaning that there is some compatibility. As a rule of thumb, the deeper cutoffs generally give better compatibility than the shallower ones. Much interestingly, every combination with the full sample of Özel and Freire (2016) gives a larger Bayes factor than those with the birth sample. This is counter-intuitive: we decided to employ two different samples from the measured masses, as we expected the mass distribution for the glitchers to have masses more similar to the stars with near-birth masses.

One of the advantages of the nested sampling algorithms (such as MULTINEST) is that the algorithm produces samples of the posterior distribution as a by-product of the evidence evaluation. We can employ this samples in order to estimate the posterior predictive distribution, namely the probability distribution of extracting a new mass m given the already-measured masses $\mathcal{D}$. To calculate this quantity, it is necessary to marginalise the chosen model $\mathcal{M}$ for the mass distribution ($P(m|\mathcal{P},\mathcal{M})$, i.e. normal or bimodal) with the posterior distribution for that model ($P(\mathcal{P}|\mathcal{D},\mathcal{M})$):

$$P(m|\mathcal{D},\mathcal{M}) = \int P(m|\mathcal{P},\mathcal{M})\,P(\mathcal{P}|\mathcal{D},\mathcal{M})\,\mathrm{d}\mathcal{P}\,. \tag{3.50}$$

The mass distribution $P(m|\mathcal{P},\mathcal{M})$ has been chosen for each sample to be the one yielding the largest evidence. We plot the posterior predictive distribution for all the single samples in Figure 3.13. We can here better visualise the results of the two-sample test. The posterior predictive distribution for the birth mass sample is unimodal, and peaked around $1.4M_{\odot}$. This is probably due to the presence in the

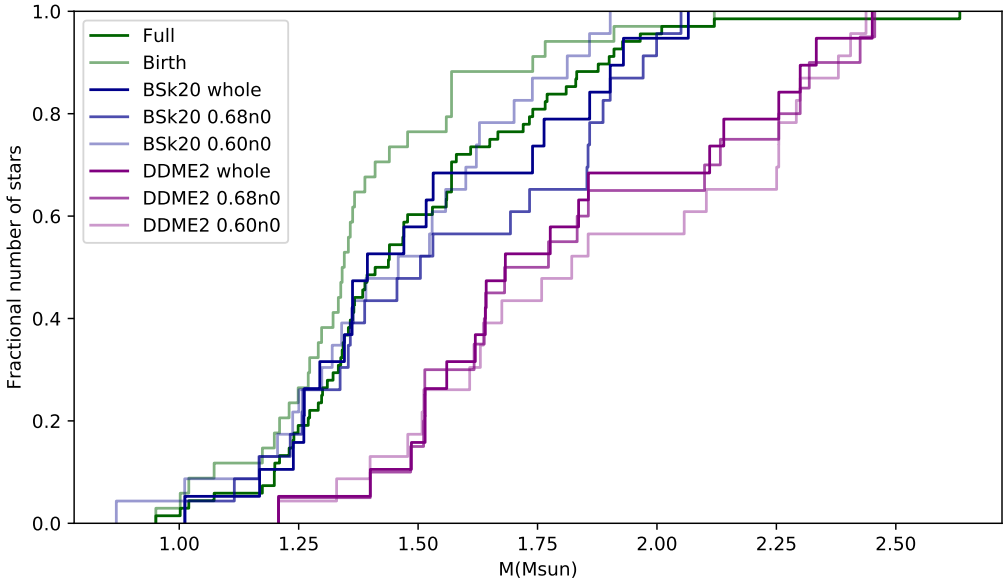

Figure 3.14: Empirical distribution functions for the eight samples under consideration.

sample of a large number of binary neutron stars, which show a very strongly peaked mass distribution (Kiziltan et al., 2013). On the other hand, the posterior predictive for the full sample of Özel and Freire (2016) is bimodal, with a smaller peak over $1.5 M_{\odot}$, and it is somewhat broader. This effect has already been seen in Antoniadis et al. (2016) for a millisecond pulsar sample, in Kiziltan et al. (2013) and in Alsing et al. (2018), and it is probably caused by the presence of stars which have undergone accretion. Note that, however, the two distribution are only mildly different. The $M_{\rm act}$ distributions are generally much broader, and in the case of the DDME2 EoS, peaked on rather large values of masses.

In order to double-check the results obtained until now, we also performed a two-sample Kolmogorov-Smirnov (KS) test on all the couples of samples considered. The idea of the KS test is to calculate the KS statistic, which is the maximum vertical distance between the two empirical distribution functions of the two samples under consideration. We plot in Figure 3.14 the empirical distribution for all the eight samples we employ here. The KS statistic and the corresponding p-value have been calculated employing the `ks_2samp` function defined in `scipy.stats` Python module. A large p-value means that we cannot exclude the hypothesis that the distributions of the two samples are the same. It is not possible, however, to use the KS test directly on the data, as they present uncertainties, which are quite large in some cases (see Figure 3.11). To solve this issue, we randomly extract one value for each measurement of the two samples from the asymmetric normal distribution (3.45), and we perform the KS test on these extracted data. We then re-extract the samples again from the asymmetric normal distributions, and calculate the KS statistic and p-value again. By

doing this procedure ten thousand times, we obtain the histograms for the p-values presented in Figure 3.15. The trend is the same of the Bayes factor study: the BSk20 samples show much more compatibility with the measured masses compared with those with the DDME2 EoS, and the agreement is better with the full Özel and Freire sample than with the birth sample. The only different thing is the fact that the $0.60n_0$ cutoff seems to have a larger p-value than the $0.68n_0$ case.

We would like to stress that the Bayesian two-sample test and the KS two-sample test are intrinsically different. They are based on completely different statistics, and while the former requires a deep modelling of the probability distributions for the mass measurements and the mass population (thus allowing for a natural implementation of the measurement uncertainties), the latter is simpler and non-parametric. We note that – albeit so different – they give essentially the same results. Finally, it is important to notice that throughout all this Section we have assumed $M_{\rm act}$ to be the true mass of the star, rather than an upper limit: this hypothesis was necessary in order to make the comparisons presented here. We do not know how different from the true mass of the star this upper limit is. If the error made by making this assumption is large (i.e. $M_{\rm act}$ is much larger than the true mass of the star), then it is possible that the $M_{\rm act}$ predictions made by stiffer equations of state (like DDME2) are compatible with the measured masses, but not the predictions made by soft EoSs like BSk20. On the other hand, if $M_{\rm act}$ is similar to the true mass of the star, then the results presented in this Section hold.

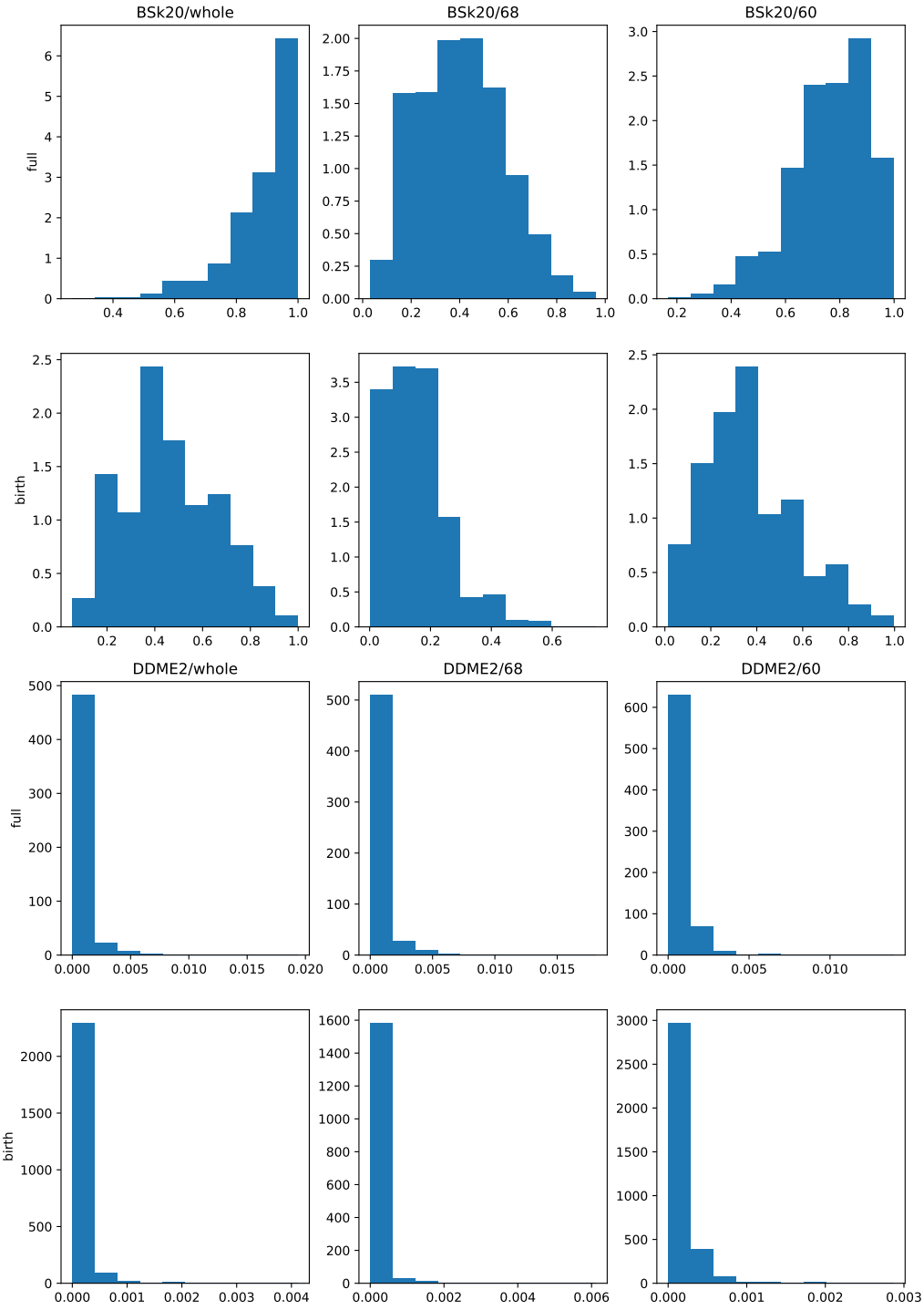

Figure 3.15: Histograms of the KS p-values for all the combination of samples, one taken from Özel and Freire (2016) (rows) and one of the $M_{\rm act}$ cases (columns).

CHAPTER 4

Angular velocity evolution

Until now, most of the information extracted from pulsar glitches and used to constrain neutron star structure has been obtained by the overall glitching behaviour of a pulsar, i.e. how frequent and large the events it displays are. Some more information can be obtained from the angular velocity evolution of a pulsar during a glitch. Among this information, we mention the presence of a slow relaxation of the angular velocity after the glitch towards the pre-glitch spin down rate, which is the main evidence for the involvement of a superfluid component in the star. On very short timescales, however, things are more obscure. In fact, although they have been modelled since the Eighties (see, e.g., Alpar et al., 1984a), glitch rises are generally not resolved, due to intrinsic noise in the time of arrival of single pulsations and the fact that pulsars are not observed continuously, thus it is easy to miss a glitch in the act. As an example, in spite of the fact that the Vela pulsar has been monitored for fifty years, only a couple of notable events allowed to put an upper limit of 40 s on the timescale of the glitch spin-up (Dodson et al., 2002, 2007). Only recently, the detection of a glitch in the Vela pulsar on 12 December 2016 has provided a great deal of new information for glitch modelling (Palfreyman et al., 2018). The peculiarity of this detection lies in the fact that this is the first pulse-to-pulse observation of a glitch, allowing for unprecedented timing resolution during the glitch trigger. Thanks to this, a new strong upper limit of 12.6 s on the timescale of the glitch spin-up has been determined by Ashton et al. (2019b), obtained through a Bayesian analysis with a phenomenological three-component model, and a new upper limit of ~ 6 s has been proposed in Montoli et al. (2020b) with a more refined and model-dependent framework (see Section 4.3). This kind of observations gives us a glimpse of how rapidly the two components (the charged and the superfluid ones) exchange angular momentum and opens a new window for theoretical speculations (Graber et al., 2018; Ashton et al., 2019b; Pizzochero et al., 2020; Gügercinoğlu and Alpar, 2020; Montoli et al., 2020b).

Complex behaviour during the spin-up and the first minute of the post-glitch relaxation has been predicted in simulations based on hydrodynamical models of the neutron star internal structure, when more than just two rigid components are

considered (Haskell et al., 2012; Haskell and Antonopoulou, 2014; Antonelli and Pizzochero, 2017; Graber et al., 2018): when the superfluid component is allowed to sustain non-uniform rotation, different regions may experience different friction and hence recouple to the observable normal component on different timescales, giving rise to different types of post-glitch frequency evolution. In particular, depending on the strength of the couplings and on the initial conditions for the relative motion between the various components, a glitch overshoot – a transient interval in which the observable component spins at a higher rate than the post-glitch equilibrium value, obtained by emptying the whole angular momentum stored into the superfluid reservoir (Antonelli and Pizzochero, 2017) – is observed in such models. Many recent studies have already used the data from the 2016 Vela glitch to study this phenomenon: in Graber et al. (2018), the drag between the charged crust and the crustal and core superfluids has been constrained; in Ashton et al. (2019b), different phenomenological models have been compared to the timing results, obtaining the best current limits on the glitch rise timescale; finally, in Pizzochero et al. (2020) and Montoli et al. (2020b), an analytical solution to a simple three-component model has been proposed, and it has been employed to study the values of different quantities of interest, such as the moment of inertia fractions and the coupling parameters. All these studies also confirmed the presence of an overshoot.

The present Chapter is outlined as follows: after a theoretical introduction in which we will discuss the three-component model and its analytical solution (Section 4.1), we will present a first attempt to employ it on the 2016 Vela glitch data with a frequentist approach (Section 4.2). Finally, we will present a more thorough analysis in the Bayesian framework in Section 4.3.

4.1 Three-component model

As we told in the introduction to this Chapter, many simulations of models with two differentially-rotating components or meridional circulation have been performed, many of which foresee the presence of a peculiar time evolution of the observable charged component during the first moments after a glitch, the glitch overshoot (van Eysden and Melatos, 2010; Haskell et al., 2012; Haskell and Antonopoulou, 2014; Antonelli and Pizzochero, 2017; Graber et al., 2018). It is difficult, however, to compare simulations like these – with a differentally-rotating superfluid component – with the data: the models need some simplification in order to obtain some information by fitting the data. One easy way to accomplish this would be that of employing rigidly-rotating components. Nevertheless, this poses another problem: two rigidly-rotating components (which is the case of Equation (1.17)) yield a monotonic increase in the angular velocity of the star, as the angular momentum excess is simply transferred from the superfluid component to the normal one, thus not allowing for the presence of a glitch overshoot. The minimal model which allows for an overshoot requires at least three components: one normal component and two superfluid components, of

which one stores most of the angular momentum excess (pinned component, which could be the crustal superfluid) and the other very little or no angular momentum surplus (passive component, which could be the core superfluid). In this way, different couplings between the two superfluid components and the normal one yield different transfer rates of angular momentum. If the pinned component transfers its angular momentum excess on a faster rate than the normal component to the passive component, then a glitch overshoot occurs. Therefore, in complete analogy with the model of Baym et al. (1969b), we need a total angular momentum conservation equation, plus two equations for the exchange of angular momentum between the superfluid components (labelled with 1,2) and the normal one (labelled with p):

$$\begin{aligned} &x_p\dot{\Omega}_p + x_1\dot{\Omega}_1 + x_2\dot{\Omega}_2 = -|\dot{\Omega}_\infty| \\ &\dot{\Omega}_1 = -b_1\left(\Omega_1 - \Omega_p\right) \\ &\dot{\Omega}_2 = -b_2\left(\Omega_2 - \Omega_p\right) \end{aligned} \tag{4.1}$$

where x_i indicates the moment of inertia of the i-component with respect to the total one, b_i the coupling parameter between the i-th superfluid component with respect to the normal one and $|\dot{\Omega}_\infty|$ is the spin-down rate. Note that $|\dot{\Omega}_\infty|$ is the spin-down rate averaged over several years (steady-state spin down), which thus considers glitches in its measurement. For this reason, this spin down acts on the whole star, including the superfluid components. We impose that the three partial moment of inertia ratios x_i sum up to 1, i.e. we are explicitly asking the three components to comprise the whole star. In this case, the moment of inertia fraction for the normal component can be written as:

$$x_p = 1 - x_1 - x_2\,. \tag{4.2}$$

Note that this is not a compulsory hypothesis, as the system of equations above is solvable even without this assumption. In that case, however, we would have one more free parameter – x_p – to be fitted with the data. To keep things simple, we neglect this possibility, assuming that all the star participates in the glitch mechanism. It is interesting to notice that a model with a differentially-rotating superfluid component is similar to a limit of an infinite number of rigidly-rotating superfluid components: in this model only two have been taken, so to have the simplest model which is able to account for an overshoot. The system in (4.1) is valid for $t \geq 0$, where we have set $t = 0$ as the time at which the glitch is triggered. Prior to the glitch moment, the values of $b_{1,2}$ could have a different value, e.g. they may be assumed to be equal to zero if the two superfluid components are perfectly pinned (Anderson and Itoh, 1975), but their actual pre-glitch value is not important for our scope. Since $b_{1,2}$ set the post-trigger creep rate of vortex lines (Alpar et al., 1984b), what is important in the present analysis is that their value remain almost constant during the glitch spin-up phase and the first moments of the relaxation, namely long enough (approximately one minute) to describe the first exponential decay in the angular velocity (see, e.g., Celora et al., 2020, for models where these mutual friction coefficients are functions

of the velocity lag between the components). Hence, a limitation of the model will be that we drop the still poorly understood problem of the post-glitch repinning process, during which the creep rate is expected to decrease as the velocity lag between the superfluid and the normal component becomes smaller and smaller (Sedrakian, 1995; Haskell and Melatos, 2016).

We can solve the system of equations (4.1) analytically (see Pizzochero et al., 2020; Montoli et al., 2020b). As a first step, let us perform a change of variables: it is convenient to use the superfluid angular velocities as measured in the frame of the normal component $\Omega_{ip} \equiv \Omega_i - \Omega_p$, with $i = 1, 2$. Furthermore, it is convenient to integrate directly the first equation for Ω_p to find that the angular velocity for the normal component with respect to the steady-state spin down solution is given by

$$\Delta\Omega_p(t) := \Omega_p(t) - \Omega_p^0 + |\dot{\Omega}_\infty|\, t = -\mathbf{x}\cdot(\mathbf{y}(t) - \mathbf{y}_0), \tag{4.3}$$

where we have defined the vectors

$$\begin{aligned} \mathbf{x} &= (x_1\,,\, x_2) \\ \mathbf{y} &= (\Omega_{1p}\,,\, \Omega_{2p}) \\ \mathbf{y}_0 &= (\Omega_{1p}^0\,,\, \Omega_{2p}^0)\,. \end{aligned} \tag{4.4}$$

In this way we only have to solve the dynamics of the lag vector $\mathbf{y}$, that must satisfy the matrix equation (given by the last two equations of (4.1))

$$\dot{\mathbf{y}} = \mathbf{a} - B\,\mathbf{y}, \tag{4.5}$$

where

$$\mathbf{a} = \begin{bmatrix} \alpha \\ \alpha \end{bmatrix}, \qquad B = \begin{bmatrix} (1-x_2)\beta_1 & x_2\beta_2 \\ x_1\beta_1 & (1-x_1)\beta_2 \end{bmatrix} \tag{4.6}$$

and

$$\alpha = |\dot{\Omega}_\infty|/(1-x_1-x_2) \tag{4.7}$$

$$\beta_i = b_i/(1-x_1-x_2) \qquad \text{for} \quad i = 1, 2\,. \tag{4.8}$$

The matrix B has two eigenvalues λ_+ and λ_-, given by

$$\begin{aligned} \lambda_\pm = \frac{1}{2}\Big[& \beta_1(1-x_2) + \beta_2(1-x_1) \pm \\ & \pm \sqrt{[\beta_1(1-x_2) + \beta_2(1-x_1)]^2 - 4\beta_1\beta_2 x_p}\Big]. \end{aligned} \tag{4.9}$$

We call the respective eigenvectors $\mathbf{e}_+$ and $\mathbf{e}_-$, defined up to a normalisation constant; their explicit form is not necessary here. Using the fact that the parameters b_i are positive and that the sum of the moment of inertia fractions x_i cannot exceed unity, it is easy to prove that both the eigenvalues are always positive and in particular

that $\lambda_+ > \lambda_- > 0$. Because of this positivity property, Equation (4.5) allows a stable steady-state solution $\mathbf{y}(t) = \mathbf{y}_\infty$ that is constant in time:

$$\mathbf{y}_\infty = B^{-1}\mathbf{a} = (\alpha/\beta_1\,,\,\alpha/\beta_2)\,. \tag{4.10}$$

This particular solution is an attractor for the dynamics of the lag vector $\mathbf{y}$: the internal forces induced by dissipation (set by the parameters b_i) and the driving force (set by the parameter $|\dot{\Omega}_\infty|$) tend to balance, killing off initial transients and settling the system into its typical behaviour described by $\mathbf{y}_\infty$. Since in the problem we have two natural timescales (one short, $1/\lambda_+$, and one long, $1/\lambda_-$), we can conclude that the steady state is reached in the limit $t \gg 1/\lambda_-$.

The above property of the system allows to define the asymptotic amplitude of the glitch $\Delta\Omega_p^\infty$: we just have to take the limit $t \gg 1/\lambda_-$ in Equation (4.3) to obtain

$$\Delta\Omega_p^\infty = \mathbf{x}\cdot(\mathbf{y}_0 - \mathbf{y}_\infty)\,. \tag{4.11}$$

Instead of the lag vector $\mathbf{y}$, it is more convenient to consider the dynamics of the residual with respect to the steady-state

$$\Delta\mathbf{y} = \mathbf{y} - \mathbf{y}_\infty\,, \tag{4.12}$$

that satisfies the linear equation

$$\Delta\dot{\mathbf{y}} = -B\,\Delta\mathbf{y}\,. \tag{4.13}$$

Decomposing $\mathbf{y}_0 - \mathbf{y}_\infty$ in the basis of the eigenvectors,

$$\mathbf{y}_0 - \mathbf{y}_\infty = \delta y_-\mathbf{e}_- + \delta y_+\mathbf{e}_+\,, \tag{4.14}$$

the general solution of (4.13) is expressible as

$$\Delta\mathbf{y}(t) = e^{-tB}(\mathbf{y}_0 - \mathbf{y}_\infty) = \sum_{j=+,-}\mathbf{e}_j\,\delta y_j\,e^{-t\lambda_j}\,. \tag{4.15}$$

Employing the decomposition (4.14) and (4.15) into (4.3), it is easy to find

$$\Delta\Omega_p(t) = \Delta\Omega_p^\infty\left[1 - \omega\,e^{-t\lambda_+} - (1-\omega)\,e^{-t\lambda_-}\right], \tag{4.16}$$

where we have defined

$$\omega = \delta y_+\,(\mathbf{x}\cdot\mathbf{e}_+)/\Delta\Omega_p^\infty\,. \tag{4.17}$$

Instead of using the eigenvectors, it is easier to find the value of ω in terms of the parameters of the system (4.1) by considering the value of the derivative of (4.16) at $t = 0$

$$\omega = \frac{\Delta\dot{\Omega}_p(0)}{\Delta\Omega_p^\infty(\lambda_+ - \lambda_-)} - \frac{\lambda_-}{\lambda_+ - \lambda_-}\,. \tag{4.18}$$

Finally, to write the general solution (4.16) in terms of the basic parameters of the model, we need to know that

$$\Delta\Omega_p^{\infty} = x_1\left(\Omega_{1p}^0 - \frac{\alpha}{\beta_1}\right) + x_2\left(\Omega_{2p}^0 - \frac{\alpha}{\beta_2}\right) \tag{4.19}$$

$$\Delta\dot{\Omega}_p(0) = x_1\,\beta_1\,\Omega_{1p}^0 + x_2\,\beta_2\,\Omega_{2p}^0 - (x_1 + x_2)\,\alpha\,. \tag{4.20}$$

Let us comment on the solution (4.16) of the system. This solution has been presented in Montoli et al. (2020b), as a generalisation of a first solution presented in Pizzochero et al. (2020). The angular velocity of the observable component shows an evolution with two different timescales, one given by $1/\lambda_+$ and a longer one given by $1/\lambda_-$. The form of this solution has already been noted in other works, as Equation (4.16) has the same functional form of the model used to fit the Vela 2016 glitch by Ashton et al. (2019b); the difference here is that we make an exact connection between the phenomenological parameters in (4.16) and the "structural" parameters in (4.1), which have a more clear physical interpretation.

Let us now study the conditions under which an overshoot of the normal component can be produced, a situation that – as we told before – can never occur in a model with only two rigid components and a constant coupling parameter like the one of Baym et al. (1969b). Note, however, that it is possible to obtain an overshoot with a two-component model of the kind pioneered by Alpar et al. (1981), where the superfluid can develop non-uniform rotation (see, e.g., Alpar et al., 1984b; Larson and Link, 2002; Haskell et al., 2012; Antonelli and Pizzochero, 2017; Graber et al., 2018), due to the fact that the coupling with the normal component – which depends on the non-uniform lag itself and on stratification – may not be constant in both space and time. This is not surprising as a fluid model has infinite degrees of freedom that can react on different timescales, not only two (i.e. Ω_1 and Ω_2) as the present minimal model. An overshoot is realised if there exists a certain time $t_{\rm max} > 0$ such that $\Delta\dot{\Omega}_p = 0$ and $\Delta\ddot{\Omega}_p < 0$. For the minimal model in (4.1), the nulling of the first derivative of (4.16) gives

$$t_{\rm max} = \frac{1}{\lambda_+ - \lambda_-}\left[\log\left(\frac{\lambda_+}{\lambda_-}\right) + \log\left(\frac{\omega}{\omega - 1}\right)\right], \tag{4.21}$$

which needs to be positive. Since $\lambda_+ > \lambda_- > 0$ (see Equation 4.9), we have that $t_{\rm max}$ is a real number when $\omega < 0$ or $\omega > 1$. The additional condition $\Delta\ddot{\Omega}_p(t_{\rm max}) < 0$ requires $\omega > 0$. Therefore, the overshoot occurs for $\omega > 1$, which also guarantees that $t_{\rm max} > 0$. Note that this overshoot condition, as well as the functional form of Equation (4.16), are somewhat similar to those in van Eysden and Melatos (2010), although the idea is different: here, the time evolution of the angular velocity is continuous at the time of the glitch, while in van Eysden and Melatos (2010) there is a discontinuous jump at the glitch time.

If we consider the time residuals with respect to the steady spin-down evolution, which are given by (see Equation (1.13))

$$r_p(t) = -\frac{1}{\Omega_p^0}\int_0^t \Delta\Omega_p(t')\mathrm{d}t' , \tag{4.22}$$

we can translate the overshoot condition in terms of them: for an overshooting glitch, $t_{\max}$ corresponds to an inflexion point, after which $\ddot{r}_p(t)$ is positive. On the other hand, in a non-overshooting glitch there is no inflexion point, and $r_p(t)$ is always concave down.

We remark that all the equations displayed above are symmetric by exchange of the label 1 with 2. To physically distinguish one superfluid component from the other, we should impose, for example, that the superfluid component 2 is the one with the largest initial lag, $\Omega_{2p}^0 > \Omega_{1p}^0$. This may be due to a stronger pinning in the region of component 2, or simply because it happened that the glitch initiated in this condition (the initial conditions are unknown and depend on the past history of the system). Hence, the superfluid component 1 is, by definition, the one with a smaller initial lag, i.e.

$$\Omega_{1p}^0 < \Omega_{2p}^0 . \tag{4.23}$$

4.1.1 Constraint on the moment of inertia of the slow component

In the previous Section we presented the general solution to a three-component system, first presented in Pizzochero et al. (2020) and then extended in Montoli et al. (2020b). Building on the particular solution of Pizzochero et al. (2020), which assumes the presence of only one superfluid reservoir (i.e. Ω_{2p}^0 only is different from the steady state lag, see Section 4.2), Sourie and Chamel (2020) recently proposed a simple formula to constrain the moment of inertia fraction of the other superfluid component. It is worth to extend their treatment in view of the more general approach used here.

Let us define the maximum angular velocity $\Delta\Omega_{\rm over}$ achieved by the star during the overshoot, which can be obtained by finding the maximum in Equation (4.16). Using $\Delta\Omega_{\rm over} = \Delta\Omega_p(t_{\max})$ and Equation (4.21), we immediately obtain

$$\frac{\Delta\Omega_{\rm over}}{\Delta\Omega_p^\infty} = 1 - \omega\left(\frac{\lambda_-(\omega-1)}{\lambda_+\omega}\right)^{\frac{\lambda_+}{\lambda_+-\lambda_-}} + (\omega-1)\left(\frac{\lambda_-(\omega-1)}{\lambda_+\omega}\right)^{\frac{\lambda_-}{\lambda_+-\lambda_-}} . \tag{4.24}$$

This quantity depends on the phenomenological input parameters of the model (i.e. the x_i, b_i and $|\dot{\Omega}_\infty|$) as well as on the initial condition Ω_{ip}^0, for $i = 1, 2$. We stress that, to obtain this equation, the role of the superfluid components 1 and 2 has been considered as totally symmetric and all the formulas are invariant under the exchange of the two. However, let us relax this hypothesis and assume that one of the two components, say the component 2, has a higher drag parameter with respect to the other one, i.e. $b_1 \ll b_2$:

$$a_{1/2} = b_1/b_2 = \beta_1/\beta_2 \ll 1 . \tag{4.25}$$

Having all the parameters but the coupling parameters fixed, it is possible to study the value of $\Delta\Omega_{\rm over}$ as a function of b_1/b_2. It is easy to see that the maximum value of the overshoot can be obtained if $b_1/b_2 \to 0$. In that case, in fact, the superfluid 2 would cede all its extra angular momentum to the normal component on a much faster rate than the normal component to the other superfluid. No further assumptions are needed on x_1 and x_2 (i.e. we do not need to specify which of the two components has higher inertia). This case is of physical interest (since we expect the nature and the strength of the friction mechanism to vary in different layers of the star) and allows to perform an expansion in the parameter $a_{1/2}$. Inserting the expansions

$$\omega = \omega^* + a_{1/2}\,\omega' + O(a_{1/2}^2) \tag{4.26}$$

$$\lambda_+ = \lambda_+^* + a_{1/2}\,\lambda_+' + O(a_{1/2}^2) \tag{4.27}$$

$$\lambda_- = a_{1/2}\,\lambda_-' + O(a_{1/2}^2)\,, \tag{4.28}$$

into (4.24), it is possible to safely take the limit $a_{1/2} \ll 1$ to show that

$$\frac{\Delta\Omega_{\rm over}}{\Delta\Omega_p^\infty} = \omega^* + O(a_{1/2}) \tag{4.29}$$

and

$$\frac{\Delta\Omega_{\rm over} - \Delta\Omega_p^\infty}{\Delta\Omega_{\rm over}} = \frac{\omega^* - 1}{\omega^*} + O(a_{1/2})\,. \tag{4.30}$$

Thanks to (4.9), we find that (4.27) and (4.28) read

$$\lambda_+ = \frac{b_2\,(1-x_1)}{1-x_1-x_2} + \frac{a_{1/2}\,b_2\,x_1\,x_2}{(1-x_1)(1-x_1-x_2)} + O(a_{1/2}^2) \tag{4.31}$$

$$\lambda_- = \frac{a_{1/2}\,b_2}{1-x_1} + O(a_{1/2}^2)\,. \tag{4.32}$$

The lowest-order term ω^* in (4.26) can now be obtained by inserting the above equations into (4.17). Finally, the ratio in (4.30) turns out to be

$$\frac{\Delta\Omega_{\rm over} - \Delta\Omega_p^\infty}{\Delta\Omega_{\rm over}} = x_1 - \frac{x_1(1-x_1)(b_1\Omega_{2p}^0 - |\dot\Omega_\infty|)}{b_1\,x_2\,\Omega_{2p}^0} + O(a_{1/2})\,. \tag{4.33}$$

Finally, we observe that to obtain a positive glitch amplitude both $\Delta\Omega_p^\infty$ in (4.19) and $\Delta\dot\Omega_p(0)$ in (4.20) should be positive. This constrains the initial lags and it is possible to show that this requirement is fulfilled for any possible value of x_1 and x_2 if

$$|\dot\Omega_\infty| < \min_{i=1,2}\left[\, b_i\,\Omega_{ip}^0 \,\right]. \tag{4.34}$$

Under the assumption (4.25), the constraint (4.34) tells us that

$$|\dot\Omega_\infty| < a_{1/2}\,b_2\,\Omega_{1p}^0 \qquad \text{and} \qquad |\dot\Omega_\infty| < b_2\,\Omega_{2p}^0\,. \tag{4.35}$$

Equation (4.35) tells us that the second term in the right-hand side of (4.33) is always negative, so that, to the lowest order in $a_{1/2}$, the detection of an overshoot allows to constrain the fractional moment of inertia of the "slow" component (in this case x_1) as

$$x_1 > \frac{\Delta\Omega_{\rm over} - \Delta\Omega_p^{\infty}}{\Delta\Omega_{\rm over}} \qquad \text{for} \quad b_1 \ll b_2 \,. \tag{4.36}$$

This is in complete accordance with equation (12) of Sourie and Chamel (2020).

4.1.2 Including corrections

It is straightforward to include the entrainment effect into our system of equations, provided that a wise choice of the dynamical variables is made. In fact, it has been shown that using the superfluid momenta instead of the velocities naturally leads to a redefinition of the phenomenological parameters of the hydrodynamic model (here the x_i and the b_i for $i = 1, 2$), but the form of the dynamical equations remains unchanged (Antonelli and Pizzochero, 2017, but also Chapters 2 and 3). Originally the argument has been presented in the very special case of straight and rigid vortex lines permeating the superfluid component in a Newtonian context, but it can be generalised to the case of tensionless vortices and of different superfluid domains, as well as to take into account for general relativistic corrections in the slow-rotation approximation (Antonelli et al., 2018).

The present discussion is analogous to the one made by Sidery et al. (2010) and differs from it only for a different choice of variables, that is nonetheless quite convenient in the present framework where we have to deal with three different components. Locally, the momentum per particle $\mathbf{p}_n$ of the superfluid neutrons is a linear combination of the neutron velocity $\mathbf{v}_n$ and of the velocity of the normal component $\mathbf{v}_p$ (which is a mixture of all the charged species and we assume it to be rigid),

$$\mathbf{p}_n / m_n = (1 - \varepsilon_n)\, \mathbf{v}_n + \varepsilon_n \mathbf{v}_p \,, \tag{4.37}$$

where m_n is the neutron mass and ε_n is the entrainment parameter (Prix et al., 2002; Chamel, 2017b; Haskell and Sedrakian, 2018). If we have two different (non-overlapping) superfluid regions and the motion is circular, the above equation suggests defining two additional angular velocities Ω_ν^i as (see also Equation (2.18))

$$\Omega_\nu^i = (1 - \varepsilon_n^i)\, \Omega_n^i + \varepsilon_n^i\, \Omega_p \,, \tag{4.38}$$

where Ω_p is the observable angular velocity of the normal p-component while Ω_n^i is the angular velocity of the neutrons in the region $i = 1, 2$. In some situations, working with the Ω_ν^i may be convenient because, due to the Feynman-Onsager relation, they are a direct measure of the number of vortices in a certain superfluid region. Hence, the Ω_ν^i cannot change as long as the number of vortices is conserved. This defines the

form of the equations of motion at a certain location $\mathbf{x}$ inside the star (Antonelli and Pizzochero, 2017),

$$\partial_t \Omega_v^i(t,\mathbf{x}) \approx -2\Omega_v^i(t,\mathbf{x})\frac{\mathcal{R}_i}{1+\mathcal{R}_i^2}(\Omega_n^i(t,\mathbf{x})-\Omega_p(t)) \tag{4.39}$$

where $\mathcal{R}_i$ is the drag-to-lift ratio that appears in the vortex-mediated mutual friction force between the superfluid and normal components (Andersson et al., 2006). With the aid of (4.38), the above equation reads

$$\partial_t \Omega_v^i(t,\mathbf{x}) \approx -2\Omega_p \mathcal{B}_i(r)(\Omega_v^i(t,\mathbf{x})-\Omega_p(t)), \tag{4.40}$$

where we have used that $\Omega_v^i \approx \Omega_p$ because the lags are small and the coefficient $\mathcal{B}_i(r)$ depends on the local values $\mathcal{R}_i(r)$ and $\varepsilon_n^i(r)$ at a certain radius r inside the star (we assume spherical stratification), namely

$$\mathcal{B}_i(r) = \frac{1}{1-\varepsilon_n^i}\frac{\mathcal{R}_i}{1+\mathcal{R}_i^2}. \tag{4.41}$$

Both $\mathcal{B}_i$ and $\mathcal{R}_i$ are expected to have a spherical radial dependence as their value depends on the physical quantities in the stellar interior and on the particular mechanism that operate to dissipate energy at the microscopic scale of a vortex core. When the variables Ω_v^i are used, the total angular momentum of the star L_{tot} is given by

$$L_{\text{tot}} = (I - I_v^1 - I_v^2)\Omega_p + I_v^1 \langle \Omega_v^1 \rangle_1 + I_v^2 \langle \Omega_v^2 \rangle_2, \tag{4.42}$$

where I is the total moment of inertia and[1]

$$I_v^i = \frac{8\pi}{3}\int_i dr\, r^4 \frac{\rho_n(r)}{1-\varepsilon_n(r)} \tag{4.43}$$

is a rescaled moment of inertia for the superfluid component (the integration extends over the region i and $\rho_n(r)$ is the density of unbounded neutrons). Using standard spherical coordinates where θ is the colatitude, the parameters I_v^i play the role of normalisation factors for the averages of functions over the i-region,

$$\langle f \rangle_i = \frac{1}{I_v^i}\int_i d^3x\, f(\mathbf{x})\frac{(\sin\theta\, r)^2 \rho_n(r)}{1-\varepsilon_n(r)}. \tag{4.44}$$

We now take the spatial average of equation (4.40),

$$\langle \dot{\Omega}_v^i \rangle_i \approx -\langle 2\Omega_p \mathcal{B}_i(\Omega_v^i - \Omega_p)\rangle_i, \approx -2\Omega_p \langle \mathcal{B}_i \rangle_i \langle \Omega_v^i - \Omega_p \rangle_i. \tag{4.45}$$

[1] Since the integration is over the i-region, and the two superfluid regions do not overlap, we can drop the unnecessary i labels on the density and on the entrainment parameter. We do the same in (4.44).

Clearly, the last step is not rigorous but neglecting possible correlations between the local value of $\mathcal{B}_i$ and the spatial fluctuations of the lag $\Omega_v^i - \Omega_p$ is the price we have to pay to obtain a rigid model from a fluid one. Finally, the spin-down torque has the only effect to transport the angular momentum to infinity, so it can be introduced exactly as

$$\dot{L}_{\rm tot} = (I - I_v^1 - I_v^2)\dot{\Omega}_p + I_v^1 \langle \dot{\Omega}_v^1 \rangle_1 + I_v^2 \langle \dot{\Omega}_v^2 \rangle_2 = -I|\dot{\Omega}_\infty| \,. \tag{4.46}$$

Equations (4.45) and (4.46) are formally equivalent to the system in (4.1), provided that we make the following identifications:

$$x_i = I_v^i / I \tag{4.47}$$

$$x_p = (I - I_v^1 - I_v^2)/I = 1 - x_1 - x_2 \tag{4.48}$$

$$b_i = 2\Omega_p \langle \mathcal{B}_i \rangle_i \tag{4.49}$$

$$\Omega_i = \langle \Omega_v^i \rangle_i \,. \tag{4.50}$$

Note that including all the entrainment corrections into the definition of the phenomenological parameters of the model has the advantage that the final system of equations does not change because of the additional entrainment couplings. Hence, no new calculations are needed to find the general solution of the system, which is formally identical to the case with no entrainment. In particular, the generalisation of the formula of Sourie and Chamel (2020) to the case in which there is entrainment is still our equation (4.36), where

$$x_1 = \frac{I_v^1}{I} > \frac{\Delta\Omega_{\rm over} - \Delta\Omega_p^\infty}{\Delta\Omega_{\rm over}} \qquad \text{for} \quad \langle \mathcal{B}_1 \rangle_1 \ll \langle \mathcal{B}_2 \rangle_2 \,. \tag{4.51}$$

Although this is a completely Newtonian model, it is easy to expect that a fully relativistic treatment would start from a system like that in (4.1) as well, at least in the slow rotation approximation (Hartle, 1967). What changes is the definition of the different parameters inside the equation: the moments of inertia are no longer those described in a Newtonian framework, but the relativistic ones, by following a line of reasoning very similar to that for the entrainment parameter. It is interesting to note, however, that the moment of inertia fractions in both the Newtonian and the slow rotation approximation are numerically very similar, as it has been noticed in Antonelli et al. (2018) (see Chapter 2). Other works concentrate on other aspects of the glitch dynamics, as for example the glitch rise time. This is not an easy combination of the parameters of the model, but the fact that the relativistic value of this varies from the Newtonian one up to a factor of two, also in the more massive stars, is somewhat comforting (Sourie et al., 2016; Gavassino et al., 2020). We have however to stress the importance of a fully consistent general relativistic derivation for the model with three rigidly-rotating components. Only in this way it is possible to make a more clear and direct link between the phenomenological parameters described in (4.1) and the microphysical parameters.

4.2 Application to the 2016 Vela glitch: frequentist approach

A first fit to the 2016 Vela glitch has been performed in Ashton et al. (2019b). In that work, the authors performed a Bayesian fit to the Palfreyman et al. (2018) data, by assuming a time dependence of the angular velocity of the form (4.16). The fit was based on a phenomenological model: the objectives were the glitch rise time and decay time ($1/\lambda_-$ and $1/\lambda_+$), and the prefactors in front of each exponential (i.e. the overshoot size and the long term glitch size). We show here the different approach presented in Pizzochero et al. (2020). The idea is – instead of using the phenomenological parameters – to fit the more "physical" parameters, such as the moment of inertia fractions x_i and the coupling parameters b_i. To do so, a first fit has been performed in Pizzochero et al. (2020), by employing a simplified version of (4.16) and a frequentist approach. The analysis have been made more thoroughly in a subsequent work (Montoli et al., 2020b, see also Section 4.3).

The simplifying working assumption made in Pizzochero et al. (2020) is that we assume that only one of the two superfluid components stores an excess of angular momentum. We are thus asking that the other component (the 1-superfluid component) has an initial lag at the glitch time that is equal to the steady state solution, i.e. $\dot{\Omega}_1 = \dot{\Omega}_\infty$. This condition translates in (see Equation (4.10)):

$$\Omega_{1p}^0 = \frac{|\dot{\Omega}_\infty|}{b_1}\,. \tag{4.52}$$

We will discuss in Section 4.3 the acceptability of this hypothesis. With this assumption, it can be shown (see Pizzochero et al., 2020) that the overshoot condition $\omega > 1$ can be translated into $b_1/b_2 < 1$. In other words, the condition for an overshoot is that the post-glitch coupling parameter b_2 associated to the "active" component (that in the pre-glitch state was only loosely coupled to the rest of the star) must be larger than the coupling parameter b_1 of the "passive" component. From the physical point of view, the overshoot occurs if the "active" superfluid region that stores the angular momentum for the glitch can transfer its excess of angular momentum to the normal component faster than the typical timescale the "passive" superfluid component reacts with.

The data made available by Palfreyman et al. (2018) span a 4200 s time window, with the glitch time positioned roughly at the centre of the dataset. The authors calculate a first estimate of the glitch date, to be set at $t_g^P = 57734.4849906\,\mathrm{MJD}$. Moreover, they identify some peculiarities during the glitch: soon after a null (missing) pulse at time t_0, a sudden and persistent increase of the timing residuals has been detected in the time interval between $t_1 = t_0 + 1.8\mathrm{s}$ and $t_2 = t_0 + 4.4\mathrm{s}$ (see Figure 4.2 for the relative positions of these times). This kind of phenomena can be linked to an effective slow-down of the star before the actual glitch (Graber et al., 2018; Ashton et al., 2019b) or to a magnetospheric change that could cause a delay on the emission

of the pulsations of the star, maybe due to a starquake (Bransgrove et al., 2020). Of course, this phenomenon cannot be described using the model described in Section 4.1, thus we add a phenomenological offset r_0 to the time residuals in (4.22). Finally, we ask (4.22) to be valid only after a glitch, i.e. we ask $r_p(r)$ to be zero for $t < t_g$, where t_g is the glitch instant. In conclusion, the function we would like to fit is:

$$r_p(t) = \vartheta(t - t_g)\left(r_0 - \frac{1}{\Omega_p^0} \int_0^{t-t_g} \Delta\Omega_p(t')\mathrm{d}t' \right), \tag{4.53}$$

where $\Delta\Omega_p(t)$ is given by Equation (4.16) – with the condition of Equation (4.52) – and ϑ is the Heaviside theta function.

We now fit this expression to the data of the residuals made available by Palfreyman et al. (2018) using a least-squares method. The parameters to fit are seven: the two moment of inertia fractions $x_{1,2}$, the two coupling parameters $b_{1,2}$, the offset r_0, the glitch time t_g and the glitch size $\Delta\Omega_p^\infty$. As we have only one angular momentum reservoir, the glitch size $\Delta\Omega_p^\infty$ is linearly dependent on the initial lag Ω_{2p}^0 (see Equations (4.19) and (4.52)). Hence, we will use the glitch size as a parameter, as it allows for a direct comparison with the result obtained in Palfreyman et al. (2018). Although the glitch time t_g and amplitude $\Delta\Omega_p^\infty$ were already estimated by Palfreyman et al. (2018), here we will take them as free parameters, thus allowing for a check of our results.

Due to the presence of the increase in the timing residuals, we will have to neglect some of the data after the occurrence of the glitch. We expect that during the interval $\Delta t_m = t_2 - t_1$ the emitting magnetosphere has decoupled from (i.e. is not corotating with) the rapidly accelerating crust: the persistent positive offset in the mean of the timing residuals and their associated low variance observed by Palfreyman et al. (2018) during Δt_m cannot describe the overshooting normal component, which instead would correspond to decreasing residuals. Therefore, the data around the interval Δt_m do not describe the crust rotation and should be excluded from the fit. In order to decide how much data to neglect, we proceed as follows: defining t_{cut} as the time before which the data are neglected, we perform the fit varying t_{cut} between $t_2 - 1\,\mathrm{s}$ and $t_2 + 4\,\mathrm{s}$ by steps of 0.1 s (the frequency of the Vela being about 11 Hz, this amounts to eliminating one data point at each successive fit). The fitted parameters can then be plotted as a function of t_{cut}: in Figure 4.1 this is shown for $\Delta\Omega_p^\infty$ (the best determined parameter in our model, due to the extension of the data well after relaxation has completed), and other parameters of the model, $x_{1,2}$ and b_1. The fitted $\Delta\Omega_p^\infty$ first decreases until $t_{\mathrm{cut}} = t_2 + 0.5\,\mathrm{s}$, then stabilises until $t_{\mathrm{cut}} = t_2 + 2\,\mathrm{s}$, then decreases to stabilise at a slightly smaller value until $t_{\mathrm{cut}} = t_2 + 3\,\mathrm{s}$. Short after that, the fitting of the data with expression (4.53), containing two exponentials, does not converge any more, probably because too much data has been omitted to resolve the shorter time component and determine its parameters. The variations of $\Delta\Omega_p^\infty$ even during the "stable" phase shows the sensitivity of our fit to the choice of data range: even the removal of one data point affects the result, which reflects the inherent noise in

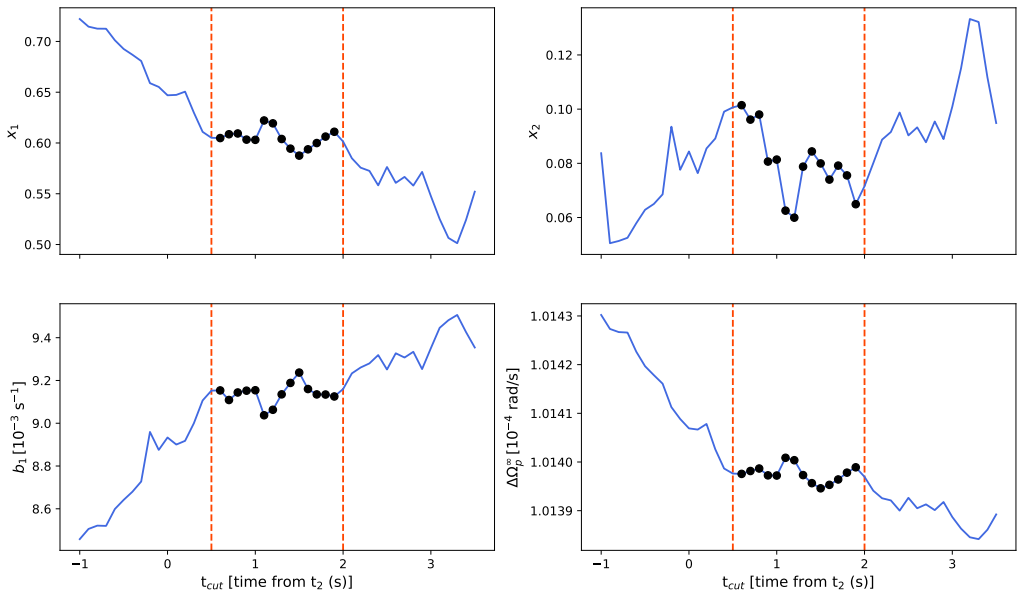

Figure 4.1: Result of the fit for the parameters x_1, x_2, b_1, and $\Delta\Omega_p^\infty$ as a function of $t_{\rm cut}$, the time (measured with respect to t_2) before which we neglect the data. We vary $t_{\rm cut}$ by steps of 0.1s, and connect the results by a line for clarity. The vertical lines define the region we have chosen to evaluate the parameters; the means and standard deviations reported in Table 4.1 are taken for the values marked by black dots.

the timing residual data. We then decide to take as final result for each parameter the mean and standard deviation calculated from the values it assumes when $t_{\rm cut}$ varies in the interval $[t_2 + 0.5\,{\rm s},\ t_2 + 2\,{\rm s}]$. We have also checked that taking the mean and standard deviation in the longer interval $[t_2 + 0.5\,{\rm s},\ t_2 + 3\,{\rm s}]$ yields mean values within the previous errors and larger standard deviations. However, we prefer to adopt the smaller interval (whose data point are marked in orange in Figure 4.2), which eliminates less information about the short time component.

The fact that $\Delta\Omega_p^\infty$ "stabilises" only five pulsar revolutions after t_2 seems to indicate that shortly after Δt_m the magnetosphere recouples with the normal component. To our knowledge, no theoretical work on the decoupling and recoupling of the magnetosphere following a glitch has been performed, so that the timescale of order $\Delta t_m = 2.6$ s for the duration of this process remains, at present, only speculative. Incidentally, the recent work by Bransgrove et al. (2020) studies the response of the magnetosphere to a quake in the crust, arguing that this is the cause of the null pulse at t_0 and speculating that the quake may be the trigger of the glitch.

The results for the seven independent parameters of Equation (4.53) are reported in Table 4.1; in its lower part, we also show some dependent quantities, that can be derived from the equations in the previous section. The residuals of the glitch (see Equation (4.53)) corresponding to the parameters in the Table are shown superimposed

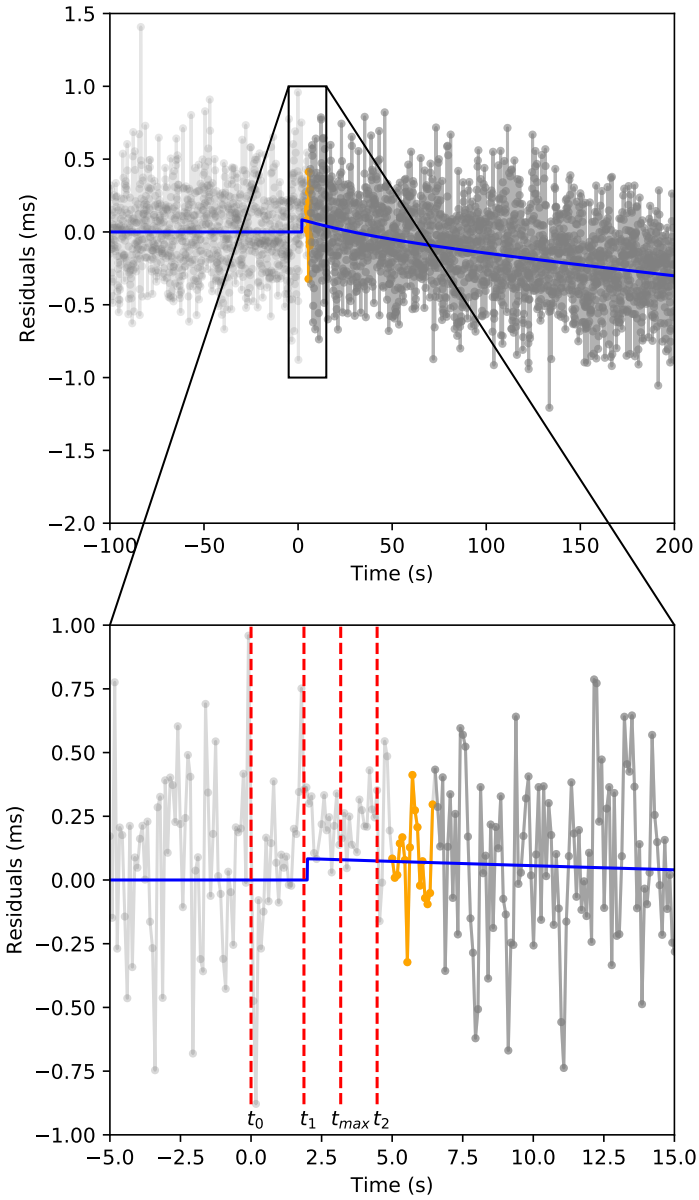

Figure 4.2: The timing residuals around the time of the glitch, as obtained in Palfreyman et al. (2018). Superimposed in blue, we plot our best fit for the residuals (Equation (4.53) with the parameters of Table 4.1). In the zoom we indicate the times t_0, t_1, t_2 defined in Palfreyman et al. (2018) and our result for $t_{\max}$. The glitch begins right after t_1. The data points are connected by a line for clarity: in light grey those always omitted from the fit, in dark grey those always included, in orange the region corresponding to the interval of t_{cut} over which we evaluate the parameters of the model, as explained in the text (see Figure 4.1).

Parameter	Value
x_1	0.60 ± 0.01
x_2	0.08 ± 0.01
b_1	$(9.24 \pm 0.84) \cdot 10^{-3}$ s^{-1}
b_2	3.92 ± 3.09 s^{-1}
$\Delta\Omega_p^\infty$	$1.014 \cdot 10^{-4}$ rad/s
r_0	0.086 ± 0.002 ms
t_g	2.0 ± 0.1 s
x_p	0.32 ± 0.02
$1/\lambda_-$	0.20 ± 0.14 s
$1/\lambda_+$	43.3 ± 2.1 s
$t_{\max}$	1.2 ± 0.7 s
$\mathcal{B}_1$	$(6.6 \pm 0.6) \cdot 10^{-5}$
$\mathcal{B}_2$	$(2.8 \pm 2.2) \cdot 10^{-2}$

Table 4.1: Results of the fit for the 7 independent parameters of Equation (4.53). The time of beginning of the glitch, t_g, is given with respect to t_0, while $t_{\max}$ is given with respect to t_g. The relative error on $\Delta\Omega_p^\infty$ is of order 10^{-5}, while the other errors are at 1σ confidence level. The second part of the table reports some dependent quantities and their propagated errors, obtained from Equations (4.9), (4.21) and (4.49) (without entrainment).

to the data in Figure 4.2. The results of Table 4.1 yield some interesting considerations. First of all, the glitch size $\Delta\Omega_p^\infty$ is the same as what obtained in Palfreyman et al. (2018) ($\Delta\Omega_p^\infty = 1.006 \cdot 10^{-4}$ rad/s) once their long-term ($\tau_d = 0.96$ day) decay term $\Delta\Omega_d = 0.008 \cdot 10^{-4}$ rad/s (absent in our model, since the data we use extend to about 34 minutes after the glitch time) has been added.

Moreover, we find a decay timescale $1/\lambda_+ = 43.3 \pm 2.1$ s, close to the shortest timescales measured in the 2000 and 2004 Vela glitches (Dodson et al., 2002, 2007) and within the errors of the value obtained in Ashton et al. (2019b). The rise time $1/\lambda_- = 0.20 \pm 0.14$ s is over two order of magnitude shorter than $1/\lambda_+$; it has quite large errors, reflecting the difficulty to resolve the short time behaviour, but it is well within the upper limit of 12.6 s determined by Ashton et al. (2019b).

The mutual friction parameters $\mathcal{B}$ can be directly compared to the constraints given by (Graber et al., 2018), namely $3 \times 10^{-5} < \mathcal{B}_{\rm core} < 10^{-4}$ for the drag between the core superfluid and the normal component, and $\mathcal{B}_{\rm cr} > 10^{-3}$ for that between the crustal superfluid and the normal component. These values possibly correspond to electron scattering off magnetised vortices in the core and Kelvon scattering in the crust, the latter parameter being poorly predicted by theory, with differences of more than one order of magnitude at higher densities between different calculations (Graber et al., 2018). If we interpret the two superfluid components of our model as the core ($i = 1$) and the crustal reservoir ($i = 2$), then the value $\mathcal{B}_1 = (6.6 \pm 0.6) \cdot 10^{-5}$ lies

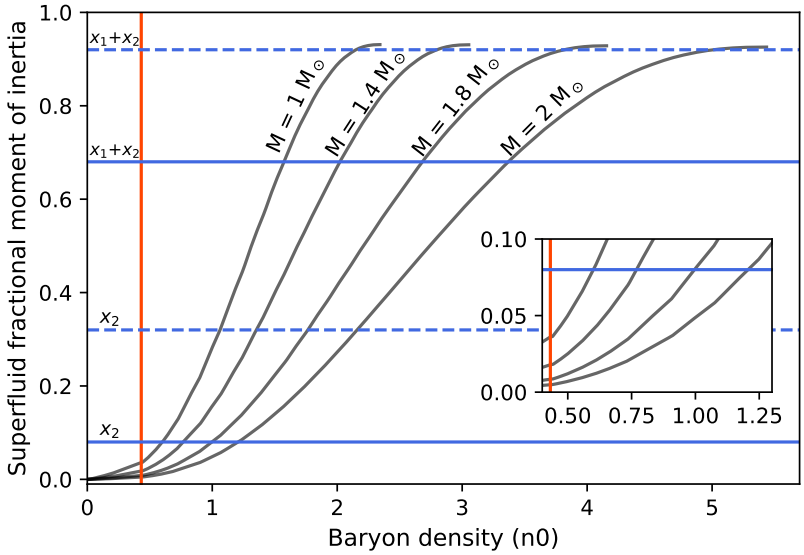

Figure 4.3: Moment of inertia fraction of the neutrons enclosed in a spherical shell extending from the radius at which the neutron drip starts to the radius corresponding to a certain baryon number density. The baryon density corresponding to the internal boundary of the shell is given in units of n_0 (nuclear saturation). The vertical line marks the core-crust transition at $0.45n_0$. The horizontal line represent x_2 and $x_1 + x_2 = 1 - x_p$ without (solid lines: $m_1^* = m_2^* = 1$) and with strong entrainment in the crust (dashed lines: $m_1^* = 1,\ m_2^* = 4$). We used the SLy4 equation of state and four reference masses: 1, 1.4, 1.8 and 2 $M_\odot$. The inset is a zoom on the outermost regions of the core.

right in the constrained interval for $\mathcal{B}_{\rm core}$; the parameter $\mathcal{B}_2$ is affected by a large error (reflecting the large uncertainty of all short time parameters, as seen in Table 4.1) but it also satisfies the lower limit on $\mathcal{B}_{\rm cr}$. Since to date calculations of the drag coefficients $\mathcal{R}_i$ are uncertain, the present model provides a simple technique to extract average values of these parameters from glitch observations, which may help to clarify the theoretical issues concerning the microphysics involved in the dissipative channels at work during a glitch. Note that the different orders of magnitude of the two coupling parameters (with $\mathcal{B}_2 \gg \mathcal{B}_1$, and so are the $b_{1,2}$ parameters) confirm the presence of a glitch overshoot.

Regarding the time when the glitch begins, t_g, our value is before what estimated in Palfreyman et al. (2018), but within their error bars. We find $t_g \approx t_1$, which supports the idea that the magnetosphere decoupling is associated to the onset of the glitch.

We finally discuss the fractional moments of inertia. In Figure 4.3 we display the partial fraction of neutrons for shells starting from the surface and going deeper into the star, using a unified nucleonic equation of state (SLy4, Douchin and Haensel, 2001) and for different values of the stellar mass. We see that the value $x_2 \approx 8\%$ implies that the reservoir cannot be limited to the crust (which contains at most 4%

of the neutron fraction for the lightest neutron star), but extends into the outer core to densities below nuclear saturation. For a standard $1.4M_\odot$ star, the intersection of the curve with the solid horizontal line representing x_2 in Figure 4.3 shows that the reservoir extends to about $0.75n_0$ (with $n_0 = 0.168\,\mathrm{fm}^{-3}$ the nuclear saturation density); this is compatible with some calculations of S-wave pairing gaps (Ho et al., 2015; Montoli et al., 2020c). We also see that $x_1 + x_2 \approx 68\%$, implies that the moment of inertia fraction associated to normal matter is $x_p \approx 32\%$. This is much more than the value predicted by equations of state without an inner core (between 5% and 10%, as shown for SLy4 by the endpoints of the curves in Figure 4.3, which give the total neutron fraction of the star, x_n, the remaining $1 - x_n$ then being the charged fraction). Therefore, our results suggest the presence of non-superfluid neutrons, a strong coupling between superfluid neutrons and superconductiong protons or an inner core of matter strongly coupled to the charged component. For each mass in Figure 4.3, the intersection of the curve with the solid horizontal line corresponding to $x_1 + x_2$ identifies the transition density to the innermost region that is rigidly coupled to the normal component. For a standard $1.4M_\odot$ star, such a core would start around $2n_0$. This is compatible with microscopic calculations, which predict the appearance of an inner core of non-nucleonic matter (hyperons, meson condensates, quarks) at densities in the range $2n_0 - 3n_0$. Other possibilities, however, can be proposed, such as strong coupling of the neutron superfluid to the proton superconductor in the inner core, due to the (still poorly known) vortex-fluxoid interaction.

Until now we have studied the fitted parameters without speaking of entrainment. Entrainment enters in the equations as discussed in Section 4.1.2, and in particular, the parameters fitted here are modified as in Equations (4.47) and (4.49). We will not employ the integrations defined in those equations, but we will simply employ a dimensionless effective mass of the neutron m_i^* in order to account for entrainment. This value is a mean value of the effective mass of the neutron, averaged over the neutron star (see Equation (4.44))

$$\frac{1}{m_i^*} = \langle 1 \rangle_i \,. \tag{4.54}$$

Within this approximation, the parameters of the three-component model become:

$$\tilde{x}_i \approx \frac{x_i}{m_i^*} \qquad (i = 1, 2) \tag{4.55}$$

$$\tilde{x}_p = 1 - \tilde{x}_1 - \tilde{x}_2 \approx x_p - (1 - m_1^*)\tilde{x}_1 - (1 - m_2^*)\tilde{x}_2 \tag{4.56}$$

$$\tilde{\mathcal{B}}_i \approx \frac{\mathcal{B}_i}{m_i^*} \qquad (i = 1, 2) \tag{4.57}$$

It follows that, in presence of entrainment, the timing solutions are still represented by Equations (4.16) and (4.53) for the glitch and its residuals, but with tilded parameters instead of untilded ones. Therefore we do not need to repeat the fit: all the results reported in Table 4.1 are still valid, but they now represent the rescaled quantities. We

Parameter	Value
x_1	0.60 ± 0.01
x_2	0.32 ± 0.04
x_p	0.08 ± 0.05
$\mathcal{B}_1$	$(6.6 \pm 0.6) \cdot 10^{-5}$
$\mathcal{B}_2$	$(1.1 \pm 0.9) \cdot 10^{-1}$

Table 4.2: Fractional moments of inertia and drag parameters obtained in the presence of strong entrainment in the reservoir ($m_1^* = 1$ and $m_2^* = 4$). The quantities and their propagated errors were obtained by rescaling the results of Table 4.1, as explained in the text.

can then go back to the physical variables using the previous relations: of course, the "observable" parameters (rise and decay timescale of the overshoot, amplitudes of the exponentials, $\Delta\Omega_p^\infty$, t_g and r_0) remain the same, while only the "internal" parameters (fractional moment of inertia and mutual friction coefficients) must be rescaled.

For example, we consider the case of no entrainment in the core component and strong entrainment in the reservoir; this is justified by some theoretical calculation, which suggest an effective mass slightly smaller than 1 in the core (Chamel and Haensel, 2006) and quite large in the crust (Chamel, 2012). In particular, we take $m_1^* = 1$ and $m_2^* = 4$, the latter being close to the average value of 4.3 (Andersson et al., 2012; Chamel, 2013), but other values could be tested: to date, the issue of strong entrainment in the crust is still open to debate (Chamel, 2012; Martin and Urban, 2016; Watanabe and Pethick, 2017; Sauls et al., 2020).

In Table 4.2 we report the physical quantities whose values are changed because of entrainment, namely the fractional moments of inertia and the mutual friction coefficients; with entrainment being confined to the crust ($i = 2$), only the values of the reservoir are affected, namely $\mathcal{B}_2 = m_2^* \tilde{\mathcal{B}}_2$ and $x_2 = m_2^* \tilde{x}_2$. In particular, the value of $\mathcal{B}_2 = (1.1 \pm 0.9) \cdot 10^{-1}$ is four times larger than before and still satisfies the constraint of Graber et al. (2018); due to the mentioned uncertainty of theoretical calculations, no strong conclusion can be drawn at this stage. As for the fractional moments of inertia, the normal component now results $x_p \approx 8\%$, in agreement with standard neutron star models without an exotic inner core (in Figure 4.3 the dashed horizontal line corresponding to $x_1 + x_2 = 1 - x_p$ is very close to the endpoints of the curves for the neutron fraction). On the other hand, now the reservoir is $x_2 \approx 32\%$, a very large fraction extending into the outer core up to densities above nuclear saturation. For a standard $1.4 M_\odot$ star, the intersection of the curve with the dashed horizontal line representing x_2 in Figure 4.3 shows that the reservoir extends to about $1.25 n_0$. This suggests strong non-crustal pinning, possibly with the pasta phase and/or the magnetic fluxoids in the superconducting core, but other mechanisms could be envisaged.

4.3 Application to the 2016 Vela glitch: Bayesian approach

We now employ again the model discussed in Section 4.1 to analyse the data obtained for the 2016 glitch of the Vela pulsar (Palfreyman et al., 2018). This time we will follow a Bayesian approach, so to find the posterior probability distribution for the phenomenological parameters of the model. Differently from Section 4.2, this time we will keep both the superfluid reservoir, namely we will use Ω^0_{1p} and Ω^0_{2p} as free parameters to be fitted.

Like in the previous Section, the presence of an increase in the timing residuals in the data has to be modelled, as this phenomenon cannot be described using the solution (4.16). To do so, this time we assume that the magnetosphere instantaneously decouples and recouples from the rotation of the crust of the star, lagging behind the actual angular velocity of the charged component. This amounts to introduce a fourth component with negligible inertia (the magnetosphere) that is always locked to the p-component apart for an instantaneous jump at $t = t_M$, namely

$$\Omega_M(t) = \Omega_p(t) - \Omega^0_p \Delta r_0 \delta(t - t_M), \tag{4.58}$$

where Δr_0 and t_M are additional phenomenological parameters that have to be fitted together with x_i, b_i, and the initial lags Ω_{ip}. Equation (4.58) is non-physical but provides a simple mathematical form for this magnetospheric slip; its impulsive character is a crude simplification of a complex dynamical problem. Hence, the modelling in (4.58) represents the minimal choice to extend the system (4.1) to take into account this additional piece of physics that is present in the data of Palfreyman et al. (2018). The residual function of the "observable component" (that now is the magnetosphere) takes the form

$$r(t) = r_p(t - t_g)\vartheta(t - t_g) + \Delta r_0 \vartheta(t - t_M), \tag{4.59}$$

where we extended the function $r_p(t - t_g)$ (Equation (4.22)) to pre-glitch times $t < t_g$ by means of the usual Heaviside step function ϑ. The quantity t_M is unknown and the magnetospheric change can happen before ($t_g > t_M$) or after ($t_g < t_M$) the glitch. Finally, the data provided by Palfreyman et al. (2018) are lacking of the uncertainty on the single measure of the residual. We estimate it from the standard deviation of all the data before t_1, as it is quite sure that before that time the star has not undergone the glitch yet. In this way, we find $\sigma = 0.25\,\mathrm{ms}$ and we assume this value to be valid also for the post-glitch measurements.

4.3.1 Bayesian modelling

Now we describe the statistical modelling used to obtain a probability distribution for the parameters involved in the model. From Equation (4.22) we have up to a maximum of six parameters: the two coupling parameters $b_{1,2}$, the two moment of inertia fractions $x_{1,2}$ and the two initial lags $\Omega^0_{1,2\,p}$. The residuals of Equation (4.22)

have to be considered with respect to the glitch date t_g, which is itself a parameter of the model. Moreover, the magnetospheric slip defined in Equation (4.58) has to be included in the model as well. In other words, the residual function $r(t)$ which describes all the pre-glitch and post-glitch data is the one in Equation (4.59). In the following, the estimate of these two date parameters, t_g and t_M, is given with respect to the glitch date t_g^P calculated in the analysis of Palfreyman et al. (2018).

We collectively call all the nine parameters of the model as

$$\mathcal{P} = \{ x_1, x_2, b_1, b_2, \Omega_{1p}^0, \Omega_{2p}^0, \Delta r_0, t_g, t_M \}. \tag{4.60}$$

The probability distribution for these parameters can be obtained as the posterior distribution of a Bayesian inference (see, e.g., MacKay, 2003),

$$P(\mathcal{P} \,|\, \mathcal{D}) = \frac{P(\mathcal{D} \,|\, \mathcal{P}) P(\mathcal{P})}{P(\mathcal{D})}, \tag{4.61}$$

where

$$\mathcal{D} = \{ (t_i, r_i) \}_{i \in \text{data}} \tag{4.62}$$

represents the data used for the fit, i.e. the time of arrival of the pulses t_i and the measured residual r_i with respect to the model of a uniform spin down. In (4.61), the functions $P(\mathcal{D} \,|\, \mathcal{P})$, $P(\mathcal{P})$ and $P(\mathcal{D})$ are the likelihood, the prior and the evidence, respectively.

Assuming that the measurement for a single pulsation is independent on the measurements of the others, we write down the likelihood as (see also Ashton et al. 2019b):

$$P(\mathcal{D} \,|\, \mathcal{P}, \sigma) = \prod_i \frac{1}{\sqrt{2\pi\sigma^2}} \exp\left(-\frac{(r(t_i) - r_i)^2}{2\sigma^2} \right), \tag{4.63}$$

where σ is the uncertainty on the single measure as calculated before. By writing the likelihood like this, however, we made a further simplification: in this way the uncertainty σ is referred only to the time residual r_i, while the same uncertainty must affect the time of arrival t_i as well, as the two quantities are dependent. In fact, an hypothetical variation of the time of arrival would generate the same variation in r_i and vice versa. Thus, the correct likelihood should be a normal distribution with variance σ^2 and set diagonally on the (t_i, r_i) space. Since the uncertainty on the measure of the TOAs is of the order of a fraction of ms, while the pulsations arrive on timescales of a tenth of a second, we neglect this correction, and use the distribution in (4.63).

We assume most of the variables to be independent from the others, so to factorise our prior for the parameters $P(\mathcal{P})$ into smaller parts. We set the probability distribution of the moment of inertia fractions x_i as a uniform distribution between 0 and 1, with the constraint that the sum is less than unity,

$$x_1, x_2 \sim \begin{cases} \text{Unif}(0,1)\ \text{Unif}(0,1) & \text{if } x_1 + x_2 < 1 \\ 0 & \text{elsewhere} \end{cases} \tag{4.64}$$

For each of the two coupling parameters b_i we choose a log-uniform distribution, as we do not know the order of magnitude of the coupling parameters and we would like to explore a wide range of orders of magnitude,

$$b_1\,[\mathrm{s}^{-1}] \sim \mathrm{LogUnif}(10^{-6}, 10^{0}) \tag{4.65}$$

$$b_2\,[\mathrm{s}^{-1}] \sim \mathrm{LogUnif}(10^{-4}, 10^{2})\,. \tag{4.66}$$

For the same reason, we choose a similar log-uniform distribution for the prior of the initial lags Ω^0_{ip}. We already made a first step to break the symmetry between the two superfluid components by setting two different priors on the two coupling parameters. By setting a prior on the initial lags with the condition that $\Omega^0_{2p} > \Omega^0_{1p}$, we unambiguously break this symmetry, implicitly asking the second superfluid component to be the one that acts as a primary angular momentum reservoir:

$$\Omega^0_{1p}, \Omega^0_{2p}\,[\mathrm{rad/s}] \sim \begin{cases} \mathrm{LogUnif}(10^{-10}, 10^{-1}) \times & \text{if } \Omega^0_{1p} < \Omega^0_{2p} \\ \quad \times \mathrm{LogUnif}(10^{-5}, 10^{-1}) & \\ 0 & \text{elsewhere} \end{cases} \tag{4.67}$$

We ask the shift on the timing residuals given by the magnetospheric change to be as broad as possible: since the pulsation of the Vela has a frequency of $\approx 10\,\mathrm{Hz}$, we set the prior on Δr_0 to be a uniform distribution between -100 ms and 100 ms. In this way, we cover a whole pulsation, which can be up to 0.1 seconds early or 0.1 seconds late,

$$\Delta r_0\,[\mathrm{ms}] \sim \mathrm{Unif}(-100, 100). \tag{4.68}$$

Finally, we set the two priors on the two dates t_g and t_M respectively to be uniform between -100 s and 100 s and between -1000 s and 100 s with respect to the glitch date t^P_g obtained by Palfreyman et al. (2018). We do not set further conditions on the relation between them. In this way, it is in principle possible to understand whether the magnetospheric change proceeded the glitch, or *vice versa* (see also Ashton et al., 2019b):

$$t_g\,[\mathrm{s}] \sim \mathrm{Unif}(\text{-}100, 100) \tag{4.69}$$

$$t_M\,[\mathrm{s}] \sim \mathrm{Unif}(\text{-}1000, 100) \tag{4.70}$$

The whole prior distribution $P(\mathcal{P})$ is the product of all these independent probability distributions, defined in Equations (4.64) to (4.70):

$$P(\mathcal{P}) = P(x_1, x_2)\,P(b_1)\,P(b_2)\,P(\Omega^0_{1p}, \Omega^0_{2p})\,P(\Delta r_0)\,P(t_g)\,P(t_M)\,. \tag{4.71}$$

4.3.2 Results of the Bayesian fit

To set the angular velocity at the time of the glitch Ω^p_0 and the angular velocity derivative $|\dot{\Omega}_\infty|$ we use the values reported in Dodson et al. (2002). The posterior distribution

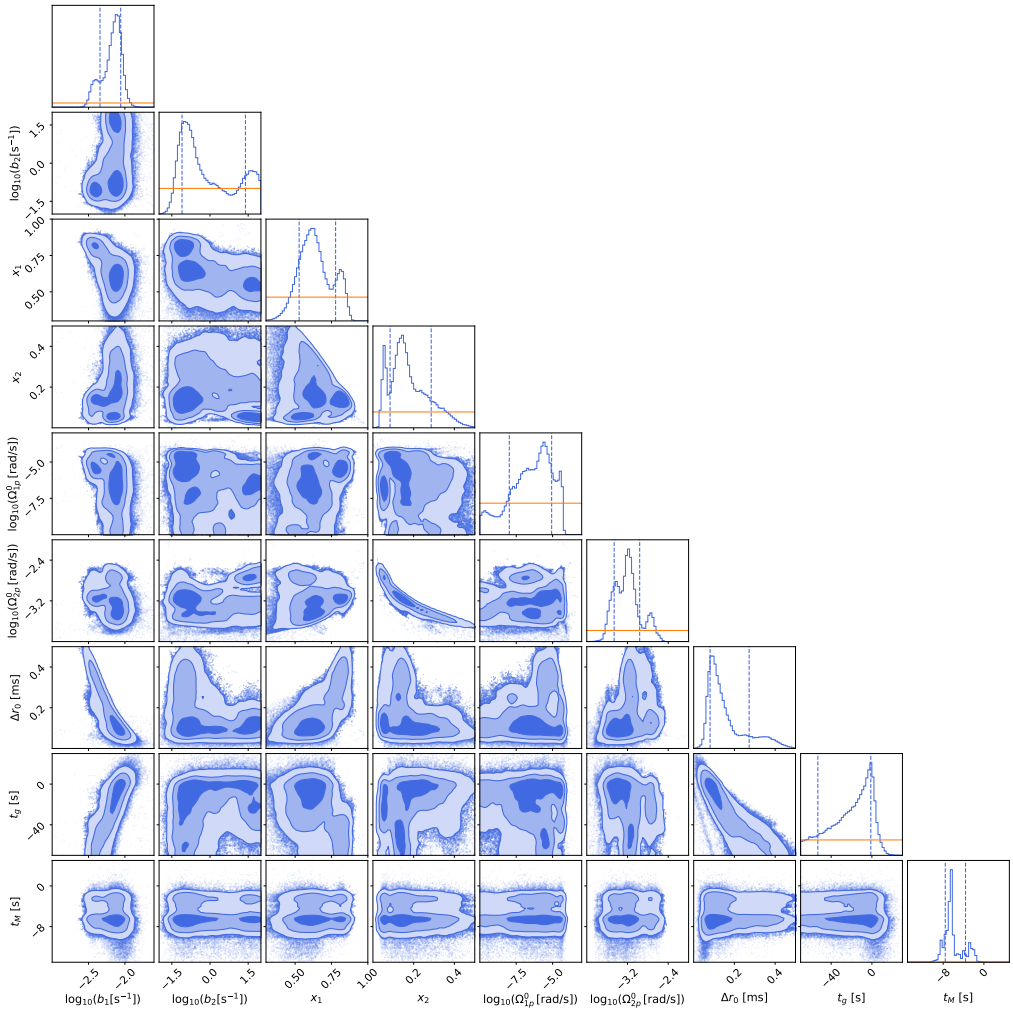

Figure 4.4: Cornerplot of the posterior distribution. On the diagonal the marginalised posterior distribution for each parameter of the model is plotted. The vertical lines represent the 16th and 84th percentiles of these distributions. The numerical values are reported in Table 4.3. The prior distribution is plotted in orange as a comparison: for the jump in the residuals Δr_0 and the magnetospheric time t_M this is almost invisible, due to the width of the distribution. The covariance plots are located off-diagonal.

for the nine parameters in (4.60) has been inferred employing the `dynesty` nested sampler (Speagle, 2020), as implemented in the `Bilby` Python package (Ashton et al., 2019a). The results for these nine parameters are shown in Figure 4.4, with the 16th, 50th and 84th percentiles for each variable reported in Table 4.3.

The posterior of the parameters t_g, t_M and Δr_0 yield some information about this particular glitch event. In Figure 4.5 we show the two distributions for the glitch time t_g and the magnetospheric change time t_M, along with some characteristic times

Variable	16th percentile	Median	84th percentile
b_1 [s^{-1}]	0.004	0.007	0.009
b_2 [s^{-1}]	0.08	0.37	24.64
x_1	0.53	0.63	0.78
x_2	0.08	0.16	0.29
Ω^0_{1p} [rad/s]	1.06e-08	5.18e-07	8.61e-06
Ω^0_{2p} [rad/s]	0.0003	0.0006	0.0011
Δr_0 [ms]	0.08	0.12	0.27
t_g [s]	-53.1	-18.2	-1.1
t_M [s]	-7.59	-6.46	-3.61

Table 4.3: 16th, 50th and 84th percentiles for the marginalised posterior for the different variables of the model. The values of b_1 and b_2 are given in units of s^{-1}, Ω^0_{1p} and Ω^0_{1p} are in rad/s, Δr_0 in ms, t_g and t_M in seconds, using the date t^P_g of Palfreyman et al. (2018) as reference time origin.

defined in Palfreyman et al. (2018): the authors detected a missing pulse at time t_0 and a persistent increase of the residuals which took place between t_1 and t_2. The glitch time t_g is not particularly well constrained in the model, yielding a broad distribution with 68% of the probability lying between the glitch time calculated in Palfreyman et al. (2018) and 53.1 seconds before it. A strong correlation is also present between the glitch time t_g and the initial residual due to the magnetospheric "slip". As we can notice from Figure 4.6, this is probably due to the fact that an anticipated glitch with a higher initial residual and a postponed glitch with a lower initial residual can fit the data equally well (see also Ashton et al. 2019b about this). A tighter prior on the glitch time would allow for a better resolution on the probability distribution for the other parameters, for example x_1, which present a correlation of one of its peaks with the glitch time (see Figure 4.4). The magnetospheric time t_M presents two clear peaks, one 6.4 s and one 2.6 s before the Palfreyman et al. (2018) glitch time. Unfortunately, the low resolution on the glitch time obtained in this model does not allow us to determine if the magnetospheric change is before or after the triggering of the glitch at t_g.

The probability distributions for the rise timescale $1/\lambda_+$, the relaxation timescale $1/\lambda_-$, the overshoot parameter ω and the asymptotic glitch size $\Delta\Omega^\infty_p$ are given in Figure 4.7. The rise time $1/\lambda_+$ is peaked close to 0 s (the limit in which the rise is practically instantaneous) and the 90% of the distribution lies within 6.02 s (cf. with Figure 2 of Ashton et al. 2019b). This is a more stringent constraint with respect to the $\sim$ 12s obtained in Ashton et al. (2019b), probably due to the different type of theoretical modelling underneath the fit: in fact, on the one hand they used a single-timescale model to fit this parameter, and on the other we used a prior based on completely different parameters (thus intrinsically different) which causes different results for the posterior distribution. The value obtained for the relaxation timescale

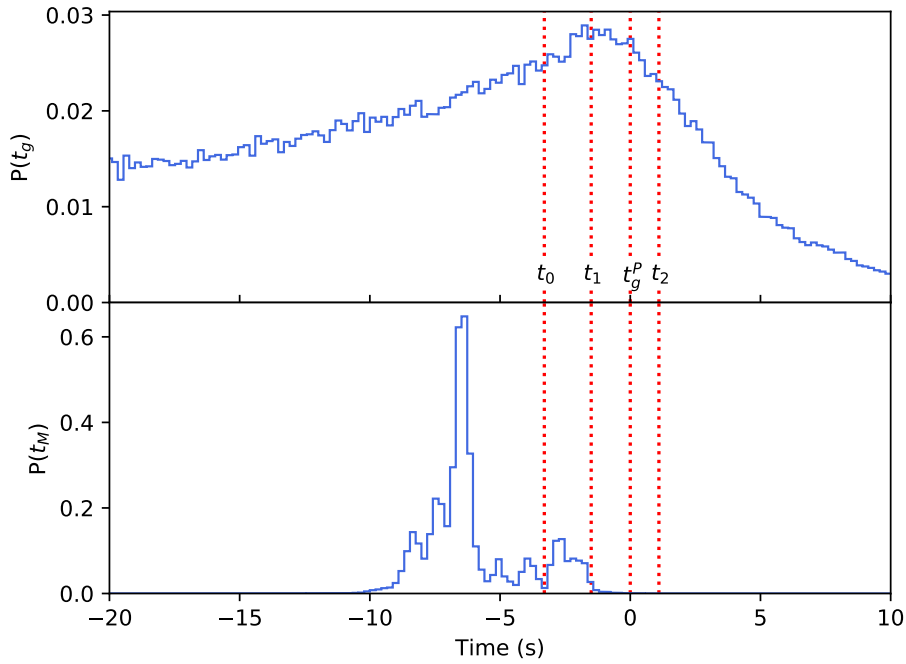

Figure 4.5: Probability distribution for the inferred glitch time t_g and the time of the magnetospheric change t_M. We also plot some characteristic times obtained in Palfreyman et al. (2018): the time of a null pulse t_0, the start and the end of the rise of the residuals t_1 and t_2, and the glitch time t_g^P as calculated in that paper.

is $1/\lambda_- = 55.07^{+15.58}_{-11.99}$ s: this value is also similar to that of previous glitches of the Vela, for example the 2000 and the 2004 glitches (Dodson et al., 2002, 2007).

Finally, the parameter ω obtained here has a value of $2.56^{+1.38}_{-0.51}$, which is a clear indication of the presence of an overshoot (Ashton et al., 2019b), and the glitch size is $1.014 \pm 0.002 \cdot 10^{-4}$ rad/s, is in good accordance with the previous estimates in Pizzochero et al. (2020) and Section 4.2.

To better compare with the results in Section 4.2, a fit has also been performed by keeping $\Omega^0_{1p} = |\dot{\Omega}_\infty|/b_1$, the value corresponding to the steady-state lag. In this way, we are asking the 1-component to be a "passive" one (a superfluid that rotates with the steady state lag does not contribute to the angular momentum reservoir, which is the scenario considered in Pizzochero et al., 2020). In this case, we have to fit eight parameters and not nine. We will not report the results here, as it yields fully compatible values for all the parameters shown in Figure 4.4. This establishes that the differences with respect to Section 4.2 are mostly due to the different fitting procedure and not to the assumption that the 1-component is at the steady state at $t = 0$ (i.e. is "passive"). Moreover, the steady-state lag for the 1-superfluid, which is of the order of $10^{-8} \div 10^{-9}$ rad/s, as calculated with the inferred values, is compatible to the results obtained here for the model with a free initial condition for Ω^0_{1p}, again indicating a

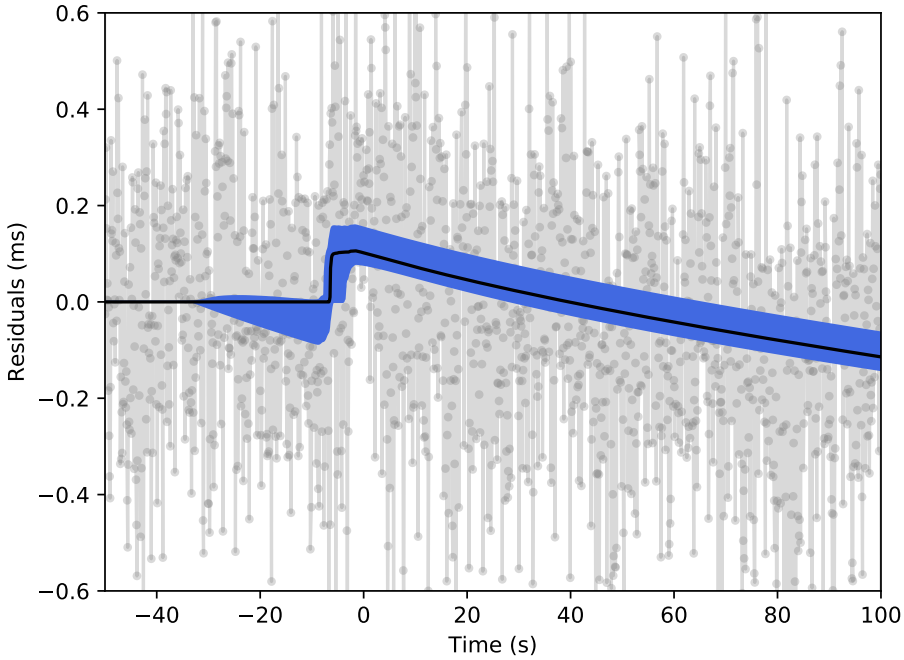

Figure 4.6: Result of the fit. We plot the data obtained by Palfreyman et al. (2018) in grey, joined by a line, and the fitted curve: the median of the probability distribution for the residual function (4.59) is plotted in black, while the blue region indicates the 16th-84th percentile zone. The reference time $t = 0$ is set to be the glitch time t_g^p calculated in Palfreyman et al. (2018).

single reservoir. Regarding the Bayes factors, the 8-parameters model with Ω_{1p}^0 fixed is only marginally preferable to that with a free initial condition, having a Bayes factor of $\ln Z \approx 1.4$, which does not allow us to claim a strong preference between the two models (Kass and Raftery, 1995).

Some more interesting considerations can be made for the other initial lag Ω_{2p}^0. The 68% of probability for this distribution lies in the range between $\approx 3 \cdot 10^{-4}$ and $\approx 1.1 \cdot 10^{-3}$ rad/s. In the years just before the glitch considered here, the Vela has undergone two glitches, as reported by the Jodrell Bank Glitch Catalogue[2] (Espinoza et al., 2011): one in 2014, which is at least three orders of magnitude smaller than the one considered here, and one in 2013, which is the largest ever achieved and of a comparable size with respect to the 2016 one. If we assume that the largest glitch has completely emptied the angular momentum reservoir (that is, the lag between the components is on average null after the glitch), and we calculate the maximum lag obtainable by the spin down of the star between the 2013 and the 2016 glitches (obtained by multiplying the inter-glitch time with the spin down rate of the star

[2] http://www.jb.man.ac.uk/pulsar/glitches.html

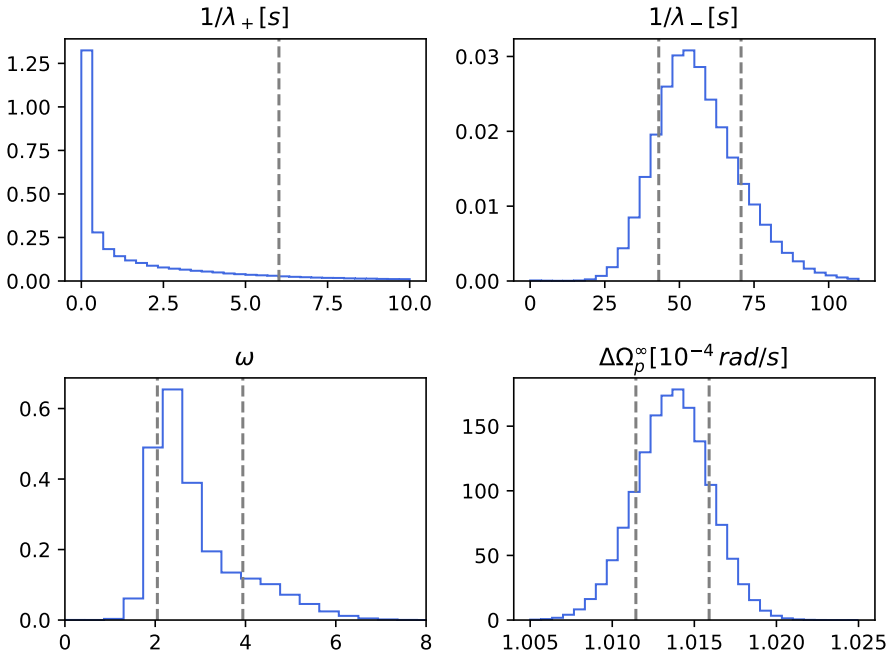

Figure 4.7: Probability distributions for the glitch rise timescale $1/\lambda_+$, the relaxation timescale $1/\lambda_-$, the overshoot parameter ω and the glitch size $\Delta\Omega_p^\infty$. For the glitch rise timescale the 90th percentile is plotted, while for the other three quantities the 16th and 84th percentiles are plotted.

measured in Dodson et al. 2002), we obtain a value of ≈ 0.01 rad/s, which is one order of magnitude larger than what obtained from the fit. This discrepancy can be interpreted in several ways: one possibility is that vortex creep is very efficient in the crust, so that only 10% of the maximum achievable lag is actually stored. We have also to consider that a small glitch occurred between these two events, lowering the amount of lag available for this last event. The presence of entrainment, which is strong in the crust of the star, is expected to make things worse, as it would lower the true lag between the components. Finally, Figure 4.4 reveals the presence of a strong correlation between the moment of inertia fraction x_2 and the lag Ω_{2p}^0: a different prior on the superfluid fraction x_2 would give a smaller value for it, thus yielding greater values of the lag.

4.3.3 Physical interpretation of the fit

We now discuss what information can be extracted from the fitted values of the phenomenological parameters x_i and b_i. As we told before, the physical interpretation of the parameters x_i and b_i is a little subtle, due to the presence of entrainment between each superfluid component and the normal component (see Section 4.1.2).

The idea to treat entertainment in a simple way is to redefine the lags between the two superfluid components and the normal one according to (4.38), so that a system like that in Equation (4.1) still holds without the need to encode additional "entrainment torques" (Antonelli and Pizzochero, 2017). The downside is that the moments of inertia fractions x_i contain a dependence on the entrainment parameter (Equation (4.47)). Similarly, also the coupling parameters b_i, when expressed as spatial averages over some internal region of the star, contain some entrainment correction (see (4.41) and (4.49)).

The coupling parameters b_1 and b_2 yield some interesting information about the phenomena which cause the interaction between the superfluid component and the normal component. For the core superfluid, it is thought that the electron scattering off magnetised vortices causes the drag between the superfluid and the normal component, and the subsequent exchange of angular momentum (Alpar et al., 1984a). For the crustal superfluid, two different phenomena may occur, whether the relative velocity between the two components is small (phonon excitation, Jones 1990) or large (Kelvin waves excitation, Jones 1992; Epstein and Baym 1992). These two phenomena are believed to yield coupling parameters with rather different orders of magnitude. If we interpret the results obtained here for b_1 and b_2 as the coupling parameters for the core and the crustal superfluid, respectively, then we are able to compare these results with the theoretical calculations done in the literature: from (4.49) it is immediate to obtain

$$\begin{aligned} \langle \mathcal{B} \rangle_{\text{crust}} &\approx \frac{\langle 1-\varepsilon_n \rangle_{\text{crust}}}{2\,\Omega_p^0}\, b_2 \;\approx\; 0.03\, b_2(\text{s}^{-1}) \\ \langle \mathcal{B} \rangle_{\text{core}} &\approx \frac{\langle 1-\varepsilon_n \rangle_{\text{core}}}{2\,\Omega_p^0}\, b_1 \;\approx\; 0.007\, b_1(\text{s}^{-1}) \end{aligned} \tag{4.72}$$

where the average values $\langle 1-\varepsilon_n \rangle_{\text{crust}} \approx 4$ and $\langle 1-\varepsilon_n \rangle_{\text{core}} \approx 1$ have been taken from Chamel (2012) and Chamel and Haensel (2006) respectively, while $\Omega_p^0 \approx 70\,\text{rad/s}$ has been employed. Using the percentile values in Table 4.3, we obtain

$$\begin{aligned} \langle \mathcal{B} \rangle_{\text{crust}} &\approx 2.4 \times 10^{-3} \div 0.7 \\ \langle \mathcal{B} \rangle_{\text{core}} &\approx 2.8 \times 10^{-5} \div 6.3 \times 10^{-5}\,. \end{aligned} \tag{4.73}$$

However, if the crustal lattice is amorphous or contains a large number of defects, only weak entrainment is expected (Sauls et al., 2020), so we may use $\langle 1-\varepsilon_n \rangle_{\text{crust}} \approx 1$ and obtain

$$\langle \mathcal{B} \rangle_{\text{crust}} \approx 5.6 \times 10^{-4} \div 0.17\,. \tag{4.74}$$

The orders of magnitude of the coupling parameters calculated here are in good agreement with the most recent theoretical calculations for both the crust (Graber et al., 2018) and the core superfluid (Andersson et al., 2006). While this is a Newtonian model, a fully relativistic model would yield values for $\langle \mathcal{B} \rangle_{\text{crust}}$ corrected by a factor of the order of ≈ 2 (Sourie et al., 2017; Gavassino et al., 2020).

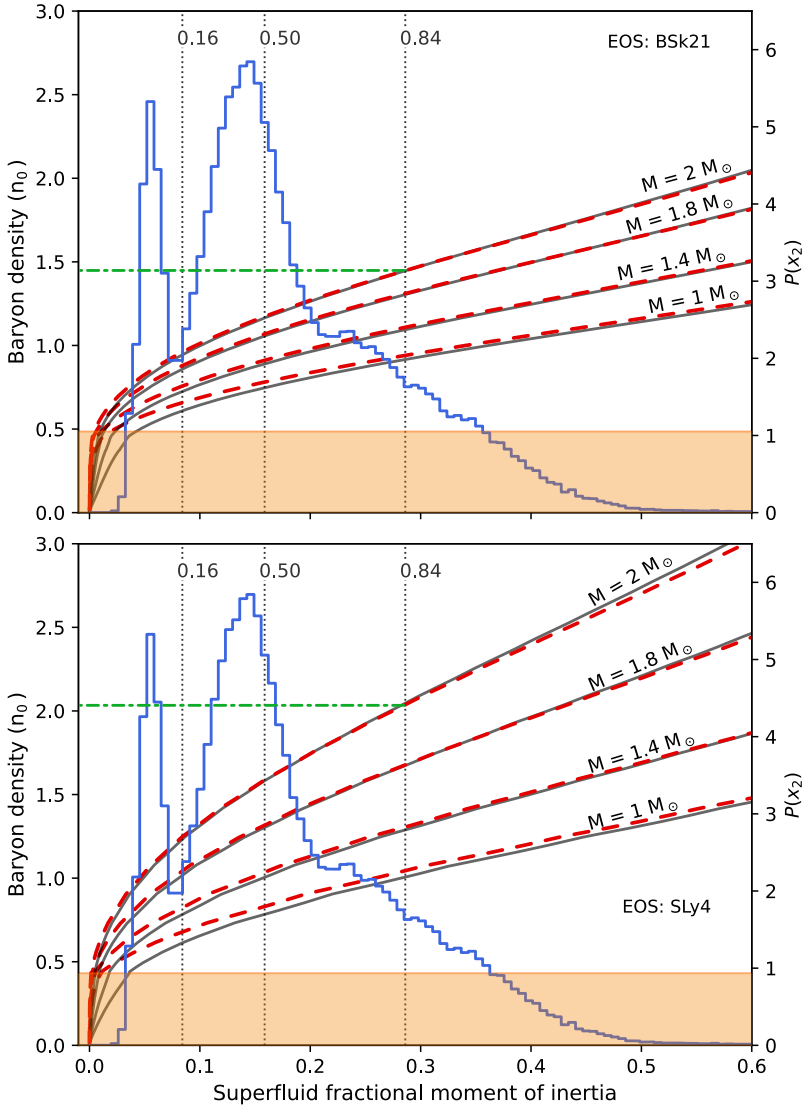

Figure 4.8: Moment of inertia fraction of the superfluid present in the spherical region (r, R) as obtained from 4.43, plotted with respect to the baryon density $n_B(r)$ (expressed in units of the nuclear saturation density n_0). The upper panel refers to the BSk21 EoS (Goriely et al., 2010), the lower one to the SLy4 EoS (Douchin and Haensel, 2001). The red-dashed curves represent the inertia fraction $I_v(r)/I$ when entrainment corrections are included (Chamel and Haensel, 2006; Chamel, 2012), the gray-solid ones represent $I_n(r)/I$ (i.e. when entrainment coupling is zero). The crustal region is depicted orange-shaded in the plot. The posterior distribution for x_2 is plotted as a background histogram, with the 16th, 50th and 84th percentiles shown with black dotted lines.

The fitted values for $x_{1,2}$ allows us to make some speculation on the spatial extension of the angular momentum reservoir. Similarly to Pizzochero et al. (2020) (Section 4.2), the results show that nearly the $x_1 \approx 60\%$ of the total moment of inertia refers to the component with a smaller initial lag (i.e. the component that before the glitch was likely to be only weakly pinned, so it did not develop a large lag). On the other hand, we find $x_2 \approx 15\%$ for the "strongly pinned" superfluid. This value is too large to be accommodated in the crust of the star alone, whatever the value of the entrainment in the crust, thus requiring that some of the reservoir superfluid should be located in the core of the star (Ho et al., 2015; Montoli et al., 2020c). This can be seen visually in Figure 4.8: here we plot the moment of inertia fraction for different masses and two different unified EoSs (SLy4 and BSk21) integrated from the neutron drip line up to different values of the baryon number density, along with the posterior distribution for x_2. We plot the cases with (red dashed lines) and without (grey solid lines) entrainment, where the coefficients ε_n for the core and the crust of the star are taken from Chamel and Haensel (2006) and Chamel (2012), respectively. Although the posterior distribution of x_2 is doubly peaked (see also Figure 4.4), even the narrower peak on the left lies outside the crustal region for both the EoS, for all the masses considered, and for the cases with and without entrainment. Moreover, this peak falls rapidly to 0 as x_2 tends to 0: due to this reason, in almost all the cases considered the value of x_2 calculated at the crust-core interface lies in regions with very small or null values of the probability density $P(x_2)$.

To check this result, we have decided to replicate the fit, but imposing that $x_1 + x_2 < 0.05$ and keeping all the priors on the other parameters untouched. In this way we limit the moment of inertia fraction to a portion that should coincide with the crust of the star: this value is an upper limit to the crustal moment of inertia when realistic equations of state and entrainment corrections are taken into account (see, e.g., Figure 2.3).

With the restriction $x_1 + x_2 < 5\%$, we obtain non-physical posteriors for some of the parameters, in particular for the glitch rise time t_g, the initial residual Δr_0 and the magnetospheric time t_M. More importantly, since the nested sampling algorithm allows to estimate the evidence of the two models (the one with $x_1 + x_2 < 1$ and the one with $x_1 + x_2 < 5\%$), the natural logarithm of the Bayes factor between the two models is ≈ 5.6 in favour to the model with $x_1 + x_2 < 1$. As claimed by Kass and Raftery (1995), a natural logarithm of a Bayes factor larger than 5 can be considered a strong evidence for a model with respect to another one. This test thus proves again the necessity of the inclusion of the superfluid in the core for the glitch process. Note that differently from the earlier results of Andersson et al. (2012) and Chamel (2013), this kind of result is independent of the presence of strong entrainment in the crust: this is because our limiting value of the 5% can easily accommodate for the moment of inertia fraction of the superfluid in the whole crust either with or without entrainment corrections.

Finally, considering the value of $x_2 \approx 0.3$ at the 84th percentile as an upper limit to $I_v(r)/I$, from Figure 4.8 we can also conclude that the region relative to this superfluid

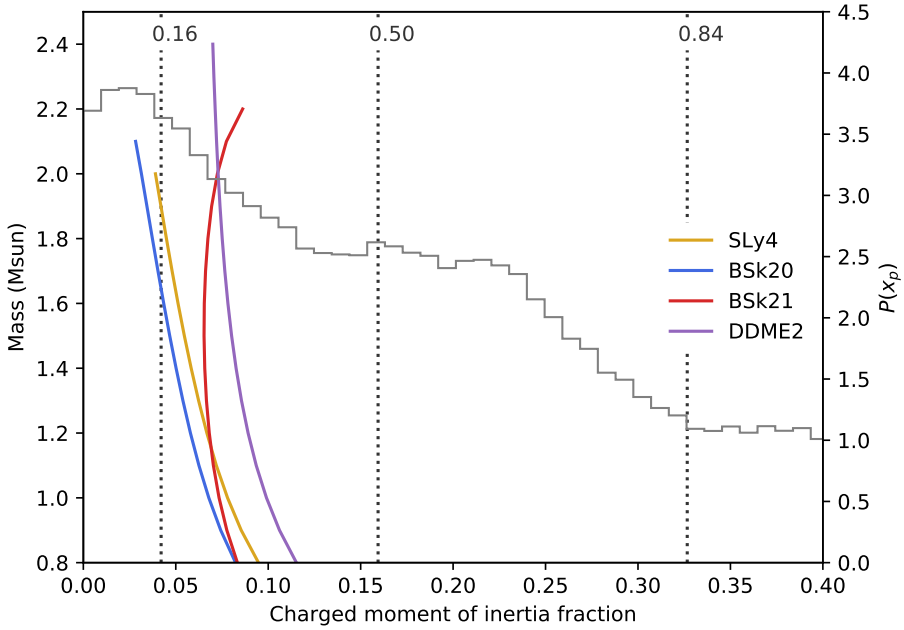

Figure 4.9: Moment of inertia fraction of the normal component, as a function of mass plotted for some EoSs. We also plot the probability distribution for this parameter (grey histogram), as obtained as a fit from the 2016 Vela glitch. Some percentiles of this distribution are also plotted (vertical dashed lines).

component is the one extending from the drip point to $n_B \approx 1.5 n_0$ at most (for the BSk21 EoS and a star of $2M_\odot$, as indicated by the horizontal dash-dotted line in the upper panel). Similarly we obtain that the region corresponding to the 2-component extends at most up to $n_B \approx 2n_0$ if the SLy4 EoS is used.

We have to stress that the moment of inertia fractions for the two superfluid components do not necessarily correspond to crust and core superfluid, as the three-component model is sufficiently flexible to assume any location for the superfluid components (as, for example, two superfluid components in the core of the star, see Sourie and Chamel, 2020). It is more clear, however, what is the normal component of the star: this comprises all the charged particles, along with all the neutrons which are not superfluid. Some uncertainties regarding the triplet pairing gap make the amount of non-superfluid neutrons difficult to calculate: given this uncertainty, all we can do is just, once fixed the star's mass and EoS, to calculate the moment of inertia of the charged particles, as all the EoSs provide the composition of the nuclear matter as a function of its density. We plot in Figure 4.9 the result of the fit for the moment of inertia fraction of the normal component, along with the same quantity calculated as a function of mass for different EoSs. The probability distribution is rather broad, but we have to notice that all the equations of state considered in the Figure are well within the median of the distribution (around $x_p \approx 15\%$). However, we do not expect this

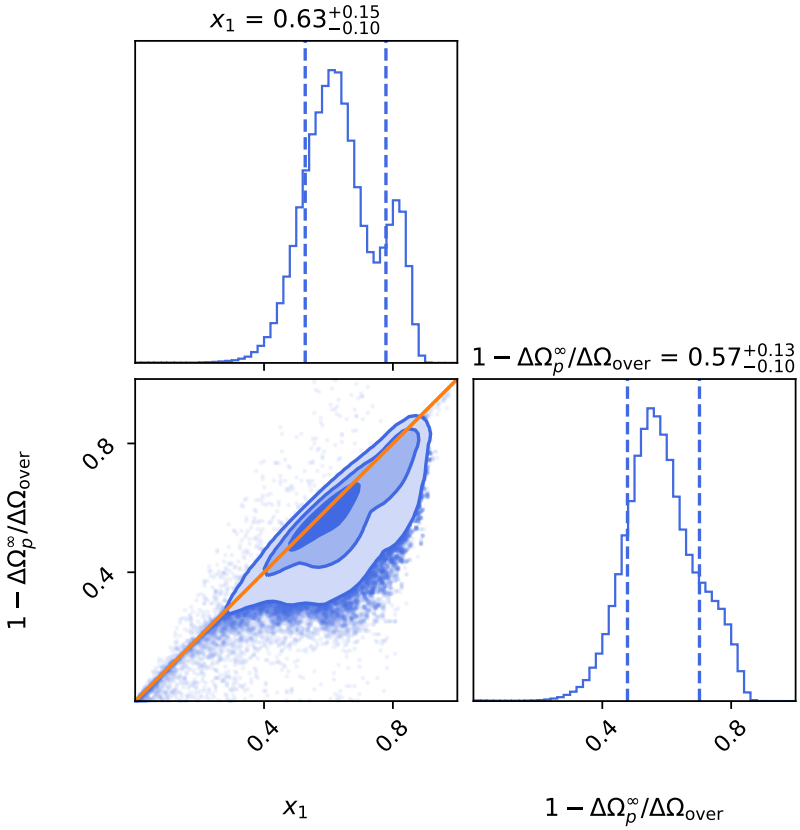

Figure 4.10: Constraint obtained in Sourie and Chamel (2020) (in orange), plotted with the probability distribution obtained in Montoli et al. (2020b).

quantity to vary much from one Vela glitch to another, so we can cross the information obtained from many future glitches in order to narrow it – by using the posterior distribution of x_p as a prior for future observations – and put a tighter constraint on the EoS composition.

Finally, we would like to test the validity of the Sourie and Chamel (2020) constraint on the weakly coupled component (i.e. Equation (4.36)). The glitch jump $\Delta\Omega_p^\infty$ and the overshoot angular velocity $\Delta\Omega_{\rm over}$ can be obtained by fitting the data and extracting the phenomenological parameters (Ashton et al., 2019b). By employing the posterior distribution obtained in this Section and Equations (4.19) and (4.24), it possible to study the constraint directly from the "physical" parameters (Figure 4.10). We can notice that the median of the probability distribution of x_1 is larger than that of $1-\Delta\Omega_p^\infty/\Delta\Omega_{\rm over}$, as expected. More information can be extracted from the covariance plot: we can see that most of the plot lies on the region below the diagonal, thus respecting the constraint described above. This is a direct consequence that in the 2016 Vela glitch the two coupling parameters have values different by orders of magnitude.

Future directions

In this thesis we have discussed different ways to constrain the internal structure of a neutron star by employing different characteristics of its glitching behaviour.

First of all, we talked about the largest glitch observed in a pulsar. It is possible to calculate the maximum amount of angular momentum storable in a star as a function of the mass, the EoS and the pinning force density profile. If we fix the last two quantities, we can calculate the largest glitch achievable by a stellar model as a function of the mass, and the comparison with the largest observed glitch in a pulsar can provide a strong upper limit on the mass of that star (Antonelli and Pizzochero, 2017; Pizzochero et al., 2017; Antonelli et al., 2018). This constraint can always improve in the future: the observation of a new largest glitch in a particular object lowers its mass upper limit (see, e.g., the case of the Crab pulsar, Shaw et al., 2018). We note that the maximum glitch achievable is not dependent on the extensions of the vortices in the core of the star, as long as we assume crustal pinning. Moreover, there is a weak dependence on the vortex tension (i.e. if the vortices are rigid or completely tensionless), which completely disappears in the Newtonian context. Finally, a small correction on the mass constraints (of about some percent) is present if General Relativity is enforced. Of course, this constraint is dependent on the EoS and pinning force we have chosen as inputs. It is interesting to notice, however, that the observation of a large glitch in a star whose mass has been previously measured can put interesting constraints on these two microphysical inputs, by comparing the inferred upper limit with the measured mass. Unfortunately, the possibilities of measuring the mass of a glitching pulsar are low, since glitchers are not usually in binary systems and, on the other hand, pulsars in binary systems are generally old and with low spin-down rates.

Secondly, we discussed about the activity parameter. This quantity should describe the average acceleration of a pulsar because of glitches and, unlike the largest observed glitch, it requires some modelling to be calculated. Since this parameter is usually viewed as an intrinsic characteristic of a glitching pulsar, and since we are able to observe only a small time interval of its life, it has to be inferred in some way. For some pulsars the activity parameter seems to have converged, namely it does not

change much by adding new glitches. In any case, it is important to develop a correct methodology to extract activity from glitch history. In many works the activity has been calculated as a linear fit to the cumulative glitch history of a pulsar (Wong et al., 2001). This way of calculating it, however, assumes a strong correlation between glitch sizes and waiting times between them, which is not observed in almost all the most glitching objects (Melatos et al., 2018). We proposed a different way to calculate this quantity, by employing a bootstrap method (Montoli et al., 2020a): the main result is that the uncertainty on the activity parameter calculated in this way is much larger than that evaluated with the linear fit. In other words, the assumption of a correlation between glitch sizes and waiting times underestimates the uncertainty on the activity parameter. This underestimation can also be seen by comparing the activity calculated glitch by glitch, and observing how its variance is much larger than the uncertainty provided by the linear fit. While the maximum glitch amplitude is related to the maximum pinning force, as it is necessary to find the maximum reservoir of angular momentum storable in a star, the activity parameter is strongly related to entrainment, as this phenomenon affects the motion of the superfluid and, as a consequence, how fast the superfluid reservoir replenishes. We then showed an alternative way to obtain the classic constraint of Link et al. (1999), in a general relativistic slow-rotation framework. The result is the same as in Andersson et al. (2012) and Chamel (2013): the combination of a crust-limited superfluid participating in the glitch, the entrainment parameter calculated in Chamel (2012) and the measured activity yield a constraint on the moment of inertia for the neutron superfluid which requires exceptionally low masses for the pulsars, especially for high-activity pulsars like the Vela. Marginally better results are obtained if one employs the new uncertainty calculated with the bootstrap method. A similar conclusion can be reached with a different model, which includes the information provided by both the activity parameter and the largest observed glitch (see Montoli et al., 2020c): also in this improved upper limit on the mass (with respect to the one obtained with the largest glitch), pulsars with crust-limited reservoir have too small masses. Things become better when some superfluid in the core of the star is included in the reservoir. It is not necessary to include the whole core superfluid, as including the superfluid at densities larger than the saturation density does not modify the results. It is then possible to statistically compare the mass distribution extracted with this method (assuming the upper limits to be the actual mass of the star) with the distribution of the masses measured in binary systems, in order to see if these two distributions are compatible. It seems there is some compatibility, especially between soft EoSs (like BSk20) and the complete sample of measured masses (thus, even with the inclusion of non-birth-mass stars), but with a superfluid reservoir extended outside the crust. This method can also be used the other way around: if enough pulsars are eligible for this kind of constraint, then it is possible to perform a comparison with the distribution of masses, yielding constraints on the microphysical inputs of the models (i.e. maximum pinning, entrainment and density of cutoff for the neutron star superfluid). Of course, this is possible if we assume that both the isolated glitching pulsar and the binary neutron stars for which a

mass measurement has been performed come from the same underlying distribution. From the observational point of view, nothing much can be done in order to resolve the activity issue, if not that of continuously monitoring stars to observe more glitches when they occur. However, we do not expect pulsar activity to change much, especially for stars like Vela, where the activity is well measured. It is more likely that the problem of the activity constraint can be solved only in a theoretical way, understanding where the superfluid participating in the glitch resides and how strong the entrainment in the crust actually is (Sauls et al., 2020).

Finally, the most promising way for constraining neutron stars using glitches is arguably that of catching them in the act. The development of a simple phenomenological model, based on the only assumption of angular momentum conservation and rigid rotation (Pizzochero et al., 2020), and its application for studying the 2016 Vela glitch (Palfreyman et al., 2018) has produced a string of interesting results (Montoli et al., 2020b). Using Bayesian methodologies, it has been possible to infer the presence of a glitch overshoot, and the probability distribution for the moment of inertia of the superfluid components, the coupling timescales between superfluid and normal components and the initial lags. All this has been possible with a single glitch: distributions are quite broad, but some information has been obtained. If the instrumental error can be reduced further, more information can be extracted, with more precision. The presence of an increase in the timing residuals is an intriguing feature of the data: one interesting question would be if this characteristic is a particular feature of the 2016 Vela glitch or a more general one that occurs frequently in glitching pulsars. In the latter case, we would need a more careful modelling of the magnetospheric term we showed, as in that case an involvement of the magnetosphere in the glitch phenomenon is likely. In any case, we have to stress the importance of a Bayesian approach to this problem: a series of glitches from the same pulsar would surely require different initial lags, and probably also different moment of inertia for the superfluid fractions, as the regions of the star involved in the glitch can be different from one glitch to another. What is not expected to change from glitch to glitch is the moment of inertia of the charged component. We can thus use the inferred posterior distribution for this quantity after a glitch as the prior distribution for the inference in a subsequent glitch. In this way it is possible to constrain the phenomenological parameters of the model even more than it would have been possible after a single glitch. The probability distribution of the moment of inertia fraction for the charged component can be an interesting constrain for the EoS of nuclear matter. In fact, the moment of inertia fraction of the charged component is somewhat constant as a function of the mass of the star (see Figure 4.9). If the probability distribution is narrow enough, its information can be crossed with the constraints given in other ways, like that of the largest glitch and it is possible to fix some characteristics of the EoS. About the moment of inertia fraction of the two superfluid components, the model is sufficiently agnostic to allow the two superfluid components to be divided in the core and in the crust of the star, or both in the core (as assumed by Sourie and Chamel, 2020). It is interesting to notice, however, that most of the probability distribution

for both the superfluid component's moments of inertia predicts values that are too large to be accommodated in the crust of the star, even in the absence of entrainment. Moreover, it has been shown that the evidence for both the superfluid to be contained in the crust is low: it is statistically unlikely that all the superfluid involved in the glitch is contained in the crust of the neutron star. This is a stronger result with respect to that obtained with the activity parameter, as here the result is independent of the presence of entrainment. The initial lag for the "reservoir" component is predicted to be around the 10% of the expected lag if perfect pinning between two glitches is assumed: this can be a hint of the presence of vortex creep inside the star, or the fact that even in large glitches a small part of angular momentum reservoir is exploited. Finally, the fit on the Vela glitch has constrained the coupling parameters between the two superfluid components and the normal component. The estimates from the 2016 Vela glitch are in full accordance with the theoretical estimation for the coupling parameters in both the crust and the core of the star. We do not expect these values to be constant between different glitches, as they are coupling parameters averaged by means of the superfluid moment of inertia fractions. However, different glitches can at least confirm the order of magnitude of these parameters, and give us an idea of the physical phenomenon behind these quantities. Given the amount of information we extracted from a single glitch, it is thus clear that it is necessary to observe many more glitches "in the act" in order to obtain much more stringent constraints on the neutron star structure.

Appendices

Appendix A

Moments of inertia in the slow rotation approximation

Neutron stars are extremely compact objects, needing a general relativistic description. Among the many corrections which can be made on the structure of neutron stars, we cite the general relativistic hydrostatic equilibrium, which is described by the TOV equation, and the correction on the moment of inertia of the star. One of the most popular prescription for calculating this quantity is the slow rotation approximation, which assumes the star to be rigidly and slowly rotating in an axisymmetric spacetime. In this Appendix, we will rapidly review how to derive the TOV equation for hydrostatic equilibrium, and we will tackle the problem of calculating the dragging of the inertial frames due to the rotation of the star and its moment of inertia in the slow rotation approximation. In the following, we will use the Einstein notation, for which the summation over repeated indices is implicit. Moreover, we will use the "MTW" (Misner et al., 1973) notation: spatiotemporal coordinates will be denoted with Greek letters, while purely spatial coordinates will be denoted with Latin ones.

In the general relativistic framework, the presence of a massive and compact object curves the spacetime. The distance between two points on a curved spacetime is described by a metric:

$$\mathrm{d}s^2 = -c^2\mathrm{d}\tau^2 = g_{\mu\nu}\mathrm{d}x^\mu \mathrm{d}x^\nu, \tag{A.1}$$

where $g_{\mu\nu}$ denotes the components of the metric tensor[1] and τ is the proper time. The amount of spacetime's curvature is described by the Einstein field equations:

$$G_{\mu\nu} = \frac{8\pi G}{c^4} T_{\mu\nu}, \tag{A.2}$$

where $G_{\mu\nu}$ is the Einstein tensor, which expresses the curvature of the spacetime and can be obtained directly from the metric tensor once a connection is defined, and $T_{\mu\nu}$

[1] Metrics will be written with the "mostly plus" signature $(-+++)$. We will try to keep the constants c and G.

is the stress-energy tensor, which describes the properties of the body which generates the curvature.

In the case of a spherically symmetric star, it can be demonstrated that, if we assume the star to be static (i.e. $\partial_t g_{\mu\nu} = 0$) the metric inside the star can be written as (see, e.g., Haensel et al., 2007):

$$\mathrm{d}s^2 = -e^{2\Phi(r)}c^2\mathrm{d}t^2 + e^{2\Lambda(r)}\mathrm{d}r^2 + r^2(\mathrm{d}\vartheta^2 + \sin^2\vartheta\mathrm{d}\varphi^2), \tag{A.3}$$

where (r, ϑ, φ) denotes the spherical coordinates, with ϑ the polar angle and φ the azimuthal one, and $\Phi(r)$ and $\Lambda(r)$ are two metric functions. Note that this metric is a generalisation in the matter of the famous Schwarzschild metric in the vacuum, which describes the spacetime outside the event horizon of a black hole. Let us assume the star to be comprised of a perfect fluid, which is a fluid in which the shear stress, viscosity and energy transport are negligible on the hydrodynamical timescale. It can be described by a stress-energy tensor of the form:

$$T^{\mu\nu} = \left(\rho + \frac{P}{c^2}\right)u^\mu u^\nu + P g^{\mu\nu}, \tag{A.4}$$

where $u^\mu = \mathrm{d}x^\mu/\mathrm{d}\tau$ is the fluid four-velocity, P its pressure and ρ its mass density in the fluid rest frame. We stress the fact that ρ is not the rest mass density, but the mass-energy density. Thus, this value is not simply $\rho = mn$, where m is the mass of a particle of fluid and n the particle number density. Since we are considering a static star, every fluid element is at rest in the static coordinate system: the worldlines are lines of constant r, ϑ and φ. Then, the only non-null component of the fluid four-velocity is the temporal one:

$$u = e^{-\Phi}\partial_t.$$

Our aim now is that of finding the quantities that describe the star, which are $\rho(r)$, $P(r)$, $n(r)$ and the two metric functions $\Phi(r)$ and $\Lambda(r)$. These functions can be calculated by using the Einstein equation (A.2), and an equation for the conservation of the stress-energy tensor (continuity equation):

$$\nabla_\nu T^{\mu\nu} = T^{\mu\nu}{}_{;\nu} = 0\,, \tag{A.5}$$

where ∇_ν or the semicolon "; ν" notation indicate covariant differentiation with respect to the ν component. From these two tensor equations, we can derive the system of equations describing the internal structure of the star:

$$\begin{cases} \Lambda(r) = -\dfrac{1}{2}\ln\left(1 - \dfrac{2Gm(r)}{rc^2}\right) \\ \dfrac{\mathrm{d}P}{\mathrm{d}r} = -\dfrac{G(\rho(r) + P(r)/c^2)(m(r) + 4\pi r^3 P(r)/c^2)}{r(r - 2Gm(r)/c^2)} \\ \dfrac{\mathrm{d}\Phi}{\mathrm{d}r} = \dfrac{G}{c^2}\dfrac{m(r) + 4\pi r^3 P(r)/c^2}{r(r - 2Gm(r)/c^2)} \\ \dfrac{\mathrm{d}m}{\mathrm{d}r} = 4\pi r^2\rho(r) \end{cases} \tag{A.6}$$

where $m(r)$ represents the mass-energy included in a radius r. In particular, we have to notice that the value $M \equiv m(r = R)$, where R denotes the star radius, is the mass we measure at infinite distance. We can spot in the system the TOV equation (Tolman, 1939; Oppenheimer and Volkoff, 1939). Now we have six unknown quantity and four equations. The other two equations that close the system constitute the EoS:

$$P = P(n) \qquad \text{and} \qquad \rho = \rho(n).$$

The most general form of an EoS is a couple of equations in the form $P = P(n, s)$ and $\rho = \rho(n, s)$, where s is the specific entropy. Nevertheless, a neutron star can be considered a "cold" object, in a sense that the internal temperature can be considered null, since the thermal energy is much smaller than the Fermi one. Therefore, s is usually fixed to 0. EoSs with this characteristic are called "one parameter" EoSs.

The boundary conditions for the system are readily expressed as:

$$\begin{cases} m(r=0) = 0 \\ \rho(r=0) = \rho_c \\ P(r=R) = 0 \\ \Lambda(r=R) = -\dfrac{1}{2}\ln\left(1 - \dfrac{2GM}{Rc^2}\right) \\ \Phi(r=R) = \dfrac{1}{2}\ln\left(1 - \dfrac{2GM}{Rc^2}\right) \end{cases} \tag{A.7}$$

Most of these conditions have been already discussed in the first Chapter. In particular, we stress the fact that the central mass-energy density ρ_c is not *a priori* known, so it constitutes a parameter describing a family of stars with different central density (and thus, different mass M and radius R). The boundary conditions for the two metric functions Λ and Φ can be obtained from the matching with the Schwarzschild metric in the vacuum (i.e. outside the star).

Until now, we have considered a static and spherically symmetric star. The presence of rotation, however, might flatten the star more or less depending on the star's angular velocity. Spherical symmetry is thereby broken, but we expect the star to maintain axial symmetry. The most general metric for a static axially symmetric spacetime with time-translational invariance can be demonstrated to be (see, e.g., Hartle and Sharp, 1967, §V):

$$\mathrm{d}s^2 = -e^{2\Phi(r,\vartheta)}c^2\mathrm{d}t^2 + e^{2\Lambda(r,\vartheta)}\mathrm{d}r^2 + e^{2\mu(r,\vartheta)}\left[r^2\mathrm{d}\vartheta^2 + r^2\sin^2\vartheta(\mathrm{d}\varphi - \omega(r,\vartheta)\mathrm{d}t)^2\right]. \tag{A.8}$$

In this case, the star is assumed to be static in the sense that it rotates rigidly, thus static in the corotating frame. The hypothesis of rigid rotation is important for our derivation (see below). Note that in the metric appears a new off-diagonal term $g_{t\varphi}$ and all the metric functions are now dependent on the polar angle ϑ, due to the rotational flattening and broken spherical symmetry. The metric can be led back to the

non-rotating Schwarzschild one (A.3), in the particular case of spherical symmetry (i.e. $\omega = 0$ and $\mu = 0$). Finally, the metric functions in (A.8) depend implicitly on the star's angular velocity Ω, and the metric has to be the same under a reversal of time and angular velocity: thus, ω depends only on odd powers of the angular velocity of the star Ω, while the other ones on even powers of Ω.

The metric function $\omega(r, \vartheta)$ has a quite interesting physical meaning: it is the angular velocity of the local inertial frames (see Glendenning, 2000). Let us consider a particle dropped at infinite distance from the star, on the equatorial plane of the rotation ($\vartheta = \pi/2$). If the star were not rotating, the particle would eventually fall toward the centre of the star. However, if the star were rotating, the particle would acquire an increasing angular velocity in the same direction of the star's rotation as approaching. This can be demonstrated in a simple way, starting from the geodesic equation, written for the covariant acceleration, which defines the particle's trajectory:

$$\frac{\mathrm{d}^2 x_\mu}{\mathrm{d}\tau^2} - \Gamma^\kappa_{\ \mu\nu} \frac{\mathrm{d}x_\kappa}{\mathrm{d}\tau} \frac{\mathrm{d}x^\nu}{\mathrm{d}\tau} = 0. \tag{A.9}$$

Recalling that $u^\mu = \mathrm{d}x^\mu/\mathrm{d}\tau$ and employing the explicit form of the Christoffel symbols, we can write the second term of the equation as:

$$\begin{aligned}
\Gamma^\kappa_{\ \mu\nu} u_\kappa u^\nu &= \frac{1}{2} g^{\kappa\lambda} (g_{\lambda\nu,\mu} + g_{\lambda\mu,\nu} - g_{\mu\nu,\lambda}) u_\kappa u^\nu \\
&= \frac{1}{2} (g_{\lambda\nu,\mu} + g_{\lambda\mu,\nu} - g_{\mu\nu,\lambda}) u^\lambda u^\nu \\
&= \frac{1}{2} (g_{\lambda\nu,\mu} + g_{\mu[\lambda,\nu]}) u^\lambda u^\nu ,
\end{aligned}$$

where the comma notation "$,\nu$" indicates partial differentiation with respect to the ν component and the square brackets indicate antisymmetrisation with respect to the components in between them. In the above expression we have also exploited the symmetry of the metric tensor. In particular, we can see that the second term of the left member of the equation is null, since it is the contraction of a symmetric tensor with an antisymmetric one. Thus, Equation (A.9) can be written as:

$$\frac{\mathrm{d}u_\mu}{\mathrm{d}\tau} = \frac{1}{2} g_{\lambda\nu,\mu} u^\lambda u^\nu . \tag{A.10}$$

This form of the geodesic equation can easily lead to interesting considerations: if all the components of the metric tensor are independent of some coordinate, say x^μ, then the derivative $g_{\lambda\nu,\mu}$ is null, and the covariant component u_μ of the four-velocity is constant along the particle's trajectory. In our particular case, we have that u_φ is constant along the particle's trajectory, since the metric functions are independent of φ. We can write the contravariant components of the four-velocity as:

$$\begin{aligned}
u^\varphi &= g^{\varphi\varphi} u_\varphi + g^{\varphi t} u_t \\
u^t &= g^{tt} u_t + g^{t\varphi} u_\varphi .
\end{aligned}$$

Since the particle is initially at rest, the three spatial contravariant components of the four-velocity are null. Moreover, because at infinity the metric is the flat Minkowski one, we have $g^{\varphi t} = 0$ and from the above equations we can state that also u_φ is initially null. Hence – due to the conservation of u_φ – we have $u_\varphi = 0$ along the entire trajectory. Therefore, we can write for the particle:

$$\frac{\mathrm{d}\varphi}{\mathrm{d}t} = \frac{u^\varphi}{u^t} = \frac{g^{\varphi t}}{g^{tt}}.$$

The inverse components $g^{\mu\nu}$ of the metric tensor can be obtained by inverting the part of the covariant metric tensor which is not in diagonal form:

$$\begin{pmatrix} g_{tt} & g_{t\varphi} \\ g_{\varphi t} & g_{\varphi\varphi} \end{pmatrix}.$$

It can be easily demonstrated that, in the case of $\vartheta = \pi/2$, the particle's coordinate φ varies according to (see Glendenning, 2000):

$$\frac{\mathrm{d}\varphi}{\mathrm{d}t} = \frac{-g_{\varphi t}}{g_{tt}} = \frac{-r^2 e^{2\mu(r,\pi/2)}\omega(r,\pi/2)}{-r^2 e^{2\mu(r,\pi/2)}} = \omega(r,\pi/2).$$

As we can see from the above equation, if the star is rotating, the particle does not fall toward the centre, but it is deflected in the φ direction. Moreover, since the particle is freely falling in the gravitational field of the star, it defines inertial frames, which have angular velocities ω as measured by an observer at infinity with respect to the star. Thus ω defines the dragging of the local inertial frame by the rotating star.

The problem of calculating the new metric function has been addressed in Hartle (1967). The author started from the φt component of the Einstein equation

$$G_{\varphi t} = \frac{8\pi G}{c^4} T_{\varphi t}, \tag{A.11}$$

which makes its appearance, in contrast to the spherically symmetric case, due to the presence of the off-diagonal term of the metric tensor $g_{\varphi t}$. This equation simplifies a lot if we consider the slow rotation approximation, namely:

$$\frac{R^3\Omega^2}{GM} \ll 1. \tag{A.12}$$

This approximation can be translated into the fact that we are considering the star's angular velocity to be much smaller than the Kepler one. Although a pulsar is a rapidly rotating neutron star, this approximation is quite reasonable: even if we consider the fastest observed pulsar (J1748-2446ad, with an angular velocity $\Omega = 4501$ rad s^{-1}) and assume $M = 1.4 M_\odot$ and $R = 10$ km, we obtain $R^3\Omega^2/(GM) \approx 0.11$ for this pulsar. Moreover, since we are dealing with pulsar glitches, it is interesting to evaluate this quantity for the fastest glitcher observed, the millisecond pulsar B1821-24A (also known with the J-name J1824-2452A, Cognard and Backer 2004). Only

one more millisecond pulsar has been seen glitching (J0613-0200, McKee et al. 2016) but its spinning frequency was lower. Using the same hypothesis for the neutron star's mass and radius, but this time using B1821-24A's angular velocity $\Omega = 2057.15$ rad s^{-1}, we obtain the much lower value of $R^3\Omega^2/(GM) \approx 0.023$. Therefore, while this approximation might not work well for all millisecond pulsars, it is a very good one for the glitching ones. All metric functions in (A.8) depend on even powers of Ω, except for $\omega(r)$, which depends on odd powers. Thus, at the lowest (0-th) order in Ω, the metric in Equation (A.8) reduces to the spherically symmetric one (A.3).

Using the slow rotation approximation, Equation (A.11) becomes:

$$\frac{1}{r^4}\frac{\mathrm{d}}{\mathrm{d}r}\left(r^4 j(r)\frac{\mathrm{d}\overline{\omega}}{\mathrm{d}r}\right) + \frac{4}{r}\frac{\mathrm{d}j}{\mathrm{d}r}\overline{\omega}(r) = 0, \tag{A.13}$$

where $\overline{\omega}(r)$ has been defined as

$$\overline{\omega}(r) \equiv \Omega - \omega(r) \tag{A.14}$$

and $j(r)$ is:

$$j(r) \equiv \begin{cases} e^{-(\Phi(r)+\Lambda(r))} & r < R \\ 1 & r \geq R \end{cases} \tag{A.15}$$

where $\Phi(r)$ and $\Lambda(r)$ are the metric functions of the spherically symmetric metric, as at the lowest order they are independent of Ω, and they can thereby be obtained from the system (A.6). We can note from this equation that, at the lowest order in Ω, ω does not depend on ϑ any more, but only on the radius r. The boundary conditions for this equation are readily given: since at infinity the spacetime is described by the Minkowski metric, we require that $\omega(r) \to 0$ at $r \to +\infty$. Moreover, we expect the drag of the local inertial frames to be regular at $r = 0$.

The problem described in Equation (A.13) can be divided in two parts: an external problem, from the edge of the star and beyond, which takes place in vacuum, and an internal problem, in which we have to take into account the internal structure of the star. The solutions of these two problems must be matched at the star's radius. Since for $r \geq R$ $j(r) = 1$, the external problem can be rewritten in a simple way as:

$$\frac{1}{r^4}\frac{\mathrm{d}}{\mathrm{d}r}\left(r^4\frac{\mathrm{d}\overline{\omega}}{\mathrm{d}r}\right) = 0 \tag{A.16}$$

whose solution is:

$$\overline{\omega}(r) = A - \frac{B}{3r^3},$$

where A and B are two integration constants. The value of A can be easily inferred from the boundary condition $\omega(r \to +\infty) = 0$ – or, better, from $\overline{\omega}(r \to +\infty) = \Omega$. Thus we have $A = \Omega$. The value of B can be calculated from dimensional analysis:

$$B = \frac{6GL}{c^2},$$

where L represents the total angular momentum of the star, and the choice of the factor 6 it will be clear from a comparison of the form of the relativistic moment of inertia with the Newtonian one. The external ($r \geq R$) solution therefore reads:

$$\overline{\omega}(r) = \Omega - \frac{2GL}{c^2 r^3}. \tag{A.17}$$

Let us now consider the internal problem. This is, of course, described by Equation (A.13), with the condition of a regular drag of the local inertial frames at the centre of the star. We have to notice that Equation (A.13) is linear for the multiplication of a constant: thus, if $\overline{\omega}(r)$ is a solution, $a\overline{\omega}(r)$ – with a denoting a real number – is a solution as well. We can exploit this fact and choose a fictitious boundary condition $\overline{\omega}(r=0) = 1$. The real value of $\overline{\omega}(r=0)$ can be obtained by rescaling the internal solution to match the external one. A particularly useful prescription is given in (Haensel and Proszynski, 1982). Equation (A.13) can be rewritten as:

$$\begin{cases} \dfrac{\mathrm{d}\ell}{\mathrm{d}r} = \dfrac{8\pi}{3} r^4 e^{-\Phi(r)+\Lambda(r)} \left(\rho(r) + \dfrac{P(r)}{c^2}\right) \overline{\omega}(r) \\ \dfrac{\mathrm{d}\overline{\omega}}{\mathrm{d}r} = \dfrac{6G\ell(r) e^{\Phi(r)+\Lambda(r)}}{c^2 r^4} \end{cases} \tag{A.18}$$

which can be obtained from (A.13) defining $\ell(r)$ as:

$$\ell(r) \equiv \frac{c^2 r^4}{6G e^{\Phi(r)+\Lambda(r)}} \frac{\mathrm{d}\overline{\omega}}{\mathrm{d}r}. \tag{A.19}$$

Rewriting Equation (A.13) in this form has a lot of benefits. First of all, it splits a second-order differential equation in a system of two first-order differential equations, which makes the numerical integration easier. Moreover, the value $\ell(r)$ corresponds to the angular momentum of the star included in a sphere of radius r. Since at $r = 0$ the angular momentum is null, the boundary conditions for this system are therefore given by:

$$\begin{cases} \overline{\omega}(r=0) = 1 \\ \ell(r=0) = 0 \end{cases} \tag{A.20}$$

The total angular momentum of the star can be obtained by $L = \ell(r = R)$. It is easy now to infer the relativistic moment of inertia of the star, in the approximation of slow rotation:

$$I = \frac{L}{\Omega} = \frac{8\pi}{3} \int_0^R \mathrm{d}r \; r^4 e^{-\Phi(r)+\Lambda(r)} \left(\rho(r) + \frac{P(r)}{c^2}\right) \frac{\overline{\omega}(r)}{\Omega}. \tag{A.21}$$

Let us make some considerations. First of all, in the non-relativistic limit (that is, $\Lambda(r) = 0$, $\Phi(r) = 0$, $\omega(r) = 0$ and $\rho c^2 \gg P$) the above expression reduces to the Newtonian one. Moreover, the moment of inertia in the slow rotation approximation does not depend on the value of the angular velocity Ω of the star. In fact, due to the already explained linearity of Equation (A.13), we have that the ratio $\overline{\omega}(r)/\Omega$

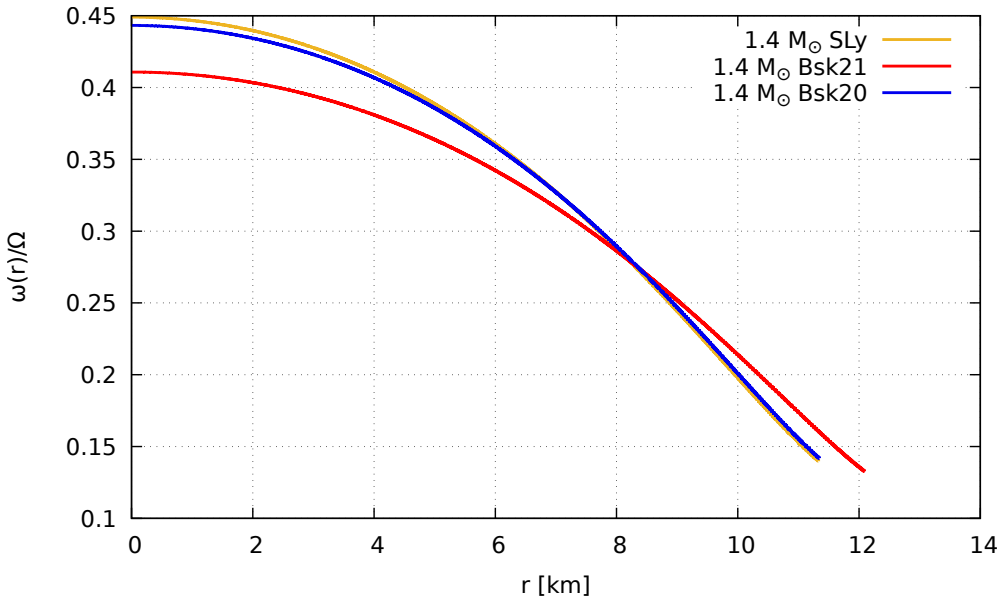

Figure A.1: Drag of the local inertial frame for a $1.4M_\odot$ star with three EoSs. Note that the softer EoSs SLy4 (Douchin and Haensel, 2001) and BSk20 – which are also more relativistic, since they are more compressible – shows a bigger drag in the central zone than the stiffer BSk21 (Goriely et al., 2010).

(or, similarly, $\omega(r)/\Omega$) depends only on the chosen EoS and central density. We have plotted on Figure A.1 the drag of the local inertial frame for three stars of different EoSs and same mass.

Finally, it is interesting to give a quick look to an alternative prescription for the relativistic moment of inertia in the slow rotation approximation. It has been noticed by Ravenhall and Pethick (1994) that for a large number of EoSs the product $j(r)\overline{\omega}(r)/\Omega$ is remarkably constant in the neutron star interior. For this reason, it seems justifiable to evaluate it at the neutron star radius R

$$j(R)\frac{\overline{\omega}(R)}{\Omega} = 1 - \frac{2GI}{c^2R^3},$$

and bring it outside the integral in (A.21). In this way, the relativistic moment of inertia can be simplified in:

$$I \simeq \frac{I_0}{1 + 2GI_0/R^3c^2}, \tag{A.22}$$

with I_0 defined by:

$$I_0 = \frac{8\pi}{3}\int_0^R \mathrm{d}r\; r^4 e^{2\Lambda(r)}\left(\rho(r) + \frac{P(r)}{c^2}\right). \tag{A.23}$$

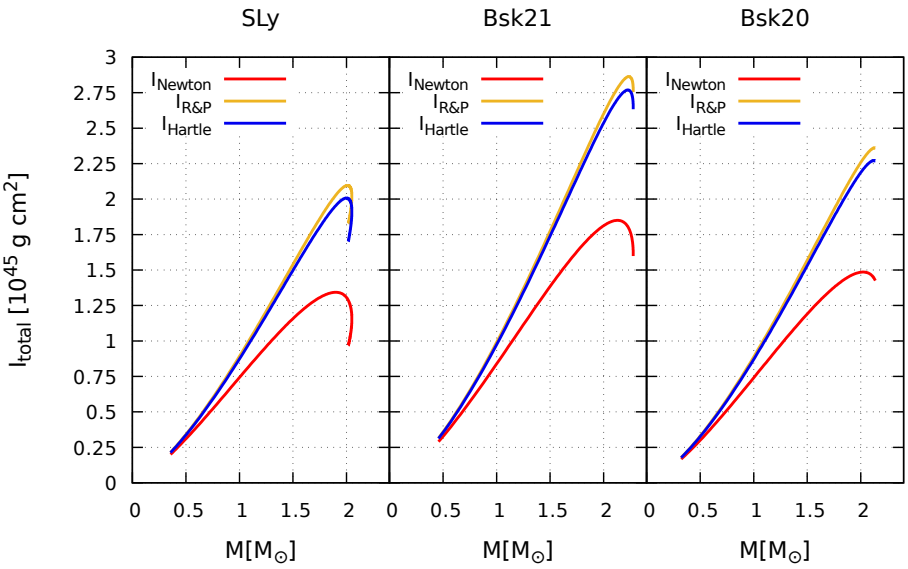

Figure A.2: Newtonian moments of inertia (red), in the Hartle approximation (blue) and in the Ravenhall and Pethick approximation (yellow) for the three EoSs SLy4, BSk21 and BSk20.

This approximation is quite important, since many papers about pulsar glitches use it. In Figure A.2 we make a comparison between the three types of moment of inertia considered: the Newtonian, that of Hartle and that of Ravenhall and Pethick. Let us make some considerations about this figure. First of all, we observe that a low mass neutron star, which also has a higher radius and thus it is less compact, has a relativistic moment of inertia similar to the Newtonian one. On the contrary, for a high mass star differences are important. This was expected, since a high mass neutron star is more compact, and thus more relativistic. Secondly, we can easily notice that the Ravenhall & Pethick prescription represents a good approximation to the more realistic Hartle one, although always a bit overestimated. Finally, with the aid of Figure A.3, we observe that if we fix the neutron star mass, a softer EoS gives a higher correction to the moment of inertia. This is expected as well, as a softer EoS produces more compact – thus, more relativistic – stars with respect to a stiffer one. Corrections to the Newtonian moments of inertia are important and rise quickly with the mass: for a typical neutron star of $1.4 M_\odot$ general relativistic corrections can modify the value of the moment of inertia of $\approx 25\%$, while high mass neutron stars obtain higher corrections, up to $50 - 55\%$.

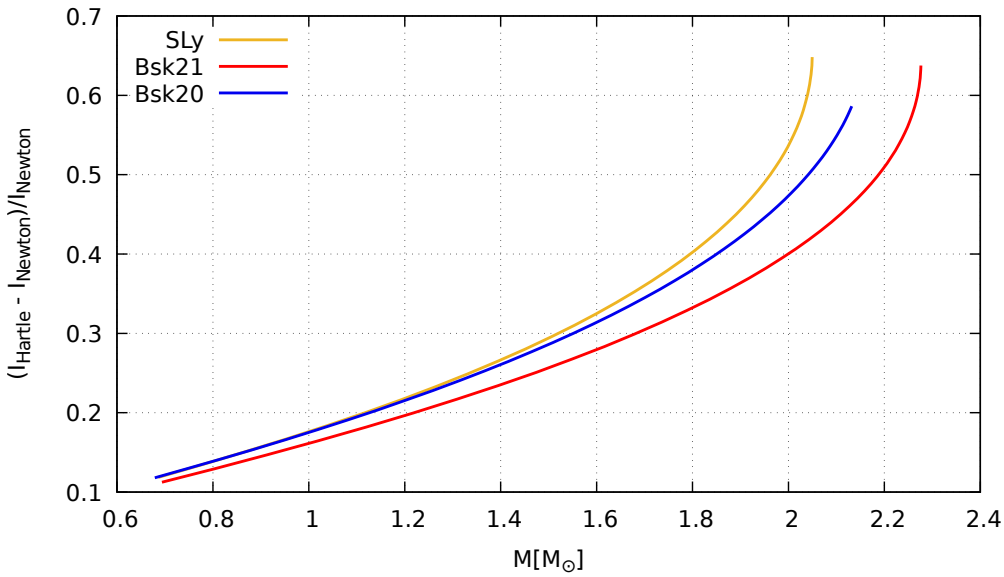

Figure A.3: Comparison between the Hartle and Newtonian moments of inertia, expressed as a fraction of I_{Newton}.

Bibliography

Abbott B.P., Abbott R., Abbott T.D., Acernese F., Ackley K., Adams C., Adams T., Addesso P., Adhikari R.X., Adya V.B., et al. "Multi-messenger observations of a binary neutron star merger". *Astrophys. J. Lett.* **848**: L12 (2017).

Akbal O., Alpar M.A. "Minimum glitch of the Crab pulsar and the crustquake as a trigger mechanism". *Mon. Not. R. Astron. Soc.* **473**: 621 (2018).

Akmal A., Pandharipande V.R., Ravenhall D.G. "Equation of state of nucleon matter and neutron star structure". *Phys. Rev. C* **58**: 1804 (1998).

Alpar M.A. "Pinning and Threading of Quantized Vortices in the Pulsar Crust Superfluid". *Astrophys. J.* **213**: 527 (1977).

Alpar M.A., Anderson P.W., Pines D., Shaham J. "Giant glitches and pinned vorticity in the VELA and other pulsars." *Astrophys. J. Lett.* **249**: L29 (1981).

Alpar M.A., Chau H.F., Cheng K.S., Pines D. "Postglitch Relaxation of the Crab Pulsar: Evidence for Crust Cracking". *Astrophys. J. Lett.* **427**: L29 (1994).

Alpar M.A., Chau H.F., Cheng K.S., Pines D. "Postglitch Relaxation of the Crab Pulsar after Its First Four Major Glitches: The Combined Effects of Crust Cracking, Formation of Vortex Depletion Region and Vortex Creep". *Astrophys. J.* **459**: 706 (1996).

Alpar M.A., Cheng A.F., Ruderman M.A., Shaham J. "A new class of radio pulsars". *Nature* **300**: 728 (1982).

Alpar M.A., Langer S.A., Sauls J.A. "Rapid postglitch spin-up of the superfluid core in pulsars." *Astrophys. J.* **282**: 533 (1984).

Alpar M.A., Pines D., Anderson P.W., Shaham J. "Vortex creep and the internal temperature of neutron stars. I - General theory". *Astrophys. J.* **276**: 325 (1984).

Alsing J., Silva H.O., Berti E. “Evidence for a maximum mass cut-off in the neutron star mass distribution and constraints on the equation of state”. *Mon. Not. R. Astron. Soc.* **478**: 1377 (2018).

Anderson P.W., Itoh N. “Pulsar glitches and restlessness as a hard superfluidity phenomenon”. *Nature* **256**: 25 (1975).

Andersson N., Comer G.L. “Slowly rotating general relativistic superfluid neutron stars”. *Classical and Quantum Gravity* **18**: 969 (2001).

Andersson N., Comer G.L., Prix R. “Are Pulsar Glitches Triggered by a Superfluid Two-Stream Instability?” *Phys. Rev. Lett.* **90**: 091101 (2003).

Andersson N., Glampedakis K., Ho W.C.G., Espinoza C.M. “Pulsar Glitches: The Crust is not Enough”. *Phys. Rev. Lett.* **109**: 241103 (2012).

Andersson N., Sidery T., Comer G.L. “Mutual friction in superfluid neutron stars”. *Mon. Not. R. Astron. Soc.* **368**: 162 (2006).

Andreev A.F., Bashkin E.P. “Three-velocity hydrodynamics of superfluid solutions”. *Soviet Journal of Experimental and Theoretical Physics* **42**: 164 (1976).

Antonelli M., Haskell B. “Superfluid vortex-mediated mutual friction in non-homogeneous neutron star interiors”. *Mon. Not. R. Astron. Soc.* **499**: 3690 (2020).

Antonelli M., Montoli A., Pizzochero P.M. “Effects of general relativity on glitch amplitudes and pulsar mass upper bounds”. *Mon. Not. R. Astron. Soc.* **475**: 5403 (2018).

Antonelli M., Pizzochero P.M. “Axially symmetric equations for differential pulsar rotation with superfluid entrainment”. *Mon. Not. R. Astron. Soc.* **464**: 721 (2017).

Antoniadis J., Freire P.C.C., Wex N., Tauris T.M., Lynch R.S., van Kerkwijk M.H., Kramer M., Bassa C., Dhillon V.S., Driebe T., Hessels J.W.T., Kaspi V.M., Kondratiev V.I., Langer N., Marsh T.R., McLaughlin M.A., Pennucci T.T., Ransom S.M., Stairs I.H., van Leeuwen J., Verbiest J.P.W., Whelan D.G. “A Massive Pulsar in a Compact Relativistic Binary”. *Science* **340**: 448 (2013).

Antoniadis J., Tauris T.M., Ozel F., Barr E., Champion D.J., Freire P.C.C. “The millisecond pulsar mass distribution: Evidence for bimodality and constraints on the maximum neutron star mass”. *arXiv e-prints* arXiv:1605.01665 (2016).

Antonopoulou D., Espinoza C.M., Kuiper L., Andersson N. “Pulsar spin-down: the glitch-dominated rotation of PSR J0537-6910”. *Mon. Not. R. Astron. Soc.* **473**: 1644 (2018).

Ashton G., Hübner M., Lasky P.D., Talbot C., Ackley K., Biscoveanu S., Chu Q., Divakarla A., Easter P.J., Goncharov B., Hernandez Vivanco F., Harms J., Lower M.E., Meadors G.D., Melchor D., Payne E., Pitkin M.D., Powell J., Sarin N., Smith R.J.E., Thrane E. "BILBY: A User-friendly Bayesian Inference Library for Gravitational-wave Astronomy". *Astrophys. J. Suppl. Ser.* **241**: 27 (2019).

Ashton G., Lasky P.D., Graber V., Palfreyman J. "Rotational evolution of the Vela pulsar during the 2016 glitch". *Nature Astronomy* page 417 (2019).

Ashton G., Prix R., Jones D.I. "Statistical characterization of pulsar glitches and their potential impact on searches for continuous gravitational waves". *Phys. Rev. D* **96**: 063004 (2017).

Audi G., Wapstra A.H. "The 1995 update to the atomic mass evaluation". *Nucl. Phys. A* **595**: 409 (1995).

Baldo M., Burgio G.F., Schulze H.J. "Hyperon stars in the Brueckner-Bethe-Goldstone theory". *Phys. Rev. C* **61**: 055801 (2000).

Bardeen J., Cooper L.N., Schrieffer J.R. "Theory of Superconductivity". *Physical Review* **108**: 1175 (1957).

Baym G., Pethick C., Pines D. "Superfluidity in Neutron Stars". *Nature* **224**: 673 (1969).

Baym G., Pethick C., Pines D., Ruderman M. "Spin Up in Neutron Stars : The Future of the Vela Pulsar". *Nature* **224**: 872 (1969).

Baym G., Pines D. "Neutron starquakes and pulsar speedup." *Annals of Physics* **66**: 816 (1971).

Bohr A., Mottelson B.R., Pines D. "Possible Analogy between the Excitation Spectra of Nuclei and Those of the Superconducting Metallic State". *Physical Review* **110**: 936 (1958).

Bombaci I. "The Hyperon Puzzle in Neutron Stars". In "Proceedings of the 12th International Conference on Hypernuclear and Strange Particle Physics (HYP2015)", page 101002. (2017).

Borgwardt K.M., Ghahramani Z. "Bayesian two-sample tests". *arXiv e-prints* arXiv:0906.4032 (2009).

Bransgrove A., Beloborodov A.M., Levin Y. "A Quake Quenching the Vela Pulsar". *Astrophys. J.* **897**: 173 (2020).

Buchner J., Georgakakis A., Nandra K., Hsu L., Rangel C., Brightman M., Merloni A., Salvato M., Donley J., Kocevski D. "X-ray spectral modelling of the AGN obscuring region in the CDFS: Bayesian model selection and catalogue". *Astron. Astrophys.* **564**: A125 (2014).

Carlin J.B., Melatos A. "Autocorrelations in pulsar glitch waiting times and sizes". *Mon. Not. R. Astron. Soc.* **488**: 4890 (2019).

Carlin J.B., Melatos A. "Generating quasi-periodic pulsar glitches using a state-dependent Poisson process". *Mon. Not. R. Astron. Soc.* **483**: 4742 (2019).

Carlin J.B., Melatos A., Vukcevic D. "Temporal clustering of rotational glitches in the Crab pulsar". *Mon. Not. R. Astron. Soc.* **482**: 3736 (2019).

Carreau T., Gulminelli F., Margueron J. "General predictions for the neutron star crustal moment of inertia". *Phys. Rev. C* **100**: 055803 (2019).

Celora T., Khomenko V., Antonelli M., Haskell B. "The effect of non-linear mutual friction on pulsar glitch sizes and rise times". *Mon. Not. R. Astron. Soc.* **496**: 5564 (2020).

Chadwick J. "Possible Existence of a Neutron". *Nature* **129**: 312 (1932).

Chamel N. "Neutron conduction in the inner crust of a neutron star in the framework of the band theory of solids". *Phys. Rev. C* **85**: 035801 (2012).

Chamel N. "Crustal Entrainment and Pulsar Glitches". *Phys. Rev. Lett.* **110**: 011101 (2013).

Chamel N. "Entrainment in Superfluid Neutron-Star Crusts: Hydrodynamic Description and Microscopic Origin". *Journal of Low Temperature Physics* **189**: 328 (2017).

Chamel N. "Superfluidity and Superconductivity in Neutron Stars". *Journal of Astrophysics and Astronomy* **38**: 43 (2017).

Chamel N., Haensel P. "Entrainment parameters in a cold superfluid neutron star core". *Phys. Rev. C* **73**: 045802 (2006).

Chamel N., Haensel P. "Physics of Neutron Star Crusts". *Living Reviews in Relativity* **11**: 10 (2008).

Chandrasekhar S. "The Maximum Mass of Ideal White Dwarfs". *Astrophys. J.* **74**: 81 (1931).

Cognard I., Backer D.C. "A Microglitch in the Millisecond Pulsar PSR B1821-24 in M28". *Astrophys. J. Lett.* **612**: L125 (2004).

Comella J.M., Craft H.D., Lovelace R.V.E., Sutton J.M. "Crab Nebula Pulsar NP 0532". *Nature* **221**: 453 (1969).

Crawford F., Demiański M. "A Comparison of Measured Crab and Vela Glitch Healing Parameters with Predictions of Neutron Star Models". *Astrophys. J.* **595**: 1052 (2003).

Cromartie H.T., Fonseca E., Ransom S.M., Demorest P.B., Arzoumanian Z., Blumer H., Brook P.R., DeCesar M.E., Dolch T., Ellis J.A., Ferdman R.D., Ferrara E.C., Garver-Daniels N., Gentile P.A., Jones M.L., Lam M.T., Lorimer D.R., Lynch R.S., McLaughlin M.A., Ng C., Nice D.J., Pennucci T.T., Spiewak R., Stairs I.H., Stovall K., Swiggum J.K., Zhu W.W. "Relativistic Shapiro delay measurements of an extremely massive millisecond pulsar". *Nature Astronomy* **4**: 72 (2020).

Datta B., Alpar M.A. "Implications of the crustal moment of inertia for neutron-star equations of state." *Astron. Astrophys.* **275**: 210 (1993).

Delsate T., Chamel N., Gürlebeck N., Fantina A.F., Pearson J.M., Ducoin C. "Giant pulsar glitches and the inertia of neutron star crusts". *Phys. Rev. D* **94**: 023008 (2016).

Demorest P.B., Pennucci T., Ransom S.M., Roberts M.S.E., Hessels J.W.T. "A two-solar-mass neutron star measured using Shapiro delay". *Nature* **467**: 1081 (2010).

Dodson R., Lewis D., McCulloch P. "Two decades of pulsar timing of Vela". *Astrophys. Space Sci.* **308**: 585 (2007).

Dodson R.G., McCulloch P.M., Lewis D.R. "High Time Resolution Observations of the January 2000 Glitch in the Vela Pulsar". *Astrophys. J. Lett.* **564**: L85 (2002).

Douchin F., Haensel P. "A unified equation of state of dense matter and neutron star structure". *Astron. Astrophys.* **380**: 151 (2001).

Drago A., Lavagno A., Pagliara G. "Can very compact and very massive neutron stars both exist?" *Phys. Rev. D* **89**: 043014 (2014).

Drago A., Lavagno A., Pagliara G., Pigato D. "The scenario of two families of compact stars. Part 1. Equations of state, mass-radius relations and binary systems". *European Physical Journal A* **52**: 40 (2016).

Drago A., Pagliara G. "The scenario of two families of compact stars. Part 2: Transition from hadronic to quark matter and explosive phenomena". *European Physical Journal A* **52**: 41 (2016).

Duncan R.C., Thompson C. "Formation of Very Strongly Magnetized Neutron Stars: Implications for Gamma-Ray Bursts". *Astrophys. J. Lett.* **392**: L9 (1992).

Easson I. "Postglitch behavior of the plasma inside neutron stars." *Astrophys. J.* **228**: 257 (1979).

Efron B. "Bootstrap methods: Another look at the jackknife". *Ann. Statist.* **7**: 1 (1979).

Epstein R.I., Baym G. "Vortex Pinning in Neutron Stars". *Astrophys. J.* **328**: 680 (1988).

Epstein R.I., Baym G. "Vortex drag and the spin-up time scale for pulsar glitches". *Astrophys. J.* **387**: 276 (1992).

Espinoza C.M., Antonopoulou D., Stappers B.W., Watts A., Lyne A.G. "Neutron star glitches have a substantial minimum size". *Mon. Not. R. Astron. Soc.* **440**: 2755 (2014).

Espinoza C.M., Lyne A.G., Stappers B.W., Kramer M. "A study of 315 glitches in the rotation of 102 pulsars". *Mon. Not. R. Astron. Soc.* **414**: 1679 (2011).

Fantina A.F., Chamel N., Pearson J.M., Goriely S. "Neutron star properties with unified equations of state of dense matter". *Astron. Astrophys.* **559**: A128 (2013).

Fasano M., Abdelsalhin T., Maselli A., Ferrari V. "Constraining the Neutron Star Equation of State Using Multiband Independent Measurements of Radii and Tidal Deformabilities". *Phys. Rev. Lett.* **123**: 141101 (2019).

Ferdman R.D., Archibald R.F., Gourgouliatos K.N., Kaspi V.M. "The Glitches and Rotational History of the Highly Energetic Young Pulsar PSR J0537-6910". *Astrophys. J.* **852**: 123 (2018).

Fernandez C., Steel M. "On bayesian modeling of fat tails and skewness". *Journal of The American Statistical Association* **93**: 359 (1998).

Feroz F., Hobson M.P., Bridges M. "MULTINEST: an efficient and robust Bayesian inference tool for cosmology and particle physics". *Mon. Not. R. Astron. Soc.* **398**: 1601 (2009).

Fonseca E., Pennucci T.T., Ellis J.A., Stairs I.H., Nice D.J., Ransom S.M., Demorest P.B., Arzoumanian Z., Crowter K., Dolch T., Ferdman R.D., Gonzalez M.E., Jones G., Jones M.L., Lam M.T., Levin L., McLaughlin M.A., Stovall K., Swiggum J.K., Zhu W. "The NANOGrav Nine-year Data Set: Mass and Geometric Measurements of Binary Millisecond Pulsars". *Astrophys. J.* **832**: 167 (2016).

Fortin M., Providência C., Raduta A.R., Gulminelli F., Zdunik J.L., Haensel P., Bejger M. "Neutron star radii and crusts: Uncertainties and unified equations of state". *Phys. Rev. C* **94**: 035804 (2016).

Franco L.M., Link B., Epstein R.I. "Quaking Neutron Stars". *Astrophys. J.* **543**: 987 (2000).

Fuentes J.R., Espinoza C.M., Reisenegger A. "Glitch time series and size distributions in eight prolific pulsars". *Astron. Astrophys.* **630**: A115 (2019).

Fuentes J.R., Espinoza C.M., Reisenegger A., Shaw B., Stappers B.W., Lyne A.G. "The glitch activity of neutron stars". *Astron. Astrophys.* **608**: A131 (2017).

Fulgenzi W., Melatos A., Hughes B.D. "Radio pulsar glitches as a state-dependent Poisson process". *Mon. Not. R. Astron. Soc.* **470**: 4307 (2017).

Gavassino L., Antonelli M., Pizzochero P.M., Haskell B. "A universal formula for the relativistic correction to the mutual friction coupling time-scale in neutron stars". *Mon. Not. R. Astron. Soc.* **494**: 3562 (2020).

Gearheart M., Newton W.G., Hooker J., Li B.A. "Upper limits on the observational effects of nuclear pasta in neutron stars". *Mon. Not. R. Astron. Soc.* **418**: 2343 (2011).

Gelman A., Carlin J., Stern H., Dunson D., Vehtari A., Rubin D. *Bayesian Data Analysis, Third Edition*. Chapman & Hall/CRC Texts in Statistical Science. Taylor & Francis (2013).

Giacconi R., Gursky H., Paolini F.R., Rossi B.B. "Evidence for x Rays From Sources Outside the Solar System". *Phys. Rev. Lett.* **9**: 439 (1962).

Giliberti E., Antonelli M., Cambiotti G., Pizzochero P.M. "Incompressible analytical models for spinning-down pulsars". *Publ. Astron. Soc. Austr.* **36**: e036 (2019).

Giliberti E., Cambiotti G., Antonelli M., Pizzochero P.M. "Modelling strains and stresses in continuously stratified rotating neutron stars". *Mon. Not. R. Astron. Soc.* **491**: 1064 (2020).

Glampedakis K., Andersson N. "Hydrodynamical Trigger Mechanism for Pulsar Glitches". *Phys. Rev. Lett.* **102**: 141101 (2009).

Glampedakis K., Andersson N., Samuelsson L. "Magnetohydrodynamics of superfluid and superconducting neutron star cores". *Mon. Not. R. Astron. Soc.* **410**: 805 (2011).

Glendenning N.K. *Compact stars : nuclear physics, particle physics, and general relativity*. Springer-Verlag New York (2000).

Glendenning N.K., Kettner C. "Possible third family of compact stars more dense than neutron stars". *Astron. Astrophys.* **353**: L9 (2000).

Gold T. "Rotating Neutron Stars as the Origin of the Pulsating Radio Sources". *Nature* **218**: 731 (1968).

Goldreich P., Julian W.H. "Pulsar Electrodynamics". *Astrophys. J.* **157**: 869 (1969).

Goriely S., Chamel N., Pearson J.M. "Further explorations of Skyrme-Hartree-Fock-Bogoliubov mass formulas. XII. Stiffness and stability of neutron-star matter". *Phys. Rev. C* **82**: 035804 (2010).

Gotthelf E.V., Halpern J.P. "Discovery of a 112 ms X-Ray Pulsar in Puppis A: Further Evidence of Neutron Stars Weakly Magnetized at Birth". *Astrophys. J. Lett.* **695**: L35 (2009).

Graber V., Cumming A., Andersson N. "Glitch Rises as a Test for Rapid Superfluid Coupling in Neutron Stars". *Astrophys. J.* **865**: 23 (2018).

Greenstein G. "Superfluid Turbulence in Neutron Stars". *Nature* **227**: 791 (1970).

Gügercinoğlu E., Alpar M.A. "The 2016 Vela glitch: a key to neutron star internal structure and dynamics". *Mon. Not. R. Astron. Soc.* **496**: 2506 (2020).

Haensel P., Potekhin A.Y., Yakovlev D.G. *Neutron Stars 1 : Equation of State and Structure* volume 326. Springer New York (2007).

Haensel P., Proszynski M. "Pion condensation in cold dense matter and neutron stars". *Astrophys. J.* **258**: 306 (1982).

Halpern J.P., Gotthelf E.V. "Spin-Down Measurement of PSR J1852+0040 in Kesteven 79: Central Compact Objects as Anti-Magnetars". *Astrophys. J.* **709**: 436 (2010).

Harding A.K. "The neutron star zoo". *Frontiers of Physics* **8**: 679 (2013).

Hartle J.B. "Slowly Rotating Relativistic Stars. I. Equations of Structure". *Astrophys. J.* **150**: 1005 (1967).

Hartle J.B., Sharp D.H. "Variational Principle for the Equilibrium of a Relativistic, Rotating Star". *Astrophys. J.* **147**: 317 (1967).

Haskell B. "The effect of superfluid hydrodynamics on pulsar glitch sizes and waiting times". *Mon. Not. R. Astron. Soc.* **461**: L77 (2016).

Haskell B., Antonopoulou D. "Glitch recoveries in radio-pulsars and magnetars". *Mon. Not. R. Astron. Soc.* **438**: L16 (2014).

Haskell B., Melatos A. "Models of pulsar glitches". *International Journal of Modern Physics D* **24**: 1530008 (2015).

Haskell B., Melatos A. "Pinned vortex hopping in a neutron star crust". *Mon. Not. R. Astron. Soc.* **461**: 2200 (2016).

Haskell B., Pizzochero P.M., Sidery T. "Modelling pulsar glitches with realistic pinning forces: a hydrodynamical approach". *Mon. Not. R. Astron. Soc.* **420**: 658 (2012).

Haskell B., Sedrakian A. "Superfluidity and Superconductivity in Neutron Stars". In L. Rezzolla, P. Pizzochero, D.I. Jones, N. Rea, I. Vidaña, editors, "The Physics and Astrophysics of Neutron Stars", volume 457 of *Astrophysics and Space Science Library* page 401. Springer (2018).

Heinke C.O., Ho W.C.G. "Direct Observation of the Cooling of the Cassiopeia A Neutron Star". *Astrophys. J. Lett.* **719**: L167 (2010).

Hewish A., Bell S.J., Pilkington J.D.H., Scott P.F., Collins R.A. "Observation of a Rapidly Pulsating Radio Source". *Nature* **217**: 709 (1968).

Ho W.C.G., Espinoza C.M., Antonopoulou D., Andersson N. "Pinning down the superfluid and measuring masses using pulsar glitches". *Science Advances* **1**: e1500578 (2015).

Ho W.C.G., Espinoza C.M., Arzoumanian Z., Enoto T., Tamba T., Antonopoulou D., Bejger M., Guillot S., Haskell B., Ray P.S. "Return of the Big Glitcher: NICERtiming and glitches of PSR J0537-6910". *Mon. Not. R. Astron. Soc.* (2020).

Hobbs G., Archibald A., Arzoumanian Z., Backer D., Bailes M., Bhat N.D.R., Burgay M., Burke-Spolaor S., Champion D., Cognard I., Coles W., Cordes J., Demorest P., Desvignes G., Ferdman R.D., Finn L., Freire P., Gonzalez M., Hessels J., Hotan A., Janssen G., Jenet F., Jessner A., Jordan C., Kaspi V., Kramer M., Kondratiev V., Lazio J., Lazaridis K., Lee K.J., Levin Y., Lommen A., Lorimer D., Lynch R., Lyne A., Manchester R., McLaughlin M., Nice D., Oslowski S., Pilia M., Possenti A., Purver M., Ransom S., Reynolds J., Sanidas S., Sarkissian J., Sesana A., Shannon R., Siemens X., Stairs I., Stappers B., Stinebring D., Theureau G., van Haasteren R., van Straten W., Verbiest J.P.W., Yardley D.R.B., You X.P. "The International Pulsar Timing Array project: using pulsars as a gravitational wave detector". *Classical and Quantum Gravity* **27**: 084013 (2010).

Hobbs G., Lyne A.G., Kramer M. "An analysis of the timing irregularities for 366 pulsars". *Mon. Not. R. Astron. Soc.* **402**: 1027 (2010).

Howitt G., Melatos A., Delaigle A. "Nonparametric Estimation of the Size and Waiting Time Distributions of Pulsar Glitches". *Astrophys. J.* **867**: 60 (2018).

Itoh N. "Hydrostatic Equilibrium of Hypothetical Quark Stars". *Progress of Theoretical Physics* **44**: 291 (1970).

Jones P.B. "Rotation of the neutron-drip superfluid in pulsars : the resistive force." *Mon. Not. R. Astron. Soc.* **243**: 257 (1990).

Jones P.B. "Rotation of the Neutron-Drip Superfluid in Pulsars: The Interaction and Pinning of Vortices". *Astrophys. J.* **373**: 208 (1991).

Jones P.B. “Rotation of the neutron-drip superfluid in pulsars - The Kelvin phonon contribution to dissipation”. *Mon. Not. R. Astron. Soc.* **257**: 501 (1992).

Kass R.E., Raftery A.E. “Bayes factors”. *Journal of the American Statistical Association* **90**: 773 (1995).

Keane E.F., McLaughlin M.A. “Rotating radio transients”. *Bulletin of the Astronomical Society of India* **39**: 333 (2011).

Khomenko V., Antonelli M., Haskell B. “Hydrodynamical instabilities in the superfluid interior of neutron stars with background flows between the components”. *Phys. Rev. D* **100**: 123002 (2019).

Khomenko V., Haskell B. “Modelling Pulsar Glitches: The Hydrodynamics of Superfluid Vortex Avalanches in Neutron Stars”. *Publ. Astron. Soc. Austr.* **35**: e020 (2018).

Kiziltan B., Kottas A., De Yoreo M., Thorsett S.E. “The Neutron Star Mass Distribution”. *Astrophys. J.* **778**: 66 (2013).

Koranda S., Stergioulas N., Friedman J.L. “Upper Limits Set by Causality on the Rotation and Mass of Uniformly Rotating Relativistic Stars”. *Astrophys. J.* **488**: 799 (1997).

Kramer M., Lyne A.G., O’Brien J.T., Jordan C.A., Lorimer D.R. “A Periodically Active Pulsar Giving Insight into Magnetospheric Physics”. *Science* **312**: 549 (2006).

Lalazissis G.A., Nikšić T., Vretenar D., Ring P. “New relativistic mean-field interaction with density-dependent meson-nucleon couplings”. *Phys. Rev. C* **71**: 024312 (2005).

Landau L.D. “On the theory of stars”. *Physik Zeitschrift Sowjetunion* **1**: 285 (1932).

Langlois D., Sedrakian D.M., Carter B. “Differential rotation of relativistic superfluid in neutron stars”. *Mon. Not. R. Astron. Soc.* **297**: 1189 (1998).

Large M.I., Vaughan A.E., Mills B.Y. “A Pulsar Supernova Association?” *Nature* **220**: 340 (1968).

Larson M.B., Link B. “Simulations of glitches in isolated pulsars”. *Mon. Not. R. Astron. Soc.* **333**: 613 (2002).

Lattimer J.M. “The Nuclear Equation of State and Neutron Star Masses”. *Annual Review of Nuclear and Particle Science* **62**: 485 (2012).

Linares M. “Super-Massive Neutron Stars and Compact Binary Millisecond Pulsars”. *arXiv e-prints* arXiv:1910.09572 (2019).

Linares M., Shahbaz T., Casares J. “Peering into the Dark Side: Magnesium Lines Establish a Massive Neutron Star in PSR J2215+5135”. *Astrophys. J.* **859**: 54 (2018).

Link B. "Dynamics of Quantum Vorticity in a Random Potential". *Phys. Rev. Lett.* **102**: 131101 (2009).

Link B., Epstein R.I., Lattimer J.M. "Pulsar Constraints on Neutron Star Structure and Equation of State". *Phys. Rev. Lett.* **83**: 3362 (1999).

Lyne A., Hobbs G., Kramer M., Stairs I., Stappers B. "Switched Magnetospheric Regulation of Pulsar Spin-Down". *Science* **329**: 408 (2010).

Lyne A.G., Jordan C.A., Graham-Smith F., Espinoza C.M., Stappers B.W., Weltevrede P. "45 years of rotation of the Crab pulsar". *Mon. Not. R. Astron. Soc.* **446**: 857 (2015).

Lyne A.G., Shemar S.L., Graham Smith F. "Statistical studies of pulsar glitches". *Mon. Not. R. Astron. Soc.* **315**: 534 (2000).

MacKay D.J.C. *Information Theory, Inference & Learning Algorithms*. Cambridge University Press (2003).

Manchester R.N., Hobbs G.B., Teoh A., Hobbs M. "The Australia Telescope National Facility Pulsar Catalogue". *AJ* **129**: 1993 (2005).

Martin N., Urban M. "Superfluid hydrodynamics in the inner crust of neutron stars". *Phys. Rev. C* **94**: 065801 (2016).

Martinez J.G., Stovall K., Freire P.C.C., Deneva J.S., Jenet F.A., McLaughlin M.A., Bagchi M., Bates S.D., Ridolfi A. "Pulsar J0453+1559: A Double Neutron Star System with a Large Mass Asymmetry". *Astrophys. J.* **812**: 143 (2015).

Mastrano A., Melatos A. "Kelvin-Helmholtz instability and circulation transfer at an isotropic-anisotropic superfluid interface in a neutron star". *Mon. Not. R. Astron. Soc.* **361**: 927 (2005).

McKee J.W., Janssen G.H., Stappers B.W., Lyne A.G., Caballero R.N., Lentati L., Desvignes G., Jessner A., Jordan C.A., Karuppusamy R., Kramer M., Cognard I., Champion D.J., Graikou E., Lazarus P., Osłowski S., Perrodin D., Shaifullah G., Tiburzi C., Verbiest J.P.W. "A glitch in the millisecond pulsar J0613-0200". *Mon. Not. R. Astron. Soc.* **461**: 2809 (2016).

McKenna J., Lyne A.G. "PSR1737-30 and period discontinuities in young pulsars". *Nature* **343**: 349 (1990).

McLaughlin M.A., Lyne A.G., Lorimer D.R., Kramer M., Faulkner A.J., Manchester R.N., Cordes J.M., Camilo F., Possenti A., Stairs I.H., Hobbs G., D'Amico N., Burgay M., O'Brien J.T. "Transient radio bursts from rotating neutron stars". *Nature* **439**: 817 (2006).

Melatos A., Howitt G., Fulgenzi W. "Size-waiting-time Correlations in Pulsar Glitches". *Astrophys. J.* **863**: 196 (2018).

Melatos A., Link B. "Pulsar timing noise from superfluid turbulence". *Mon. Not. R. Astron. Soc.* **437**: 21 (2014).

Melatos A., Peralta C. "Superfluid Turbulence and Pulsar Glitch Statistics". *Astrophys. J. Lett.* **662**: L99 (2007).

Melatos A., Peralta C., Wyithe J.S.B. "Avalanche Dynamics of Radio Pulsar Glitches". *Astrophys. J.* **672**: 1103 (2008).

Mereghetti S., Pons J.A., Melatos A. "Magnetars: Properties, Origin and Evolution". *Space Sci. Rev.* **191**: 315 (2015).

Middleditch J., Marshall F.E., Wang Q.D., Gotthelf E.V., Zhang W. "Predicting the Starquakes in PSR J0537-6910". *Astrophys. J.* **652**: 1531 (2006).

Migdal A.B. "Superfluidity and the moments of inertia of nuclei". *Nuclear Physics* **13**: 655 (1959).

Miller M.C., Lamb F.K., Dittmann A.J., Bogdanov S., Arzoumanian Z., Gendreau K.C., Guillot S., Harding A.K., Ho W.C.G., Lattimer J.M., Ludlam R.M., Mahmoodifar S., Morsink S.M., Ray P.S., Strohmayer T.E., Wood K.S., Enoto T., Foster R., Okajima T., Prigozhin G., Soong Y. "PSR J0030+0451 Mass and Radius from NICER Data and Implications for the Properties of Neutron Star Matter". *Astrophys. J. Lett.* **887**: L24 (2019).

Milner W.R., Robinson J.M., Kennedy C.J., Bothwell T., Kedar D., Matei D.G., Legero T., Sterr U., Riehle F., Leopardi H., Fortier T.M., Sherman J.A., Levine J., Yao J., Ye J., Oelker E. "Demonstration of a Timescale Based on a Stable Optical Carrier". *Phys. Rev. Lett.* **123**: 173201 (2019).

Misner C.W., Thorne K.S., Wheeler J.A. *Gravitation*. W. H. Freeman and Company (1973).

Montoli A., Antonelli M., Haskell B., Pizzochero P. "Statistical estimates of the pulsar glitch activity". *Submitted to Universe.* arXiv:2012.01539 (2020).

Montoli A., Antonelli M., Magistrelli F., Pizzochero P.M. "Bayesian estimate of the superfluid moments of inertia from the 2016 glitch in the Vela pulsar". *Astron. Astrophys.* **642**: A223 (2020).

Montoli A., Antonelli M., Pizzochero P.M. "The role of mass, equation of state, and superfluid reservoir in large pulsar glitches". *Mon. Not. R. Astron. Soc.* **492**: 4837 (2020).

Morawski F., Bejger M. "Neural network reconstruction of the dense matter equation of state derived from the parameters of neutron stars". *Astron. Astrophys.* **642**: A78 (2020).

Most E.R., Weih L.R., Rezzolla L., Schaffner-Bielich J. "New Constraints on Radii and Tidal Deformabilities of Neutron Stars from GW170817". *Phys. Rev. Lett.* **120**: 261103 (2018).

Newton W.G., Berger S., Haskell B. "Observational constraints on neutron star crust-core coupling during glitches". *Mon. Not. R. Astron. Soc.* **454**: 4400 (2015).

Newton W.G., Gearheart M., Hooker J., Li B.A. "The nuclear symmetry energy, the inner crust, and global neutron star modeling". *arXiv e-prints* arXiv:1112.2018 (2011).

Olausen S.A., Kaspi V.M. "The McGill Magnetar Catalog". *Astrophys. J. Suppl. Ser.* **212**: 6 (2014).

Oppenheimer J.R., Volkoff G.M. "On Massive Neutron Cores". *Physical Review* **55**: 374 (1939).

Özel F., Freire P. "Masses, Radii, and the Equation of State of Neutron Stars". *ARA&A* **54**: 401 (2016).

Özel F., Psaltis D., Narayan R., Santos Villarreal A. "On the Mass Distribution and Birth Masses of Neutron Stars". *Astrophys. J.* **757**: 55 (2012).

Pacini F. "Energy Emission from a Neutron Star". *Nature* **216**: 567 (1967).

Palfreyman J., Dickey J.M., Hotan A., Ellingsen S., van Straten W. "Alteration of the magnetosphere of the Vela pulsar during a glitch". *Nature* **556**: 219 (2018).

Pearson J.M., Chamel N., Potekhin A.Y., Fantina A.F., Ducoin C., Dutta A.K., Goriely S. "Unified equations of state for cold non-accreting neutron stars with Brussels-Montreal functionals - I. Role of symmetry energy". *Mon. Not. R. Astron. Soc.* **481**: 2994 (2018).

Piekarewicz J., Fattoyev F.J., Horowitz C.J. "Pulsar glitches: The crust may be enough". *Phys. Rev. C* **90**: 015803 (2014).

Pizzochero P.M., Antonelli M., Haskell B., Seveso S. "Constraints on pulsar masses from the maximum observed glitch". *Nature Astronomy* **1**: 0134 (2017).

Pizzochero P.M., Montoli A., Antonelli M. "Core and crust contributions in overshooting glitches: the Vela pulsar 2016 glitch". *Astron. Astrophys.* **636**: A101 (2020).

Prix R., Comer G.L., Andersson N. "Slowly rotating superfluid Newtonian neutron star model with entrainment". *Astron. Astrophys.* **381**: 178 (2002).

Pudliner B.S., Pandharipande V.R., Carlson J., Wiringa R.B. "Quantum Monte Carlo Calculations of A <=6 Nuclei". *Phys. Rev. Lett.* **74**: 4396 (1995).

Radhakrishnan V., Manchester R.N. “Detection of a Change of State in the Pulsar PSR 0833-45”. *Nature* **222**: 228 (1969).

Ravenhall D.G., Pethick C.J. “Neutron Star Moments of Inertia”. *Astrophys. J.* **424**: 846 (1994).

Reichley P.E., Downs G.S. “Observed Decrease in the Periods of Pulsar PSR 0833-45”. *Nature* **222**: 229 (1969).

Rezzolla L., Zanotti O. *Relativistic Hydrodynamics*. OUP Oxford (2013).

Riley T.E., Watts A.L., Bogdanov S., Ray P.S., Ludlam R.M., Guillot S., Arzoumanian Z., Baker C.L., Bilous A.V., Chakrabarty D., Gendreau K.C., Harding A.K., Ho W.C.G., Lattimer J.M., Morsink S.M., Strohmayer T.E. “A NICER View of PSR J0030+0451: Millisecond Pulsar Parameter Estimation”. *Astrophys. J. Lett.* **887**: L21 (2019).

Roberts M.S.E. “Surrounded by spiders! New black widows and redbacks in the Galactic field”. In J. van Leeuwen, editor, “Neutron Stars and Pulsars: Challenges and Opportunities after 80 years”, volume 291 of *IAU Symposium* pages 127–132. (2013).

Ruderman M. “Neutron Starquakes and Pulsar Periods”. *Nature* **223**: 597 (1969).

Ruderman M. “Crust-breaking by neutron superfluids and the Vela pulsar glitches.” *Astrophys. J.* **203**: 213 (1976).

Samyn M., Goriely S., Heenen P.H., Pearson J.M., Tondeur F. “A Hartree-Fock-Bogoliubov mass formula”. *Nucl. Phys. A* **700**: 142 (2002).

Sauls J.A., Chamel N., Alpar M.A. “Superfluidity in Disordered Neutron Stars Crusts”. *arXiv e-prints* arXiv:2001.09959 (2020).

Schwenk A., Friman B., Brown G.E. “Renormalization group approach to neutron matter: quasiparticle interactions, superfluid gaps and the equation of state”. *Nuclear Physics A* **713**: 191 (2003).

Sedrakian A.D. “Vortex repinning in neutron star crusts”. *Mon. Not. R. Astron. Soc.* **277**: 225 (1995).

Serim M.M., Şahiner Ş., ćerri-Serim D., Inam S.ć., Baykal A. “Discovery of a glitch in the accretion-powered pulsar SXP 1062”. *Mon. Not. R. Astron. Soc.* **471**: 4982 (2017).

Serot B.D., Walecka J.D. “The Relativistic Nuclear Many Body Problem”. *Adv. Nucl. Phys.* **16**: 1 (1986).

Seveso S., Pizzochero P.M., Grill F., Haskell B. “Mesoscopic pinning forces in neutron star crusts”. *Mon. Not. R. Astron. Soc.* **455**: 3952 (2016).

Shapiro S.L., Teukolsky S.A. *Black holes, white dwarfs, and neutron stars: The physics of compact objects*. Wiley (1983).

Shaw B., Lyne A.G., Stappers B.W., Weltevrede P., Bassa C.G., Lien A.Y., Mickaliger M.B., Breton R.P., Jordan C.A., Keith M.J., Krimm H.A. "The largest glitch observed in the Crab pulsar". *Mon. Not. R. Astron. Soc.* **478**: 3832 (2018).

Shemar S.L., Lyne A.G. "Observations of pulsar glitches". *Mon. Not. R. Astron. Soc.* **282**: 677 (1996).

Shternin P.S., Yakovlev D.G., Heinke C.O., Ho W.C.G., Patnaude D.J. "Cooling neutron star in the Cassiopeia A supernova remnant: evidence for superfluidity in the core". *Mon. Not. R. Astron. Soc.* **412**: L108 (2011).

Sidery T., Passamonti A., Andersson N. "The dynamics of pulsar glitches: contrasting phenomenology with numerical evolutions". *Mon. Not. R. Astron. Soc.* **405**: 1061 (2010).

Sieniawska M., Bejger M., Haskell B. "Estimating the EOS from the measurement of NS radii with 5% accuracy". *Astron. Astrophys.* **616**: A105 (2018).

Skyrme T.H.R. "The effective nuclear potential". *Nuclear Physics* **9**: 615 (1958).

Smoluchowski R. "Frequency of Pulsar Starquakes". *Phys. Rev. Lett.* **24**: 923 (1970).

Sourie A., Chamel N. "Vortex pinning in the superfluid core of neutron stars and the rise of pulsar glitches". *Mon. Not. R. Astron. Soc.* **493**: L98 (2020).

Sourie A., Chamel N., Novak J., Oertel M. "Global numerical simulations of the rise of vortex-mediated pulsar glitches in full general relativity". *Mon. Not. R. Astron. Soc.* **464**: 4641 (2017).

Sourie A., Oertel M., Novak J. "Numerical models for stationary superfluid neutron stars in general relativity with realistic equations of state". *Phys. Rev. D* **93**: 083004 (2016).

Speagle J.S. "DYNESTY: a dynamic nested sampling package for estimating Bayesian posteriors and evidences". *Mon. Not. R. Astron. Soc.* **493**: 3132 (2020).

Suwa Y., Yoshida T., Shibata M., Umeda H., Takahashi K. "On the minimum mass of neutron stars". *Mon. Not. R. Astron. Soc.* **481**: 3305 (2018).

Tauris T.M., Kaspi V.M., Breton R.P., Deller A.T., Keane E.F., Kramer M., Lorimer D.R., McLaughlin M.A., Possenti A., Ray P.S., Stappers B.W., Weltevrede P. "Understanding the Neutron Star Population with the SKA". In "Advancing Astrophysics with the Square Kilometre Array (AASKA14)", page 39. (2015).

Thompson C., Duncan R.C. “Neutron Star Dynamos and the Origins of Pulsar Magnetism”. *Astrophys. J.* **408**: 194 (1993).

Thompson C., Duncan R.C. “The soft gamma repeaters as very strongly magnetized neutron stars - I. Radiative mechanism for outbursts”. *Mon. Not. R. Astron. Soc.* **275**: 255 (1995).

Thompson C., Duncan R.C. “The Soft Gamma Repeaters as Very Strongly Magnetized Neutron Stars. II. Quiescent Neutrino, X-Ray, and Alfven Wave Emission”. *Astrophys. J.* **473**: 322 (1996).

Tolman R.C. “Static Solutions of Einstein’s Field Equations for Spheres of Fluid”. *Physical Review* **55**: 364 (1939).

Tondeur F., Goriely S., Pearson J.M., Onsi M. “Towards a Hartree-Fock mass formula”. *Phys. Rev. C* **62**: 024308 (2000).

Traversi S., Char P., Pagliara G. “Bayesian Inference of Dense Matter Equation of State within Relativistic Mean Field Models Using Astrophysical Measurements”. *Astrophys. J.* **897**: 165 (2020).

van Eysden C.A., Melatos A. “Pulsar glitch recovery and the superfluidity coefficients of bulk nuclear matter”. *Mon. Not. R. Astron. Soc.* **409**: 1253 (2010).

Vidaña I., Polls A., Ramos A., Engvik L., Hjorth-Jensen M. “Hyperon-hyperon interactions and properties of neutron star matter”. *Phys. Rev. C* **62**: 035801 (2000).

Warszawski L., Melatos A. “A cellular automaton model of pulsar glitches”. *Mon. Not. R. Astron. Soc.* **390**: 175 (2008).

Warszawski L., Melatos A. “Knock-on processes in superfluid vortex avalanches and pulsar glitch statistics”. *Mon. Not. R. Astron. Soc.* **428**: 1911 (2013).

Watanabe G., Pethick C.J. “Superfluid Density of Neutrons in the Inner Crust of Neutron Stars: New Life for Pulsar Glitch Models”. *Phys. Rev. Lett.* **119**: 062701 (2017).

Weber F., Negreiros R., Rosenfield P. “Neutron Star Interiors and the Equation of State of Superdense Matter”. *arXiv e-prints* arXiv:0705.2708 (2007).

Wiringa R.B., Stoks V.G.J., Schiavilla R. “Accurate nucleon-nucleon potential with charge-independence breaking”. *Phys. Rev. C* **51**: 38 (1995).

Wong T., Backer D.C., Lyne A.G. “Observations of a Series of Six Recent Glitches in the Crab Pulsar”. *Astrophys. J.* **548**: 447 (2001).

Yakovlev D.G., Ho W.C.G., Shternin P.S., Heinke C.O., Potekhin A.Y. “Cooling rates of neutron stars and the young neutron star in the Cassiopeia A supernova remnant”. *Mon. Not. R. Astron. Soc.* **411**: 1977 (2011).

Yu M., Manchester R.N., Hobbs G., Johnston S., Kaspi V.M., Keith M., Lyne A.G., Qiao G.J., Ravi V., Sarkissian J.M., Shannon R., Xu R.X. "Detection of 107 glitches in 36 southern pulsars". *Mon. Not. R. Astron. Soc.* **429**: 688 (2013).

Zavlin V.E., Pavlov G.G., Shibanov Y.A. "Model neutron star atmospheres with low magnetic fields. I. Atmospheres in radiative equilibrium." *Astron. Astrophys.* **315**: 141 (1996).

List of Publications

As of December 2020

Refereed publications

- "Effects of general relativity on glitch amplitudes and pulsar mass upper bounds". Antonelli M., **Montoli A.**, Pizzochero P.M., *Mon. Not. R. Astron. Soc.*, **475**:5403, 2018
  (Chapter 2)

- "The role of mass, equation of state, and superfluid reservoir in large pulsar glitches". **Montoli A.**, Antonelli M., Pizzochero P.M., *Mon. Not. R. Astron. Soc.*, **492**:4837, 2020
  (Chapter 3)

- "Core and crust contributions in overshooting glitches: the Vela pulsar 2016 glitch". Pizzochero P.M., **Montoli A.**, Antonelli M., *Astron. Astrophys.*, **636**:A101, 2020
  (Chapter 4)

- "Bayesian estimate of the superfluid moments of inertia from the 2016 glitch in the Vela pulsar". **Montoli A.**, Antonelli M., Magistrelli F., Pizzochero P.M., *Astron. Astrophys.*, **642**:A223, 2020
  (Chapter 4)

Publications under review

- "Statistical estimates of the pulsar glitch activity". **Montoli A.**, Antonelli M., Haskell B., Pizzochero P.M., *Submitted to Universe*, `arXiv:2012.01539`
  (Chapter 3)

Ringraziamenti

Questi tre anni di dottorato sono trascorsi in maniera estremamente rapida: sono stati ricchi di soddisfazioni, ma non privi di difficoltà e di un certo grado di atipicità, soprattutto nell'ultimo periodo. Molte persone, però, sono state in grado di renderlo un viaggio piacevole e intellettualmente stimolante, che mi ha fornito molte occasioni di crescita, e non solo come ricercatore.
In primo luogo, vorrei ringraziare il prof. Pizzochero: grazie, Pierre, per l'occasione di poter vivere il mondo della ricerca e per tutti i consigli, sia scientifici che non. Un grazie speciale anche a Marco Antonelli, per le nostre discussioni durante tutto il dottorato.
Ringrazio anche tutte le persone che fanno o che hanno fatto parte del nostro piccolo gruppo di stelle di neutroni: Thomas Celora, Lorenzo Gavassino, Elia Giliberti, Bryn Haskell. Un ringraziamento particolare a Fabio Magistrelli, per avermi insegnato cosa vuol dire essere relatore di tesi.
Citerei anche tutte le persone che ho conosciuto durante le scuole e le conferenze nel corso dei tre anni: sono davvero tante per nominarle una ad una, ma ognuna di loro mi ha insegnato qualcosa, sono stati incontri preziosi.
Vorrei ringraziare anche tutti i miei compagni di ufficio, per quanto quest'ultimo termine è alquanto relativo. Forse chiamarli compagni di pranzo o di beach volley sarebbe più appropriato: Riccardo Capelli, Andrea Di Gioacchino, Vittorio Erba, Riccardo Fabbricatore, Enrico Malatesta, Mauro Pastore, Pietro Rotondo e Federica Simonetto.
Grazie ai miei genitori, mamma Eleonora e papà Alberto, e al mio fratellino Luca. Inutile dire che senza di voi non sarei riuscito ad arrivare fino a questo punto.
Grazie infine a Francesca: grazie per la pazienza nel sopportare tutte le mie lamentele e per supportarmi nei momenti difficili.

Grazie, *Alessandro*